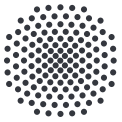

Universität Stuttgart

Accurate Quantum Simulations with Rydberg Atoms

Von der Fakultät Mathematik und Physik der Universität Stuttgart zur Erlangung der Würde eines Doktors der Naturwissenschaften (Dr. rer. nat.) genehmigte Abhandlung.

vorgelegt von

Sebastian Weber

aus Stuttgart

Hauptbericht:	Prof. Dr. Hans Peter Büchler
Mitbericht:	Prof. Dr. Maria Daghofer
Prüfungsvorsitz:	Prof. Dr. Tilman Pfau
Tag der mündlichen Prüfung:	24. November 2021

Institut für Theoretische Physik III
Universität Stuttgart

2021

Abstract

This thesis studies quantum simulations with Rydberg atoms. The idea of quantum simulations is to use a well-controllable quantum system to simulate another quantum system. Quantum simulations aim at prospectively solving challenging simulation problems that cannot be handled efficiently by classical computers, such as exploring highly entangled many-body ground states and dynamics. We focus on so-called *analog quantum simulations* that implement the system to be simulated directly and avoid the overhead of universal gate-based approaches. The class of implementable systems depends on the characteristics of the underlying platform. In general, platforms for quantum simulations must be reliable and well-controllable. Moreover, interactions must be fast in comparison to the decoherence time. Platforms that fulfill these requirements are, for example, superconducting qubits and trapped ions. Another approach is to use neutral atoms in optical tweezers. The atoms can be made interact by exciting them to the Rydberg state, i.e., an electronic state with a high principal quantum number, and harnessing the strong dipolar interactions between Rydberg atoms. Rapid developments over the last decade made it possible to use this approach to simulate various spin Hamiltonians on arbitrary two- and three-dimensional lattices, even in regimes beyond an exact numerical treatment. The research covered in this thesis contributed to this progress by providing theory support for the experimental realization of quantum simulations.

The focus of this thesis is two-fold. First, we address the calculation of Rydberg interaction potentials and their dependence on experimental parameters. Second, we use our insights about Rydberg interactions and show how accurate quantum simulations with Rydberg atoms can be applied to study various quantum spin models. Specifically, we demonstrate how different topological phases can be investigated. The latter was conducted in close collaboration with the experimental group of Antoine Browaeys in Paris. In a side project, we collaborated with the group of Andrew Daley in Glasgow and with Gregory Bentsen on a proposal for realizing a fast scrambling spin model with Rydberg atoms. In the following, we give an overview of the chapters of this thesis.

- In Chapter 1, we provide an introduction to the field of quantum simula-

tions and the Rydberg platform. We outline the current state of research, describe present challenges, and locate our work within the field.

- In Chapter 2, we discuss the theoretical foundations of our research. We provide background information about quantum simulators and discuss their applications. Afterward, we describe the Rydberg platform in detail. Since in this thesis, quantum simulations are mainly applied to study topological phases, we also provide a primer on topological phases.

- In Chapter 3, we review the non-perturbative calculation of Rydberg interaction potentials. The chapter is based on our tutorial on this topic [1]. The realization of quantum simulations requires a precise understanding of the Rydberg interaction beyond a perturbative description and a detailed knowledge about the dependence of the interaction on experimental parameters. Such an understanding is also required for applications in quantum information science, for example, for engineering two- and multi-qubit quantum gates. We have released our software `pairinteraction` for calculating Rydberg interaction potentials as open-source, see `https://pairinteraction.github.io`.

- In Chapter 4, we make use of our software to find suitable experimental parameters for mapping electronic states of a Rydberg atom to spin states. This mapping is necessary for quantum simulations of spin Hamiltonians with Rydberg atoms. For accurate simulations, experimental parameters must be tuned in a way that prevents the Rydberg interaction to couple the Rydberg states, which are mapped to spin states, to unwanted Rydberg states. Using the quantum simulation of anisotropic Ising magnets as an example [2, 3], we analyze which experimental parameters are suitable. The group of Antoine Browaeys has performed experiments that confirm our predictions. Together with the previous chapter, this chapter forms a basis for various quantum simulations of spin models.

- In Chapter 5, we discuss the quantum simulation of a symmetry-protected topological phase of interacting bosons in a one-dimensional lattice. The discussion is based on a joint theoretical and experimental project with the group of Antoine Browaeys [3, 4]. The setup uses atoms that are trapped in an array of optical tweezers and are excited into Rydberg states, giving rise to hard-core bosons with an effective hopping by dipolar exchange interaction. We show that the adiabatically prepared ground state of the system has the characteristic features [5] of a symmetry-protected

topological phase, like a robust ground state degeneracy attributed to protected edge states. The experimental results of our collaborators are in perfect agreement with our theoretical studies.

- In Chapter 6, we study non-trivial complex hopping amplitudes of Rydberg excitations and the resulting chiral motion in a minimal setup of three lattice sites that has been experimentally realized by the group of Antoine Browaeys [6, 7]. The complex hopping amplitudes can simulate effective magnetic fields in the Rydberg platform. They emerge from the intrinsic spin-orbit coupling of dipolar exchange interaction in combination with time-reversal symmetry breaking by a homogeneous external magnetic field. The resulting Peierls phase of the hopping amplitude between two sites depends on the geometry and the presence of an excitation on the third site. We compare our theoretical description of the setup with the experimental results, achieving an excellent agreement.

- In Chapter 7, we make a proposal for the quantum simulation of a fractional Chern insulator with Rydberg atoms. It is based on the interplay between the non-trivial topology of a band structure and interactions between particles. The topologically non-trivial band structure results from an effective magnetic field that can be realized as described in the previous chapter. The interaction between particles emerges from the hard-core constraint of Rydberg excitations. We obtain a robust nearly two-fold ground state degeneracy on a torus and a many-body Chern number of one for realistic experimental parameters. We show how an experiment could probe the fractional character of excitations.

- In Chapter 8, we present a side project where we collaborated with the group of Andrew Daley and with Gregory Bentsen [8]. We discuss a proposal to implement a deterministic fast scrambler, illustrating the variety of models that can be implemented using Rydberg interactions. Fast scramblers are quantum systems that produce many-body entanglement on a timescale that grows logarithmically with the system size N. We show that a fast scrambler can be realized with a one-dimensional array of neutral atoms, using $\mathcal{O}(\log N)$ shuffling and parallel gate operations, where controlled-Z gates are performed using Rydberg interactions. We analyze the information scrambling in a realistic setup, taking into account decoherence. Our protocol can be harnessed to produce highly entangled states on noisy hardware, where a fast generation of entanglement is crucial to limit effects of decoherence.

Abstract

Zusammenfassung

Diese Doktorarbeit behandelt Quantensimulationen mit Rydberg-Atomen. Unter dem Begriff Quantensimulation versteht man die Idee, gut kontrollierbare quantenmechanische Systeme zur Simulation von anderen quantenmechanischen Systemen zu verwenden. Quantensimulationen werden entwickelt, um herausfordernde Simulationsprobleme lösen zu können, die von klassischen Computern nicht effizient lösbar sind. Hierzu gehören zum Beispiel die Erforschung von Grundzuständen hoch verschränkter, quantenmechanischer Vielteilchen-Systeme und deren Dynamik. Wir konzentrieren uns auf sogenannte *analoge Quantensimulationen*, welche zu simulierende Systeme direkt und mit einem geringeren Ressourcenbedarf implementieren als universelle, gatterbasierte Systeme. Die Klasse der implementierbaren Systeme hängt von den Eigenschaften der Plattform ab, die dem Simulator zugrunde liegt. Quantensimulatoren benötigen zuverlässige und gut zu kontrollierende Plattformen, bei denen die Wechselwirkung auf signifikant schnelleren Zeitskalen abläuft als die Dekohärenz. Diese Bedingungen werden zum Beispiel von Plattformen mit supraleitenden Qubits und gefangenen Ionen erfüllt. Ein anderer Ansatz ist es, neutrale Atome zu verwenden. Die Wechselwirkung zwischen den Atomen lässt sich realisieren, indem man sie in den Rydberg-Zustand anregt, also in einen elektronischen Zustand mit hoher Hauptquantenzahl, und die starke dipolare Wechselwirkung zwischen Rydberg-Atomen ausnutzt. Der rasante Fortschritt im letzten Jahrzehnt hat es möglich gemacht, mit diesem Ansatz Spin-Hamiltonians auf beliebigen zwei- und dreidimensionalen Gittern zu simulieren, sogar in Regimen, in denen exakte numerische Simulationen nicht mehr durchführbar sind. Die in dieser Doktorarbeit behandelte Forschung hat hierzu beigetragen, in dem sie theoretischen Grundlagen für die experimentelle Realisierung von Quantensimulationen geliefert hat.

Diese Doktorarbeit hat zwei Schwerpunkte. Zunächst beschäftigen wir uns mit der genauen Berechnung der Wechselwirkung zwischen Rydberg-Atomen und ihrer Abhängigkeit von experimentellen Parametern. Danach verwenden wir diese Erkenntnisse, um zu zeigen, wie mit Rydberg-Quantensimulationen verschiedene Spinmodelle studiert werden können. Insbesondere untersuchen wir die Realisierung unterschiedlicher topologischer Phasen. Diese Forschung ist

in enger Zusammenarbeit mit der Experimentalgruppe von Antoine Browaeys in Paris erfolgt. Als Nebenprojekt haben wir mit der Gruppe von Andrew Daley in Glasgow und mit Gregory Bentsen an einem Proposal zur Realisierung schneller Scrambler gearbeitet. Im Folgenden wird ein kurzer Überblick über die Kapitel der Doktorarbeit gegeben.

- In Kapitel 1 geben wir eine Übersicht über Quantensimulatoren und die Rydberg-Plattform. Wir diskutieren den Stand der Technik, beschreiben aktuelle Herausforderungen und ordnen die Doktorarbeit in das Forschungsfeld ein.

- In Kapitel 2 behandeln wir die theoretischen Grundlagen der Arbeit. Wir geben einen Überblick über Quantensimulatoren und ihre Anwendung. Danach wird die Rydberg-Plattform im Detail beschrieben. Da wir uns hauptsächlich mit Quantensimulationen von topologischen Phasen beschäftigen, geben wir am Ende des Kapitels eine Übersicht über topologische Phasen.

- In Kapitel 3 geben wir eine Einführung in die nicht perturbative Berechnung von Wechselwirkungspotentialen zwischen zwei Rydberg-Atomen. Das Kapitel basiert auf unserem Tutorial zu diesem Thema [1]. Die Realisierung von Quantensimulationen erfordert ein genaues Verständnis der Rydberg-Wechselwirkung und deren Abhängigkeit von experimentellen Parametern. Dieses Verständnis wird auch für Anwendungen im Bereich der Quanteninformatik benötigt, zum Beispiel um Zwei- und Multi-Qubit-Gatter mithilfe der Wechselwirkung zu realisieren. Wir haben die Open-Source-Software `pairinteraction` zur Berechnung der Wechselwirkungspotentiale entwickelt, siehe `https://pairinteraction.github.io`.

- In Kapitel 4 verwenden wir die Software, um experimentelle Parameter zu finden, die es ermöglichen, elektronische Zustände eines Rydberg-Atoms auf Spinzustände abzubilden. Diese Abbildung wird für Quantensimulationen von Spin-Hamiltonians benötigt. Für akkurate Simulationen ist es wichtig, dass die experimentellen Parameter so eingestellt werden, dass die auf die Spinzustände abgebildeten Zustände des Rydberg-Atoms nicht an weitere Zustände koppeln. Am Beispiel der Quantensimulation von anisotropen Ising-Magneten [2, 3], analysieren wir, welche experimentellen Parameter geeignet sind. Die Gruppe von Antoine Browaeys hat Experimente durchgeführt, die unsere Vorhersagen bestätigen. Zusammen mit

dem vorherigen Kapitel, legt dieses Kapitel eine Grundlage für verschiedene Quantensimulationen von Spinmodellen, die wir in den nachfolgenden Kapiteln beschreiben.

- In Kapitel 5 besprechen wir die Quantensimulation einer durch Symmetrie geschützten topologischen Phase aus wechselwirkenden Bosonen in einem eindimensionalen Gitter. Das Kapitel basiert auf einem gemeinsamen Projekt mit der Experimentalgruppe von Antoine Browaeys [3, 4]. Das experimentelle Setup benutzt Atome, die in einem Array aus optischen Pinzetten gefangen und in Rydberg-Zustände angeregt sind. Mit den Rydberg-Zuständen simuliert das Experiment sogenannte Hard-Core-Bosonen mit einem effektiven Hüpfen aufgrund der dipolaren Austauschwechselwirkung. Wir zeigen, dass der adiabatisch präparierte Grundzustand die charakteristischen Eigenschaften [5] einer durch Symmetrie geschützten topologischen Phase aufweist, wie zum Beispiel eine robuste Grundzustandsentartung, die auf geschützte Randzustände zurückgeführt werden kann. Die experimentellen Ergebnisse sind in sehr guter Übereinstimmung mit unseren theoretischen Studien.

- In Kapitel 6 analysieren wir die nicht trivialen komplexen Hüpfamplituden von Rydberg-Anregungen und die daraus entstehende chirale Bewegung in einem Minimalsystem mit drei Gitterplätzen. Dieses System wurde von der Gruppe von Antoine Browaeys realisiert [6, 7]. Die komplexen Hüpfamplituden können verwendet werden, um effektive Magnetfelder zu simulieren. Sie entstehen aus der Kombination von intrinsischer Spin-Orbit-Kopplung der dipolaren Austauschwechselwirkung und gebrochener Zeitumkehrsymmetrie. Im Experiment wird die Symmetrie durch ein homogenes, externes Magnetfeld gebrochen. Der Wert der resultierenden Peierls-Phase der Hüpfamplituden zwischen zwei Gitterplätzen hängt von der Geometrie und dem Vorhandensein einer weiteren Anregung auf dem verbleibenden Gitterplatz ab. Wir vergleichen unsere theoretische Beschreibung des Setups mit experimentellen Ergebnissen und erreichen eine hervorragende Übereinstimmung.

- In Kapitel 7 präsentieren wir ein Proposal, wie ein fraktionaler Chern-Isolator mit Rydberg-Atomen realisiert werden kann. Die vorgeschlagene Realisierung basiert auf einem Zusammenspiel der nicht trivialen Topologie der Bandstruktur und der Wechselwirkung zwischen Teilchen. Die nicht triviale Topologie resultiert aus einem effektiven Magnetfeld, das wie im vorherigen Kapitel beschrieben realisiert werden kann. Die

Wechselwirkung zwischen den Teilchen kommt dadurch zustande, dass sich an einem Gitterplatz nur eine einzige Rydberg-Anregung befinden kann. Wir erhalten für realistische, experimentelle Parameter eine robuste zweifache Quasientartung des Grundzustandes auf einem Torus und eine Vielteilchen-Chern-Zahl von eins. Wir zeigen, wie der fraktionale Charakter von Anregungen experimentell detektiert werden kann.

- In Kapitel 8 stellen wir ein Nebenprojekt vor, an dem wir in Kooperation mit der Gruppe von Andrew Daley und mit Gregory Bentsen mitgewirkt haben [8]. Dieses Nebenprojekt illustriert, dass sich neben topologischen System auch vollkommen andere Systeme mit Rydberg-Wechselwirkung realisieren lassen: Wir machen einen Vorschlag, wie ein deterministischer, schneller Scrambler implementiert werden kann. Schnelle Scrambler sind Quantensysteme, die eine Vielteilchen-Verschränkung auf einer Zeitskala aufbauen, die logarithmisch mit der Systemgröße N wächst. Wir zeigen, dass sich ein schneller Scrambler mit einem eindimensionalen Array neutraler Atome unter Verwendung von $\mathcal{O}(\log N)$ Verschiebeoperationen und parallelen Gatteroperationen realisieren lässt. Die hierbei verwendeten CZ-Gatter basieren auf der Rydberg-Wechselwirkung. Wir analysieren das Scrambling von Information in einem realistischen Setup, bei dem wir Dekoheränz berücksichtigen. Unser Protokoll kann zur Erzeugung hochverschränkter Zustände auf Systemen mit geringer Rauschresistenz verwendet werden, bei denen eine schnelle Erzeugung von Verschränkung wichtig ist, um Dekoheränz zu beschränken.

List of Publications

The following publications are covered in this thesis:

- T. Hashizume*, G. S. Bentsen*, S. Weber, and A. J. Daley, "Deterministic Fast Scrambling with Neutral Atom Arrays", Physical Review Letters **126**, 200603 (2021)

- V. Lienhard*, P. Scholl*, S. Weber, D. Barredo, S. de Léséleuc, R. Bai, N. Lang, M. Fleischhauer, H. P. Büchler, T. Lahaye, and A. Browaeys, "Realization of a Density-Dependent Peierls Phase in a Synthetic, Spin-Orbit Coupled Rydberg System", Physical Review X **10**, 021031 (2020)

- S. de Léséleuc*, V. Lienhard*, P. Scholl, D. Barredo, S. Weber*, N. Lang*, H. P. Büchler, T. Lahaye, and A. Browaeys, "Observation of a symmetry-protected topological phase of interacting bosons with Rydberg atoms", Science **365**, 775 (2019)

- S. de Léséleuc*, S. Weber*, V. Lienhard, D. Barredo, H. P. Büchler, T. Lahaye, and A. Browaeys, "Accurate Mapping of Multilevel Rydberg Atoms on Interacting Spin-1/2 Particles for the Quantum Simulation of Ising Models", Physical Review Letters **120**, 113602 (2018)

- S. Weber, C. Tresp, H. Menke, A. Urvoy, O. Firstenberg, H. P. Büchler, and S. Hofferberth, "Calculation of Rydberg interaction potentials", Journal of Physics B: Atomic, Molecular and Optical Physics **50**, 133001 (2017)

Further publications:

- S. Weber*, P. Bienias*, and H. P. Büchler, "Topological bands in the continuum using Rydberg states", arXiv:2101.08363 (2021)

*These authors contributed equally.

- S. Weber, S. de Léséleuc, V. Lienhard, D. Barredo, T. Lahaye, A. Browaeys, and H. P. Büchler, "Topologically protected edge states in small Rydberg systems", Quantum Science and Technology **3**, 044001 (2018)
- C. Tresp, P. Bienias, S. Weber, H. Gorniaczyk, I. Mirgorodskiy, H. P. Büchler, and S. Hofferberth, "Dipolar Dephasing of Rydberg D-State Polaritons", Physical Review Letters **115**, 083602 (2015)

Open-source software:

- **pairinteraction:** The `pairinteraction` software simulates systems of one or two Rydberg atoms, taking into account electric and magnetic fields in arbitrary directions as well as multipole interaction up to arbitrary order. The software consists of a high-performance C++ library, a Python library as a convenient API, and an easy-to-use graphical user interface for pair potential calculations (`https://pairinteraction.github.io`).
- **mpiprocessing:** The `mpiprocessing` Python library implements a parallel map, using the message passing interface (`https://github.com/seweber/mpiprocessing`).

Contents

1

Introduction

The simulation of quantum many-body systems with classical computers is very challenging [9, 10]. The difficulty is that the number of coefficients required to describe a quantum system scales exponentially with the number of its constituents. This scaling leads to exponentially large memory requirements and exponentially long processing times. In practice, storing all the coefficients of a quantum state of 50 spin-1/2 particles would already require several petabytes of memory. Admittedly, approximative methods can simulate some quantum many-body systems classically by storing quantum states in compressed formats, such as tensor networks [11]. However, it is widely believed that classical systems cannot simulate highly entangled quantum systems efficiently [12]. In addition, it is sometimes hard to assess the range of validity of approximative methods. In 1981, Richard Feynman proposed as a solution to use a quantum – not a classical – simulator for simulating quantum systems [9]. The core of a quantum simulator is a well-controllable and accessible quantum system which can be initialized to a well-defined quantum state that evolves under a specifiable Hamiltonian in time [13–15]. The prime application of a quantum simulator is to study ground states and the dynamics of quantum many-body systems. In addition, quantum simulators are investigated as tools for solving classical optimization problems [16, 17]. Moreover, quantum simulators are of interest for benchmarking future quantum computers. They can also be applied to benchmark and refine numerical methods that treat quantum systems approximately [18]. For more details on possible applications, see Section 2.1.

One distinguishes between *digital* quantum simulators that use gate operations to simulate a quantum system, *analog* quantum simulators that implement the Hamiltonian of a system directly, and hybrids of the two. This thesis focuses on the analog approach (except for Chapter 8). One advantage of analog quantum simulations is that they are presumably more robust against imperfections

than digital ones as long as error correction is unavailable. For example, let us suppose that we perform an analog simulation of a quantum phase that occurs in nature. In this case, the phase will presumably be robust against perturbations of a small fraction of lattice sites because these imperfections exist in many natural materials as well [10]. In addition, analog simulations avoid the overhead of their digital counterparts. For digital simulations, time evolution operators must be approximated by sequences of gate operations according to the so-called Trotter decomposition [14]. There, increasing the precision of a quantum simulation requires increasing the number of gate operations. Yet, a vast number of gate operations is hardly feasible with the current noisy intermediate-scale quantum (NISQ) digital devices [19]. This could change in the future if capable fault-tolerant digital devices become available. However, until then, the reign of analog quantum simulators may persist. In particular, while quantum supremacy has been demonstrated with gate-based quantum computers [20], analog quantum simulators are promising candidates for establishing practical quantum advantage. Some of the most recent analog quantum simulations already operate in regimes that are beyond an exact numerical treatment because the number of constituents is too large. The reproduction of these quantum simulations on classical computers requires extensive calculations with approximative algorithms, such as tensor network or quantum Monte Carlo methods [21–28]. An ongoing challenge is the development of an analog quantum simulator that simulates a highly entangled system which such a high precision that approximative classical algorithms can no longer compete.

This challenge is complicated by the fact that analog quantum simulators cannot simulate arbitrary systems; instead, the class of Hamiltonians that are implementable by an analog quantum simulator depends on the details of the underlying experimental platform. However, there are many exciting models among the implementable Hamiltonians, such as Hubbard models, Ising-like models, and some other spin models [14, 15]. In addition, analog simulators are well suited to study universal features that are robust against perturbations [19]. Then, it might be acceptable to add additional terms to the Hamiltonian to make it implementable on a specific platform. Moreover, recent research shows that a variational quantum simulation scheme can widen the class of simulatable Hamiltonians. Within this scheme, an analog quantum simulator is applied to prepare and probe highly entangled variational trial states [29].

Platforms for quantum simulations must comprise a quantum system that has many degrees of freedom, and that can be initialized in a known quantum state. In addition, one must be able to perform measurements on the system,

and it must prospectively be possible to engineer Hamiltonians that cannot be efficiently simulated classically [10]. The latter implies that interactions must be fast in comparison to the decoherence time [30]. Different platforms fulfill these criteria, as shown in the review [15], each one having its own advantages and disadvantages. Before discussing the Rydberg platform in the next paragraph, we would like to give a brief overview of alternative platforms. Prominent examples are superconducting circuits [31, 32], linear ion traps [33, 34], and neutral atoms in optical lattices [35–37]. Superconducting circuits and trapped ions can be controlled precisely and are applied for analog quantum simulations, mainly of spin Hamiltonians, as well as digital quantum simulations. However, at the time of writing, these platforms only support the simulation of several tens of spins. It is a key challenge to scale these platforms up. Going beyond several tens of spins in ion traps requires demanding techniques such as shuttling around ions [38, 39]. By contrast, neutral atoms in optical lattices offer thousands of particles, albeit with less control over the particles than superconducting circuits or trapped ions. This platform was used for first analog quantum simulation in 2002 [40] and has been developed further since then. It allows for the native realization of fermions and bosons by using fermionic or bosonic atomic species. The platform is typically applied for analog quantum simulations of Hubbard models, being rather limited in the implementable lattice geometries and Hamiltonians. Cooling in optical lattices is a current challenge that is tackled by entropy redistribution [37].

In this thesis, we focus on the Rydberg platform [41]. While the Rydberg platform can take different forms, we limit ourselves to analog quantum simulations that use arrays of optical tweezers loaded with neutral atoms, which can be made interact by exciting them to Rydberg states. This approach is relatively new yet promising [42, 43].

The optical tweezers can be arranged in arbitrary one-, two-, and three-dimensional arrays [44–47]. Atoms from a laser-cooled atomic gas are loaded randomly into the tweezers; light-assisted collisions ensure that each tweezer is either empty or occupied with exactly one atom. Since 2016, the randomly loaded tweezers can be spatially rearranged into new arrays with almost unit filling [44–46]. By following this protocol, arbitrary geometries are viable with above two hundred atoms at the time of writing [24, 25].

The neutral atoms can be made interact by exciting them into Rydberg states. These are states where the outermost electron is excited to a high principal quantum number n [48–50]. As a result, the electron is less bound to the core, increasing the interaction between atoms and with fields. In fact,

the van der Waals interaction [51–54] scales as n^{11} and the dipolar exchange interaction [55] as n^4, typically reaching interaction strengths $V/h \gtrsim 1$ MHz for $n = 60$ at an interatomic distance of 10 μm (with Planck's constant h) [42, 56]. The radiative lifetime increases as n^3, reaching 100 μs at room temperature for the states considered within this thesis[1]. Thus, one can operate in a coherent regime where the interaction is much stronger than decoherence. Note that in many current experiments, the runtime is not yet limited by the lifetime but instead by the movement of the Rydberg atoms. This is because the utilized optical tweezers trap ground state atoms only. This issue is addressed, for example, by the development of so-called magic traps[2] [59].

Different kinds of spin Hamiltonians are realizable with the Rydberg platform. The general idea is to map electronic states of the atoms to spin states. To make this mapping accurate and control the interaction between the atoms, external electric and magnetic fields, light shifts, and dressing techniques can be applied. Together with the ability to realize arbitrary arrays, these tools allow for implementing various Hamiltonians in a well-controllable manner. For example, Ising-like models [23–25, 60–62] and XY-type Hamiltonians [4, 63] have been simulated. Effective magnetic fields are feasible, too [6, 64]. For a detailed overview of implementable models and technical details, see Section 2.2.

As these examples illustrate, the Rydberg platform provides an exciting mixture between versatility, controllability, and the size of implementable systems.

In the following, we place the research covered in this thesis into the context of the developments outlined above.

As described before, a significant challenge is to increase the control and accuracy of quantum simulations to outperform approximative classical simulations. A hope is that the studies of the interactions between Rydberg atoms presented in Chapters 3 and 4 help to achieve this goal in the future. We published a tutorial about the calculation of Rydberg interaction potentials [1] and wrote the `pairinteraction` software for performing this calculation. The software is released as open-source, see `https://pairinteraction.github.io`. Within

[1] By contrast, for circular Rydberg states, i.e., Rydberg states with maximum orbital and magnetic quantum numbers, even lifetimes in the range of seconds are possible. However, circular states are more challenging to prepare [57, 58].

[2] One can find magic conditions that allow for trapping both ground-state atoms and Rydberg atoms with the same tweezers. For example, alkaline earth atoms provide the tunability required to find such conditions by the polarizability of the second valence electron [59].

this thesis, the `pairinteraction` software was applied to find viable parameters for various quantum simulations with Rydberg atoms. We mainly focused on topological phases, which are discussed in Section 2.3, as they seem to be especially worthwhile targets for analog quantum simulators. This is because of two reasons. First, a topological phase does not belong to a specific Hamiltonian but an equivalence class of Hamiltonians, as it is the case for phases in general. Thus, there is no need to implement a particular Hamiltonian. Instead, one can choose the Hamiltonian that is easiest to implement from the class. Second, topologically non-trivial many-body ground states had not been studied with quantum simulators before.

We explored the simulation of a symmetry-protected topological phase of interacting bosons together with our experimental colleagues from the group of Antoine Browaeys [4], see Chapter 5. Contrary to experiments studying phenomena of topology that can be understood on the single-particle level [65–80], the experiment was the first quantum simulation that studied a topological phase of interacting particles. Recently, topological spin liquids has been studied with Rydberg atoms as well, another example for a topological phase [23, 81].

Yet another possibility for realizing topological phases is to make use of effective magnetic fields [65, 68, 69, 82–93] that can be simulated by non-trivial complex hopping amplitudes of Rydberg excitations. These emerge from the intrinsic spin-orbit coupling of dipolar exchange interactions in combination with time-reversal symmetry breaking [94]. We contributed to an experiment that demonstrated this effect in a minimal setup with three atoms [6], see Chapter 6. An effective magnetic field is an ingredient for realizing topological band structures [64] and fractional Chern insulators. Our proposal for the realization of a fractional Chern insulator was conducted with realistic experimental parameters, see Chapter 7. Hence, there is a chance that Rydberg atoms could be among the first platforms to realize fractional Chern insulators in artificial matter. Because of the microscopic control of the particles within a quantum simulator, this can help to deepen our understanding of topological states of matter.

2

Foundations

This chapter provides background information on quantum simulation, the Rydberg platform, and topological phases. The intention is not to replace a textbook but to provide a synopsis of essential concepts. For readers interested in more details, collections of handy references are given at the beginning of each section.

2.1 Quantum Simulation

For a brief primer on quantum simulation, the reader may refer to the introduction of this thesis, see Chapter 1. In the following, some specific aspects of quantum simulations are discussed in detail – in particular, possible applications, verification of results, and the relation between quantum simulators and quantum computers.

The extensive reviews listed below contain further information about quantum simulation:

- "Quantum simulation" by I. M. Georgescu *et al.* (2014) [14]: Introduction to digital and analog quantum simulation, detailed description of platforms and potential applications.
- "Quantum Simulators: Architectures and Opportunities" by E. Altman *et al.* (2021) [15]: Up-to-date overview about platforms, challenges, and opportunities for quantum simulators.

2.1.1 Applications

This section extends the discussion on potential applications of quantum simulation provided in the introduction.

Let us start by thinking about the purpose of simulations in general [95]. Simulations are supposed to provide insights about systems that cannot be obtained otherwise. In comparison to probing a natural system directly, simulations offer two advantages: First, they enable us to change the parameters of a system in ways that are hard to implement in reality, allowing us to obtain a better understanding of their respective influence (it is even possible to study entirely hypothetical systems). Second, simulations may provide access to properties that cannot be investigated otherwise.

These are also the incentives for simulating quantum systems. However, as pointed out already by Richard Feynman in 1981, quantum systems are very challenging to simulate with classical computers [9]. Thus, he proposed to use quantum simulators. Which quantum systems exactly are hard to simulate classically is yet an open question. The development of new classical algorithms and a better understanding of physics paved the way to remarkable classical simulations that had been considered very difficult before. For example, a two-dimensional system of 64×64 spins has been simulated classically, despite exhibiting area law entanglement [96]. Furthermore, numerical studies show that if one permits gate infidelities on the order of 1%, a quantum computer with quasi-one-dimensional connectivity can be simulated classically with moderate computational cost [97]. At the time of writing, such gate infidelities are typical for experiments. However, highly entangled quantum states are – from a fundamental point of view – believed to be inaccessible by classical computers [12]. Thus, for simulating these states, a quantum simulator is required. In addition, many classical simulations of quantum systems rely on sophisticated, system-specific approximations that are challenging to come up with and tricky to verify.

Thus, calculating the dynamics of interacting many-body systems and their ground states are paradigmatic use cases of quantum simulators. The ground states can be calculated, for example, by adiabatic preparation. This technique is applied for the quantum simulations discussed in Chapters 5 and 7.

Quantum simulators can also be applied to benchmark algorithms developed for simulating quantum systems classically. This application is particularly useful because for some approximative algorithms, there are no well-established error estimates that allow us to determine when the algorithms are reliable without benchmarking them [18]. Moreover, benchmarking quantum computers is a use case for quantum simulators in the future.

In addition to studying quantum systems, quantum simulators might help to solve some *classical* problems as well. Some optimization problems can be mapped to the problem of finding the ground state of certain spin models [16,

17, 98]. For example, the maximum independent set problem[3] might be solvable by a Rydberg quantum simulator [16]. However, there is still an open debate about how efficiently these optimization problems can be handled by quantum hardware. One concern is that the ground state of the obtained spin model is separated by a tiny gap from the excited states which decreases exponentially with the system size. Hence, long runtimes may be required for the adiabatic preparation of the ground state [100]. Alternatives to the adiabatic preparation scheme are explored, too [101].

Lastly, quantum simulators can be applied to prepare highly entangled states, whose correlations can be applied to beat the standard quantum limit and thus for developing sensors and clocks with enhanced precision [102].

2.1.2 Verification

Independenty of its application, the careful verification of a quantum simulator is vital to ensure the correctness of its results. For verification, different complementary techniques exist.

First, we can verify the quantum simulator's constituents and their interplay by comparing quantum simulations for small system sizes with numerical simulations. This approach is applied throughout this thesis. In regimes that can be simulated efficiently on classical computers by approximative algorithms, we can also make the comparison for larger system sizes. However, there one danger lies in quantum simulations being presumably more sensitive to disorder and noise in classically inaccessible regimes than in regimes that can be simulated on a classical computer [103].

Second, for systems that are inaccessible by classical computers, we can use the quantum simulator to probe itself. The idea is to apply the time evolution under a Hamiltonian to the initial state and then reverse it. By doing so, we can check whether the time evolution is unitary. If it is the case, we must end up with the initial state again.

Third, one can compare results between different quantum simulators and quantum computers.

Fourth, a new approach is to use randomized benchmarking to verify analog quantum simulators. Originally, randomized benchmarking was developed for

[3] In graph theory, an independent set is a set of vertices of a graph such that for every two vertices, there is no edge connecting them. It is called maximal if one cannot add another vertex without destroying its independence. The maximum independent set is the largest maximal independent set for a given graph. Finding it is an NP-hard problem [99].

digital quantum computers, but it has been recently adopted successfully to the analog setting [104].

2.1.3 Relation to Quantum Computing

This section aims at readers that are familiar with quantum computing and addresses the connection between quantum *computing* and quantum *simulation*.

Digital quantum simulators are closely related to digital quantum computers. The simulators use the Trotter decomposition to approximate the time evolution under a Hamiltonian as a sequence of gates acting on a register of qubits. If the gates constitute a universal set and if the qubits are fully addressable, the device is, in fact, a universal digital quantum computer. In this case, any local Hamiltonian can be simulated efficiently [13].

Analog quantum simulators are closely related to so-called adiabatic quantum computers. Both devices have in common that they directly implement the Hamiltonian of interest. If an analog quantum simulator can implement and adiabatically change any local Hamiltonian, the device constitutes a universal adiabatic quantum computer. Furthermore, such a device would have the same computational power as a universal digital quantum computer [105].

The close relation between quantum simulators and quantum computers is also evidenced by both requiring similar platforms. Criteria for suitable quantum computing platforms have been worked out in [106], criteria for quantum simulators in [10]. As a comparison of the two publications shows [43], the criteria for quantum computers are indeed very similar but more restrictive than the criteria for quantum simulators. Specialized analog quantum simulators are more straightforward to build than universal quantum computers. On the other hand, specialized analog quantum simulators can never reach the versatility of universal error-corrected quantum computers. However, as error correction causes a massive overhead in addition to the overhead of the Trotter decomposition, it will probably take a long time until specialized analog quantum simulators are outperformed by universal quantum computers – even if error correction was demonstrated successfully [19].

2.2 Rydberg Platform

Here, the Rydberg platform and its application to analog quantum simulations are discussed. While the Rydberg platform can take different forms, we limit ourselves to a particular setup. In the context of this thesis, the Rydberg platform involves an array of optical tweezers loaded with neutral atoms, which

can be made interact by exciting them to the so-called Rydberg state. This platform has emerged as a highly promising tool for analog quantum simulations. The following discussion addresses readers who would like to obtain a thorough overview of the platform.

Details about Rydberg physics and the platform can be found in the following comprehensive books and reviews:

- "Rydberg Atoms" by T. F. Gallagher (1994) [48]: The reference work on properties of Rydberg atoms.
- "Rydberg Physics" by N. Šibalić and C. S. Adams (2018) [50]: Recent review about new possibilities for quantum optics, simulation, and sensing offered by Rydberg atoms.
- "Many-body physics with individually controlled Rydberg atoms" by A. Browaeys and T. Lahaye (2020) [42]: Overview about the Rydberg platform as it is considered within this thesis.
- "Quantum simulation and computing with Rydberg-interacting qubits" by M. Morgado and S. Whitlock (2021) [43]: General introduction into platforms using Rydberg atoms, review of quantum simulation and computing schemes.
- In addition, Chapter 3 of this thesis discusses the calculation of Rydberg interaction potentials. The discussion is based on our tutorial [1].

2.2.1 Properties of Rydberg Atoms

Before details of the Rydberg platform are discussed, this section provides a general introduction into Rydberg physics, aiming at readers who have no previous experience in this field.

Let us begin with defining Rydberg states. In general, a Rydberg state is a highly excited electronic state in the presence of a positively charged core [48–50]. Because the state is highly excited, the electron is far away from the core and feels a Coulomb-like potential. As a consequence, a Rydberg state behaves comparably to a state of a hydrogen atom with a high principal quantum number n. Rydberg states can be prepared in different physical systems, for example, in solid-state systems [107], ions [108], and atoms. In the case of the latter, we speak about Rydberg atoms.

Typical examples of atomic species used for exploring Rydberg physics are alkali atoms or alkaline earth atoms. Our experimental collaborators from the

Property	Scaling	Value for ^{87}Rb $\|60S_{1/2}\rangle$
Orbital radius $\langle r \rangle$	$(n^*)^2$	0.26 μm
Radiative lifetime τ	$(n^*)^3$	100 μs at $T = 300$ K
Transition dipole moment[5] d	$(n^*)^2$	2127 ea_0
Binding energy E_n/h	$(n^*)^{-2}$	-1017.24 GHz
Energy splitting $(E_{n+1} - E_n)/h$	$(n^*)^{-3}$	34.85 GHz
Dipole interaction coefficient[5] C_3/h	$(n^*)^4$	4.41 GHz μm^3
Van der Waals coefficient C_6/h	$(n^*)^{11}$	137.81 GHz μm^6
Polarizability α/h	$(n^*)^7$	0.18 GHz cm^2/V^2

Table 2.1: Overview about how properties of Rydberg atoms scale with the effective quantum number n^* [48]. Here, h is Planck's constant, e the elementary charge, and a_0 the Bohr radius. The values for ^{87}Rb $|60S_{1/2}\rangle$ are calculated with our `pairinteraction` software [1] and the `ARC` library by N. Šibalić *et al.* [56].

group of Antoine Browaeys in Paris are using the alkali atom ^{87}Rb. Alkali atoms have the unique feature that the remaining electrons form a closed shell after exciting the outermost electron to the Rydberg state. Thus, it is relatively straightforward to model these Rydberg atoms numerically with great accuracy, see Chapter 3, because one only needs to consider one active electron. While this single electron picture often works out for alkaline earth atoms as well [109], one must watch out for perturber states that make the theoretical description of these systems more challenging [110]. However, the Rydberg atoms studied within this thesis do not have this difficulty and can be described very similarly to hydrogen atoms[4]. We can use the fine structure bases $|n, l, j, m_j\rangle$ to label our Rydberg states because the hyperfine splitting is negligible for the highly excited states. The fact that the potential of the positively charged core is slightly different from the Coulomb potential of the proton is taken into account via standard quantum defect theory that is reviewed in the Appendix A.1. Within this theory, the principal quantum number n gets modified by so-called quantum defects. The resulting – non-integer – effective quantum number n^* considers the effects of the modified potential, in addition to the relativistic corrections that lead to the fine structure splitting. The deviations from the Coulomb potential also alter the radial electronic wave function. The Appendix A.2 presents different methods for calculating it.

[4]That the Rydberg atoms can be modeled with high accuracy makes them ideal constituents for building a quantum simulator, because it is important that the constituents of a quantum simulator are fully understood so that one can believe its results.

In terms of the effective principal quantum number n^*, hydrogenic scaling laws hold for properties of Rydberg states, see Table 2.1. Due to the high principal quantum number, Rydberg atoms have exaggerated properties compared to atoms in low-lying states. Because the orbital radius is larger than for ground-state atoms, the electron is less bound to the core. As a result, interactions between atoms and with static electric fields or microwaves are drastically enhanced [48, 111, 112]. The $(n^*)^2$-scaling of the transition dipole moments enhances the dipole-dipole interaction by $(n^*)^4$. Together with the decreasing energy splitting of neighboring states, this leads to the van der Waals interaction increasing as $(n^*)^{11}$. Because the overlap between the electronic Rydberg wave function and the wave function of the ground state decreases, the contribution of decay channels get weakened, and the radiative lifetime increases as $(n^*)^3$ for the Rydberg states that are considered within this thesis[6]. Thus, Rydberg atoms quickly reach lifetimes beyond 100 μs while having interactions $V/h \gtrsim 1$ MHz (with Planck's constant h). Hence, we can perform experiments in a highly coherent regime, and Rydberg atoms are a good candidate for implementing Hamiltonians of interacting many-body systems. As the interactions between Rydberg atoms decrease algebraically with the interatomic distance, we can tune the interaction strength by the spatial position of the atoms. The strong interactions allow for placing the atoms on distances l that can be optically resolved, typically $\gtrsim 3$ μm.

The following sections discuss techniques for trapping and arranging the atoms in arbitrary arrays, the realization of different interactions and their application for the implementation of spin models, as well as the detection of Rydberg states.

2.2.2 Arrays of Individual Atoms

The Rydberg platform relies on Rydberg atoms that are arranged into arrays. Because the lifetime of the Rydberg state is limited and arranging the atoms in space takes comparably long (50 ms in [3]), one arranges the atoms before exciting them to the Rydberg state. Experiments use the following protocol to arrange the atoms in arbitrary arrays with almost unit filling:

- First, an atomic gas of ground-state atoms is laser cooled in a magneto-optical trap. The cooling laser is red detuned to an electronic transition of the atoms. Faster atoms see a Doppler shift that makes the cooling

[5]These quantities are calculated for the transition $|60S_{1/2}, m_j = 1/2\rangle$ to $|60P_{3/2}, m_j = 3/2\rangle$.
[6]For circular Rydberg states, the lifetime increases even as $(n^*)^5$ [57].

laser less detuned such that more photons are absorbed. The absorption takes place for photons that propagate in the opposite direction of the atoms' movement so that the photon recoil slows down the atoms. The subsequent spontaneous emission of the photon happens in a random direction. The development of laser cooling earned Steven Chu, Claude Cohen-Tannoudji, and William D. Phillips the Nobel Prize in 1997 [113].

- Second, an array of optical tweezers is immersed into the magneto-optical trap (the $1/e^2$ radius of the tweezers is typically ~ 1 μm and their depth ~ 1 mK) [114]. Such an array can be produced, for example, by spatial light modulators, digital mirror devices, or acousto-optic deflectors [44–47, 115, 116]. All these devices can be configured to realize different geometrical arrangements of the tweezers.

  The frequency of the light that makes up the tweezers is chosen to be too low to cause atomic excitations. Instead, it lowers the energy of the atomic ground state via the second-order AC Stark effect. Thus, atoms are attracted to the brightest spots, i.e., the centers of the tweezers. The randomly moving atoms enter the tweezers and get trapped. If an atom enters an occupied tweezer, the atom forms a pair state together with the already present atom. This state gets excited by the laser of the magneto-optical trap. The energy released by the spontaneous decay of the state accelerates the atoms and kicks both of them out of the tweezer. This process is known as a light-assisted collision. As a result, each tweezer is either empty or occupied by one single atom. Because the same random event can cause a change from empty to occupied and from occupied to empty, the probability to have a trap populated is about 50% [42, 50]. The fluorescence due to the laser of the magneto-optical trap makes it possible to observe which tweezers are occupied after the loading.

- Third, the atoms are rearranged into an array of almost unit filling. If acousto-optic deflectors implement the array of tweezers, we can directly shift the tweezers to form a new geometry [46]. Otherwise, we superimpose a movable tweezer that takes an atom from one position and releases it at another position [44, 45, 47]. The movable tweezer is typically realized with acousto-optic deflectors as well.

- Forth, the final array of atoms can be cooled further. For this, additional laser cooling can be applied [3]. However, to bring the atoms into the motional ground state of the tweezers, more sophisticated schemes such

as Raman sideband cooling are required [117] – but for the quantum simulations that are discussed in this thesis, it is not needed. Even without cooling into the motional ground state, the root-mean-square deviation $\sigma_{x,y,z}$ of the atomic positions is small compared to the interatomic distances. In the setup of our experimental collaborators, it is typically $\sigma_{x,y} = 0.1$ μm within the plane of atoms and $\sigma_z = 0.7$ μm perpendicular to it. Typical interatomic distances are on the order of $\sigma_{x,y} = 10$ μm. The root-mean-square deviation of the velocity of the atoms is $\sigma_v = 0.06$ m/s [3]. Finally, the desired electronic ground state is initialized via dissipative optical pumping in the presence of a magnetic field pointing along the quantization axis.

With this protocol, current experiments realize arrays of above two hundred atoms [24, 25]. The arrays can be one-, two, or three-dimensional. After the arrangement, the atoms are excited to the Rydberg state using a single or two-photon transition where the excitation happens far detuned from the intermediate state (in our case $|5P_{1/2}\rangle$) to avoid spontaneous emission [118, 119]. Because for many experimental setups, Rydberg states are anti-trapped by the tweezers, the tweezers are typically switched off before the excitation. Then, the residual velocity of the atoms makes them move and limits the duration of the experiment. New approaches are developed to address this issue. For example, after switching off the tweezers, one can switch on new tweezers designed explicitly for trapping Rydberg atoms [120]. Alternatively, one can find magic conditions that allow for trapping both ground-state atoms and Rydberg atoms with the same tweezers. Alkaline earth atoms provide the tunability required to find such conditions by the polarizability of the extra valence electron [59], but schemes are also proposed for alkali atoms [121].

Alternatively to the presented "bottom-up" protocol, there is also a "top-down" approach for preparing arrays of individual atoms. Instead of loading the tweezers from an atomic gas in a magneto-optical trap, one can load atoms into an optical lattice from a Bose-Einstein condensate. Then, by using the superfluid to Mott insulator transition, lattices of almost unit filling are realizable. However, at the time of writing, this approach has some disadvantages: First, the achievable filling fraction seems to be lower than for the other protocol – about 95% vs. 99% [25, 42]. Second, the realizable geometries are less flexible. And third, the approach is considered to be more complex and time-consuming [50].

2.2.3 Realizable Interactions

The interaction between Rydberg atoms can be calculated from the electric multipole expansion in spherical coordinates as reviewed in Chapter 3. This calculation assumes that the interatomic distance is larger than the LeRoy radius (the LeRoy radius is about $1\,\mu$m for $n = 60$) so that the electronic wave functions do not overlap [122]. In addition, we assume that the wavelengths of the involved Rydberg-Rydberg transitions are much larger than the considered interatomic distances so that we are allowed to neglect retardation effects [123]. Here, we focus on the leading order of the multipole expansion, which is in case of Rydberg atoms the dipole-dipole interaction [1, 56, 124]. The operator for the interaction between an atom at position $\mathbf{r}_i$ and another atom at $\mathbf{r}_j$ reads[7] [125]

$$V_{ij}^{\mathrm{dd}} = \frac{1}{4\pi\epsilon_0} \frac{\mathbf{d}_i \cdot \mathbf{d}_j - 3\,(\mathbf{d}_i \cdot \hat{\mathbf{r}}_{ij})\,(\mathbf{d}_j \cdot \hat{\mathbf{r}}_{ij})}{|\mathbf{r}_{ij}|^3}\,, \tag{2.1}$$

with vacuum permittivity ϵ_0 and dipole operators $\mathbf{d}_i$, $\mathbf{d}_j$. The dipole operators couple electronic states that differ in their orbital quantum number by $\Delta l = \pm 1$, in their total angular quantum number by $\Delta j = 0, \pm 1$[8], and in their magnetic quantum number by $\Delta m_j = 0, \pm 1$. The distance vector between the two atoms is $\mathbf{r}_{ij} = \mathbf{r}_j - \mathbf{r}_i$ and $\hat{\mathbf{r}}_{ij} = \mathbf{r}_{ij}/|\mathbf{r}_{ij}|$.

The resulting interactions have applications in quantum information processing [43, 126–129] and quantum optics, for example, to realize single-photon sources [130] or absorbers [131]. For analog quantum simulations, the operator (2.1) facilitates the realization of different kinds of spin models.

The general idea is to map electronic states to spin states. The electronic states must be energetically isolated from other states to make this mapping accurate. This isolation can be achieved by applying electric and magnetic fields or light shifts. In order to find a regime where the desired states are energetically isolated in the sense that the coupling to other states can be considered within perturbation theory, extensive parameter scans may be required. For these parameter scans, we typically use non-perturbative calculations of the pair interaction potentials, see Chapter 3, and check whether we can, in principle, describe the resulting pair potential curves also within perturbation theory. For this, we check whether the admixture of non-desired states is tiny. Such a parameter scan is exemplarily discussed in Chapter 4.

[7] Note that we use SI units throughout the thesis.

[8] In addition, it is necessary that the sum of the total angular quantum numbers of the coupled states is $j + j' \geq 1$. This is always the case for Rydberg states of alkali atoms.

The following section provides a qualitative overview of different types of interactions between two Rydberg atoms and the physical models that can be realized with these interactions. Note that within this overview, only the most dominant terms are stated explicitly. In reality, higher-order couplings are also present that would modify the given Hamiltonians slightly. For an example of a rigorous description of an implementable model, see Chapter 7.

Ising-Like Models

→ See also Chapter 4.

We consider two Rydberg atoms that are in the same state, for example, $|r\rangle = |61D_{3/2}, m_j = 3/2\rangle$ (this is the state that is used in Chapter 4). The operator (2.1) couples the pair state $|rr\rangle$ to other Rydberg states $|r'r''\rangle$. Assuming that $|rr\rangle$ is energetically isolated, the main effect of the coupling is that the state $|rr\rangle$ gets shifted in energy. This energy shift can be calculated perturbatively. The most dominant contribution comes from second-order perturbation theory and is called van der Waals interaction. For atoms at positions $\mathbf{r}_i$ and $\mathbf{r}_j$, it reads

$$U_{ij} = \sum_{r',r''(\neq r)} \frac{|\langle r'r''|V_{ij}^{\mathrm{dd}}|rr\rangle|^2}{E_{|rr\rangle} - E_{|r'r''\rangle}} = \frac{C_6}{|\mathbf{r}_{ij}|^6} , \tag{2.2}$$

with van der Waals coefficient C_6 that is distance-independent but in general angular dependent. For alkali atoms in the $|nS\rangle$ state, the interaction is repulsive[9] and the C_6 coefficient almost isotropic. For alkali atoms in the $|nD\rangle$ state, the interaction is attractive and the C_6 coefficient anisotropic, i.e, the coefficient depends on the angle between the interatomic axis and quantization axis. The van der Waals interaction underlies the famous Rydberg blockade [132–135].

We use the interaction to implement Ising-like models. For this, we consider an array of atoms. The basic idea is that we interpret the electronic ground state $|g\rangle$ as $|\downarrow\rangle$ and the Rydberg state $|r\rangle$ as $|\uparrow\rangle$. All other Rydberg states are shifted away in energy so that the mapping is accurate, see Chapter 4. A laser is applied that couples $|\downarrow\rangle$ and $|\uparrow\rangle$ with Rabi frequency Ω and frequency detuning δ. Then, after the rotating wave approximation, the Hamiltonian of

[9] This is in stark contrast to ground state atoms where the van der Waals interaction is always attractive.

the system reads in the rotating frame of the laser

$$H = \frac{1}{2}\sum_{i\neq j} U_{ij}\; n_i n_j + \frac{\hbar\Omega}{2}\sum_i \sigma_i^x - \hbar\delta\sum_i n_i \;, \tag{2.3}$$

with reduced Planck's constant $\hbar$, $n_i = (\sigma_i^z + 1)/2$, and Pauli matrices σ. This Hamiltonian is similar to the Hamiltonian of the Ising model with transverse field $B_\perp \propto \Omega$. The van der Waals interaction, which is a density-density interaction, gives rise to the $\sigma_i^z\sigma_j^z$ interaction of the Ising model and longitudinal fields that are also affected by the detuning δ. The model has been implemented experimentally in one-dimension [60, 61, 136] and two-dimensions [24, 25, 137–139].

Note that we can also write this Hamiltonian in the language of hard-core bosons by the identification of $b_j^\dagger = \sigma_j^+$ and $b_j = \sigma_j^-$. Then, the Pauli matrices are $\sigma_j^x = b_j + b_j^\dagger$, $\sigma_j^y = i(b_j - b_j^\dagger)$, and $\sigma_j^z = 2b_j^\dagger b_j - 1$. If we follow this interpretation, $|\downarrow\rangle$ is the vacuum state and $|\uparrow\rangle$ one particle. The hard-core constraint $(b_j^\dagger)^2 = 0$ means that there must only be zero or one particle at a site j. The constraint emerges from the fact that a Rydberg atom hosts a single excitation only.

Instead of using the Rydberg state $|r\rangle$ as $|\uparrow\rangle$, we can also use a long-lived ground state level that we off-resonantly couple to the Rydberg state [140–142]. This coupling is known as Rydberg dressing. It admixes the Rydberg state slightly to the ground state and enhances thereby the interaction of the ground state. The resulting interaction potential behaves as $1/|\mathbf{r}_{ij}|^6$ on long interatomic distances. On short distances, the potential saturates, making it a soft-core potential.

XY-Type Models

→ See also Chapter 5.

Let us now consider two different Rydberg states, for example, $|S\rangle = |60S_{1/2}, m_j = 1/2\rangle$ and $|P\rangle = |60P_{1/2}, m_j = -1/2\rangle$ (these are the states that are used in Chapter 5). Then, the two pair states $|PS\rangle$ and $|SP\rangle$ are resonant. As in our case there is a non-zero transition dipole moment between the two states, the states are coupled by the operator (2.1) in first order. For atoms at positions $\mathbf{r}_i$ and $\mathbf{r}_j$, the coupling reads

$$J_{ij} = \langle SP|V_{ij}^{\mathrm{dd}}|PS\rangle = \frac{C_3}{|\mathbf{r}_{ij}|^3} \;, \tag{2.4}$$

with dipole-dipole interaction coefficient C_3. Note that the value of this coefficient is distance-independent, but dependent on the angle θ between the interatomic axis and the quantization axis. In particular, for the considered states, there is the magic angle $\theta_m = \arccos(1/\sqrt{3}) \approx 54.7°$ for which the coefficient becomes zero. This feature is used in Chapter 5 to implement an SSH chain.

The dipolar exchange interaction can be applied to realize XY-type models. For this, we interpret $|S\rangle$ as $|\downarrow\rangle$ and $|P\rangle$ as $|\uparrow\rangle$. We can apply a microwave field with Rabi frequency $\Omega_{\mu w}$ and detuning $\delta_{\mu w}$ to drive transitions between $|\downarrow\rangle$ and $|\uparrow\rangle$. Then, an array of atoms is described by the Hamiltonian

$$H = \frac{1}{2}\sum_{i\neq j} J_{ij}\left(\sigma_i^+\sigma_j^- + \sigma_i^-\sigma_j^+\right) + \frac{\hbar\Omega_{\mu w}}{2}\sum_i \sigma_i^x - \hbar\delta_{\mu w}\sum_i n_i \,, \tag{2.5}$$

where $\sigma_i^\pm = (\sigma_i^x \pm i\sigma_i^y)/2$ and the rotating wave approximation and rotating frame have been applied. The model has been studied experimentally in [4, 63].

As for the Ising-like models, we can write the Hamiltonian in terms of hard-core bosonic operators as well. Then, the coupling gives rise to particle hopping.

Again, we can also use Rydberg-dressed ground states instead of the Rydberg states.

XXZ-Type Models

By combining density-density interaction and exchange interaction, we can realize XXZ-type models. To have both types of interactions with similar strength, it has been proposed to encode the spin states into two circular Rydberg states that are coupled in second order. For details, see the publication by T. L. Nguyen *et al.* [57].

Another possibility to engineer XXZ-type models is to start with the Hamiltonian (2.5) and apply a specifically designed periodic microwave field such that the time-averaged Hamiltonian becomes the XXZ Hamiltonian. This approach has been recently implemented in an experiment [143].

Other Models

→ See also Chapters 6 and 7.

We can extend the models that have been described before by considering more than two electronic states.

For example, we can use the three Rydberg states $|0\rangle = |60S_{1/2}, m_j = 1/2\rangle$, $|+\rangle = |60P_{3/2}, m_j = 3/2\rangle$, $|-\rangle = |60P_{3/2}, m_j = -1/2\rangle$. In this case, we do not describe a spin-1/2 model, but our system resembles a model of hard-core bosonic particles that have two different internal states. Each particle is either in the $|+\rangle$ state or the $|-\rangle$ state. As for the XY-type models, the particles hop due to the dipolar exchange interaction. In the case of an interatomic axis that does not point along the quantization axis, the total magnetic quantum number is allowed to change such that a particle in the $|+\rangle$ state can hop and become a particle in the $|-\rangle$ state and vice versa. This change of the internal state goes together with the collection of a phase (spin-orbit coupling). In Chapters 6 and 7, we explain this effect in more detail and apply it to engineer effective magnetic fields and eventually a topological phase.

2.2.4 Detection of Rydberg States

Let us assume that, for example, an XY-type model has been implemented, where the atoms are either in the Rydberg S-state or Rydberg P-state, and we would like to detect which atoms are in which Rydberg state. A possibility is to exploit the *anti-trapping* of Rydberg states. To do so, one de-excites the specific Rydberg state, which should be detected, back to the ground state and switches on the tweezers afterward. All atoms that have not been de-excited escape the trapping region quickly. Thus, only the atoms that have previously been in the specific Rydberg state are visible in a subsequent fluorescence image. Note that atoms that spontaneously decayed to the ground state can cause *false positive* detection events. Atoms that moved too much during the experiment so that they are outside the trapping region can cause *false negative* detection events. Typically, the resulting detection errors are on the single percent level [60].

2.3 Topological Phases

For an analog quantum simulator, simulations of quantum phases are suitable targets. This is because a quantum phase does not belong to a specific Hamiltonian but corresponds to an equivalence class of Hamiltonians. From this class, we can target the Hamiltonian that is most straightforward to implement with the analog quantum simulator. Chapters 5 and 7 are about quantum simulations of so-called topological phases.

Excellent reviews about topological phases can be found in the following publications:

- "Colloquium: Zoo of quantum-topological phases of matter" by Xiao-Gang Wen (2017) [144]: General introduction and brief survey about different topological phases of matter.
- "One-dimensional topological states of synthetic quantum matter" PhD thesis by Nicolai Lang (2019) [5]: The introduction of the PhD thesis contains a vivid primer on topological phases. Moreover, the one-dimensional symmetry-protected phase of Chapter 5 is thoroughly classified within that thesis.

Here, a short introduction to the concept of topological phases is provided. Let us start by thinking about the concept of phases in general. It originates from condensed matter physics, whose objective is to describe systems with many particles. Systems can be in different phases, depending on the temperature and the interaction between the particles. For systems with the same particles, different phases differ by different collective behaviors of the particles (according to the *principle of emergence*, this collective behavior determines the properties of the system). Formally, phases are defined by their boundaries: Systems are in the same phase if they can be parametrically connected without a phase transition that typically reveals itself by divergent correlation lengths or non-analytic thermodynamic potentials [5].

A very successful scheme for describing phases is Landau's paradigm of spontaneous symmetry breaking [145, 146]: A system is in the *disordered* phase if the symmetry group of the Hamiltonian of the system is the same as the symmetry group under which the equilibrium state of the system is invariant. If the system undergoes a phase transition, the state of the system breaks some symmetries spontaneously[10]. Then, the system is in an *ordered* phase.

In classical physics, phase transitions are driven by *thermal fluctuations*. However, in quantum physics, there is another possibility: *quantum fluctuations* can drive phase transitions. These phase transitions can even occur at zero temperature because the strength of quantum fluctuations is not determined by temperature but by non-commuting terms in the Hamiltonian [147]. Here, we focus on quantum phases at zero temperature.

Remarkably, not all quantum phases can be described by Landau's paradigm. In addition, there are *topological* phases. This observation has been very influential, for example, the Nobel Prize in physics has been awarded for "theoretical discoveries of topological phase transitions and topological phases of matter" in 2016 [148]. In the following, we discuss intrinsic topological phases

[10]Strictly speaking, this statement is only entirely correct in the thermodynamic limit.

and symmetry-protected topological phases. Along the way, we explain why quantum simulations of topological phases are particularly promising targets.

2.3.1 Intrinsic Topological Phases

→ *See also Chapter 7.*

Quantum phases that are disordered with respect to Landau's paradigm can still differ by their entanglement – a possibility that is unique to quantum systems. The entanglement pattern of a gapped ground state allows for the classification of phases in the absence of symmetry breaking because some global features of the entanglement pattern cannot be changed by continuous variations of local Hamiltonians that do not close the gap.

Let us consider two gapped ground states of two different Hamiltonians. If these Hamiltonians are connected by a continuous path of local and gapped Hamiltonians, the ground states belong to the same phase. An equivalent definition is that gapped ground states belong to the same phase if they can be transformed into each other by local quantum circuits with a constant depth [149]. In particular, if a ground state can be transformed into a product state, it belongs to the *trivial* phase. Otherwise, it belongs to a *topological* phase. Following the definition by Xiao-Gang Wen, a topological phase exhibits *long-range entanglement* [149].

Prominent examples of such phases are fractional quantum Hall states [150, 151]. They have a non-zero topological entanglement entropy and feature, as a consequence, exciting properties: For example, ground states are degenerate if the system is on a manifold with a non-zero genus (such as a torus) [152]. Because the ground state degeneracy is robust against perturbations that do not close the gap, the degenerate ground states are investigated as a potential resource for encoding qubits and therefore robust storage of quantum information [153, 154]. Moreover, excitations carry fractional charges and fulfill anyonic braiding statistics. The latter makes some systems with non-zero topological entanglement entropy interesting for fault-tolerant quantum computing [155, 156].

There are still fundamental open questions regarding topological phases. The mathematical framework – namely, category theory [157, 158] – for categorizing topological phases is far more complicated and less understood than the group theory that is applied in the case of spontaneous symmetry breaking. Another example for an open research question is the origin of the fractional quantum Hall state at the filling factor $\nu = 5/2$ that is not yet fully understood [159–161].

Thus, to learn more about topological phases and possibly pave the way for applications in quantum information science, analog quantum simulations of such phases are meaningful goals – especially as the necessary entanglement makes classical simulations of large systems challenging [162]. Recently, a system that is theoretically predicted to exhibit topological order has been probed for the first time on an analog quantum simulator: Rydberg atoms have been applied to investigate topological spin liquids and evaluate topological string operators [23, 81], demonstrating the capacity of the Rydberg platform. However, preparing the actual ground state of such a system is still an ongoing challenge. For the adiabatic preparation, one starts in a trivial state and ends in the topological state which is separated by a phase transition. At the transition point, the gap must vanish – except for the finite-size gap. If the finite size gap is small (which is often the case), non-adiabatic processes may take place because finite coherence times limit the maximum duration of the experiment [23]. In particular, the preparation of fractional quantum Hall states comes even with another challenge because it requires (effective) magnetic fields. There are many proposals on how these fields can be realized [65, 68, 69, 82–90], but most of them leverage Floquet engineering which is prone to unwanted heating processes that spoil the preparation of the ground state. Thus, it is no surprise that fractional quantum Hall states have not yet been realized in quantum simulators. However, the Rydberg platform facilitates effective magnetic fields without requiring a time-dependent Hamiltonian [6, 64], see also Chapter 6. In Chapter 7, we present a detailed proposal on how to make use of effective magnetic fields to realize fractional quantum Hall states with Rydberg atoms.

2.3.2 Symmetry-Protected Topological Phases

→ *See also Chapter 5.*

In the previous section, we stated that two gapped ground states belong to the same phase if their Hamiltonians are connected by a continuous path of local and gapped Hamiltonians. In addition, one can demand that all Hamiltonians along the path must preserve some symmetries[11], i.e., the operators that represent the symmetries must commute with these Hamiltonians (such symmetries are called *protecting* symmetries). Then, only some paths are allowed while others are excludes so that some gapped ground states can no longer be connected.

[11] In some cases, nature motivates that Hamiltonians must fulfill certain symmetries. For example, closed systems typically satisfy a $U(1)$ symmetry in the form of particle number conservation.

If these ground states are from the trivial intrinsic topological phase, they belong to different *symmetry-protected topological phases* [144]. While being short-range entangled, symmetry-protected topological phases can still give rise to intriguing features such as edge states.

In Chapter 5, we present the analog quantum simulation of a symmetry-protected topological phase of interacting bosons that derives from the SSH chain [4].

3

Rydberg Interaction Potentials

The main goal of this thesis is to show how to realize accurate quantum simulations of various spin models using the strong interaction between individual Rydberg atoms. The strong Rydberg interaction is also exploited in the field of quantum information science for engineering two- and multi-qubit quantum gates. A precise understanding of the interaction between Rydberg atoms is essential to find suitable experimental parameters for these applications and to understand experiments that probe the interaction with high precision or at short interatomic distances. In all these cases, perturbative methods are no longer sufficient for computing the Rydberg interaction.

In this chapter, we review all relevant aspects of the non-perturbative calculation of Rydberg interaction potentials. The chapter is based on our tutorial about the calculation of Rydberg interaction potentials [1]. We discuss the derivation of the interaction Hamiltonian from the electrostatic multipole expansion, numerical and analytical methods for calculating the required electric multipole moments, and the inclusion of electromagnetic fields with arbitrary directions. We focus specifically on symmetry arguments and selection rules, which greatly reduce the size of the Hamiltonian matrix, enabling the exact diagonalization of the Hamiltonian up to higher multipole orders on a desktop computer. Finally, we present example applications showing the relevance of the non-perturbative interaction calculations.

Our `pairinteraction` software[12] for calculating Rydberg potentials, which includes all discussed features, is available as open-source on GitHub, `https://pairinteraction.github.io`. The software has been developed together with

[12] Another open-source software that comes in handy for calculating properties of Rydberg systems is the `ARC` library by N. Šibalić *et al.* [56]. This library has more functionality built-in for calculating single atom properties but cannot calculate pair potentials in the presence of electric and magnetic fields in arbitrary directions.

Henri Menke who contributed methods for calculating radial matrix elements and shared his software engineering skills with the project. Johannes Block contributed code for calculating Rydberg pair potentials near surfaces [163]. For contributions, see also the GitHub repository of the software.

It is our hope that this software is useful to members of the Rydberg community as a general tool to explore the rich physics of Rydberg interaction. The goal of our open-source approach is to stimulate active participation of additional developers.

3.1 Introduction

Among the many fascinating properties of highly excited Rydberg atoms [48], the strong interaction between pairs of Rydberg atoms has proven to be the key feature for diverse applications in quantum information processing and quantum simulation [128]. A particularly important concept is the Rydberg blockade [127], where the excitation of two or more atoms to a Rydberg state is prevented due to the interaction. The Rydberg blockade of atomic ensembles [126] has been observed in ultracold atomic systems in the frozen Rydberg-gas regime [164, 165], both in bulk ensembles [166–177] and in small systems supporting only a single excitation [178–181]. More recently, experiments have also begun to probe Rydberg interaction effects in room-temperature thermal vapor [182–184]. Based on the Rydberg blockade, atomic two-qubit gates have been demonstrated [128, 132–134] as basic building blocks for large-scale neutral atom quantum registers [44, 46, 185–187]. In turn, the power-law decay of the Rydberg interaction provides interaction over long range and facilitates the extension to multi-qubit Rydberg-mediated gates in such registers [41, 188, 189]. Such tailored atomic ensembles are also ideal for investigating processes such as excitation transfer [63, 164, 190–192] or simulation of spin systems [4, 60, 137].

The mapping of Rydberg interactions onto photons by means of electromagnetically induced transparency (EIT) [193] has emerged as a powerful approach to realizing few-photon optical nonlinearities [194–200], enabling a variety of optical quantum information applications such as highly efficient single-photon generation [130], entanglement generation between light and atomic excitations [201], single-photon all-optical switches [202] and transistors [203–205], single-photon subtraction [206], and interaction-induced π-phase shifts [207]. Additionally, Rydberg EIT provides access to novel phenomena such as attractive interaction between single photons [208], crystallization of

photons [209], or photonic scattering resonances [210], as well as spatially resolved detection of single Rydberg atoms in a bulk medium [190, 211, 212]. Recent Rydberg EIT experiments, which simultaneously use Rydberg S- and P-states [213] or two different S-states [190, 203, 204] further increase the flexibility of manipulating weak light fields [214, 215].

Detailed understanding of the Rydberg interaction is also required for the concept of Rydberg dressing, where a small Rydberg admixture modifies the interaction between ground-state atoms in ultracold gases [140, 216–221]. In particular, by the choice of the Rydberg state, one can map the anisotropy of the Rydberg interaction onto the ground-state atoms [222–224]. Experimental demonstrations of Rydberg dressing have recently been performed using individual atoms [142] or atomic ensembles in an optical lattice [141]. Finally, the rich structure of the Rydberg interaction potentials supports bound molecular states formed by two Rydberg atoms [225], which have been observed in experiments [226–228]. Prediction of the equilibrium distance and vibrational spectra for these macro-dimers requires precise knowledge of the interaction potential [228–232].

The physics of Rydberg interaction has been well-established for decades [233]. As long as the two atoms are well separated and their wave functions do not overlap, one needs to consider only the electrostatic interaction between two localized charge distributions, most conveniently utilizing the well-known electric multipole expansion in spherical coordinates [234–236]. The leading relevant term in this expansion is the dipole-dipole interaction [55], which for unperturbed Rydberg atoms at large separation results in the extensively studied van der Waals interaction [51–54]. More generally, as long as the interaction energies are small compared to the level spacing of the unperturbed Rydberg pair states, perturbative calculations offer a very convenient method for determining the radial [51] and angular [52, 53] behavior of the Rydberg potentials.

Nevertheless, the rapid experimental progress in recent years has led to a growing number of experiments for which the perturbative calculation is no longer sufficient. For example, this approach fails when shorter atomic distances are probed and state-mixing due to the interaction becomes significant. The dipole-quadrupole contribution to the interaction has recently been observed both in ultracold [237] and room-temperature [184] systems in experiments with large excitation bandwidth, while the correct prediction of macro-dimer photoassociation spectra required the inclusion of terms up to octupolar order in the potential calculation [228, 231]. In experiments utilizing very high principal quantum numbers $n > 100$ [238–240], state-mixing and additional molecular

resonances [241] become relevant already at large interatomic distances and make non-perturbative potential calculations necessary.

The nature of the interaction also changes when coupled pair states are (nearly) resonant [242, 243]. Such degeneracies, or Förster-resonances, can occur naturally or by shifting the pair-state energies via external electric [169, 172, 176, 190, 244–248] or microwave [249–251] fields. Such resonances can greatly enhance the Rydberg interaction strength [252]. When spin-orbit coupling as well as Stark and Zeeman splitting of all involved levels are taken into account, the resonances can exhibit new features and a rich angular dependence [205, 253]. Full potential calculations including the external fields reveal the number of states which must be included in specific cases for accurate results.

As consequence of the rapid evolution of the field, it becomes more and more common to rely on numerical diagonalization of the Rydberg interaction Hamiltonian including higher orders of the multipole expansion [228, 229, 237, 240]. Here, we discuss all relevant steps required for the numerical calculation of pairwise Rydberg interaction potentials:

1. Construction of the single-atom Hamiltonian from the orbital wave functions (Appendix A.2) and their transition matrix elements (Appendices A.3 and A.4) in the absence of external fields.

2. Derivation of the interaction Hamiltonian for a pair of Rydberg atoms by multipole expansion (Section 3.2.1).

3. Inclusion of external electric and magnetic fields in arbitrary directions relative to the inter-atomic axis (Section 3.2.2).

4. Application of selection rules and symmetry arguments to reduce the size of the Hilbert space to the relevant states (Section 3.2.3).

5. Rotation of the interaction Hamiltonian to a particular coordinate system, given for example by the direction of an incident excitation laser (Section 3.2.4).

6. Diagonalization and extraction of the interaction potentials (Section 3.3). In the context of three practical applications (Section 3.4), we discuss best practices and specific considerations in the relevant scenarios. These examples illustrate the capabilities of the presented approach and the agreement with experiments.

3.2 Model

3.2.1 Rydberg Interaction

We study two neutral atoms, each having one electron excited into a Rydberg state, as depicted in Fig. 3.1(a). Because we are only interested in interatomic distances R for which the Rydberg atoms are well-separated, the interaction between the atoms is dominated by the strong interactions of the Rydberg electrons. Using the Born-Oppenheimer approximation [254], the corresponding two-atom Hamiltonian is of the form[13]

$$\hat{H}(\boldsymbol{R}) = \hat{H}_0 + \hat{H}_{\text{int}}(\boldsymbol{R}) \,, \tag{3.1}$$

where $\hat{H}_0$ contains the energies of the unperturbed Rydberg states. The operator $\hat{H}_{\text{int}}$ captures the interaction between the two Rydberg electrons, the two ionic cores, and the Rydberg electron of one atom and the ionic core of the other atom. This is the standard treatment of two interacting Rydberg atoms which is discussed in similar detail in [51, 55, 227, 231].

Because the hyperfine splitting of Rydberg levels is much smaller than typical interaction energies [256–258], we use the fine-structure basis. As we will see later, we can assume the two Rydberg electrons to be distinguishable particles. Hence, we use the product basis $|n_1 l_1 j_1 m_{j1}; n_2 l_2 j_2 m_{j2}\rangle = |n_1 l_1 j_1 m_{j1}\rangle \otimes |n_2 l_2 j_2 m_{j2}\rangle$[14]. Note that the two Rydberg atoms are allowed to be of different chemical species [259, 260]. The operator $\hat{H}_0$ can be written as

$$\begin{aligned}\hat{H}_0 = &\sum_{n_1,l_1,j_1,m_{j1}} E_{n_1 l_1 j_1} \, |n_1 l_1 j_1 m_{j1}\rangle \langle n_1 l_1 j_1 m_{j1}| \otimes \mathbb{1} \\ &+ \mathbb{1} \otimes \sum_{n_2,l_2,j_2,m_{j2}} E_{n_2 l_2 j_2} \, |n_2 l_2 j_2 m_{j2}\rangle \langle n_2 l_2 j_2 m_{j2}| \;. \end{aligned} \tag{3.2}$$

We use the common convention that the quantization axis points along the z-direction. The potential energy E_{nlj} of an electron excited to a Rydberg state

[13] Because this chapter contains a great number of different quantities, and it is not always straightforward to see whether a quantity is an operator or a variable, we put "hats" above operators to distinguish them from variables. In the other chapters of this thesis, we omit the hats.

[14] In our notation, we omit the spin quantum number $s_1 = s_2$, which equals 1/2 for alkali atoms.

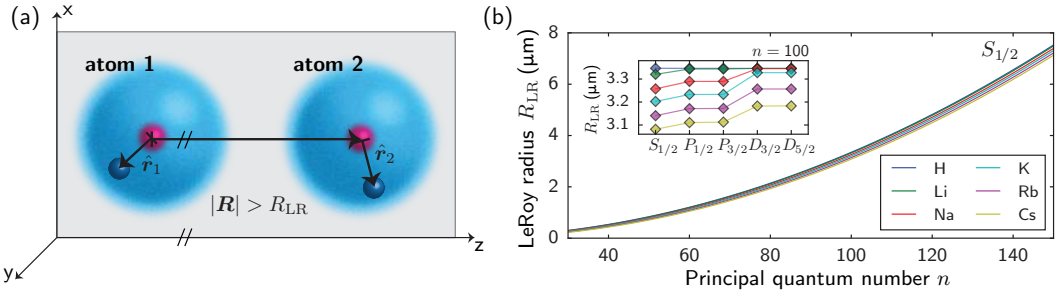

Fig. 3.1: (a) Considered system. We study two Rydberg atoms whose interatomic axis is parallel to the z-axis. The positions of the Rydberg electrons are $\hat{r}_1$ and $\hat{r}_2$. The interatomic distance R is larger than the LeRoy radius R_{LR} [122] so that the electronic wave functions do not overlap. (b) LeRoy radius for pairs of alkali atoms. For calculating the LeRoy radius, we assumed both atoms to be in the same state. The LeRoy radius increases approximately with the square of the principal quantum number. The inset shows its dependence on the momentum quantum numbers. The LeRoy radius for alkali atoms is bounded from above by the LeRoy radius for hydrogen atoms $R_{\mathrm{LR}} = a_0\sqrt{8n^2(5n^2+1-3l(l+1))}$ [255] where a_0 is the Bohr radius.

is given by a formula similar to the one known for the hydrogen atom

$$E_{nlj} = -\frac{hcR^*}{(n-\delta_{nlj})^2}\,, \tag{3.3}$$

where R^* is the modified Rydberg constant and δ_{nlj} is the quantum defect [261]. These species-dependent parameters are used to capture subtle differences between the bare Coulomb potential of a hydrogen core and the actual potential felt by the Rydberg electron. For details on these parameters, see Appendix A.1.

For calculating the interaction energy $\hat{H}_{\mathrm{int}}$, we neglect retardation effects [123] as the wavelengths of the involved Rydberg-Rydberg transitions are much larger than the considered interatomic distances. Furthermore, we assume the interatomic distance to be larger than the LeRoy radius [122]

$$R_{\mathrm{LR}} = 2\left(\sqrt{\langle n_1 l_1 j_1|\hat{r}^2|n_1 l_1 j_1\rangle} + \sqrt{\langle n_2 l_2 j_2|\hat{r}^2|n_2 l_2 j_2\rangle}\right)\,, \tag{3.4}$$

which increases approximately with the square of the principal quantum number like the radius of a Rydberg atom does, see Fig. 3.1(b). This assumption tremendously simplifies the calculations. It ensures that the electronic wave functions do not overlap, so that exchange interaction and charge overlap interaction can be neglected. Thus, we can treat the electrons as distinguishable

particles. Furthermore, it allows us to use a multipole expansion for the interaction energy. In order to do so, we first think of the two Rydberg atoms as classical charge distributions [262]. Their electrostatic interaction energy is

$$H_{\mathrm{int}}(\boldsymbol{R}) = \frac{e^2}{4\pi\epsilon_0}\left(\frac{1}{|\boldsymbol{R}+\boldsymbol{r}_2-\boldsymbol{r}_1|}+\frac{1}{|\boldsymbol{R}|}-\frac{1}{|\boldsymbol{R}-\boldsymbol{r}_1|}-\frac{1}{|\boldsymbol{R}+\boldsymbol{r}_2|}\right), \tag{3.5}$$

where $\boldsymbol{R}$ denotes the interatomic distance vector. The positions $\boldsymbol{r}_1$ and $\boldsymbol{r}_2$ of the electrons of the atom are given as relative coordinates in the body frame of the respective atom, see Fig. 3.1(a). The multipole expansion yields [234–236]

$$H_{\mathrm{int}}(\boldsymbol{R}) = \sum_{\kappa_1,\kappa_2=1}^{\infty} \frac{V_{\kappa_1\kappa_2}}{4\pi\epsilon_0|\boldsymbol{R}|^{\kappa_1+\kappa_2+1}} \ . \tag{3.6}$$

The exact form of $V_{\kappa_1\kappa_2}$ depends on the choice of the coordinate systems used to label the positions of the electrons. If we choose the coordinate systems such that the z-axis points along $\boldsymbol{R}$, i.e. along the interatomic axis, we get the comparatively simple result

$$V_{\kappa_1\kappa_2} = (-1)^{\kappa_2}\sum_{q=-\kappa_<}^{\kappa_<}\sqrt{\binom{\kappa_1+\kappa_2}{\kappa_1+q}\binom{\kappa_1+\kappa_2}{\kappa_2+q}}\, p^{(1)}_{\kappa_1 q}p^{(2)}_{\kappa_2 -q}, \tag{3.7}$$

where we use $\kappa_< = \min(\kappa_1,\kappa_2)$ and binomial coefficients to shorten our notation. This result transfers into quantum mechanics by canonical quantization. Thus, the spherical multipole moments $p^{(1)}_{\kappa q}$ and $p^{(2)}_{\kappa q}$ become the spherical multipole operators $\hat{p}^{(1)}_{\kappa q}$ and $\hat{p}^{(2)}_{\kappa q}$, that operate on the Rydberg electron of the first and second atom, respectively. The operators are of the form

$$\hat{p}^{(i)}_{\kappa q} = e\,\hat{r}_i^{\kappa}\cdot\sqrt{\frac{4\pi}{2\kappa+1}}Y_{\kappa q}(\hat{\vartheta}_i,\hat{\varphi}_i) \ , \tag{3.8}$$

where $Y_{\kappa q}(\hat{\vartheta},\hat{\varphi})$ are spherical harmonics[15]. Note that, in our notation, the spherical basis is $\{\boldsymbol{e}_\pm = \mp\frac{1}{\sqrt{2}}(\boldsymbol{e}_x \mp i\boldsymbol{e}_y),\ \boldsymbol{e}_0 = \boldsymbol{e}_z\}$[16]. The spherical multipole

[15] In the literature, different normalizations for spherical harmonics are found. We choose the convention $Y_{\kappa q}(\vartheta,\varphi) = (-1)^q\sqrt{\frac{(2\kappa+1)(\kappa-q)!}{4\pi(\kappa+q)!}}\sin^q\vartheta\frac{\mathrm{d}^q}{(\mathrm{d}\cos\vartheta)^q}P_\kappa(\cos\vartheta)\,\mathrm{e}^{\mathrm{i}q\varphi}$ that is commonly used in quantum mechanics. Here, P_κ are Legendre polynomials and $(-1)^q$ the Condon-Shortley phase.

[16] We use the common definition of the spherical multipole operators (3.8). This implies that our spherical basis is non-standard (with the standard convention, the dipole operator in the spherical basis would not be of the usual form $\hat{p}_{11}\boldsymbol{e}_+ + \hat{p}_{1-1}\boldsymbol{e}_- + \hat{p}_{10}\boldsymbol{e}_0$).

operator $\hat{p}_{\kappa q}$ corresponds to the 2^κ-pole momentum. The multipole expansion (3.6) is a series expansion of the interaction potential in powers

$$\varrho = \kappa_1 + \kappa_2 + 1 \tag{3.9}$$

of the inverse interatomic distance. The series expansion starts at $\varrho = 3$. Thus, the contribution of lowest order is the dipole-dipole interaction which reflects the neutral charge of the Rydberg atoms. Section 3.4.1 discusses the relevance of higher-order contributions. In general, the order at which we can reasonably truncate the expansion increases with decreasing interatomic distance.

The spherical multipole operators are composed of the product of a radial and an angular operator whose matrix elements can be calculated independently of one another with the formalism shown in Appendices A.3 and A.4. The independent calculation works because the potential for the Rydberg electron is spherically symmetric, so that the Rydberg wave function can be separated into the product of a radial function $\Psi^{\mathrm{rad}}_{nlj}(r)$ and a spin spherical harmonic $Y_{lsjm_j}(\vartheta, \varphi)$ [263],

$$\Psi(r, \vartheta, \varphi) = \Psi^{\mathrm{rad}}_{nlj}(r) \cdot Y_{lsjm_j}(\vartheta, \varphi) \; . \tag{3.10}$$

3.2.2 External Fields

In general, the interaction between an atom and the electromagnetic field can be taken care of by employing the minimal-coupling replacement [264, 265]. Assuming that the fields are static and homogeneous, this general approach gets reduced to adding the electric interaction

$$\hat{V}_{\mathrm{e}} = -\hat{\boldsymbol{d}} \cdot \boldsymbol{E} \quad \text{with} \quad \hat{\boldsymbol{d}} = e\hat{\boldsymbol{r}} \tag{3.11}$$

and the magnetic interaction

$$\hat{V}_{\mathrm{m}} = -\hat{\boldsymbol{\mu}} \cdot \boldsymbol{B} + \frac{1}{8m_e}|\hat{\boldsymbol{d}} \times \boldsymbol{B}|^2 \quad \text{with} \quad \hat{\boldsymbol{\mu}} = -\frac{\mu_{\mathrm{B}}}{\hbar}(g_l\hat{\boldsymbol{l}} + g_s\hat{\boldsymbol{s}}) \tag{3.12}$$

to the Hamiltonian (3.1), where $\hat{\boldsymbol{d}}$ is the electric dipole operator, and $\hat{\boldsymbol{\mu}}$ is the magnetic dipole operator. The g-factors g_l and g_s characterize the magnetic moment through orbital motion and spin. The constant μ_{B} is the Bohr magneton. The term $\frac{1}{8m_e}|\hat{\boldsymbol{d}} \times \boldsymbol{B}|^2$ is the diamagnetic interaction. Most importantly, these formulas allow for electromagnetic fields in arbitrary directions and in particular facilitate arbitrary angles between magnetic and electric fields. The

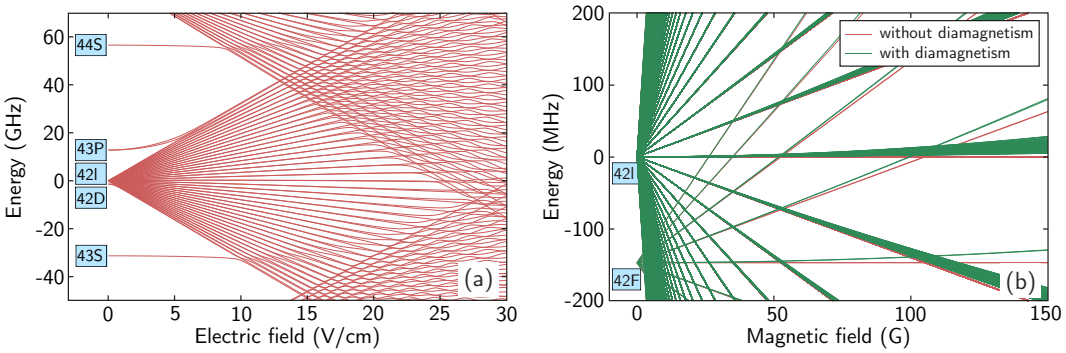

Fig. 3.2: (a) Stark map for the Na atom in the energy range of the $n = 42$ manifold. The magnetic quantum numbers do not mix under the assumption that the quantization axis is chosen parallel to the field. For clarity, only states with $m = 1/2$ are shown. (b) Zeeman map for the Na $n = 42$ manifold. Here, all the states within the plot range are depicted. The diamagnetic interaction increases the energies of the states. However, as diamagnetism does not contribute to the linear Zeeman effect it can be neglected for a weak magnetic field.

final Hamiltonian is

$$\hat{H}(\boldsymbol{R}) = \hat{H}_0 + \hat{H}_{\text{int}}(\boldsymbol{R}) + \hat{V}_{\text{e}} \otimes \mathbb{1} + \mathbb{1} \otimes \hat{V}_{\text{e}} + \hat{V}_{\text{m}} \otimes \mathbb{1} + \mathbb{1} \otimes \hat{V}_{\text{m}} \,. \tag{3.13}$$

In order to calculate matrix elements of $\hat{V}_{\text{e}}$ and $\hat{V}_{\text{m}}$, we have to do some preparatory work. In Appendix A.4, we review a powerful formalism to calculate matrix elements of spherical tensor operators. To make use of it, the notation of Eq. (3.11) and (3.12) has to be changed from the Cartesian basis to the spherical basis $\{\boldsymbol{e}_\pm = \mp\frac{1}{\sqrt{2}}(\boldsymbol{e}_x \mp i\boldsymbol{e}_y),\ \boldsymbol{e}_0 = \boldsymbol{e}_z\}$. In the spherical basis the components of, for example, the electric field are given by

$$E_\pm = \mp\frac{1}{\sqrt{2}}(E_x \pm iE_y) \,,\ E_0 = E_z \,. \tag{3.14}$$

Using this expression, the interaction with an electric field reads

$$-\hat{\boldsymbol{d}} \cdot \boldsymbol{E} = -e\,\hat{r} \cdot \sqrt{\frac{4\pi}{3}} \left(\hat{Y}_{1,0}E_0 - \hat{Y}_{1,1}E_- - \hat{Y}_{1,-1}E_+\right) \tag{3.15}$$

with spherical harmonics $Y_{\kappa q}(\hat{\vartheta}, \hat{\varphi})$. Likewise we can express the dot product of $\hat{\boldsymbol{J}} \in \{\hat{\boldsymbol{l}}, \hat{\boldsymbol{s}}\}$ and the magnetic field in the spherical basis

$$\hat{\boldsymbol{J}} \cdot \boldsymbol{B} = \hat{J}_{1,0}B_0 - \hat{J}_{1,1}B_- - \hat{J}_{1,-1}B_+ \,, \tag{3.16}$$

where $\hat{J}_{1q}$ are the spherical momentum operators. The operators $\hat{J}_{1,\pm1}$ are related to the ladder operators $\hat{J}_\pm = \mp\sqrt{2}\hat{J}_{1,\pm1}$ and $\hat{J}_z = \hat{J}_{1,0}$. The diamagnetic interaction in the spherical basis reads

$$\begin{aligned}\frac{1}{8m_e}|\hat{\boldsymbol{d}}\times\boldsymbol{B}|^2 = \frac{e^2}{12m_e}\hat{r}^2 \cdot \sqrt{\frac{4\pi}{5}}\Bigg(&\sqrt{5}\hat{Y}_{0,0}B^2 - \hat{Y}_{2,0}(B_0B_0 + B_+B_-)\\ &+ \sqrt{3}\hat{Y}_{2,1}B_0B_- + \sqrt{3}\hat{Y}_{2,-1}B_0B_+\\ &- \sqrt{\frac{3}{2}}\hat{Y}_{2,2}B_-B_- - \sqrt{\frac{3}{2}}\hat{Y}_{2,-2}B_+B_+\Bigg)\,. \end{aligned} \tag{3.17}$$

The entire atom-field interaction is now expressed in terms of spherical tensor operators, and we can proceed to calculate the matrix elements via the formalism of Appendices A.3 and A.4. This enables not only the calculation of pair potentials in the presence of external fields but also the computation of Stark/Zeeman maps, see Fig. 3.2.

3.2.3 Selection Rules and Symmetries

Knowing how to calculate matrix elements facilitates a rigorous derivation of the selection rules. The results for spherical harmonics and momentum operators are shown in Table 3.1. Note that the selection rules for spherical harmonics directly apply to the multipole operators. The selection rules greatly reduce the number of matrix elements which must be calculated explicitly for the construction of the pair Hamiltonian, enabling a significant reduction of computation time.

The considered system of two interacting Rydberg atoms has the same symmetries as any diatomic molecule. The point group of the system is $C_{\infty v}/D_{\infty h}$ if the system is heteronuclear/homonuclear [266]. The symmetries of the point group are conserved by the Hamiltonian (3.1) of the two Rydberg atoms in the absence of external fields.

From the symmetry under rotation about the interatomic axis, it follows that the projection of the total angular momentum on the interatomic axis is conserved. Since we have chosen the quantization axis to be parallel to the interatomic axis, the total magnetic quantum number

$$M = m_{j1} + m_{j2} \tag{3.18}$$

is conserved.

If the system is homonuclear, a further symmetry is the inversion symmetry

Spherical harmonics $\hat{Y}_{\kappa q}$ and multipole operators $\hat{p}_{\kappa q}$	Momentum operators $\hat{J}_{1q}$
n not restricted	n not restricted
$l = \begin{cases} l' \pm 0, 2, ..., \kappa & \text{for even } \kappa \\ l' \pm 1, 3, ..., \kappa & \text{for odd } \kappa \end{cases}$	$l = l'$
$s = s'$	$s = s'$
$j = j' \pm 0, 1, ..., \kappa$ and $j + j' \geq \kappa$	$j = j' \pm 0, 1$
$m_j = m'_j + q$ with $q \in \{-\kappa, -\kappa + 1, ..., \kappa\}$	$m_j = m'_j + q$ with $q \in \{-1, 0, 1\}$

Table 3.1: Selection rules for the matrix elements of the spherical harmonics $\langle nlsjm_j|\hat{Y}_{\kappa q}|n'l's'j'm'_j\rangle$ and momentum operators $\langle lsjm_j|\hat{J}_{1q}|l's'j'm'_j\rangle$ where $\hat{J}_{1q} \in \{\hat{l}_{1q}, \hat{s}_{1q}\}$. The selection rules for the spherical harmonics equal the selection rules for the matrix elements of spherical multipole operators $\langle nlsjm_j|\hat{p}_{\kappa q}|n'l's'j'm'_j\rangle$. The stated selection rules are explicitly tailored towards our use-case of atoms with one single Rydberg electron. They do not hold true for multi-electron atoms or molecules.

($\boldsymbol{r}_i \to -\boldsymbol{r}_i$, $\boldsymbol{R} \to -\boldsymbol{R}$). Then, a properly symmetrized basis state is of the form [231, 267, 268]

$$\begin{aligned} |\Psi\rangle_{g/u} \propto & |n_1 l_1 j_1 m_{j1}; n_2 l_2 j_2 m_{j2}\rangle \\ & - p(-1)^{l_1+l_2} |n_2 l_2 j_2 m_{j2}; n_1 l_1 j_1 m_{j1}\rangle \ , \end{aligned} \tag{3.19}$$

where $p = +1$ for states with *gerade* symmetry $|\Psi\rangle_g$ and $p = -1$ for states with *ungerade* symmetry $|\Psi\rangle_u$. The Hamiltonian does not couple states of gerade symmetry to states of ungerade symmetry.

Independenty of whether the system is homonuclear or heteronuclear, it is symmetric under reflection through a plane containing the interatomic axis [267, 268]. We choose the xz-plane as mirror plane. The reflection symmetry ($y_i \to -y_i$) can be exploited by changing into the symmetrized basis

$$\begin{aligned} |\Psi\rangle_{+/-} \propto & |n_1 l_1 j_1 m_{j1}; n_2 l_2 j_2 m_{j2}\rangle \\ & + d(-1)^{l_1+l_2+m_{j1}+m_{j2}-j_1-j_2} |n_1 l_1 j_1 - m_{j1}; n_2 l_2 j_2 - m_{j2}\rangle \end{aligned} \tag{3.20}$$

with $d = +1$ for even states $|\Psi\rangle_+$ and $d = -1$ for odd states $|\Psi\rangle_-$ under reflection. If the total magnetic quantum number is zero, we can symmetrize with respect to rotation, reflection, and inversion simultaneously. If it is non-

Symmetry	Conserved	$\hat{H}_{\text{int}}$		$\hat{V}_{\text{m}}$			$\hat{V}_{\text{e}}$		
operation	quantity	$\varrho = 3$	$\varrho > 3$	x	y	z	x	y	z
Symmetries originating from the point group $D_{\infty h}$									
Rotation about z-axis	$m_{j1} + m_{j2}$	✓	✓	⁄	⁄	✓	⁄	⁄	✓
Reflection through xz-plane	$+/-$	✓	✓	⁄	✓	⁄	✓	⁄	✓
Inversion	g/u	✓	✓	✓	✓	✓	⁄	⁄	⁄
Symmetry in case of symmetric interaction potentials									
Permutation	s/a	✓	⁄	✓	✓	✓	✓	✓	✓

Table 3.2: Overview about which symmetry operation commutes with which part of the Hamiltonian (3.13). A ✓-sign indicates that the symmetry is conserved whereas a ⁄-sign signals that the symmetry is broken. We differentiate between dipole-dipole interaction ($\varrho = 3$) and interaction up to a higher order in the multipole expansion ($\varrho > 3$). In case of the atom-field interactions $\hat{V}_m$ and $\hat{V}_e$, we distinguish between fields in the x, y, and z-direction. Inversion and permutation symmetry are only present in homonuclear systems. The reflection symmetry is only of importance if $m_{j1} + m_{j2} = 0$. Note, if both inversion and permutation symmetry are present, $(-1)^{l_1+l_2}$ is conserved as well.

zero, this is not possible since then the reflection and the rotation do not commute. In this case, we neglect the reflection symmetry.

In case of pure dipole-dipole interaction, a system of two homonuclear Rydberg atoms is subject to permutation symmetry ($\boldsymbol{R} \to -\boldsymbol{R}$) in addition to the symmetries of the point group. The interaction potential is symmetric under exchange of the two ionic cores. A properly symmetrized basis state is

$$|\Psi\rangle_{s/a} \propto |n_1 l_1 j_1 m_{j1}; n_2 l_2 j_2 m_{j2}\rangle - f\,|n_2 l_2 j_2 m_{j2}; n_1 l_1 j_1 m_{j1}\rangle \ , \tag{3.21}$$

where $f = +1$ for *symmetric* states $|\Psi\rangle_s$ and $f = -1$ for *antisymmetric* states $|\Psi\rangle_a$. Comparing Eq. (3.19) and (3.21) shows that

$$P = (-1)^{l_1+l_2} \tag{3.22}$$

is conserved when both permutation and inversion symmetry are present.

External fields might break the symmetries discussed above. If the operator of the atom-field interaction $\hat{V}_{\text{e}}$ (3.11) or $\hat{V}_{\text{m}}$ (3.12) does not commute with a symmetry operation, the symmetry is not conserved. For example, external fields that do not point along the interatomic axis can mix states of different total magnetic quantum numbers. Table 3.2 contains an overview of which

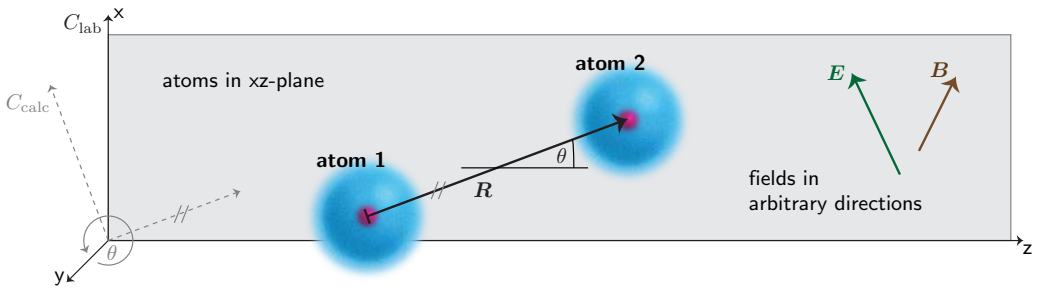

Fig. 3.3: Rotation of the coordinate system. We consider a pair of atoms whose interatomic axis is not parallel to the z-axis. In order to apply Eq. (3.7) for the atom-atom interaction, we have to rotate the coordinate system. Assuming that the interatomic axis lies in the xz-plane, a rotation around the y-axis is needed. The rotation changes the representation of the quantum mechanical states as well as the representation of the electric and magnetic fields. The figure illustrates our definition of the rotation angle θ.

symmetry operation commutes with which part of the Hamiltonian (3.13) of two interacting Rydberg atoms in the presence of external fields.

3.2.4 Angular Dependency

As discussed in Section 3.2.1, the formula for the atom-atom interaction (3.7) is only valid if we are in a coordinate system C_{calc} where the z-axis, which we chose as the quantization axis, points in the same direction as the interatomic axis. However, sometimes one would like to use a different coordinate system. For example, when the Rydberg state is excited by a laser pulse, it is convenient to use a coordinate system C_{lab} where the z-axis points along the laser beam.

To ease the calculation, let us assume that the interatomic axis lies in the xz-plane of C_{lab}. Then we can change into C_{calc} by rotating C_{lab} around the y-axis, see Fig. 3.3. The rotation angle θ is defined as the angle between the interatomic axis and the z-axis, and is called interaction angle.

Given that our coordinate systems are right-handed and the rotation of the coordinate system is counter-clockwise if the y-axis points towards the observer, the magnetic and electric fields transform according to

$$\boldsymbol{E}_{\text{calc}} = \begin{pmatrix} \cos\theta & 0 & -\sin\theta \\ 0 & 1 & 0 \\ \sin\theta & 0 & \cos\theta \end{pmatrix} \boldsymbol{E}_{\text{lab}} \,. \tag{3.23}$$

Any state $|nljm_j\rangle_{\text{lab}}$ in the lab frame, i.e. with the quantization axis parallel

to the laser beam, should be expressed as a linear superposition of states $|nljm_j\rangle_{\text{calc}}$ whose quantization axis points along the z-axis of C_{calc},

$$|nljm_j\rangle_{\text{lab}} = \sum_{m_j'} d^j_{m_j m_j'}(\theta)\, |nljm_j'\rangle_{\text{calc}} \ , \tag{3.24}$$

where the coefficients $d^j_{m_j m_j'}(\theta)$ are elements of the Wigner (lowercase) d-matrix [269]. If we had not fixed the interatomic axes in the xz-plane, we would have to use the Wigner (uppercase) D-matrix instead. Our notation is consistent with the definitions in [270].

Using the transformations (3.23) and (3.24), we can switch to the coordinate system C_{calc} and perform all calculations there.

In the absence of external electromagnetic fields, the eigenvalues of the Hamiltonian and thus the pair potentials do not depend on the interaction angle. However, the *overlap* of each unperturbed state $|n_1 l_1 j_1 m_{j1}; n_2 l_2 j_2 m_{j2}\rangle$ with a particular eigenstate does depend on the interaction angle. The quantum numbers of the unperturbed state become good quantum numbers if the interatomic distance approaches infinity and the atoms are not perturbed by external fields.

3.2.5 Extension Towards Alkaline Earth Metals

As described in Section 3.2.1, we treat Rydberg atoms as systems consisting of a single excited electron and an ionic core. This reduction to a single active electron problem is particularly justified for the alkali atoms because of the closed-shell structure of the ionic core.

If we excite one electron of an alkaline earth metal to a Rydberg state, the ionic core is no longer a closed shell because it contains the remaining valence electron. A precise numerical treatment of this system is more complicated than for the alkali atoms because the polarizability of the core is increased, and perturber states exist where both valence electrons are excited. Thus, for precise calculations, one must consider both electrons explicitly, using multichannel quantum defect theory [110]. However, for large principal quantum numbers n and large interatomic distances, the single active electron approximation is valid [109], and we can apply the same framework as for alkali atoms. This approximation relies on the assumption that $L - S$ coupling holds, and we can neglect terms that mix the singlet and triplet series. Then, we can calculate the pair interaction potentials for the singlet and triplet series independently, and the only difference to the treatment of alkali atoms is that the presence

of the second electron makes it difficult to describe the ionic core by model potentials. To avoid this problem, we use Whittaker functions for obtaining the radial wave functions and calculating radial matrix elements, see Appendix A.2. For the angular matrix elements, the formulas of Appendix A.4 hold true with spin quantum number $s = 0$ for the singlet state and $s = 1$ for the triplet state. Another possibility is to calculate matrix elements semiclassically [271]. Note that for sufficiently large n, the single active electron approximation also works well for other atomic species, such as the noble gases [272] and even the lanthanides [273].

The Appendix A.1 lists all atomic species that are supported by the `pairinteraction` software at the time of writing and provides references to quantum defects.

3.3 Construction of the Hamiltonian Matrix and Diagonalization

In the previous sections, we established the Hamiltonian of two interacting Rydberg atoms and explained how matrix elements of the Hamiltonian can be calculated using Appendices A.3 and A.4. This allows us to compute the matrix representation of the Hamiltonian. We calculate pair potentials of the unperturbed state $|n_1 l_1 j_1 m_{j1}; n_2 l_2 j_2 m_{j2}\rangle$ by numerical diagonalization of the Hamiltonian matrix for a range of interatomic distances. Then, the eigenenergies are plotted versus the distances to make up the pair potentials. By drawing lines between the eigenenergy points for which the overlap between the eigenvectors is maximal, we extract the pair potential curves. The overlap between an eigenvector and the unperturbed state tells the probability to find the unperturbed state on the corresponding pair potential curve.

In order to make the diagonalization of the Hamiltonian computationally feasible, we have to keep the matrix size small. Therefore, it is important to exploit conservation laws. As discussed in Section 3.2.3, the Hamiltonian might conserve several quantum numbers and symmetries, leading to a block diagonal structure of the Hamiltonian matrix, see Fig. 3.4(a).

Each block can be diagonalized independently, which leads to a massive speed-up as the computation of all eigenpairs of a $n \times n$-matrix costs $\mathcal{O}(n^3)$ floating-point operations [274, 275]. Furthermore, we diagonalize only those blocks that belong to the unperturbed state we are interested in. In addition, we have to restrict the basis to states having a significant influence on the pair potentials of the unperturbed state.

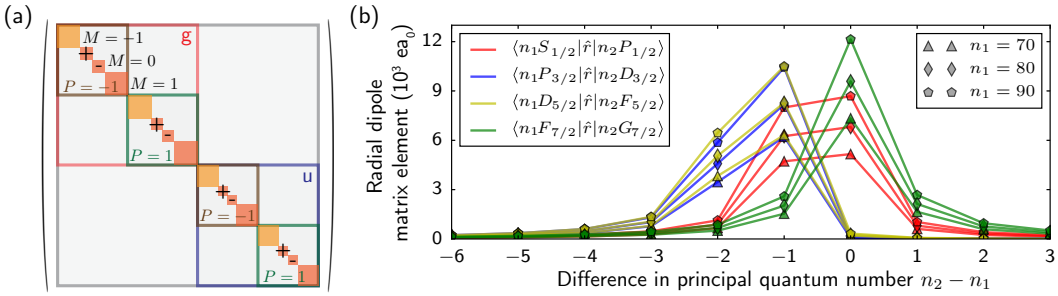

Fig. 3.4: (a) Block diagonality of the Hamiltonian matrix for a pair of dipole-dipole interacting Rydberg atoms in the absence of external fields. As discussed in Section 3.2.3, the Hamiltonian matrix for a homonuclear pair of atoms decomposes into a gerade/ungerade block (g/u) . Pure dipole-dipole interaction additionally conserves $P = (-1)^{l_1+l_2}$. Moreover, $M = m_{j1} + m_{j2}$ is conserved if the interatomic axis points along the z-axis. Blocks belonging to $M = 0$ can be further decomposed into an even/odd block under reflection (+/-). (b) Radial dipole matrix elements for rubidium as a function of the difference in principal quantum numbers $n_2 - n_1$ (for reasons of simplicity, only matrix elements with $j_1 = j_2$ are shown). The value of the matrix elements decreases rapidly with $n_2 - n_1$. This facilitates restriction of the basis set by means of the principal quantum number.

Hereto, we have several possibilities. First, we can restrict the basis to elements with similar energies as the unperturbed state. Second, it is often useful to constrain the momentum quantum numbers because interaction of high order is required to change the momentum quantum numbers by large values. However, this constraint does not work if states involved in the high order interaction are degenerate as it is the case for Stark map calculations. Third, we can constrain the principal quantum number. If two states do not have similar principal quantum numbers, their radial matrix elements and hence their interaction is negligible, see Fig. 3.4(b). Higher order interactions, which would only require matrix elements with similar principal quantum numbers, would also be weak as the required order increases with the principal quantum number. How the constraints should be chosen depends on many factors like the considered distances, the required accuracy, the quantum numbers of the unperturbed states, the order of the multipole expansion, external fields, and the atomic species. Thus, giving the right constraints is difficult a priori. In fact, the constraints have to be tested for each calculation. For obtaining a small basis size, we start with strong constraints and loosen them systematically until the pair potentials of the unperturbed state have converged within the distance threshold we are interested in. The convergence is extensively discussed in [231].

For calculating pair potentials in the presence of external electromagnetic fields, the following approach has turned out to be useful: We construct a single-atom basis and calculate the atom-field Hamiltonian for each of the two atoms independently. We enlarge the basis sets until the Stark/Zeeman maps have converged. We combine the eigenstates of the single-atom Hamiltonians into pair states and obtain a pair basis that is suitable for establishing the total Hamiltonian including atom-atom interactions. The combined eigenenergies, that are the Stark/Zeeman energies of the pair states, are located on the diagonal of the Hamiltonian. This procedure has the advantage, that we can now restrict the pair basis to the states relevant for the atom-atom interaction without losing accuracy in the treatment of the electromagnetic fields. Constraining the pair basis stronger than the single-atom basis is appropriate, in particular because the atom-field interaction typically couples over larger energy ranges than the atom-atom interaction. Furthermore, whereas atom-field interactions might change energies drastically, the small amount of admixed states is irrelevant for the atom-atom interaction in many cases of practical relevance. Despite these actions, the inclusion of electromagnetic fields can drastically increase the computational cost. Depending on the type of field, the block structure of the Hamiltonian matrix is destroyed.

3.4 Applications

In this section, we discuss three examples of the Rydberg potential calculation with relevance to recent experiments. Comparison with experimental results enables us to validate our numerical results and demonstrate the applicability of full potential calculations to state-of-the-art experiments. It also allows us to benchmark the influence of the basis size and of the truncation order on the interaction potentials.

3.4.1 Relevance of Higher-Order Multipole Terms

As a first example application, we study multipole terms in the interaction potential of order higher than dipole-dipole, i.e. $\varrho > 3$ in Eq. (3.9). The relevance of these terms has been highlighted in several recent experiments [184, 229, 231, 237]. We focus here on the observation of Rydberg aggregation dynamics in a vapor cell at room temperature by Urvoy *et al.* [184]. In this experiment, the high atomic densities and the spectral width of the laser pulses allow to probe Rydberg interaction at short interatomic distances, with one

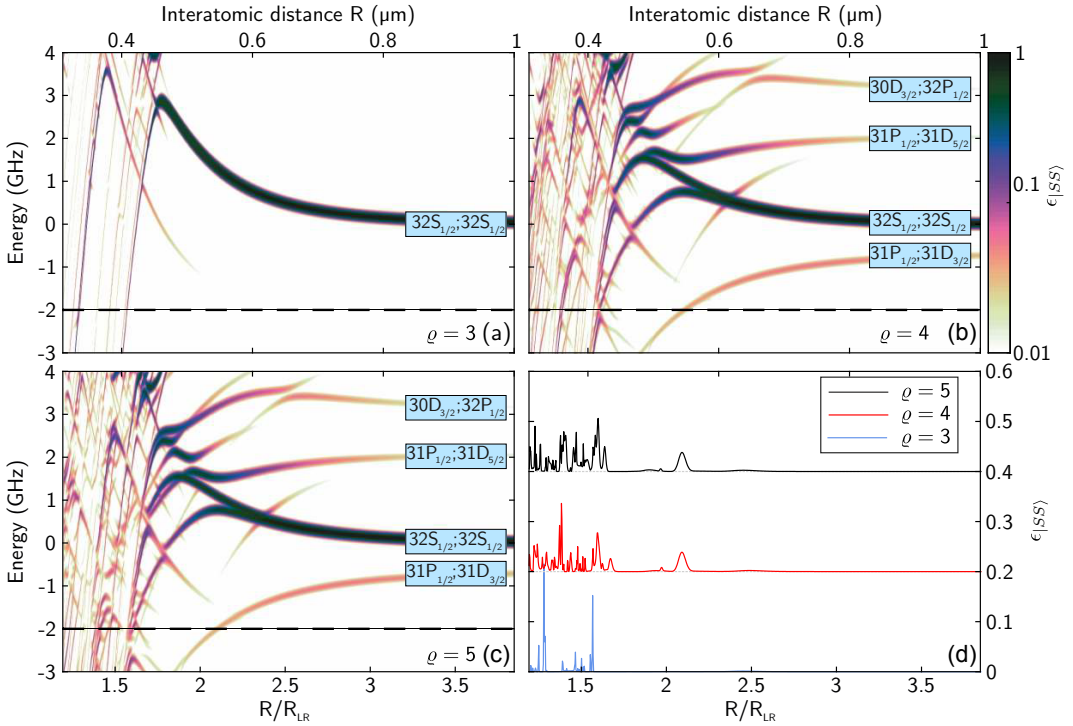

Fig. 3.5: (a-c) Potential landscape around the unperturbed Cs $|32S_{1/2}; 32S_{1/2}\rangle$ state calculated up to order $1/R^{\varrho}$ of the multipole expansion of the interaction potential: (a) $\varrho = 3$, (b) $\varrho = 4$, (c) $\varrho = 5$. (d) Admixture $\varepsilon_{|SS\rangle}$ to the perturbed pair states for a cut through the potential at a red detuning of $-2\,\mathrm{GHz}$. Cuts for $\varrho = 4$ and $\varrho = 5$ are shifted by an offset of 0.2 and 0.4, respectively. The inclusion of the dipole-quadrupole term ($\varrho = 4$) results in the resonance feature at $R/R_{\mathrm{LR}} \approx 2.1$, which is identified in [184] as the dominant underlying reason for the experimentally observed formation of Rydberg aggregates. While inclusion of one additional order somewhat changes the potential landscape, this resonance feature is not affected.

key finding being that the correlated excitation of Rydberg atoms is driven by the dipole-quadrupole ($\varrho = 4$) contribution to the interaction.

Specifically, in the experiment, Rydberg excitation in a Cesium vapor cell is driven by two-photon excitation with red detuning $\Delta = \omega_{\mathrm{Laser}} - \omega_{\mathrm{Atom}} = -2\,\mathrm{GHz}$ relative to the $32S$ Rydberg state. The pure van der Waals interaction potential resulting from dipole-dipole coupling of two atoms in this state is repulsive, see Fig. 3.5(a), suggesting that the presence of one Rydberg atom does not increase the excitation probability of further Rydberg atoms by the red-detuned driving lasers.

However, including the dipole-quadrupole interaction ($\varrho = 4$) results in admixture of the $|32S_{1/2}; 32S_{1/2}\rangle$ pair state into several close-lying, attractively interacting pair states (such as $|31P_{1/2}; 31D_j\rangle$ and $|32P_{1/2}; 30D_j\rangle$), as shown in Fig. 3.5(b). As done in [184], we quantify the admixture of, for example, $|SS\rangle = |32S_{1/2}, m_j = 1/2; 32S_{1/2}, m_j = -1/2\rangle$ to any Rydberg pair state $|\Psi\rangle$ by $\varepsilon_{|SS\rangle}(\Delta) = |\langle\Psi|SS\rangle|$. Any such admixture at detuning Δ results in efficient optical excitation of additional Rydberg atoms at specific distances to a first seed excitation. In particular, Urvoy *et al.* identified the resulting resonance at $R/R_{\mathrm{LR}} \approx 2.1$ (where R_{LR} is the LeRoy radius), which is reproduced by our calculations, as the dominant underlying mechanism for the correlated Rydberg aggregation observed in the experiment [184].

Based on this finding, an obvious question is how additional multipole orders further modify the interaction potential. In Fig. 3.5(c), we show the resulting potential map when the $\varrho = 5$ terms, corresponding to quadrupole-quadrupole and dipople-octupole interactions, are included. Significant effects of these contributions can be seen at small interatomic distances $1 < R/R_{\mathrm{LR}} < 1.7$, for example in the detuning region between 2 GHz and 4 GHz. For the experiment, the relevant figure is $\varepsilon_{|SS\rangle}(\Delta = -2\,\mathrm{GHz})$. We show the extracted values for all three potential calculations ($\varrho = 3, 4, 5$) in Fig. 3.5(d). While the inclusion of the $\varrho = 5$ terms also modifies $\varepsilon_{|SS\rangle}$ at short distances, the main relevant resonance feature at $R/R_{\mathrm{LR}} \approx 2.1$ is not modified by the higher-order terms. Thus, the quantitative differences in the potential landscape due to the next higher-order terms do not affect the conclusions in [184].

In contrast, the features at small distances are relevant for example for formation of bound pair states of Rydberg atoms [226–230], requiring inclusion of even further orders in the calculation [228, 231]. In general, when increasing ϱ, care has to be taken that the pair-state basis truncation is appropriately adapted to include enough coupled states. In this example, we have used the constraints $\Delta n = 5$ and $\Delta l = 6$ on the differences in quantum numbers of the individual Rydberg states with respect to the state $|32S_{1/2}; 32S_{1/2}\rangle$. These cutoff criteria are motivated by the selection rules for the different interaction orders discussed in Section 3.2.3 and the scaling of the electric multipole matrix elements, see Section 3.3. Of particular importance for precise calculations at distances $1 < R/R_{\mathrm{LR}} < 1.7$ are the symmetry considerations of Section 3.2.3, which help to greatly reduce the size of the relevant pair-state basis [231].

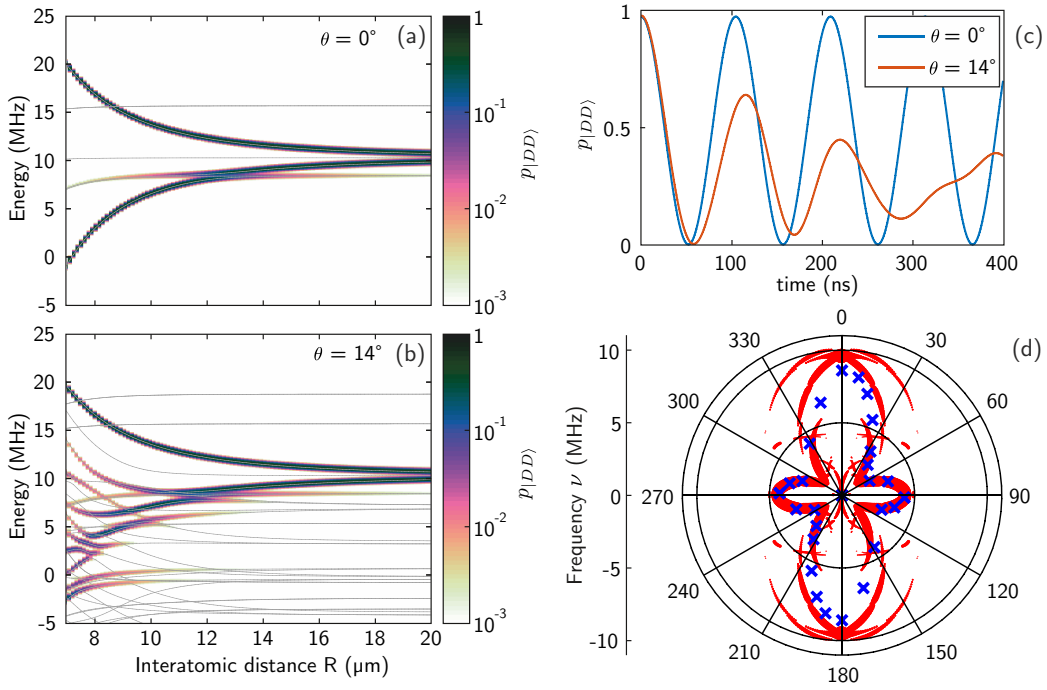

Fig. 3.6: (a) Pair potential of the $|DD\rangle = |59D_{3/2}, m_j = 3/2; 59D_{3/2}, m_j = 3/2\rangle$ state tuned into Förster resonance with the $|PF\rangle = |61P_{1/2}, m_j = 1/2; 57F_{5/2}, m_j = 5/2\rangle$ state by applying an electric field of 34.3 mV/cm for both atoms aligned along the quantization axis, i.e. $\theta = 0°$. (b) Same pair potential as in (a) but for an angle of $\theta = 14°$ between the interatomic and the quantization axis. (c) Time evolution of the probability to find the system in the $|DD\rangle$ state in the presence of an electric field. For $\theta = 0°$ the system undergoes undamped oscillations between the $|DD\rangle$ and $|PF\rangle_{+/-}$ state with a frequency of 9.2 MHz. The multi level structure relevant for $\theta = 14°$ in (b) results in damping out of the oscillations due to dephasing (red line). (d) Angular dependence of the multiple oscillation frequencies out of the $|DD\rangle$ state. To illustrate how strong different frequencies do show up in the time evolution the size of the points encodes the relative weight of each frequency. The blue crosses depict the experimental results of Ravets *et al.* [252].

3.4.2 Angular Dependence Near a Förster Resonance

As a second example application, we demonstrate the calculation of anisotropic Rydberg interactions in the presence of electric and magnetic fields, as discussed in Sections 3.2.2 and 3.2.4. In this context, we calculate the interaction potentials measured in the experiments of Ravets *et al.* in [252]. Here, two single ^{87}Rb atoms were prepared in their ground state in two tightly focussed optical

tweezers. Both the distance R between the two atoms and the angle θ between the interatomic axis and the external fields could be precisely tuned. Using a two-photon excitation scheme, both atoms were excited to the $|59D_{3/2}, m_j = 3/2\rangle$ state by applying a π-pulse. In the pair-state basis and at zero electric field, the state $|DD\rangle = |59D_{3/2}, m_j = 3/2; 59D_{3/2}, m_j = 3/2\rangle$ is detuned by 8.69 MHz from the state $|PF\rangle = |61P_{1/2}, m_j = 1/2; 57F_{5/2}, m_j = 5/2\rangle$. Due to the different polarizabilities of the states, both pair states could be tuned into degeneracy by applying a weak electric field of 34.3 mV/cm. With this approach, Ravets *et al.* could map out the angular shape of the electric dipole-dipole interaction between the two atoms [252].

More specifically, the strength of the interaction was measured by letting the two-atom system evolve after the Rydberg excitation and in the presence of the electric field. After a variable hold time, a second optical π-pulse coupling to the $|DD\rangle$ state was employed to bring the atoms back to their ground state. By measuring the ground-state population after the full sequence, the time-evolution of the $|DD\rangle$ Rydberg pair-state population could be reconstructed. Performing this experiment for various angles θ and fixed distance $R = 9.1\,\mu$m resulted in the beautiful dipole-dipole pattern of the interaction shown by the blue crosses in Fig. 3.6(d).

For comparison with the experimental results, we calculate the full potentials for different angles θ including the finite electric and magnetic fields. Here, the optimized matrix construction discussed in Section 3.3 is particularly relevant to make precise calculations feasible. As an example, we show in Fig. 3.6(a) and (b) the potentials obtained for $\theta = 0°$ (atoms aligned with respect to the external fields) and $\theta = 14°$, respectively. Besides the energy shifts caused by the interaction, we encode here the probability $a_k = |\langle DD|\varphi_k\rangle|^2$ to find an admixture of the initially prepared unperturbed $|DD\rangle$ state in the new eigenstate $|\varphi_k\rangle$ as a density plot. For $\theta = 0°$, Fig. 3.6(a) show that a two-level approximation is valid for most of the distances between 7 µm and 20 µm. Most importantly, at the experimentally relevant distance $R = 9.1\,\mu$m, the system can be treated as a two-level system.

However, the situation changes for an angle of $\theta = 14°$, where the two-level approximation breaks down. This is caused by mixing of the different fine structure states of the $|57F\rangle$ state and of different magnetic levels coupled for non-zero interaction angles.

From the calculated potentials and more specifically the overlap probabilities a_k, it is straight-forward to calculate the coherent evolution of the interacting Rydberg atom pair. Specifically the time-dependent probability of being in the $|DD\rangle$ state in the presence of interaction is given by $p_{|DD\rangle}(t) =$

$|\sum_k a_k \exp\left(i\frac{E_k}{\hbar}t\right)|^2$. Examples for two different angles and $R = 9.1\,\mu\text{m}$ are shown in Fig. 3.6(c). For $\theta = 0°$, we obtain an undamped sinusoidal oscillation with a frequency of $\nu = 9.2\,\text{MHz}$, which corresponds to the splitting of the most strongly populated pair potentials. In the case of $\theta = 14°$ the significant coupling to multiple other pair states leads to dephasing that effectively damps out the Rabi oscillations. These results agree very well with the experimental time-evolution reported in [252].

In Fig. 3.6(d), we show all frequencies contributing to the time evolution for $R = 9.1\,\mu\text{m}$ and varying θ, obtained from the energy differences $E_m - E_n$ of the pair states to which the initial state couples (red points). The size of each point encodes the relative weight of each frequency, which is proportional to $a_m \cdot a_n$. For comparison, the single frequencies at each θ extracted from the experiment are shown by the blue crosses. One can see that for $0° \leq \theta \leq 5°$ and for $55° \leq \theta \leq 90°$ our calculations find a single dominant contribution, which is in excellent agreement with the experimental data. In contrast, for angles outside these regions, the increased number of pair states contributing to the time evolution explains the damped oscillations measured in the experiment. We thank Antoine Browaeys and Thierry Lahaye for providing the experimental data.

3.4.3 Finding Parameters for the Realization of Spin Models

As a third example application, we show how the Rydberg potential calculation can be applied to find experimental parameters for realizing spin models with Rydberg atoms, harnessing the atom-atom interaction. As described in the foundations in Section 2.2.3, the general idea is to map electronic states of the Rydberg atom to spin states, and the challenge is to find experimental conditions under which the mapped states are isolated from other states. In other words, the mapped states must be located in a subspace of the total Hilbert space that is energetically well separated from neighboring states, i.e., the separation in energy must be significantly larger than the interaction that couples states from the subspace to neighboring states.

To find experimental conditions that isolate the subspace, we can calculate Rydberg potentials for different external fields and check whether the admixture of non-desired states to the pair potential curves is small. Such a parameter scan is exemplarily discussed in Chapter 4. It ensures that all interactions between two Rydberg atoms can be described accurately within the subspace. Note that in principle, higher-order couplings can still occur that act on more than two Rydberg atoms, causing a leakage out of the subspace. This leakage

mechanism can only be excluded entirely if all states of more than two atoms are isolated as well. However, as it is a higher-order effect, it can often be neglected, assuming that one does not hit a resonance accidentally.

When we have succeeded in isolating the subspace, we can treat the coupling to the neighboring states perturbatively. By doing so, neighboring states get admixed to the states of the subspace, i.e., the subspace gets dressed, and effective interactions emerge. For obtaining the effective Hamiltonian that governs the dynamics of the resulting spin model, we can apply perturbation theory [276–278]. Such an effective Hamiltonian can then be simulated by a Rydberg quantum simulator, see also Chapters 5 to 7.

3.5 Conclusions and Outlook

In this chapter, we discussed the calculation of interaction potentials between pairs of atoms excited to Rydberg states. Precise knowledge of the full potential landscape has become relevant to a wide range of experiments utilizing Rydberg atoms in recent years. Our goal was to give a comprehensive summary of all the relevant calculation steps of the Rydberg potential for describing current and future experiments. We reviewed the symmetry properties of the interaction Hamiltonian and the selection rules of the different multipole orders. These considerations are crucial for efficient calculation of the interaction potentials. Two further aspects important for experiments are the angular dependence of the interaction and the inclusion of external magnetic and electric fields of arbitrary direction. Particularly, electric fields offer the powerful ability to strongly modify the Rydberg interaction by tuning to Förster resonances of Rydberg pair states. With the rapid progress of both experiments and theory investigating interacting Rydberg systems, it seems likely that more features of the Rydberg potentials will be explored and exploited in the future.

4

Accurate Mapping of Rydberg Atoms on Spin-1/2 Particles

For performing quantum simulations of spin Hamiltonians with Rydberg atoms, it is necessary to identify electronic states of a Rydberg atom that can be mapped to spin states.

In this chapter, we discuss an illustrative example of such a mapping [2]. We study arrays of atoms that are laser-driven to the $nD_{3/2}$ Rydberg state and analyze how accurately the atoms can be mapped onto spin-1/2 particles for the quantum simulation of anisotropic Ising magnets. We use non-perturbative calculations of Rydberg interaction potentials, see Chapter 3, to carefully determine experimental parameters for which the excitation of unwanted Rydberg states is avoided and the mapping accurate. The group of Antoine Browaeys has performed experiments to test our predictions, using systems of up to 49 atoms [2]. Comparisons between the results of the experiments and numerical simulations of spin-1/2 models confirm that the determined parameter set allows for an accurate mapping. For details on the experiments, see the PhD thesis by Sylvain de Léséleuc [3].

4.1 Introduction

One of the main ingredients to realize quantum simulations of spin Hamiltonians with Rydberg atoms is the mapping of suitable Rydberg levels to spin states and a full characterization of the interaction potentials. In the simplest case, one identifies the atomic ground state as the spin-down state $|\downarrow\rangle$ and the Rydberg excitation as the spin-up state $|\uparrow\rangle$ for the implementation of spin-1/2 Hamiltonians [60, 61, 137, 279]. However, in practice, describing the atom as a two-level system is an approximation that can be difficult to fulfill due to the

small splittings between levels in the Rydberg manifold. For a single atom, it is sufficient to apply a magnetic field of a few Gauss to isolate a single two-level transition. But already for two atoms, the density of pair-states becomes quite large, and, due to the interactions, mixing between different levels occurs in configurations without special symmetries (Fig. 4.1). Finding the optimal parameters such that the system is accurately described as a spin-1/2 system with a well-defined interaction potential is thus a non-trivial task, that needs to be addressed in view of applications in quantum simulation.

A natural choice for implementing spin Hamiltonians with Rubidium Rydberg atoms is to use nS Rydberg states [61], as they possess only two Zeeman sublevels and do not feature Förster resonances [52]. However, many experiments use nP or nD states: the former are the only ones accessible from the ground state using single-photon dipole transitions [167, 280] and are used in particular for Rydberg dressing [141, 142, 281, 282], while the latter [60, 132, 133] require less laser power for excitation from the ground state as compared to nS states. Moreover, for both nP and nD states, the van der Waals interaction can be anisotropic, opening the way for simulating exotic matter [222, 223]. Nevertheless when implementing an anisotropic Ising model with $nD_{3/2}$ states, deviations from the prediction of a spin-1/2 model can occur, as observed in [60].

In this chapter, we thus focus on Rydberg $nD_{3/2}$ states, and derive under which conditions the simple picture of a spin-1/2 model with an effective anisotropic interaction potential between the pair states is valid, despite the large number of Rydberg levels involved. For that purpose, we use our `pairinteraction` software [1] to numerically calculate the exact pair-state potentials in the presence of external electric and magnetic fields. We find a remarkable sensitivity of the interaction spectrum to weak static electric fields, which can lead to a breakdown of the Rydberg blockade not considered in previous studies [52, 53, 241, 243, 283, 284]. Our collaborators from the group of Antoine Browaeys then experimentally corroborate this prediction. Finally, we extend our study to a ring of 8 atoms and a 7×7 square array, the settings for which some deviations from the spin-1/2 model were observed in [60], and now demonstrate a much better agreement with a numerical simulation.

4.2 Setup

We use the Rydberg state $|r\rangle = |nD_{3/2}, m_J = 3/2\rangle$ and couple it to the atomic ground state $|g\rangle = |5S_{1/2}, F = 2, m_F = 2\rangle$ by a two-photon transition, see

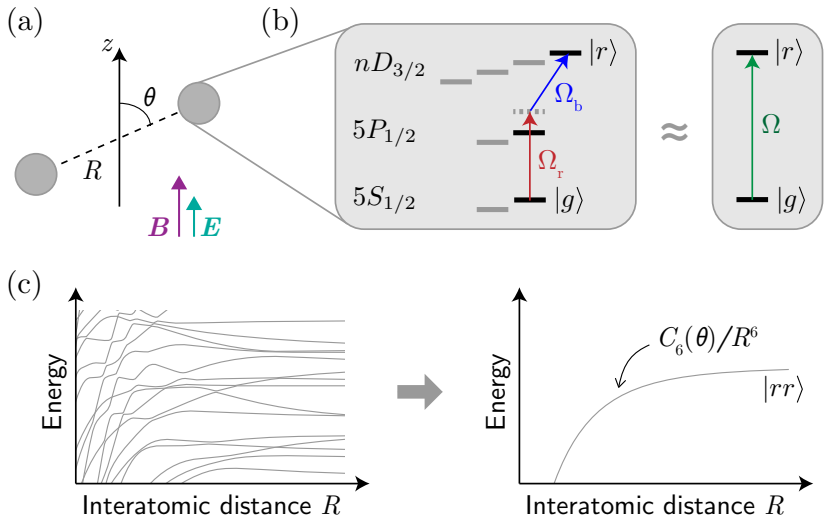

Fig. 4.1: **Mapping a system of multilevel Rydberg atoms onto a spin-1/2 model.** (a) System: two atoms separated by a distance R; θ is the angle between the interatomic axis and the quantization axis z defined by a magnetic field B. An electric field E can be applied along z. (b) A two-photon transition couples coherently the ground state $|g\rangle$ to a target Rydberg state $|r\rangle$ with an effective two-photon Rabi frequency Ω. (c) Full energy spectrum of the atom pair. The mapping consists in replacing this complex structure by an effective interaction potential.

Fig. 4.1(b). Ideally we want to identify the states $|g\rangle$ and $|r\rangle$ with pseudo spin-1/2 states $|\downarrow\rangle$ and $|\uparrow\rangle$. In this case, when taking into account interactions between atoms in $|r\rangle$, the system maps onto an Ising-like model in a transverse field [60, 61, 137, 279] governed by the Hamiltonian

$$H = \frac{\hbar\Omega}{2}\sum_i \sigma_i^x + \frac{1}{2}\sum_{i\neq j} U_{ij} n_i n_j. \tag{4.1}$$

Here, Ω is the Rabi frequency corresponding to the laser driving, $\sigma_i^x = |r\rangle\langle g|_i + |g\rangle\langle r|_i$, $n_i = |r\rangle\langle r|_i$, and the rotating wave approximation and rotating frame have been applied. The interaction between atoms i and j is given at large distances by an anisotropic van der Waals potential $U_{ij} = C_6(\theta_{ij})/R_{ij}^6$, where R_{ij} is the interatomic distance and θ_{ij} the angle between the internuclear axis and the quantization axis, see Fig. 4.1(a). For shorter distances, deviations from the $1/R^6$ behavior are expected.

4.3 Requirements for an Accurate Mapping

4.3.1 Lifting the Zeeman Degeneracy

We now look for conditions allowing us to describe the interaction spectrum for a pair of atoms by a single potential curve $U(R, \theta)$ as shown in Fig. 4.1(c). To approach this problem quantitatively, purely analytic approaches are of little use, and we use numerical methods to diagonalize the dipole-dipole Hamiltonian [56] (as well as higher-order multipole contributions) in the presence of arbitrarily oriented external electric and magnetic fields, see also Chapter 3. In view of reproducing the experiment of reference [60], we chose the state $|r\rangle = |61D_{3/2}, m_J = 3/2\rangle$. Fig. 4.2 shows the interaction spectrum for a generic angle $\theta = 78°$. The shading of the various interaction potentials shows the overlap of the states with $|rr\rangle$. In Fig. 4.2(a), no magnetic and electric fields are applied, and some Zeeman pair states interact very weakly, while they are still coupled to $|gg\rangle$. Consequently, the Rydberg blockade is broken as the double excitation of Rydberg states is possible even at short distances [53, 243]. Fig. 4.2(b) shows the interaction potentials, but now in the presence of a magnetic field $B = -6.9$ G. The Zeeman effect splits the various potentials and the state $|rr\rangle$ is now well isolated from the other eigenstates. However, since the sign of the Zeeman shift is opposite to that of the van der Waals interaction, there are some specific values of the interatomic distance R where the laser excitation of other Zeeman pair states is resonant; these *magic distances*, predicted by [284], can thus lead to a breakdown of the blockade. In order to avoid this effect, one can simply use an opposite value for the B field. This is what we do in Fig. 4.2(c), where $B = 6.9$ G. These parameters are similar to the ones applied in [60], and in these conditions, it is a good approximation to describe the system by a single state for $R > 6\,\mu$m.

4.3.2 Avoiding E-Field Sensitivity

It turns out, however, that the interaction potentials are extremely sensitive to electric fields E. Fig. 4.2(d) corresponds to the same parameters as in Fig. 4.2(c), but now in the presence of an electric field $E = 20$ mV/cm along z. A naive calculation of the Stark shift of pair states for such a value of E, neglecting resonance effects, would give shifts in the 100 kHz range, which would have hardly any influence on the potentials. However, the exact diagonalization shows that the interaction potentials are strongly affected, with many states being resonant with the excitation laser. We thus expect a significant breakdown

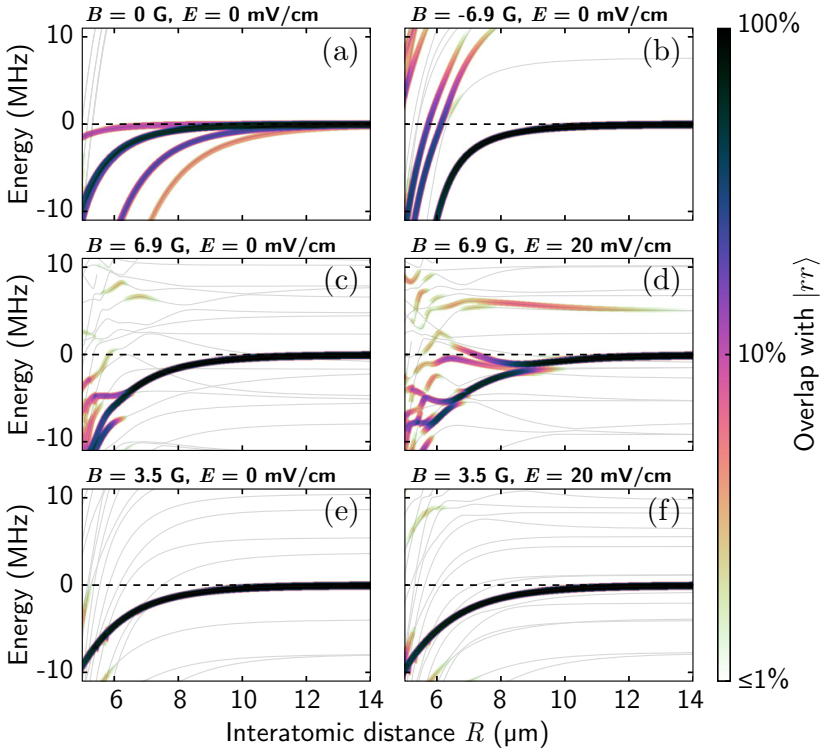

Fig. 4.2: **Influence of magnetic and electric fields on the interaction potentials around the pair-state $|rr\rangle$ for $\theta = 78°$.** Here, $|r\rangle = |61D_{3/2}, m_j = 3/2\rangle$. The shading encodes the overlap of the eigenstates with the non-interacting state $|rr\rangle$. (a) $B = 0$ and $E = 0$: $|rr\rangle$ overlaps with all the degenerate Zeeman pair states. (b) $B = -6.9$ G and $E = 0$: the interaction curves are split due to the Zeeman effect. Some curves still strongly mix with $|rr\rangle$ due to the interaction. (c) $B = 6.9$ G and $E = 0$: one potential curve dominates. However, (d) the addition of a small electric field $E = 20$ mV/cm is enough to strongly perturb the pair states. (e-f) This behavior is absent for $B = 3.5$ G.

of the Rydberg blockade in these conditions. Remarkably, this effect is absent for lower magnetic fields $B = 3.5$ G, see Fig. 4.2(e-f). In the optimal regime where a single potential curve $U(R, \theta)$ can be identified, we check if we can describe it by a van der Waals potential with an angular dependence $C_6(\theta)/R^6$. Fig. 4.3(a) shows the energy dependence as a function of R for $\theta = 78°$ together with a $1/R^6$ fit. We observe, that for $R \gtrsim 8\,\mu$m, the van der Waals description is a reasonable approximation. Fig. 4.3(b) shows the angular dependence of the coefficient $C_6(\theta)$. We have thus extended the anisotropic effective potential approach developed in [191, 284] beyond the strong blockade regime.

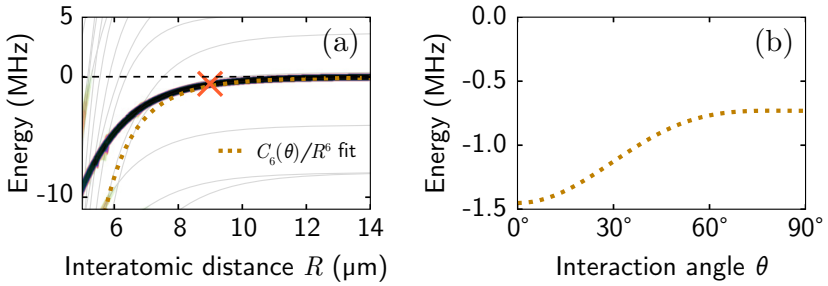

Fig. 4.3: **Approximation of the interaction by an anisotropic van der Waals potential $C_6(\theta)/R^6$.** (a) Comparison of the exact interaction energy (solid line) with the asymptotic determination of the van der Waals potential (dashed line) for a fixed angle $\theta = 78°$ and $B = 3.5$ G. (b) Angular dependence of $C_6(\theta)/R^6$ at $R = 9\,\mu$m marked by the cross on (a).

4.4 Testing the Predictions

4.4.1 Two-Atom Blockade Experiments

We now turn to the experimental test of the above predictions. The setup of our experimental collaborators has been described in detail elsewhere [60] (for a brief review of the Rydberg platform, see also Section 2.2). Their setup consists of a configurable two-dimensional array of optical tweezers, fully-loaded with atoms optically pumped into $|g\rangle$. After switching off the tweezers, the atoms are illuminated with a Rydberg excitation pulse of duration τ and effective Rabi frequency $\Omega = 2\pi \times 1.2$ MHz. At the end of the sequence, the tweezers are switched on again, resulting in a recapturing of atoms in $|g\rangle$ and a repulsion of atoms in a Rydberg state. Thus, in a subsequent fluorescence image, atoms in $|g\rangle/|r\rangle$ are observed as occupied/empty sites.

As a first test of the influence of electric and magnetic fields on the potential curve, two-atom blockade experiments are performed [132, 133] with $R = 6.5\,\mu$m and $\theta = 78°$, i.e., the same parameters as in Fig. 4.2. Four different settings of the external fields are applied: the magnetic field is either 3.5 or 6.9 G, and the electric field either zero (within the accuracy ~ 5 mV/cm of the cancellation of stray fields) or 20 mV/cm. In order to quantify the Rydberg blockade, the probability P_{rr} to have two Rydberg excitations after illuminating the atoms with the excitation pulse is measured. The results are displayed in Fig. 4.4. Our collaborators observe as expected a strong suppression of $|rr\rangle$ for all settings, except for $B = 6.9$ G and $E = 20$ mV/cm, where the probability to excite the two atoms is significant. To compare with the theory, we simulate the dynamics of the two-atom system solving the Schrödinger equation and calculate the

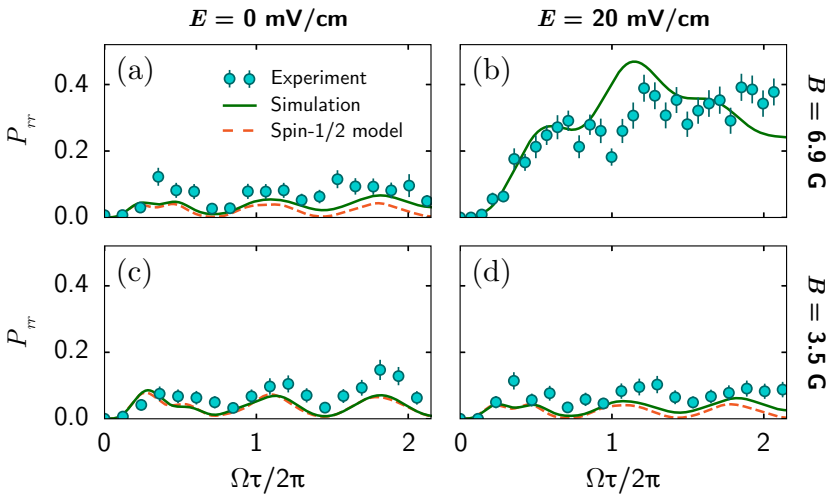

Fig. 4.4: **Two-atom blockade experiments.** Probability P_{rr} to excite the two atoms as a function of the pulse area $\Omega\tau$. For $B = 6.9$ G (a-b), increasing E from 0 to 20 mV/cm breaks the Rydberg blockade. At $B = 3.5$ G (c-d), an efficient blockade is maintained, even in the presence of the electric field. The dots depict the experimental data measured by our collaborators. The solid lines result from a simulation taking into account the full interaction spectrum (see text). The dashed lines are obtained by modeling the atoms as spin-1/2 particles with a single interaction potential for $|rr\rangle$, except in case (b) where the pair-state is too perturbed. The error bars show the standard error of the mean.

probability to excite the two atoms[17]. We assume two different models to describe the interacting system: in the first one (Fig. 4.4 solid line), we use the full interaction spectrum and include around 800 pair-states within 2 GHz from the resonance (a bigger electric field would drastically increase the basis size). This simulation with no adjustable parameter is in excellent agreement with the experimental data. In the second model (dashed line), we describe the interaction in the $|rr\rangle$ state with the single potential curve identified above, thus solving the spin-1/2 model governed by the Hamiltonian (4.1).

Geometry Dependency of the Blockade

We now investigate more systematically how the geometry and the value of the electric and magnetic fields affect the accuracy of the mapping on a spin-1/2

[17]We include the residual shot-to-shot fluctuations of the interatomic distance by averaging the result of the Schrödinger equation over 200 realizations of the random positions of the atoms in their tweezers.

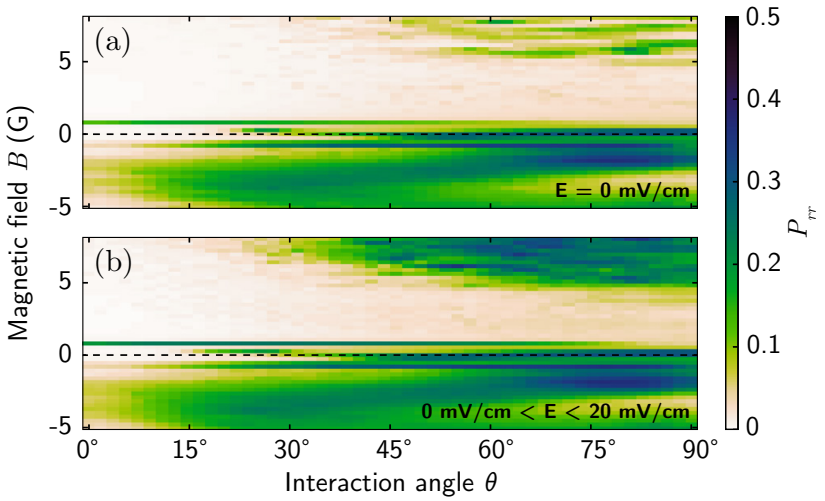

Fig. 4.5: **Influence of θ, B, E on the mapping onto a spin-1/2 system.** Probability of double excitations at long times (see text) as a function of the magnetic field B and the angle θ. The interatomic distance is fixed at $R = 6.1\,\mu$m. The electric field is $E = 0$ in (a) and chosen between 0 and 20 mV/cm such that the probability for two Rydberg excitations is maximized in (b).

model. Using the exact simulation taking into account the full interaction spectrum, as done for Fig. 4.4, we calculate the average value of the double excitation probability P_{rr} at long times and look at the range of parameters for which P_{rr} remains small. Fig. 4.5(a) corresponds to the case $E = 0$, while Fig. 4.5(b) shows a *worst-case scenario* where E is chosen in the range $0 - 20$ mV/cm so as to maximize P_{rr}. For $\theta \approx 0$ the system is faithfully described by a spin-1/2 system. For increasing angle θ, we identify the range of magnetic fields where Rydberg blockade is maintained. In addition, we observe a breaking of the Rydberg blockade for negative magnetic fields as predicted in [284]. A similar analysis for various principal quantum numbers n indicates that the presence of a Förster resonance at $n = 59$ is responsible for this sensitivity to weak electric fields [285].

4.4.2 Dynamics of an Ensemble of Atoms

Now that we have identified parameters allowing to map our two-atom system onto a spin-1/2 model, we extend the study to larger systems. We first revisit the experimental realization of an 8-atom ring, reported in [60], where a discrepancy with the spin-1/2 model was observed. Our experimental collaborators

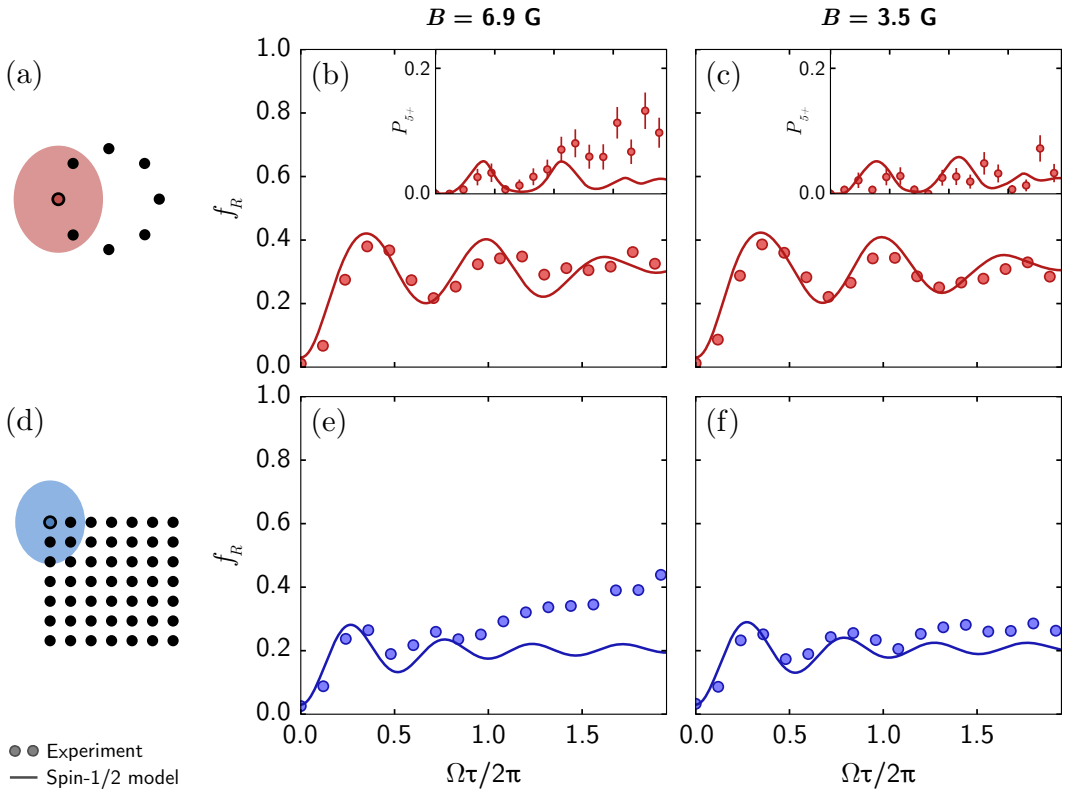

Fig. 4.6: **Dynamics of an ensemble of atoms under Rydberg excitation.** (a) 8-atom ring with a nearest-neighbor spacing of 6.5 μm. The shaded ellipse illustrates the range of the anisotropic blockaded region $U > \hbar\Omega$. (b) Evolution of the Rydberg fraction f_{R} with the pulse area $\Omega\tau$ for $B = 6.9$ G. The inset shows the probability P_{5+} to observe configurations with at least 5 excitations. At large times, the experimental points systematically lie above the results of a simulation of the corresponding spin-1/2 model (solid line). (c) Same parameters with $B = 3.5$ G. (d) Square lattice of 7×7 traps (lattice spacing 6.1 μm). The blockade extends over nearest and next-nearest neighbors. (e) Evolution of the Rydberg fraction for $B = 6.9$ G. Here the data shows a slow increase in f_{R} at long times, while the spin-1/2 model predicts a saturation. (f) For $B = 3.5$ G, the agreement with the spin-1/2 model becomes very good. All figures: error bars depict the standard error of the mean and are often smaller than the symbol size.

illuminate the atoms with a Rydberg excitation pulse and observe the ensuing dynamics following this quench by measuring the fraction f_{R} of atoms that are excited to Rydberg states. They also extract the probability P_{5+} that more than

five atoms are excited, i.e., that the blockade condition is violated as for our parameters nearest-neighbor excitation is thwarted. Prior to this experiment the stray electric field is compensated better than 5 mV/cm. Fig. 4.6(a-c) shows the results for two values of the magnetic fields. For $B = 6.9$ G, the experiment shows a slow rise of P_{5+} above the prediction of the spin-1/2 model. Contrarily, for $B = 3.5$ G, we find a much better agreement with the spin-1/2 model as expected from the above analysis.

In a second experiment, our collaborators probe a square array of 7×7 atoms. The evolution of f_{R} is shown in Fig. 4.6(d-f). As an exact simulation of the dynamics of the 49-atom system is no longer possible, we use the fact that two neighboring atoms cannot be excited due to the Rydberg blockade to truncate the Hilbert space from 2^{49} to $\sim 2^{30}$ states. We have checked with systems of up to 25 atoms, that the truncation gives the same results as an exact calculation. We solve the time-dependent Schrödinger equation using a split-step approach. Again, we find a deviation with respect to the spin-1/2 model for $B = 6.9$ G, while at lower B the agreement is much better. We have thus identified the conditions where the system can be used as a quantum simulator of anisotropic spin-1/2 Ising model.

4.5 Conclusions and Outlook

In conclusion, we have explored the mapping on spin-1/2 models of interacting multilevel Rydberg atoms by taking into account the underlying details of the atomic structure in the presence of electric and magnetic fields. We searched for conditions under which the interaction between two Rydberg atoms can be faithfully described by a single potential curve. We found that this approximation can be sensitive to electric fields, thus extending previous studies on the breakdown of the Rydberg blockade [52, 53, 241, 243, 283, 284], and searched numerically for an optimal region of parameters. Then, using atomic arrays of increasing size, from a pair of atoms to a 7×7 array, we confirmed that the experimentally observed dynamics under a quench is accurately reproduced by a spin-1/2 model with anisotropic Ising interaction. This work opens exciting prospects for harnessing the rich interaction spectrum of Rydberg atoms, for the engineering of various spin Hamiltonians. These insights could also help to improve the control of interactions in Rydberg dressing experiments using $nP_{3/2}$ states [142], as well as for Rydberg slow light polaritons with nD states [240].

5

Symmetry-Protected Topological Phase of Interacting Bosons

The concept of topological phases is a powerful tool for characterizing quantum many-body ground states beyond Landau's paradigm of symmetry breaking. While a few topological phases appear in condensed matter systems, it has been an outstanding goal to realize a topologically non-trivial many-body ground state in artificial matter.

In this chapter, we discuss the quantum simulation of a symmetry-protected topological phase of interacting bosons in a one-dimensional lattice. The discussion is based on our joint theoretical and experimental project [4] that was performed together with the group of Antoine Browaeys. They realized the symmetry-protected topological phase experimentally with Rydberg atoms and demonstrated a robust ground state degeneracy that is attributed to protected edge states. The setup is based on atoms that are trapped in an array of optical tweezers and excited into Rydberg levels, which gives rise to hard-core bosons with an effective hopping by dipolar exchange interaction.

Here, we mostly concentrate on our theoretical contributions to the project and compare experimental results with simulations. To present a coherent story, we also provide an overview about the experimental setup. For more information about the experiment, see the reference [4] and the PhD thesis by Sylvain de Léséleuc [3]. For details about the classification of the realized symmetry-protected topological phase of interacting bosons and its connection to the celebrated Haldane state, see the PhD thesis by Nicolai Lang [5].

5.1 Introduction

The paradigm of symmetry breaking has proven very successful for characterizing quantum phases. However, not all of them follow this paradigm, and some of these phases are nowadays characterized in the framework of topological phases. The most prominent example of a topological phase is the integer quantum Hall state with its remarkably robust edge states giving rise to a quantized Hall conductance [286]. For a long time, it was believed that such phases occurred only in the presence of a magnetic field, until the prediction of topological insulators [287] revealed a novel class of topological states of matter, nowadays denoted as symmetry-protected topological phases (SPT). They occur in systems displaying an excitation gap in the bulk, i.e., bulk insulators, and an invariance under a global symmetry. Their defining property is that the ground state at zero-temperature cannot be transformed into a conventional insulating state upon deformations of the system that do not close the excitation gap or violate the symmetry. In particular, the edge states are robust to any perturbation commuting with the symmetry operators.

SPT phases were first predicted and observed in materials where the interaction between electrons can be effectively neglected [288, 289]. In this specific case of non-interacting fermions, SPT phases can be classified based on the action of the Hamiltonian on a single particle [290, 291]. Thus, the appearance of robust edge states is fully understood from the single-particle eigenstates. This remarkable simplification motivated experimental studies of topological phenomena at the single-particle level with artificial quantum matter realized on ultracold atoms platforms [65–71], and in classical systems of coupled mechanical oscillators [72, 73], as well as optical [74–77] or radio-frequency circuits [78], and plasmonic systems [79, 80].

In contrast, the situation is different for bosonic SPT phases as the ground state of non-interacting bosons is a Bose-Einstein condensate. Therefore, it is well established that strong interactions between the particles are required for the appearance of topological phases. Their classification is not derived from single-particle properties, but requires the analysis of the quantum many-body ground state; a classification of bosonic interacting SPT phases based in terms of group cohomology has been achieved [292]. A notable example is the Haldane phase of the anti-ferromagnetic spin-1 chain [293], which has been experimentally observed in some solid-state materials [294, 295]. However, the realization of topological phases in artificial matter, where one has full microscopic control on the particles, would allow to gain a deeper understanding on the nature of such topological states of matter. A first step has recently

been achieved by introducing interactions between bosonic particles in a system with a topological band structure [71, 296], but studies were restricted to the two-body limit, still far from the many-body regime.

Here, we discuss the first realization of a many-body SPT phase of interacting bosonic particles in an artificial system. Our setup is based on a staggered one-dimensional chain of Rydberg atoms, each restricted to a two-level system, resonantly coupled together by the dipolar interaction [124]. We use this to encode hard-core bosons, i.e., bosonic particles with infinite on-site interaction energy, coherently hopping along the chain. The system then realizes a bosonic version of the Su-Schrieffer-Heeger (SSH) model [297]; the latter originally described fermionic particles hopping on a dimerized lattice, giving rise to a SPT phase of non-interacting fermions. Similarly, our bosonic setup gives rise to two distinct phases of an half-filled chain: a trivial one with a single ground state and an excitation gap, and a SPT phase, with a four-fold ground state degeneracy due to edge states, and a bulk excitation gap. Following an adiabatic preparation of a half-filled chain, our experimental collaborators detect the ground state degeneracy in the topological phase and probe the zero-energy edge states. Furthermore, they experimentally demonstrate the robustness of the SPT phase under a perturbation respecting the protecting symmetry. We show that this robustness cannot be explained at the single-particle level, a feature that distinguishes our system from non-interacting SPT phases. All experimental results are in excellent agreement with our numerical simulations.

5.2 SSH Model for Hard-Core Bosons

The SSH model is formulated on a one-dimensional lattice with an even number of sites N and staggered hopping of particles, see Fig. 5.1(a). It is convenient to divide the lattice into two sub-lattices: $A = \{1, 3, \ldots, N-1\}$, involving odd lattice sites, and $B = \{2, 4, \ldots, N\}$, with even sites. Then, a particle on site i of one sub-lattice can hop to a site j of the other sub-lattice with a hopping amplitude J_{ij} (we do not restrict the system to nearest-neighbor hopping). The many-body Hamiltonian is

$$H_{\mathrm{SSH}} = -\sum_{i\in A, j\in B} J_{ij}\left[b_i^\dagger b_j + b_j^\dagger b_i\right], \tag{5.1}$$

with $b_i^\dagger$ (b_i) the creation (annihilation) operator of a particle on site i. In the original formulation of the SSH model, the particles are non-interacting fermions. Here, we consider hard-core bosons and the operators $b_i^\dagger$ (b_i) satisfy

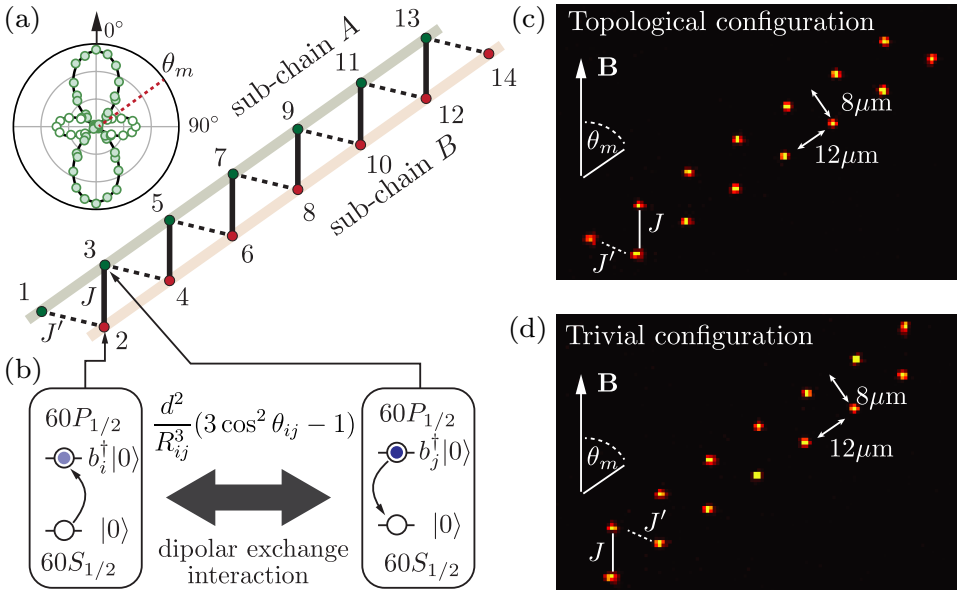

Fig. 5.1: **Bosonic SSH model**. (a) Dimerized one-dimensional lattice and the two sub-lattices A and B. The staggered nearest-neighbor hopping energies are denoted as J and J' with $|J| > |J'|$. (b) Each lattice site hosts a Rydberg atom with two relevant levels: $60S_{1/2}$ being the vacuum state $|0\rangle$ and $60P_{1/2}$ describing a bosonic particle $b_i^\dagger|0\rangle$. The dipolar exchange interaction provides a hopping of the particles. (Inset in a) Angular dependence of the hopping amplitude measured between two sites; filled (empty) disk: positive (negative) amplitude. It vanishes and changes sign at the angle $\theta_m \simeq 54.7°$. The solid line is the theoretical prediction. Error bars, denoting the standard error of the mean, are smaller than the symbol size. (c-d) Single-shot fluorescence images of the atoms assembled in the artificial structure for the topological (c) and the trivial (d) configuration. The chain is tilted by the angle θ_m to cancel couplings between sites in the same sub-lattice.

bosonic commutation relations on different sites $i \neq j$, and additionally the hard-core constraint $(b_i^\dagger)^2 = 0$, as two bosons cannot occupy the same site i. In our realization, the nearest-neighbor hoppings are dominant with their energies denoted as $J_{2i,2i+1} = J$ and $J_{2i-1,2i} = J'$ with $|J'| < |J|$, and are sufficient to describe the qualitative behavior of the model.

At the *single-particle level*, the spectrum of the Hamiltonian in Eq. (5.1), shown in Fig. 5.2(a), is obtained by diagonalizing the coupling matrix J_{ij}. It displays two bands separated by a spectral gap $2(|J| - |J'|)$ and, depending on the boundaries of the chain, localized zero-energy edge modes. There are two such modes for a chain ending with weak links J' (topological configuration,

Fig. 5.1(c)) and none if the chain ends with strong links J (trivial configuration, Fig. 5.1(d)). The topology of the bands emerges from the sub-lattice (or chiral) symmetry of the SSH Hamiltonian [290, 291], which notably constrains the hopping matrix J_{ij} to connect only sites of different sub-lattices, e.g., next-nearest-neighbor hoppings $J_{i,i+2} = J''$ are forbidden. The existence and degeneracy of edge modes are topologically protected from any perturbation that does not break the sub-lattice symmetry. These single-particle properties of the coupling matrix J_{ij}, defining the SSH model, have been observed in many platforms such as, e.g., ultracold atoms [298, 299], polaritons in array of micropillars [79], or mechanical granular chains [300].

We now turn to the properties of the *quantum many-body ground state*[18] corresponding to a half-filled chain. For non-interacting fermions, the properties of the SSH chain follow from the Fermi sea picture based on the single-particle eigenstates: in the trivial configuration one obtains a single insulating ground state, while, in the topological configuration, (i) an excitation gap appears in the bulk, and (ii) the ground state is four-fold degenerate as the two zero-energy edge modes can be either empty or occupied. For interacting bosons, the description of the many-body ground state is much more challenging. In the special case with only nearest-neighbor hoppings J and J', the bosonic many-body ground states for hard-core bosons can be derived via a Jordan-Wigner transformation from the fermionic ones, and inherits the properties of a bulk excitations gap and a four-fold ground state degeneracy in the topological configuration, see the supplementary material to our publication [4] and the PhD thesis by Nicolai Lang [5]. Based on the general classification of bosonic SPT phases [292], these properties are robust by adding longer-range hoppings as well as additional interactions between the bosons as long as the bulk gap remains finite, and the protecting symmetry is respected. Here, the protecting symmetries are the particle number conservation and the anti-unitary operator

$$\mathcal{S}_B = \prod_{i=1}^{N} \left[b_i + b_i^\dagger \right] K, \tag{5.2}$$

where $b_i + b_i^\dagger$ is a particle-hole transformation and K denotes the complex conjugation. In contrast to the chiral symmetry (protecting the single-particle properties and the fermionic SPT phase), next-nearest-neighbor hoppings $J'' = J_{i,i+2}$ are symmetry allowed, i.e., $[H_{\mathrm{SSH}}, \mathcal{S}_B] = 0$ even when including J''.

[18] Note that technically speaking, the simulations as well as the experiment do not realize the ground state of the Hamiltonian H_{SSH} as defined in Eq. (5.1), but the highest-energy state of $-H_{\mathrm{SSH}}$. However, since our setup is a closed system, both states are equivalent.

We will demonstrate this fundamental difference by engineering a perturbation which shifts the edge modes away from zero-energy at the single-particle level, but preserves the ground state degeneracy in the bosonic many-body system.

5.3 Realization with Rydberg Atoms

5.3.1 Experimental Setup

Our bosonic SSH model is realized on an artificial structure with $N = 14$ sites of individually trapped ^{87}Rb atoms [44, 46, 187], see Fig. 5.1(c-d). The motion of the atoms is frozen during the experiment of our collaborators. Coupling between the atoms is achieved, despite the large inter-atomic distance ($\sim 10\,\mu$m), by considering Rydberg states for which the dipole-dipole coupling is enhanced to a few MHz [124, 128].

Our experimental collaborators first prepare each atom in a Rydberg S-level, $|60S_{1/2}, m_J = 1/2\rangle$, using a two-photon STImulated Raman Adiabatic Passage (STIRAP) with an efficiency of 95%. From there, the atom can be coherently transferred to a Rydberg P-level, $|60P_{1/2}, m_J = -1/2\rangle$, using a microwave field. We denote the state with all Rydberg atoms in the S-level as the vacuum $|0\rangle$ of the many-body system, while a Rydberg atom at site i excited in a P-level is described as a bosonic particle $b_i^\dagger|0\rangle$. Since each Rydberg atom can only be excited once to the P-level, we obtain naturally the hard-core constraint. The resonant dipolar interaction occuring between the S- and P-levels of two Rydberg atoms at site i and j gives rise to hopping of these particles [124], as illustrated in Fig. 5.1(b). We use this to engineer the hopping matrix J_{ij}.

At the end of the experiment, our collaborators de-excite atoms in the Rydberg S-level to the electronic ground state and detect them by fluorescence imaging, while an atom in the Rydberg P-level is lost from the structure. To obtain occupancy probabilities, the measured occupancy of each site is averaged over several experimental runs.

To implement the sub-lattice symmetry, we use the angular dependence of the dipolar coupling $J_{ij} = d^2(3\cos^2\theta_{ij} - 1)/R_{ij}^3$ with d the transition dipole moment between the two Rydberg levels. The hopping depends on the separation R_{ij}, as well as the angle θ_{ij} with respect to the quantization axis defined by the magnetic field $B_z \simeq 50$ G. In Fig. 5.1(a), we show the measured angular dependence, vanishing at the *magic angle* $\theta_m = \arccos(1/\sqrt{3}) \approx 54.7°$, which allows us to suppress the hopping along this direction. By arranging the atoms in two sub-chains aligned along the magic angle, we thus satisfy the sub-lattice symmetry. The measured nearest-neighbor couplings are $J/h = 2.42(2)$ MHz

and $J'/h = -0.92(2)$ MHz, in full agreement with our numerical determination of the pair potential, using the `pairinteraction` software [1]. Note that calculations in first order perturbation theory were not sufficient to get a high level of agreement, but it was necessary to read off the interaction strengths from the non-perturbatively calculated pair potentials.

5.3.2 Numerical Simulation

To verify the experimental results and our understanding of the system, we simulate the experiments numerically with no adjustable parameters, allowing for quantitative comparisons between theory and experiment.

Within our simulations, we do not model the preparation of the Rydberg S-level explicitly but only study the dynamics after the atoms have been prepared in the Rydberg state. There is a finite preparation error, measured to be $\eta = 5 - 7$ %, that an atom is not transferred to the Rydberg level. This gives rise to lattice defects, that are taken into account in the numerical simulations by averaging over typically ~ 1000 lattice realizations.

Our simulations calculate the dynamics under the Hamiltonian

$$H = H_{\mathrm{SSH}} + \frac{\hbar\Omega_{\mu\mathrm{w}}(t)}{2} \sum_i \left[b_i^\dagger + b_i \right] - \hbar\Delta_{\mu\mathrm{w}}(t) \sum_i b_i^\dagger b_i \,, \tag{5.3}$$

where H_{SSH} is given by Eq. (5.1). Our Hamiltonian explicitly accounts for the microwave field that is applied by our experimental collaborators to coherently transfer atoms from the S-level to the P-level, which we treat in the rotating frame using the rotating wave approximation. The detuning from the transition is $\Delta_{\mu\mathrm{w}}$, and the Rabi frequency is $\Omega_{\mu\mathrm{w}}/(2\pi) \sim 0.1 - 20$ MHz. Moreover, within H_{SSH}, we take into account that dipolar interaction also gives rise to longer range hoppings, for example a hopping to third-nearest neighbors on the order of ~ 0.2 MHz. These processes do not qualitatively change the properties of our system but are important to obtain accurate results. All dipolar interactions are extracted from pair potential curves calculated with our `pairinteraction` software [1], taking into account the applied magnetic field $B_z = 47\,\mathrm{G}$. The time evolution governed by (5.3) is calculated using a Krylov subspace method [301].

As a final step, we account for two different error processes in the experimental detection process: First, a ground state atom may have moved away so that it cannot be recaptured. This happens with a measured probability of $\varepsilon = 0.05(1)$. Second, an atom left in the Rydberg manifold might have decayed spontaneously so that it is recaptured by mistake. The probability of the latter is $\varepsilon' = 0.05(1)$

as well. Both processes are considered via Monte Carlo sampling of the simulation results.

5.4 Single-Particle Properties

5.4.1 Single-Particle Spectrum

As a benchmark of our system, we first study the properties of a single-particle in the chain. The single-particle spectrum is probed by microwave spectroscopy, see Fig. 5.2(a). Initializing the vacuum state $|0\rangle$ with all Rydberg atoms in the S-level, a weak microwave probe with a Rabi frequency $\Omega_{\mu\mathrm{w}}/(2\pi) = 0.2$ MHz applied for a time $t = 0.75\,\mu$s can lead to the coherent creation of a particle only if an eigenstate energy matches the microwave detuning $\Delta_{\mu\mathrm{w}}$ and if this state is coupled to $|0\rangle$ by the microwave field. We show in Fig. 5.2(b) the site-resolved probability to find a particle on a given site for the two different chain configurations. In both cases, we observe a clear signal for $\hbar\Delta_{\mu\mathrm{w}} < |J'| - |J|$ from lower band modes delocalized along the chain. States in the upper band are not observed as the microwave coupling from $|0\rangle$ to these states is very small. Only in the topological configuration, we observe an additional signal localized at the boundaries around zero energy, corresponding to the two edge modes.

To allow for a quantitative comparison of these experimental results with a simulation, we calculate the average occupancy at the edge (sites 1 and 14) and in the bulk (sites 2 to 13) as a function of the microwave detuning $\Delta_{\mu\mathrm{w}}$. For both the trivial and topological chain, we perform this calculation with the experimental data and with data that we obtained by our simulation approached described in Section 5.3.2. We achieve an excellent agreement between theory and experiment, see Fig. 5.2(c), including the positions and widths (due to microwave power broadening) of the spectroscopic features. For the topological configuration, the excitation of the edge modes is seen beautifully in the simulation as well as in the experimental data. Careful assessment of the spectrum shows that there is a slightly increased probability for creating particles at zero energy for the bulk as well. We explain this feature by the presence of lattice vacancies that can result in zero-energy modes within the bulk. The main effect of the detection errors is that the probability for detecting a particle off-resonantly is increased by $\epsilon = 0.05$.

In Fig. 5.2(d), we show the localization of edge modes at the boundary by post-selecting experimental runs where at most one particle was created. We observe that the particle populates significantly only the leftmost and rightmost

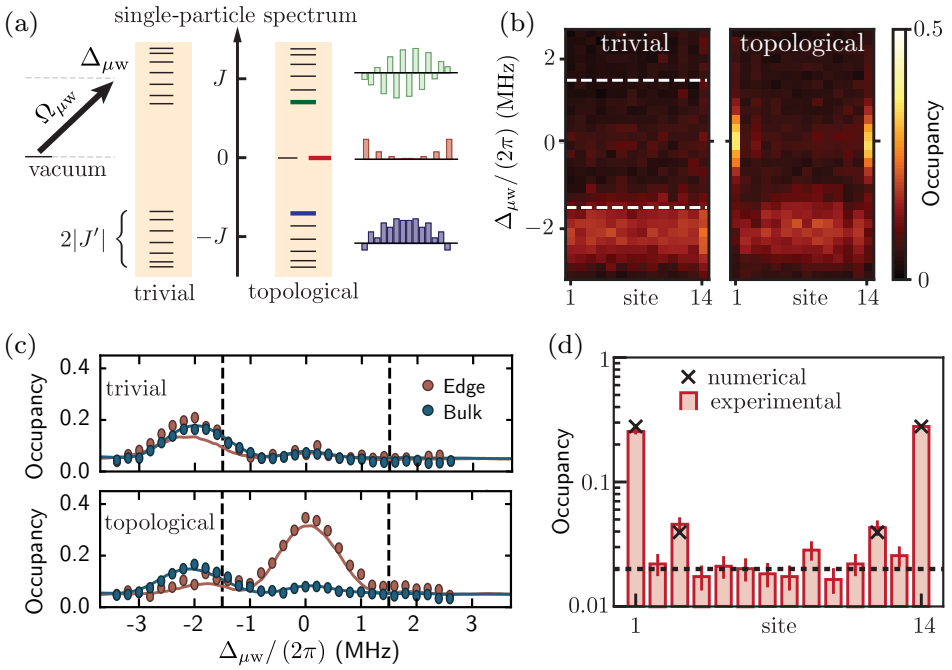

Fig. 5.2: **Single-particle spectrum.** (a) Single-particle spectrum for the trivial and the topological configuration probed by microwave spectroscopy. Right: selection of single-particle wavefunctions calculated by our collaborators. (b) Experimental site-resolved spectra showing the averaged occupancy of each site as a function of $\Delta_{\mu w}$. The lower band bulk states are always observed, whereas the upper band is not visible due to a suppressed coupling to the microwave probe. Edge states at zero energy appear only for the topological configuration. The white dashed lines indicate the band gap. (c) Comparison of the measured single-particle spectra (dots) with theory (lines). The spectra show the probability to find a particle on the leftmost or rightmost site, as well as the site-averaged probability to find a particle in the bulk as a function of the microwave detuning $\Delta_{\mu w}$. Error bars are standard errors of the mean and smaller than the symbol size. (d) Spatial distribution of the edge states, observed (red bars) and calculated (black crosses), showing an exponential localization on the edges. The dashed line indicates the 2 % noise level caused by preparation and detection errors.

sites, and their second neighbors, as expected from the sub-lattice symmetry (edge states have support on one of the two sub-chains only) and in a good agreement with a parameter-free calculation (black crosses).

5.4.2 Hybridization of Edge Modes

For any finite chain, the left and right edge modes hybridize to form symmetric and antisymmetric states with an energy difference $E_{\mathrm{hyb}} \propto J'|J'/J|^N$, which breaks the degeneracy of the edge modes but decreases exponentially with the chain length N. While this remains negligible compared to the experimental time scale for a long chain of 14 sites ($E_{\mathrm{hyb}} \simeq h \times 20$ kHz), the hybridization is observable for smaller chains. Notably, it gives rise to a coherent transfer of a particle between the two boundaries without involving the bulk modes, as sketched in Fig. 5.3(a). To observe this experimentally, our collaborators prepare a localized particle on the leftmost site with an efficiency of ~ 94 % using a combination of an addressing beam and microwaves sweeps [302], and then let the system evolve freely. Fig. 5.3(b) shows the experimental results for three chains of 4, 6 and 8 sites.

Fig. 5.3(c-d) compares measurements, taken from Fig. 5.3(b), with a simulation for a chain of 6 atoms. For this simulation, we took the state with one particle on the leftmost site as the initial state, i.e., we did not model the creation of the particle explicitly. The dominant oscillation frequency, which gives the hybridization energy, agrees well between theory and experiment. The high-frequency oscillations which are visible in the simulation average out in the experiment due to shot-to shot fluctuations of atomic positions as well as motions of atoms, causing varying hopping strengths. The transfer probability is smaller than one because of lattice defects.

The hybridization energy E_{hyb} can be obtained numerically by diagonalizing the coupling matrix J_{ij} for different chain lengths up to $N = 100$ sites, see Fig. 5.3(e). After initially decreasing exponentially, E_{hyb} scales algebraically with the chain length, as the direct coupling $J_{1,N} \propto 1/N^4$ between the edges dominates over the higher-order coupling via nearest-neighbor interactions $J_{i,i+1}$. The $1/N^4$ scaling is a combination of the $1/R^3$-dependence of the dipolar interaction and the pair of edge sites getting closer to the magic angle. Note that the transition to the algebraic regime happens for significantly longer chains than studied in the experiment. To determine the hybridization energy experimentally, our collaborators measure the frequency of the particle transfer between the two edges, see zoom-in of Fig. 5.3(e). Their results are in excellent agreement with our theoretical calculations.

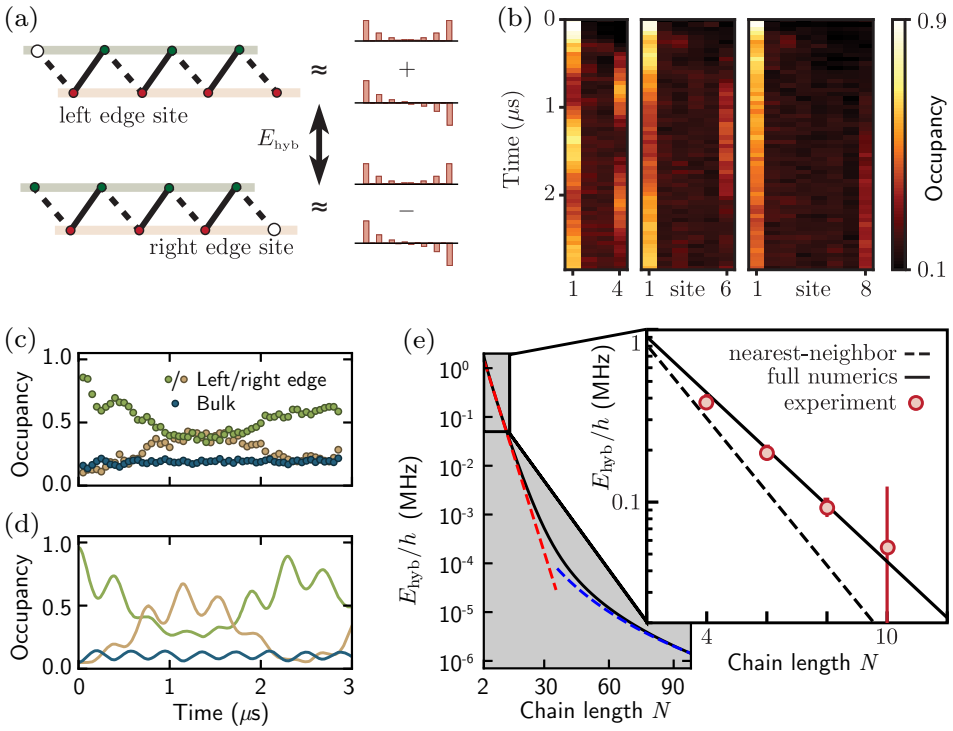

Fig. 5.3: **Particle transfer between the two edges**. (a) A particle on the left edge is essentially a superposition of the symmetric and antisymmetric zero-energy modes, split in energy by E_{hyb} due to the hybridization for finite chains. (b) Experimental observation of the transfer for chains of $N = 4$, 6 and 8 sites after injecting a particle on the leftmost site. (c) Measured and (d) simulated time evolution of the probability to find a particle on the left or right edge or in the bulk for $N = 6$. (e) Scaling of the hybridization energy E_{hyb}. The red curve is an exponential fit for short chain lengths. For longer chains, the hybridization energy scales algebraically as $1/N^4$ (blue curve). The zoom-in shows the hybridization energy obtained experimentally from the transfer frequency (red dots) and compares it to calculations keeping only nearest-neighbor hoppings (dashed line) and including the full dipolar interaction (solid line).

5.5 Many-Body Ground State

5.5.1 Adiabatic Preparation

We now turn to the study of the many-body system. In Fig. 5.4(b-c), we show the full energy spectrum in the trivial and topological configurations, calculated by our collaborators using exact diagonalization, and ordered by increasing number of particles. In the trivial case, there is a single ground state

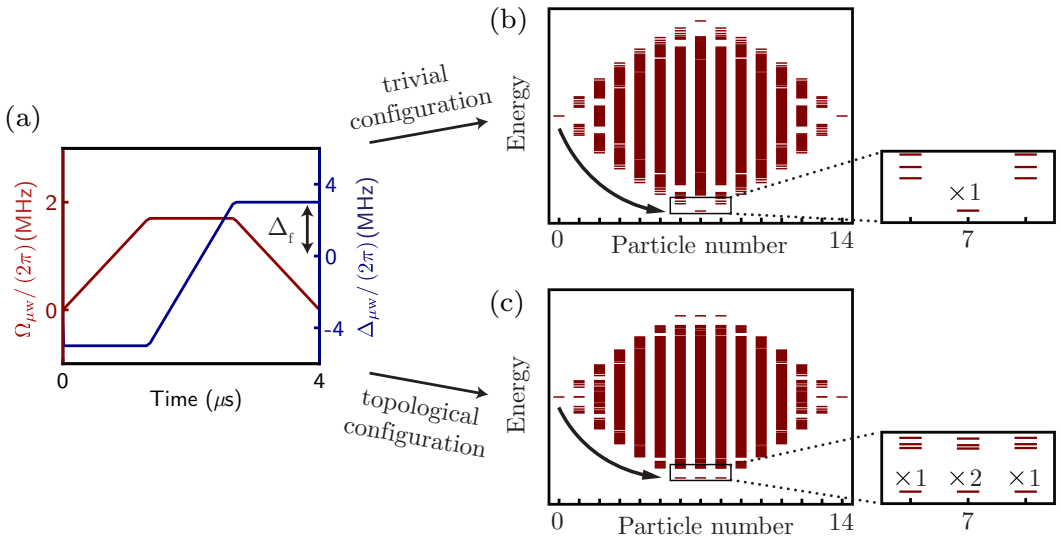

Fig. 5.4: **Preparing the many-body phase at half-filling.** (a) Microwave sweep with time-varying Rabi frequency $\Omega_{\mu w}$ and detuning $\Delta_{\mu w}$; the latter ends at Δ_f. Energy spectrum of the many-body system in the trivial (b) and the topological (c) configuration for different particle numbers as calculated by our collaborators. The trivial chain exhibits a single gapped ground state with 7 particles, while the topological configuration exhibits a four-fold degeneracy involving 6, 7 (two-fold degenerate), and 8 particles. Starting from the empty chain, the microwave adiabatic sweep loads hard-core bosons in the lattice and prepares the lowest energy states.

at half-filling. In contrast, the topological configuration exhibits four degenerate ground states corresponding to the bulk half-filled, and which are characterized by additional or missing particles mainly residing at the edges[19]. In order to prepare the ground state, we perform an adiabatic microwave sweep[20], shown in Fig. 5.4(a), where the final detuning Δ_f plays the role of a chemical potential tuning the number of particles loaded in the chain: for large negative (positive) values, the chain is completely empty (filled), while there is a finite region for a detuning around 0 where the bulk of the chain is half-filled.

[19] Experimentally, only three of the four states are actually easy to access: both edges empty, both edges occupied, and the symmetric superposition of a particle on the left and a particle on the right edge.

[20] We remark that the gap to the excited states never closes during the chosen path in the parameter space connecting the empty chain to the half-filled state (even in the limit of an infinite number of particles). The gap is allowed to stay open even in case of the transition from the trivial to the topological sector because the applied microwave field does not conserve the particle number and thus breaks a protecting symmetry.

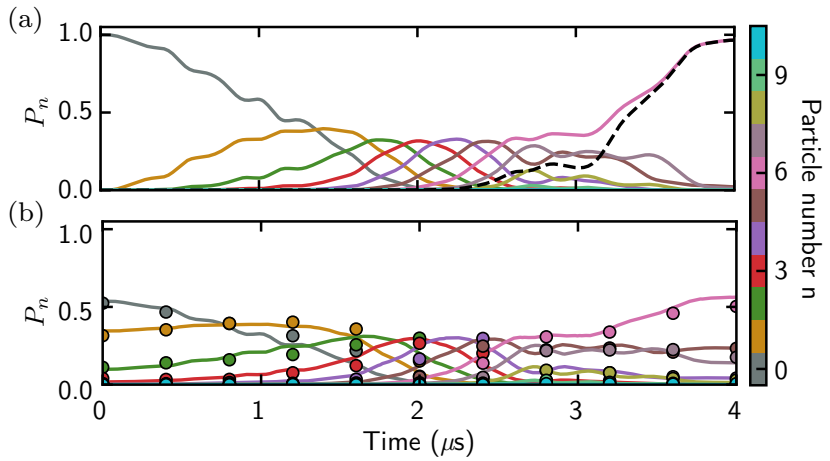

Fig. 5.5: **Evolution of particle number and ground state overlap during the adiabatic preparation.** (a) Numerically calculated evolution of the number of excitations during an adiabatic microwave sweep with $\Delta_\mathrm{f}/(2\pi) = 1\,\mathrm{MHz}$, neglecting preparation and detection errors for a chain of 10 sites. The probability P_n for finding n excitations within the system is depicted. As expected, there are mainly 6 particles at the end of the sweep. The dashed curve shows the overlap with the target state with a final value of 0.965. (b) Evolution of the number of excitations, measured experimentally (dots) and calculated (lines) including preparation and detection errors $\varepsilon = 0.06$ and $\varepsilon' = 0.07$, which were slightly higher for this dataset.

In particular, this enables the adiabatic preparation of the many-body ground state at half-filling with empty edges (using a sweep ending at $\Delta_\mathrm{f}/(2\pi) \simeq -1$ MHz) or filled edges ($\Delta_\mathrm{f}/(2\pi) \simeq 1$ MHz). In the following, we demonstrate exemplarily how to create the latter. To do so, we calculate the fidelity of the ground state preparation by simulating the time evolution of the system under the adiabatic sweep ending at $\Delta_\mathrm{f}/(2\pi) = 1$ MHz. Fig. 5.5(a) shows how the overlap with the targeted many-body ground state develops during the sweep, reaching its final value 0.96 (neglecting preparation and detection errors). In addition, the figure reveals how the number of particles in the system evolves. When including the experimental errors, the simulation is in very good agreement with experimental results, see Fig. 5.5(b). The decrease in the probabilities P_n is mainly caused by the detection errors. This makes us confident that a high fidelity of the ground state preparation is reached not only in theory but also in practice.

Now let us study systematically the dependence of the local density of particles on Δ_f, see Fig. 5.6: The bulk sites occupancy (blue curves) exhibits a

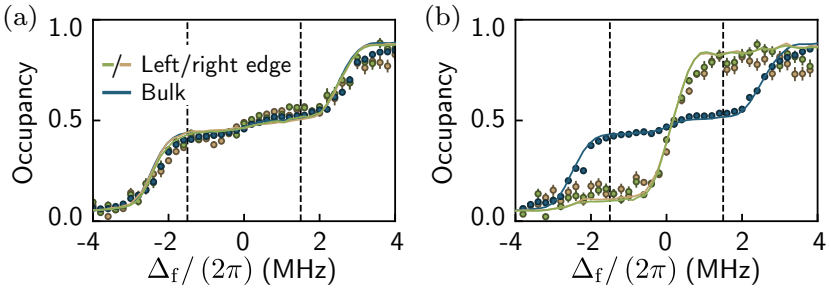

Fig. 5.6: **Occupancy as a function of the final detuning.** We simulate (lines) and our collaborators measure (dots) the occupancy of bulk and edge sites as a function of the final detuning Δ_f for the trival (a) and topological chain (b). For a sweep ending in the single-particle gap (dashed lines), the bulk of the chain is half-filled. Bosons are loaded in the edge sites of the topological configuration when $\Delta_f > 0$. The error bars represent the standard errors of the mean.

characteristic plateau at half-filling within the single-particle gap, demonstrating the existence of a bulk excitation gap. Especially, the fluctuations of the number of particles in the bulk are strongly reduced with a probability of 48 % to find exactly 6 particles on the 12 bulk sites (mainly decreased from 100 % by detection errors). Note that the small jump of the bulk density around $\Delta_f = 0$, even in the trivial configuration, is caused by preparation errors creating lattice defects: such a defect gives rise to two chains, one of which starts with a weak link, and thus supports a zero-energy edge-state which gets populated when Δ_f becomes positive.

While the local bulk properties are independent of the topology of the setup, the situation is drastically different for the edge occupancy: in the trivial configuration, the edge sites behave the same as the bulk sites, whereas for the topological chain the boundaries remain depleted for $\Delta_f < 0$ and exhibit a sharp transition to full occupancy for $\Delta_f > 0$. This behavior is consistent with the expected ground state degeneracy.

Our numerical simulations (lines) that take into account preparation and detection errors show a good agreement with the experimentally measured particle densities (dots) in Fig. 5.6.

5.5.2 Correlations and String Orders

We gain more insight about the many-body state by analyzing the correlations between particles, that our experimental collaborators can measure as their

	C^z	C^x	C^z_{string}	C^x_{string}
Theory (no errors)	-0.96	0.98	0.65	0.88
Full simulation	-0.69(1)	0.68(2)	0.11(2)	0.10(2)
Experiments	-0.67(1)	0.48(2)	0.11(2)	0.05(2)

Table 5.1: Theoretical predictions (with and without experimental imperfections) and experimental measurements of the intra-dimer correlators C^z and C^x, as well as of the string order parameters C^z_{string} and C^x_{string}.

detection scheme provides the full site-resolved particle distribution. In the strongly dimerized regime $|J| \gg |J'|$, we expect the $\sim N/2$ particles in the bulk to be highly correlated as they can minimize their energy by each delocalizing on a dimer (two sites connected by a strong link J). This picture remains valid even in our regime where $|J| \simeq 2.6|J'|$. A large and negative density-density correlation is measured $C^z(2i, 2i+1) = \langle Z_{2i} Z_{2i+1} \rangle \simeq -0.67(1)$ with $Z_i = 1 - 2b_i^\dagger b_i$, corresponding to a suppressed probability to find two particles on the same dimer. Our collaborators also access the off-diagonal correlations, $C^x(i,j) = \langle X_i X_j \rangle$ with $X_i = b_i + b_i^\dagger$ measuring the coherence between two sites i and j, by applying a strong microwave pulse before the detection which rotates the local measurement basis around the Bloch sphere, for details see our publication [4]. The obtained correlation $C^x(2i, 2i+1) \simeq 0.48(2)$ indicates that a particle is coherently and symmetrically delocalized on two sites forming a dimer. Furthermore, the experimental detection scheme allows for the determination of string order parameters, which have emerged as an indicator of topological states [303, 304]:

$$C^z_{string} = -\left\langle Z_2 \, e^{i\frac{\pi}{2}\sum_{k=3}^{N-2} Z_k} \, Z_{N-1} \right\rangle \tag{5.4}$$

and in analogy for C^x_{string}. Indeed, the measured string orders are finite in the topological phase with $C^z_{string} = 0.11(2)$ and $C^x_{string} = 0.05(2)$, while in the trivial phase they are consistent with zero, e.g., $C^z_{string} = -0.02(3)$.

Table 5.1 compares the measured correlators to numerical simulations. The agreement is excellent for measurements along the Z axis, whereas C^x and C^x_{string} are below the predicted values, suggesting that the rotation of the measurement basis suffers from experimental imperfections.

5.6 Probing the Protecting Symmetry

We finally probe the robustness of the four-fold ground state degeneracy to small perturbations, which respect the protecting symmetry $\mathcal{S}_B$. To do so, we distort the chain on one side by moving the rightmost site out of the sublattice B, see Fig. 5.7(a). As the edge site and its second neighbor are not at the magic angle anymore, this creates a coupling $J''/h \simeq 0.26$ MHz between them. This perturbation breaks the chiral symmetry protecting the fermionic SSH model, and correspondingly leads to a splitting of the single-particle edge modes. However, such a perturbation commutes with the symmetry $\mathcal{S}_B$ and therefore should not break the many-body ground state degeneracy. To check these expectations experimentally, our collaborators first repeat the spectroscopic measurement in the single-particle regime (applying the microwave probe on an empty chain, as shown in Fig. 5.2(a)), and observe a splitting of the edge modes, see Fig. 5.7(b). In contrast, the spectroscopic measurement for the bosonic many-body ground state (applying the probe after the adiabatic preparation reaching half-filling of the bulk) indeed reveals a near degenerate ground state, see Fig. 5.7(c). As shown in Appendix B, the results agree well with our numerical simulations and the tiny remaining splitting of the edge modes in the many-body regime can be attributed to van der Waals interactions.

The above experiment illustrates that, in contrast to a non-interacting SPT phase, the robustness of the bosonic many-body ground state at half-filling cannot be understood at the single-particle level. To gain an intuition for the differences between the SPT phase of non-interacting fermions and of hard-core bosons, we use the following simple picture. Considering only the three rightmost sites (the edge and a dimer), and taking the perturbative limit ($J \gg J', J''$), we first obtain the energy of having no particle on the edge site and one delocalized on the dimer: $-J - (J' + J'')^2/(2J)$ (the second term is an energy correction due to virtual hopping of the particle from the bulk to the edge). On the contrary, when there is one particle on the dimer and one on the edge, we obtain $-J - (J' \pm J'')^2/(2J)$ with an energy correction now depending on the particle quantum statistics (+ sign for bosons, − for fermions, due to commutation rules). This simplified model captures why the fermionic degeneracy is broken by the J'' term, while this is not the case for hard-core bosons.

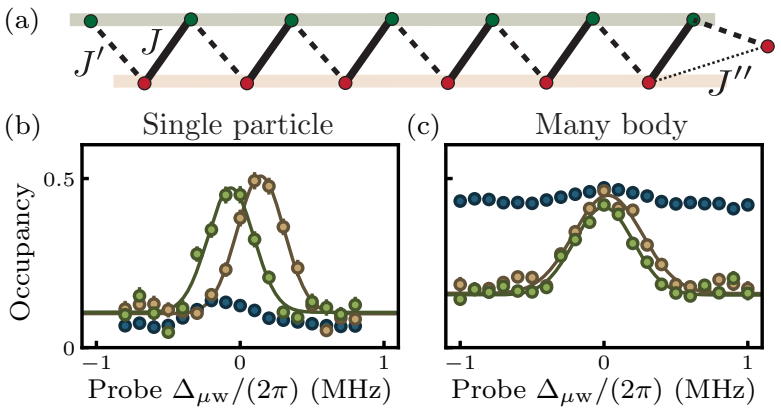

Fig. 5.7: **Perturbation and robustness of the bosonic topological phase.** (a) The rightmost site is shifted upwards to give a finite hopping amplitude J'' to the second neighbor. (b-c) Probability to find a particle in the left (green) and right (brown) edge sites when scanning the detuning $\Delta_{\mu w}$ of the microwave probe. The experiment is performed either on (b) an initially empty chain to observe the energy difference between the two single-particle edge modes caused by the perturbation J'' or (c) on the many-body ground state with a half-filled bulk (6 particles in a 14-site chain) to observe the protection of the ground state degeneracy. Solid lines are Gaussian fits from which we extract an energy difference of 0.21(1) MHz in (b) and 0.03(2) MHz in (c).

5.7 Conclusions and Outlook

In this work, we analyzed quantum many-body states in two topologically different phases, and observed four characteristic signatures of a SPT phase for interacting bosons in one-dimension: (i) a ground state degeneracy characterized by zero-energy edge states, (ii) an excitation gap in the bulk, (iii) a non-vanishing string order, and (iv) a robustness of these properties against perturbations respecting the protecting symmetry $\mathcal{S}_B$. The experimental results of our collaborators and our numerical simulations agreed excellently.

Our work demonstrates that Rydberg platforms, which combine flexible geometries and natural access to the strongly correlated regime via the hard-core constraint, are capable to explore unconventional quantum many-body states of matter.

6

Density-Dependent Peierls Phase

Effective magnetic fields can be simulated by complex hopping amplitudes of Rydberg excitations. Non-trivial[21] complex hopping amplitudes are realizable by combining the intrinsic spin-orbit coupling of dipolar exchange interaction with time-reversal symmetry breaking, for example, by applying a homogeneous external magnetic field.

In this chapter, we analyze effects of such complex hopping amplitudes in a minimal setup of three lattice sites. This analyzes is based on our joint publication [6], where the system was experimentally realized by the group of Antoine Browaeys. They observed that an excitation performs a chiral motion that is characteristic for a non-zero Peierls phase which emerges from the complex hopping amplitudes in perturbation theory. The value of the Peierls phase of the hopping between two sites depends on the geometry and the presence of an excitation on the third site.

Here, we mainly focus on our theoretical contributions. For completeness, we review the experimental setup. Details on the experiment are discussed in the references [6] and the PhD thesis of Vincent Lienhard [7]. Note that the visualizations of the setup and of the hopping processes that are shown within this chapter have been created by our experimental collaborators. To give the reader a better understanding of the physics that underlies our simulations, we present these visualizations as well.

[21] Here, non-trivial means that the complex value of the hopping amplitudes cannot be gauged away, i.e., an excitation that hops on a closed path can collect a complex phase.

6.1 Introduction

Quantum simulators are appealing to study many-body phenomena inspired by condensed matter physics [14]. One of the current challenges is to implement simulations of fractional quantum Hall-like states that use the interplay between the non-trivial topology of a band-structure, resulting from, e.g., an effective magnetic field, and the interactions between the particles [86, 305], see also Chapter 7. An effective magnetic field can be realized by implementing complex hopping amplitudes $te^{i\varphi}$ between the sites of an array, characterized by a Peierls phase φ [306–308]. A particle circulating around a closed loop then acquires a phase analog to the Aharonov-Bohm phase, which is proportional to the enclosed magnetic flux. Effective magnetic fields and complex-valued hopping amplitudes have been implemented on ultra-cold atom-based platforms [82–86], by using laser-assisted tunneling in an optical superlattice [87], high-frequency driving of a lattice [65, 88, 89], and synthetic dimensions [68, 69, 90]. Alternative platforms have also emerged such as superconducting qubits where complex-valued hopping amplitudes were demonstrated [91], and photonic [92] or phononic [93] systems operating so-far in the non-interacting regime. Here, we use the Rydberg platform to implement Peierls phases.

The Rydberg platform is a promising candidate to realize strongly interacting synthetic quantum matter [41, 128]. The assembly of above two hundred atoms in tunable geometries has already been achieved [24, 25, 44, 46, 47, 187, 309, 310]. The two different regimes of interaction, van der Waals and resonant dipole-dipole [124], have been used respectively to implement Ising-like [60–62] or XY-type spin Hamiltonians [4, 63]. In the resonant dipole-dipole regime, when the Rydberg atoms can be considered as two-level systems with states nS and nP, the interaction results in the hopping of the nP excitation between two sites, making it possible to explore transport phenomena. We recently used this fact to investigate a symmetry-protected topological phase for interacting bosons [4], see also Chapter 5. Going beyond this two-level configuration, it has been proposed to engineer situations where the effective particle features an internal degree of freedom. There, the dipole-dipole interaction couples this internal degree of freedom with the motional one, resulting in an intrinsic spin-orbit coupling [311]. In combination with breaking of the time reversal symmetry, this can lead to topological band structures characterized by non-zero Chern numbers [64, 94, 312].

In this chapter, we analyze this intrinsic spin-orbit coupling in a minimal setup of three Rydberg atoms in a triangle in a joint theoretical and experimental project. A combination of static magnetic and electric fields perpendicular to the

triangle allows us to isolate two levels in the nP manifold, thus giving rise to an excitation with two internal states. The external magnetic field naturally breaks the time-reversal symmetry, which, combined with the spin-orbit coupling, leads to a characteristic chiral motion for a single excitation. Our experimental collaborators from the group of Antoine Browaeys demonstrate this chiral motion using their Rydberg platform and show that the dynamics is reversed by inverting the direction of the magnetic field. The chiral motion is well understood in an effective description, where one internal state of the excitation is adiabatically eliminated. In this case, the effective Hamiltonian is described by a non-trivial Peierls phase φ in the hopping amplitude, corresponding to a finite magnetic flux through the triangle. Remarkably, in this approach the Peierls phase depends on the absence or presence of a second excitation, and naturally gives rise to density-dependent hoppings, which are required for the creation of dynamical gauge fields [313], as recently realized for ultracold atoms in optical lattices [314, 315]. Here, this density-dependent hopping is demonstrated by observing the absence of chiral dynamics for two excitations. Finally, our experimental collaborators demonstrate the ability to tune the effective magnetic flux through the triangle by varying the geometrical arrangement of the three atoms. All the experimental results are in good agreement with our numerical simulations, demonstrating the reliability of the Rydberg platform and that the physics which underlie the platform is well understood. We conclude by discussing the implications of the spin-orbit coupling on square and honeycomb plaquettes.

6.2 Spin-Orbit Coupling by Dipolar Exchange Interactions

Our system consists of three ^{87}Rb atoms trapped in optical tweezers placed in an equilateral configuration, see Fig. 6.1(a). For each atom, we consider three Rydberg states from the $60S_{1/2}$ and the $60P_{3/2}$ manifolds (separated in frequency by 17.2 GHz) in a V-structure, as shown in Fig. 6.1(b). The state $|0\rangle = |60S_{1/2}, m_j = 1/2\rangle$ corresponds to the absence of an excitation. The two excited states $|+\rangle = |60P_{3/2}, m_j = 3/2\rangle$ and $|-\rangle = |60P_{3/2}, m_j = -1/2\rangle$, correspond to the two internal states of the excitation. We describe these two components of the excitation on a site i by the bosonic operators $a_i^\dagger$ and $b_i^\dagger$ defined by $a_i^\dagger|0\rangle = |+\rangle_i$ and $b_i^\dagger|0\rangle = |-\rangle_i$. The energy difference $\mu = E_+ - E_-$ between $|+\rangle$ and $|-\rangle$ is controlled by a magnetic field B_z and an electric field E_z, both orthogonal to the atomic array, defining the quantization axis z. The

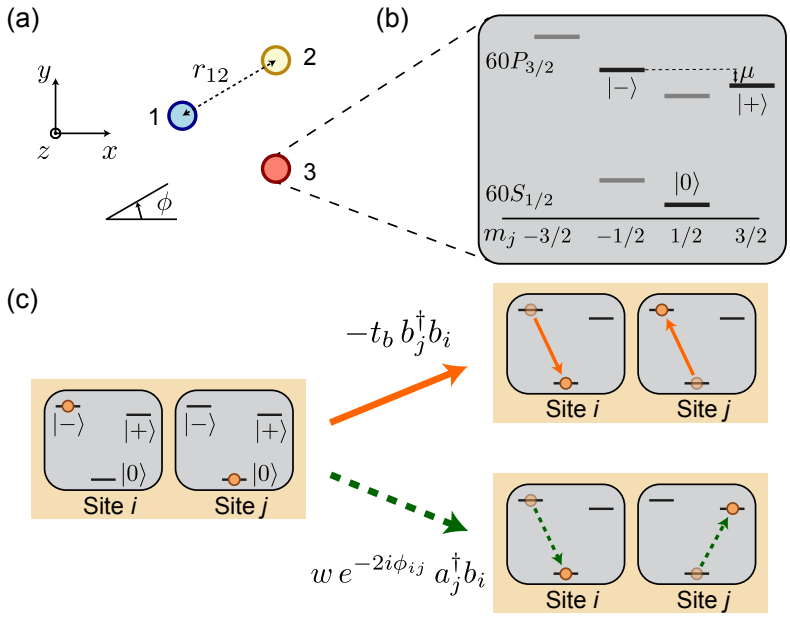

Fig. 6.1: **Spin-orbit coupling induced by dipolar exchange interaction.** (a) Configuration of three atoms trapped in a tunable geometry. The quantization axis z, along the magnetic field, is perpendicular to the array of atoms. (b) Schematic Zeeman structure of the two Rydberg manifolds $60S_{1/2}$ and $60P_{3/2}$ used in this chapter. The three levels $|0\rangle$, $|+\rangle$ and $|-\rangle$ of the V-structure involved in the dipole-dipole interaction are indicated as black lines. The energy difference between $|+\rangle$ and $|-\rangle$ is μ, controlled by DC magnetic and electric fields perpendicular to the triangle. (c) The two processes for a $|-\rangle$ excitation to hop from site i to site j are illustrated: The $|-\rangle$ excitation is annihilated on site i, and a $|-\rangle$ (solid arrow) or a $|+\rangle$ (dashed arrow) excitation is created on site j.

excitation transfer between two Rydberg atoms is governed by the dipole-dipole interaction $V_{ij} = (\boldsymbol{d}_i \cdot \boldsymbol{d}_j - 3(\boldsymbol{d}_i \cdot \hat{\boldsymbol{r}}_{ij})(\boldsymbol{d}_j \cdot \hat{\boldsymbol{r}}_{ij}))/(4\pi\epsilon_0 r_{ij}^3)$ with the distance vector $\boldsymbol{r}_{ij} = \boldsymbol{r}_j - \boldsymbol{r}_i$. In our configuration, the normalized distance vector $\hat{\boldsymbol{r}}_{ij} = (\cos\phi_{ij}, \sin\phi_{ij}, 0)$ lies in the (x, y) plane, and V_{ij} thus reads

$$V_{ij} = \frac{1}{4\pi\epsilon_0 r_{ij}^3}\left[d_i^z d_j^z + \frac{1}{2}\left(d_i^+ d_j^- + d_i^- d_j^+\right) - \frac{3}{2}\left(d_i^+ d_j^+ e^{-i2\phi_{ij}} + d_i^- d_j^- e^{i2\phi_{ij}}\right)\right]. \tag{6.1}$$

Here, d_i^x, d_i^y, d_i^z are the components of the dipole operator $\boldsymbol{d}_i$, $d_i^\pm = \mp(d_i^x \pm i d_i^y)/\sqrt{2}$, and r_{ij} and ϕ_{ij} denote the separation and the polar angle between the

two Rydberg atoms. The first three terms in Eq. (6.1) correspond to a transfer of excitation conserving the total internal angular momentum of the two atoms. The last two terms describe the spin-orbit coupling: the excitation changes its internal state by two quanta during the transfer, and the conservation of the total angular momentum requires that the corresponding hopping amplitudes acquire a phase $e^{\pm i2\phi_{ij}}$. Therefore, the dipolar interaction leads to two ways for an excitation to hop from site i to site j, as illustrated in Fig. 6.1(c) by our experimental collaborators: a resonant process, with amplitude $-t_a$ or $-t_b$, where the internal state of the excitation is conserved, and an off-resonant process (by an energy offset μ) with complex amplitude $w\mathrm{e}^{\pm 2i\phi_{ij}}$, where the excitation changes its internal state. The amplitudes $t_{a,b}$ and w scale as $1/r_{ij}^3$ and are related to the dipole matrix elements by

$$t_{a,b} = \frac{|\langle \pm| d_+ |0\rangle|^2}{8\pi\epsilon_0 r_{ij}^3},\ w = \frac{3\langle +| d_+ |0\rangle \langle 0| d_- |-\rangle}{8\pi\epsilon_0 r_{ij}^3}\ . \tag{6.2}$$

6.3 Chiral Motion of a Single Excitation

We now discuss the situation where three atoms are arranged in an equilateral triangle and derive the expression of the complex hopping amplitude of a *single* $|-\rangle$ excitation. We restrict ourselves to the case $|\mu| \gg t_{a,b}, w$ and treat the hoppings perturbatively. As the internal state-flipping hopping is off-resonant, the $|-\rangle$ excitation has only a small probability of becoming a $|+\rangle$ excitation. In addition, as the interaction conserves the number of excitations, once the atoms are initialized in the three-site state $|-00\rangle$, they mostly remain in the one excitation subspace consisting of the states $|-00\rangle$, $|0-0\rangle$ and $|00-\rangle$. The hopping of a $|-\rangle$ excitation from site 1 to 2, i.e. the change of the three-atom state from $|-00\rangle$ to $|0-0\rangle$, see Fig. 6.2(a), proceeds either by a direct hopping with amplitude $-t_b$, or by a second-order coupling via the intermediate state $|00+\rangle$ consisting in two successive flips of the internal state. The latter has an amplitude $-w^2\,\mathrm{e}^{2i(\phi_{32}-\phi_{13})}/\mu$, with $\phi_{32} - \phi_{13} = 2\pi/3$. Consequently, the hopping amplitude $-te^{i\varphi}$ from site 1 to 2 is the sum of the amplitudes of these two processes

$$te^{i\varphi} = t_b + e^{i4\pi/3}\frac{w^2}{\mu}. \tag{6.3}$$

The representation of the amplitudes in the complex plane is shown in Fig. 6.2(b). In this perturbative picture, the $|+\rangle$ excitation is adiabatically eliminated, and the problem reduces to the hopping of the $|-\rangle = b_i^\dagger|0\rangle$ excitation described by

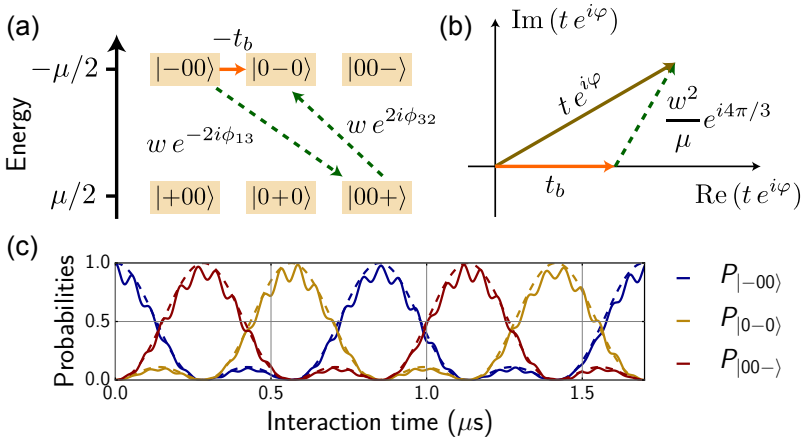

Fig. 6.2: **Peierls phase on a triangle.** (a) The two available processes for a $|-\rangle$ excitation to hop from $|-00\rangle$ to $|0-0\rangle$: direct hopping with amplitude $-t_b$, or virtual hoppings via $|00+\rangle$. (b) Complex plane representation of the effective hopping, which is the sum of the two processes depicted in (a). (c) Calculated evolution of the site probabilities after preparing $|-00\rangle$ with total flux $3\varphi = \pi/2$, using two different approaches: The dynamics represented by the dashed lines are calculated using the effective Hamiltonian (6.4). The solid lines depict the dynamics obtained by considering the three levels of the V-structure explicitly. The excitation does not spread as time flows, and moves from site to site in a chiral way.

the effective Hamiltonian

$$H_{\text{eff}} = -t \sum_{i=1}^{3} \left[e^{i\varphi} b_{i+1}^{\dagger} b_i + e^{-i\varphi} b_i^{\dagger} b_{i+1} \right] \ , \tag{6.4}$$

with $b_4 = b_1$. The Peierls phase φ can be interpreted as the result of an effective magnetic field and the magnetic flux through the triangle is thus 3φ. Experimentally, both the effective hopping amplitude t and the flux 3φ are controlled by the distance between the atoms and the energy separation μ. For non-zero flux (modulo π), the excitation exhibits a chiral motion when evolving in the triangle. In particular, for $3\varphi = \pm\pi/2$ [91], the excitation hops sequentially from site to site in a preferred direction. Fig. 6.2(c) shows this expected motion for the parameters used in the experiment (see Section 6.3.1): We plot the probability to find a $|-\rangle$ excitation at a certain site as a function of time. The dashed lines show the dynamics governed by the effective Hamiltonian (6.4). The solid lines depict the dynamics, considering all the three states of the V-structure explicitly, including the $|+\rangle$ state. The fast oscillations exhibit a

frequency close to μ/h, and result from the non-perfect elimination of the $|+\rangle$ state. Note that while these calculations show qualitatively correct results, we need to consider all the six Zeeman sublevels of the $60S_{1/2}$ and $60P_{3/2}$ manifolds to obtain accurate results, see Fig. 6.3.

6.3.1 Finding Suitable Experimental Parameters

To experimentally demonstrate the chiral motion of a $|-\rangle$ excitation resulting from the complex hopping of Eq. (6.3), our collaborators use three ^{87}Rb atoms trapped in optical tweezers arranged in an equilateral triangle [44]. The experimental parameters must be chosen carefully to isolate the chosen V-structure from other Rydberg states, see also Chapter 4. To do so, we worked together to find optimal parameters under the constraint that the condition for chiral propagation is fulfilled, i.e, $3\varphi = \pi/2$. We ended up with the following parameter set:

- A magnetic field of 8.5 G is applied to lift the degeneracy of the Zeeman sub-levels of a single atom.
- If we used the magnetic field alone, the pair state $|--\rangle$ (which will be considered in Section 6.4) would still be degenerate with $|60P_{3/2}, m_j = -3/2, 60P_{3/2}, m_j = 1/2\rangle$. To avoid leakage to this state due to interactions emerging from higher order processes, we lift the degeneracy by additionally applying an electric field. We choose $E_z = 0.4$ V/cm, for which the static dipole moment induced by the electric field is still small.
- The interatomic distances must not be selected too short to avoid intermixing of other states through Rydberg-Rydberg interactions. On the other hand, strong interactions and thus, fast dynamics are necessary to neglect the decay of the Rydberg levels and the motion of atoms. For the experiment, a side length of 11 μm for the triangle is a good trade-off.

The chosen electric and magnetic fields yield $\mu/h = -16\,\text{MHz}$.

For these experimental parameters, our collaborators measured $t_a/h \simeq 1.5\,\text{MHz}$ and $t_b/h \simeq 0.55\,\text{MHz}$, using a spin exchange experiment with two atoms [63]. These values are in good agreement with our theoretical calculations of the interaction energies using the `pairinteraction` software [1]. We then deduce $w/h \simeq 2.7\,\text{MHz}$ using the values of the angular part of the dipole matrix elements.

6.3.2 Experimental Realization

To prepare the array of atoms into the initial state $|-00\rangle$, our collaborators first initialize all three atoms to $|0\rangle$. To do so, they switch off the tweezers (because the tweezers anti-trap Rydberg states) and excite the atoms, which have been optically pumped to a well-defined ground state, to $|0\rangle$ using a STImulated Raman Adiabatic Passage (STIRAP) [4]. Then, our collaborators address the atom on site 1 with a focused laser beam and apply a microwave π-pulse of duration 400 ns resonant to the *light-shifted* $|0\rangle \rightarrow |-\rangle$ transition. The value of the light shift is typically 6 MHz. The π-pulse prepares a $|-\rangle$ excitation on the addressed atom. After the preparation of the array of atoms into the state $|-00\rangle$, the system evolves under the action of the dipole exchange interaction for a time τ. To read out the final state of the atoms, $|0\rangle$ is de-excited to the ground state and recaptured by the tweezers that are switched on again. Atoms in other Rydberg states are lost so that in a subsequent fluorescence image, $|0\rangle$ is visible as occupied sites and $|\pm\rangle$ as empty sites. Note that the experimental detection scheme cannot distinguish between the Rydberg states $|+\rangle$ and $|-\rangle$. Thus, we denote both states as a single state $|1\rangle$. Note that the Rydberg state $|+\rangle$ gets barely populated during the experiment because $|\mu| \gg t_{a,b}, w$ so that the $|1\rangle$ state consists mostly of the $|-\rangle$ state. For more details on the experimental realization, see our joint publication [6] and the PhD thesis of Vincent Lienhard [7].

The result of this first experiment is presented in Fig. 6.3(a), where the three-site probabilities to be in the states $|100\rangle$, $|010\rangle$ and $|001\rangle$ is plotted as a function of the interaction time τ. As expected, we observe a chiral motion of a localized $|-\rangle$ excitation in the *counterclockwise* direction $1 \rightarrow 3 \rightarrow 2 \rightarrow 1$. This is the signature of an effective magnetic field acting on the hopping excitation. The fact that the three probabilities do not sum to 1 comes from the imperfect preparation of the state $|100\rangle$ and detection errors.

To reverse the direction of motion, the sign of the magnetic field B_z is reversed. Then, the states of the V-structure that are accessed by the experiment are $|0\rangle = |60S_{1/2}, m_J = -1/2\rangle$, $|+\rangle = |60P_{3/2}, m_J = -3/2\rangle$, and $|-\rangle = |60P_{3/2}, m_J = +1/2\rangle$. Note that the value of μ remains unchanged because the Stark shift only depends on $|m_j|$. However, the hopping of a $|-\rangle$ to a $|+\rangle$ excitation now corresponds to a decrease of the internal momentum by two quanta: The orbital phase factor is thus $\mathrm{e}^{2i\phi_{ij}}$, and the sign of the Peierls phase is changed. Fig. 6.3(b) shows the same three-site probabilities as in Fig. 6.3(a) for this opposite direction of B_z. We now observe a chiral motion of the $|-\rangle$

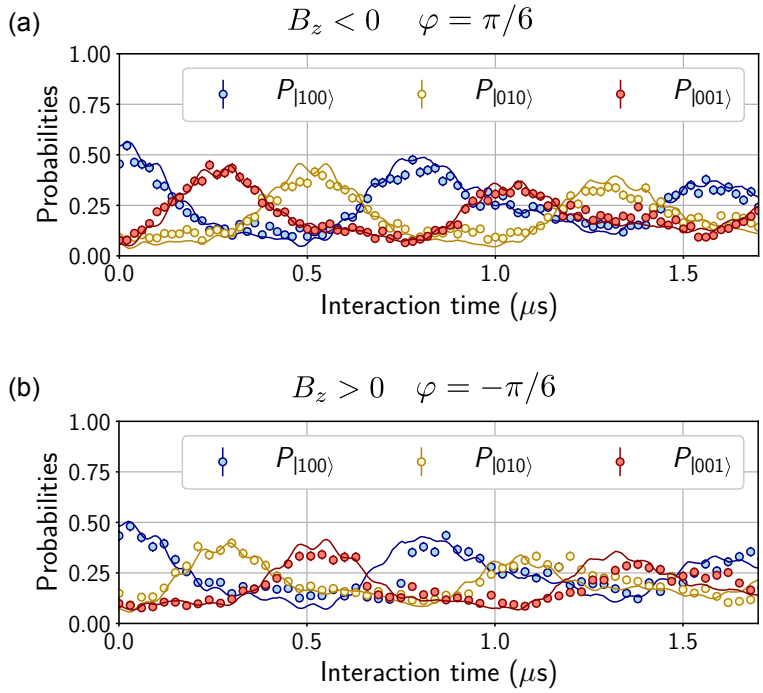

Fig. 6.3: **Observation of the chiral motion of a single $|-\rangle$ excitation.** Evolution of the three-site probabilities to be in the states $|100\rangle$, $|010\rangle$ and $|001\rangle$ as a function of the interaction time for $B_z < 0$ (a) and $B_z > 0$ (b). Experimental results (dots) and the full simulation (solid lines) are in good agreement. The simulation considers all the Zeeman sublevels, experimental errors in the preparation and the detection, and shot-to-shot fluctuations in the atomic position (see 6.3.3). The experimental errors and fluctuations lead to the observed damping of the oscillations. Error bars denote the standard error on the mean, and are often smaller than the symbol size.

excitation in the *clockwise* direction $1 \to 2 \to 3 \to 1$[22].

[22]From an intuitive point of view, we can understand that reversing the direction of B_z reversed the direction of the motion as follows: Reversing the direction of B_z and E_z is *in the case of our setup* equivalent to looking at the triangle "from behind" instead of "from the front". From this perspective, the propagation is clockwise instead of counterclockwise. Admittedly, our collaborators did not actually reverse the direction of E_z. However, as the Stark shift does not depend on the direction of E_z, this makes no difference. Note that Fig. 6.3(a) and (b) differ not only by the direction of the motion but also by some tiny varieties because of small experimental differences and imperfections that we tried to take into account in our full simulations as well, see Section 6.3.3.

6.3.3 Numerical Simulation

As seen in Fig. 6.2(c), the dynamics of the excitations in the triangle can be qualitatively reproduced by considering only the exchange interactions between the levels of the V-structure. For a rough understanding, simulating the time evolution under the effective Hamiltonian (6.4) has been sufficient. However, to obtain a quantitative agreement between numerical simulation and experiment, we must take into account additional effects that are not captured by these *idealized simulations*. In the following, we describe in detail how we achieve a *full simulation* of the experiment:

For an accurate simulation, we must keep in mind that the dipole-dipole interaction (6.1) contains not only the terms $d_i^+ d_j^-$, $d_i^- d_j^+$, $d_i^+ d_j^+$, $d_i^- d_j^-$ that keep the system inside the V-structure consisting of the three states $\{|0\rangle, |+\rangle, |-\rangle\}$. However, it also contains the term $d_i^z d_j^z$ that couples to Zeeman states outside the V-structure. The effect of the latter is inhibited thanks to the electric and magnetic fields, which energetically isolate the V-structure, but must not be neglected to obtain quantitative agreement. In principle, one could include this additional coupling and the resulting higher-order hopping processes within perturbation theory. However, it is easier for us to include all the six Zeeman sublevels of the $60S_{1/2}$ and $60P_{3/2}$ manifolds directly within the simulation. As we only consider three atoms, the enlarged local basis can still be handled numerically without any problems. Note that the numerical results show that the chiral motion gets a bit faster by including all the Zeeman sublevels.

Considering the Rydberg states outside these two manifolds results in Van der Waals interactions between the atoms, which we include in the simulation as well. However, these interactions have only a tiny influence on the dynamics for the parameters used in the experiment. The strengths of both dipolar exchange and van der Waals interactions are calculated in the presence of the applied electric and magnetic fields using our `pairinteraction` software [1].

The simulation starts with a triangle where each atom is in the $|0\rangle$ state. As a first step, we simulate the preparation of the $|-\rangle$ excitations considering the local light-shift and the globally applied microwave field. To do so, we start by prediagonalizing the single-atom Hamiltonians describing the interaction of the atoms with the applied static fields. Then, we shift the $|0\rangle$ state of atom 1 by 5 or 6 MHz to account for the light shift (for $B_z < 0$, the experiment used a shift of 6 MHz; for $B_z > 0$, 5 MHz was used). Finally, we apply the microwave π-pulse of duration 400 ns resonant to the *light-shifted* $|0\rangle \to |-\rangle$ transition. The microwave couples the Stark- and Zeeman-shifted states of the $60S_{1/2}$ manifold to the $60P_{3/2}$ manifold. During the excitation process,

we take into account the van der Waals and exchange interactions between Rydberg states. The computations are performed in the rotating frame within the rotating wave approximation. The simulation of the preparation process indicates leakage to other states outside the V-structure, on the order of 5%. Presumably, this leakage could be reduced using optimal control. As a second step, we simulate the time evolution of the prepared state under the influence of the dipolar exchange interaction.

We take into account experimental imperfections by sampling over 500 different realizations of the initial configuration of the triangles. Firstly, we take for the probability for lattice vacancies the measured value 0.17 (due to missing atoms or errors in the STIRAP process). Secondly, we consider shot-to-shot fluctuations of the positions of the atoms in their tweezers. The root-mean-square deviation of the atomic positions is $\sigma_{x,y} = 0.12$ μm within the plane of atoms and $\sigma_z = 0.6$ μm perpendicular to it, resulting in varying hopping strengths. Importantly, due to these fluctuations, the atoms can also be positioned in such a way that the interatomic axis is not exactly perpendicular to the quantization axis. In this case, the dipolar interaction can change the magnetic quantum number by one, provoking additional leakage to states outside the V-structure. These experimental imperfections are responsible for the observed damping of the dynamics.

As a last step, detection errors are included through Monte Carlo sampling of the numerical results [4, 316]. In the simulation we account for the fact that the detection scheme does not distinguish between states other than $|0\rangle$ by computing the probabilities $P_{|100\rangle}$, $P_{|010\rangle}$ and $P_{|001\rangle}$ as measured in the experiment. Note that the preparation of a state with two excitations is experimentally challenging and prone to additional errors. Therefore, we have scaled vertically the theory curve shown in Fig. 6.4(b) by a factor 0.8.

Fig. 6.3(a-b) shows the results obtained by this full simulation together with the experimental data for the chiral motion in both directions. We get a good agreement – the frequency, the amplitude, and the damping of the chiral motion is reproduced.

6.4 Density Dependence of the Peierls Phase

For ensembles of two-level atoms in resonant interaction, the excitations can be mapped onto hard-core bosons, a fact used in our previous work [4]. A natural question to ask in our present multi-level situation is the consequence of the hard-core constraint on the dynamics of the $|-\rangle$ excitations.

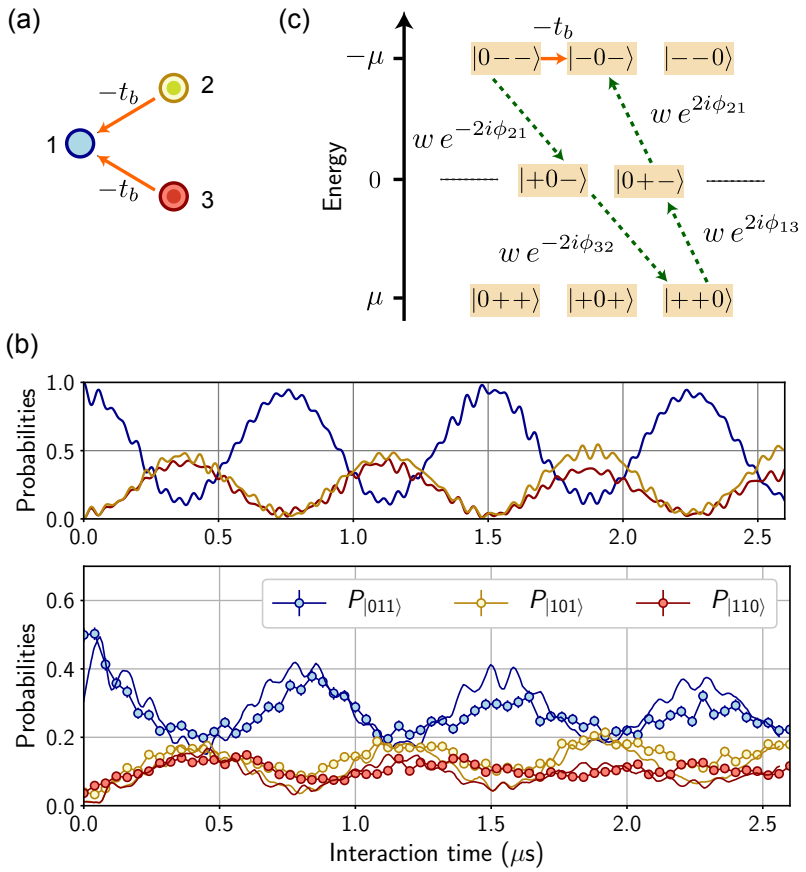

Fig. 6.4: **Demonstration of density-dependent hopping for two excitations.** (a) The presence of a $|-\rangle$ excitation on site 3 prevents the internal state-flipping process responsible for the complex hopping of the $|-\rangle$ excitation from 2 to 1. Thus, only the real coupling remains. (b) Probability to be in the doubly excited three-site states $|011\rangle$ (targeted initial state), $|101\rangle$ or $|110\rangle$ as a function of the interaction time τ. Upper panel: simulations in an idealized case including only the three levels of the V-structure. Lower panel: experimental results together with the results of the full simulation. (c) Hopping processes to go from site 1 to site 2 in the two-excitation case, showing the direct coupling and the fourth-order process via $|0++\rangle$. The latter leads to a slight asymmetry in the dynamics.

6.4.1 Experimental Results

In order to explore this experimentally, we now initialize the three-atom system with *two* $|-\rangle$ excitations on sites 2 and 3, while site 1 is in state $|0\rangle$, thus preparing the three atom state $|0--\rangle$. To do so, our experimental collaborators

use again the addressing laser on site 1 (this time, inducing a light shift of 40 MHz), but tune the π microwave pulse on resonance with the *free space* $|0\rangle \rightarrow |-\rangle$ transition. All other parameters are left the same as for the single excitation experiments.

In the case of hard-core bosons evolving with the Hamiltonian (6.4), one would expect the hole (state $|0\rangle$) to propagate in the opposite direction to the single $|-\rangle$ excitation case, as observed using superconducting circuits [91]. However, in our system, this is not the case! Remarkably, we do not observe any chiral motion, see Fig. 6.4: The hole state $|0\rangle$ propagates almost symmetrically towards sites 2 and 3, suggesting that the hopping amplitude between sites is now real, and that the description of the dynamics by the Hamiltonian (6.4) is no longer valid.

6.4.2 Theoretical Description

To understand this, we come back to the hard-core constraint in our system. Two particles, irrespective of their internal state $|+\rangle$ or $|-\rangle$, can not reside on the same site. As a consequence, the effective hopping from site 1 to 2 is modified if an excitation is already present on site 3. This suppresses the off-resonant process, which is at the origin of the complex hopping amplitude in the single excitation case, leaving only the direct hopping described by $-t_b$. Therefore, the hard-core constraint generates a density-dependent hopping, where the phase of the hopping amplitude, as well as its strength, depends on the occupation of the third lattice site. The effective Hamiltonian describing this situation generalizes the one of Eq. (6.4) to the case of more than one $|-\rangle$ excitation:

$$H_{\text{eff}}^{\text{many}} = -t \sum_{i=1}^{3} \left[e^{i\varphi(1-n_{i+2})} b_{i+1}^{\dagger} b_i + \Delta b_{i+1}^{\dagger} b_i n_{i+2} + \text{h.c.} \right] , \tag{6.5}$$

with the occupation of the third site $n_{i+2} = b_{i+2}^{\dagger} b_{i+2}$ and $\Delta = (t_b - t)/t$. The first term in the effective Hamiltonian shows that the Peierls phase is now density-dependent. The second term describes a conventional correlated hopping, which does not modify the real or complex nature of the couplings between sites. In addition, the adiabatic elimination leads to two-body interaction terms $\propto (w^2/\mu) n_i n_j$, that do not play a role in an equilateral triangle and that we therefore drop.

We still observe a residual asymmetry in the dynamics, see Fig. 6.4(b). This indicates that the complex-valued hopping is not fully suppressed. Following

the same effective Hamiltonian approach as the one outlined in Section 6.2, the internal state-flipping hopping is now a fourth-order process, as shown in Fig. 6.4(c). Considering the hopping from site 1 to site 2, the hole can directly hop with an amplitude $-t_b$, or virtually go through $|{+}{+}0\rangle$, leading to a total amplitude $te^{i\varphi} = t_b + w^4/\mu^3 e^{-4i\pi/3}$. As $w \ll |\mu|$, the complex part of this hopping is extremely small compared to the single particle case, thus leading to the observed quasi-symmetric dynamics.

To ensure that our understanding of the experimental results is correct, we compare them with numerical simulations. The upper panel of Fig. 6.4(b) shows an idealized simulation that takes into account only the three levels of the V-structure. The features of the experimentally observed dynamics are qualitatively reproduced by this simulation. The lower panel of Fig. 6.4(b) depicts the experimental data and the results of a full simulation modeling the experiment as described in Section 6.3.3, achieving good agreement.

6.5 Tunability of the Peierls Phase

Finally, we go back to the single excitation sector and demonstrate the control of the Peierls phase by tuning the geometry of the triangle while keeping the same value for μ. To do so, we study an isosceles triangle parametrized by the angle γ, see Fig. 6.5(a). In this configuration, the distance between sites 1 and 3 varies with γ. The effective coupling, and hence the Peierls phase, is then different for each link: the direct hoppings are $t_{12} = t_{23}$ and $t_{13} = \kappa t_{12}$ with $\kappa = 1/(2\cos[\gamma/2])^3$; the virtual coupling are $\kappa w^2 e^{i\gamma}/\mu$ for the $1 \to 2$ and $2 \to 3$ couplings and $w^2 e^{-2i\gamma}/\mu$ for the $3 \to 1$ coupling. The variation of the magnetic flux through the triangle, which is the sum of the three Peierls phases, is represented in Fig. 6.5(b) as a function of the angle γ. It exhibits an almost linear dependence for $\gamma \in [0°, 90°]$.

Our demonstration of the control over the Peierls phase is achieved by observing how a single $|{-}\rangle$ excitation prepared initially on site 2 splits between site 1 and site 3 after a given evolution time: For a negative flux (modulo 2π) the excitation propagates towards site 1, while it propagates towards site 3 for a positive flux. For zero flux (modulo π) the propagation is symmetric, see Fig. 6.5(c). We plot the population imbalance between site 1 and site 3, $\mathcal{I} = (P_{|100\rangle} - P_{|001\rangle})/(P_{|001\rangle} + P_{|100\rangle})$, at time $\tau = 0.4\,\mu$s, as a function of the angle γ. We chose $\tau = 0.4\,\mu$s as it corresponds to the excitation mainly located on sites 1 and 3 for $\gamma = 0°$. As expected, we observe that the imbalance varies with the angle γ, and hence with the magnetic flux, see Fig. 6.5(b). For $\gamma = 0°$

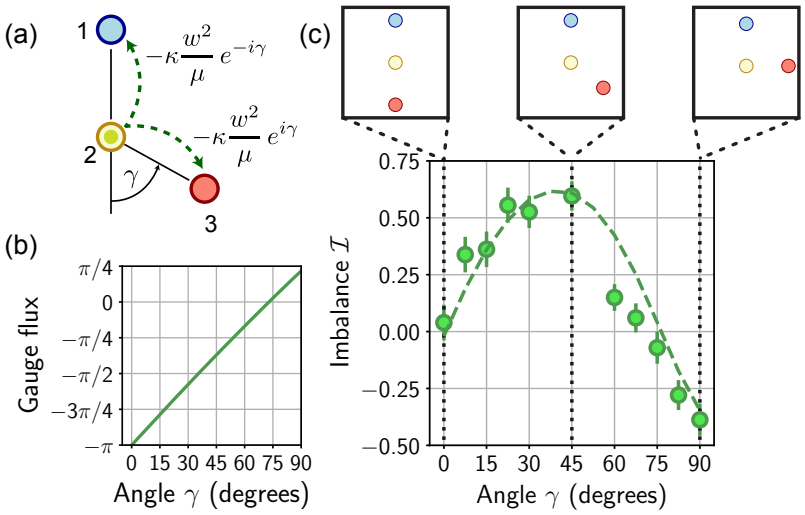

Fig. 6.5: **Tunability of the Peierls phase**. (a) Tunable geometry based on an isosceles triangle with $r_{12} = r_{23} = 11\,\mu$m. (b) Calculated angle dependence of the magnetic flux threading through the isosceles triangle. (c) Imbalance $\mathcal{I}$ between site 1 and site 3 after having prepared an excitation on site 2 and letting the system evolve for $\tau = 0.4\,\mu$s, as a function of the angle γ. A positive imbalance means that the excitation mainly resides on site 1. The three insets represent the triangle configurations for three values of γ, marked on the graph by the three dotted lines. The experimental results (points) and our full simulation (dashed line) agree reasonably.

and 75° the flux is zero and thus the propagation symmetric. The results of our experimental collaborators are in reasonable agreement with our full simulation of the dynamics as shown in Fig. 6.5(c).

6.6 Extension to Other Geometries

As demonstrated in the previous section for the case of an isosceles triangle, the Peierls phase depends on the geometrical arrangement of the atoms. A natural question to ask is what happens for geometries other than a triangle. In the following, we discuss theoretically the Peierls phase patterns for plaquettes of square and honeycomb lattices, considering the perturbative regime where the $|+\rangle$ excitation can be eliminated.

For a square geometry, see Fig. 6.6(a), we find a nearest neighbor hopping $te^{i\varphi}$ with a Peierls phase φ, as the adiabatic elimination gives rise to two distinct virtual processes of equal strength. On the contrary, the next-nearest-neighbor

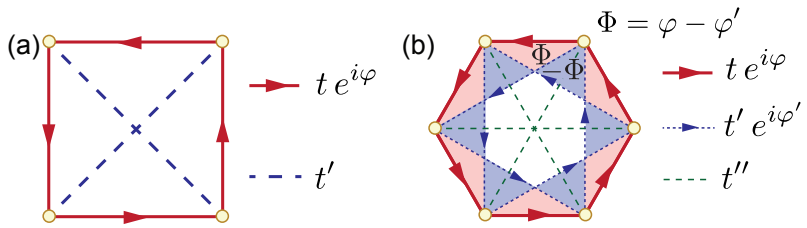

Fig. 6.6: **Flux pattern resulting from the complex hopping for plaquettes of various geometries.** (a) Square geometry. The effective Hamiltonian approach yields $te^{i\varphi} = t_b + iw^2/(\mu\sqrt{2})$ and $t' = t_b/2^{3/2} - 2w^2/\mu$ as calculated by Rukmani Bai. In this case, the flux 4φ through the square corresponds to a homogeneous magnetic field. (b) Honeycomb geometry. Here $te^{i\varphi} = t_b + 3w^2/(4\sqrt{3}\mu)e^{i\pi/3}$, $t'e^{i\varphi'} = t_b/3^{3/2} + 139w^2/(108\mu)e^{2i\pi/3}$ and $t'' = t_b/8 - 4w^2/(3\sqrt{3}\mu)$. The flux pattern is well described as an homogeneous magnetic field with flux 6φ through the honeycomb in combination with an alternating flux $\Phi = \varphi - \varphi'$ through the red and blue triangles.

hopping remains real valued. Consequently, a single excitation experiences a homogeneous effective magnetic field with a flux 4φ through the square. As for the triangle case, the presence of a second excitation gives rise to a density-dependent hopping and quenches the virtual processes. Therefore, the dynamics of two excitations is accounted for by a modified homogeneous magnetic field. Finally, for three excitations, all virtual processes are forbidden, and we recover a time reversal symmetric dynamics.

For atoms on a honeycomb array, the situation can no longer be described by a homogeneous magnetic field. As shown in Fig. 6.6(b), the Peierls phase φ resulting from the nearest-neighbor hopping gives rise to a homogeneous magnetic field with total flux 6φ. In addition considering the next-nearest-neighbor coupling introduces a second Peierls phase φ'. The combination of the two phases leads to an alternating flux pattern. Such a pattern has been previously discussed in the context of the Haldane model on a honeycomb lattice [317] and provides an intuitive explanation for the appearance of non-trivial Chern numbers with $C = \pm 1$ reported in [64, 94]. For a lattice geometry consisting of many plaquettes, the Peierls phase φ for the nearest-neighbor hopping would now vanish by symmetry, whereas the second Peierls phase φ' of next-nearest hopping remains finite. We would thus be able to observe chiral edge states in the single-particle regime. In [64], we obtained these chiral edge states by analyzing the band structure of the system and computing the associated Chern numbers for the V-structure levels scheme. The perturbative

approach presented here provides more intuition on the link between the honeycomb configuration and the Haldane model.

6.7 Conclusions and Outlook

We analyzed the spin-orbit coupling present in dipolar exchange interactions. Together with our experimental collaborators, we found a parameter set that allowed them to observe a chiral motion of an excitation in a minimal triangular setup of three Rydberg atoms. This motion is characteristic for the presence of a homogeneous magnetic field through the triangle. It can be understood best in the perturbative regime, where the spin-orbit coupling gives rise to Peierls phases. Remarkably, the Peierls phase depends on the occupation of neighboring sites and therefore naturally gives rise to a dynamical gauge field. By varying the spatial arrangement, we engineered geometry-dependent Peierls phases and explored theoretically configurations beyond the triangle. In particular, for the honeycomb plaquette, we showed that at the single-particle level and in the perturbative approach, our system shows the same couplings as those of the celebrated Haldane model, which is characterized by a non-trivial topological band structure.

Together with the strong interaction between particles that is given naturally in Rydberg systems through the hard-core constraint, this finding makes the Rydberg platform an interesting candidate for the realization of fractional Chern insulators – especially as theoretical studies have already demonstrated that fractional quantum Hall states can emerge in Haldane-like model with hard-core bosons [318, 319].

As we will see in Chapter 7, we can indeed find a highly promising experimental parameter set for the realization of a fractional Chern insulator. Notably, for the theoretical studies conducted in that chapter, it is crucial to explicitly consider *all states of the V-structure* to achieve sufficiently flat bands. That the perturbative approach is not sufficient to obtain meaningful results is in strong contrast to the current chapter, where the adiabatic elimination of the $|+\rangle$ state was convenient.

7

Fractional Chern Insulator

A current challenge is the investigation of the interplay between the non-trivial topology of a band structure and interactions between particles. A topologically non-trivial band structure [64] can result from an effective magnetic field that can be realized in a Rydberg setup as described in Chapter 6. Interaction between particles emerges from the hard-core constraint of Rydberg excitations.

In this chapter, we show that on a honeycomb lattice, this setting can give rise to a many-body ground state that can be understood as a fractional Chern insulator. Our theoretical study is conducted for realistic experimental parameters. Using exact diagonalization, we demonstrate that the ground state features a robust nearly two-fold degeneracy on a torus, an exponential decay of local correlations, and that is has a many-body Chern number of one. We discuss how the fractional character of excitations can be detected in a possible experiment.

7.1 Introduction

Many-body ground states that feature intrinsic topological order are of broad interest in physical and quantum information science. These states are of practical relevance for fault-tolerant quantum computing [155, 156] and robust quantum memory [153, 154]. Moreover, these states are actively explored as a subject of basic research. For example, their classification [158] and the origin of the $\nu = 5/2$ state in the fractional quantum Hall effect [159, 161] are intriguing topics. To address the open questions and pave the way for applications of topological order in quantum information, simulations are necessary to deepen our understanding. However, the long-range entanglement makes classical simulations of large systems challenging [162]. Thus, the study of topological order is a worthwhile target for quantum simulation.

Over the last few years, programmable arrays of Rydberg atoms have emerged as a highly promising platform for quantum simulation [42, 43]. Individual atoms are trapped in optical tweezers that are arranged to form arbitrary arrays of several hundred sites with almost unit-filling [24, 25]. To make the atoms interact, they are excited to Rydberg states [48, 50]. The resulting van der Waals or dipolar exchange interactions enable the realization of different spin models where the spin states are encoded in the electronic states of the atoms. Recent examples include Ising-like models [24, 25, 60–62], XY-type models [4, 63], and a symmetry-protected topological phase [4]. Most recently, topological spin liquids has been probed with the Rydberg platform, observing features of topological order with a quantum simulator for the first time [23, 81]. However, the quantum simulation of fractional quantum Hall-like states remains an open challenge. Their implementation requires two main ingredients: strong interactions between particles and the realization of an effective magnetic field. The latter is a key challenge. While many approaches exist for different platforms [65, 68, 69, 82–90], the realization of effective magnetic fields typically requires some form of Floquet engineering that can give rise to heating and hence hampers the preparation of a ground state. Not long ago, it became apparent that Rydberg atoms allow for the realization of effective magnetic fields without requiring a time-dependent Hamiltonian, thus avoiding the heating [64, 312]. The strong interactions between particles are given naturally in Rydberg systems as infinite on-site interactions [6].

Here, we present a detailed proposal for the realization of a bosonic fractional Chern insulator with Rydberg atoms that features a 1/2-Laughlin-like state [320, 321]. We consider a system similar to the models whose single-particle sector has been studied in [64]. There, and in the experimental publication [6], it has been demonstrated that the spin-orbit coupling of the dipolar exchange interaction between Rydberg atoms can give rise to effective magnetic fields and potentially to topological band structures. We extend this analysis and study such a system in the many-body regime where the fact that each Rydberg atom can host only one excitation leads to an infinite on-site interaction. As topological phases are typically fragile, we take care to model the Rydberg system accurately to ensure that our results are realistic and applicable to recent Rydberg quantum simulation platforms.

This project consists of three parts: In Section 7.2, we describe the microscopic Hamiltonian. In Section 7.3, we provide extensive numerical evidence that the ground state of the system features topological order at 1/4-filling, using exact diagonalization. In Section 7.4, we show how a Rydberg quantum simulator could detect fractional charges [322] as a smoking gun of topological order,

using the density matrix renormalization group (DMRG) method [323].

7.2 Setup

Our system consists of ^{87}Rb atoms arranged in a two-dimensional honeycomb lattice. For each atom, we consider the Rydberg states $|0\rangle = |nS_{1/2}, m_j = 1/2\rangle$, $|+\rangle = |nP_{3/2}, m_j = 3/2\rangle$, and $|-\rangle = |nP_{3/2}, m_j = -1/2\rangle$. These states form a V-level structure. We apply a homogeneous electric field E_z and magnetic field B_z perpendicular to the plane of atoms, along the quantization axis z, and use the resulting Stark and Zeeman shifts to energetically isolate these states from other Rydberg states [64], see Fig. 7.1(a-b). The fields also allow for tuning the energy difference $\Delta = E_{|+\rangle} - E_{|-\rangle}$ between $|+\rangle$ and $|-\rangle$. We interpret $|0\rangle$ as the vacuum state and an excitation into one of the two other states as a bosonic particle, where $|+\rangle$ and $|-\rangle$ correspond to the possible internal states of the particle. We introduce the bosonic operators $a_i^\dagger$ and $b_i^\dagger$ that create a particle at lattice site i in the internal state $a_i^\dagger |0\rangle = |+\rangle_i$ and $b_i^\dagger |0\rangle = |-\rangle_i$, respectively. Because each atom has one Rydberg electron only, the operators fulfill the hard-core constraint, meaning that each lattice site can be either empty or occupied by one particle.

The dipolar exchange interaction between the Rydberg states give rise to the hopping Hamiltonian [64, 94]

$$H_0 = \sum_{i \neq j} \begin{pmatrix} a_i \\ b_i \end{pmatrix}^\dagger \begin{pmatrix} -t_{ij}^a & \omega_{ij}\, \mathrm{e}^{-2i\phi_{ij}} \\ \omega_{ij}\, \mathrm{e}^{2i\phi_{ij}} & -t_{ij}^b \end{pmatrix} \begin{pmatrix} a_j \\ b_j \end{pmatrix} + \Delta \sum_i n_i^a \,, \tag{7.1}$$

with $n_i^a = a_i^\dagger a_i$. Here, t_{ij}^a and t_{ij}^b are the amplitude of the hopping of a $|+\rangle$-particle and a $|-\rangle$-particle, respectively, between sites i and j. The internal state of the particle is conserved by these hoppings. In contrast, the hopping that is associated with the amplitude ω_{ij} changes a $|+\rangle$-particle into a $|-\rangle$-particle and vice versa. This change of the internal state of the particle goes together with the collection of a phase $\pm 2\phi_{ij}$ (spin-orbit coupling), where the angle ϕ_{ij} is the polar angle of the distance vector $\mathbf{r}_{ij} = \mathbf{r}_j - \mathbf{r}_i$ between sites i and j [6]. While this angle depends on the chosen coordinate system, the physically meaningful phase, which is collected on a closed hopping path, is independent on the choice.

Van der Waals interaction and other higher order interaction processes can give rise to density-density interaction. Another contribution comes from the applied electric field that induces static dipole moments to the Rydberg states.

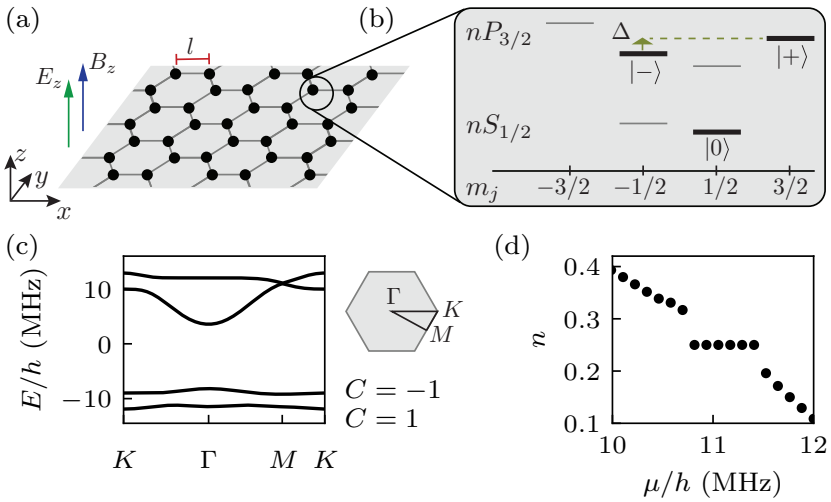

Fig. 7.1: **Setup for the realization of a fractional Chern insulator.** (a) Rydberg atoms are arranged in a honeycomb lattice with lattice spacing l. A homogeneous electric field E_z and magnetic field B_z are applied perpendicular to the plane of atoms, along the quantization axis z. (b) The fields isolate the Rydberg levels of the V-structure $|0\rangle$, $|+\rangle$, and $|-\rangle$ (black lines) that are involved in dipolar exchange interaction. The state $|0\rangle$ is treated as the vacuum state and the excitations $|\pm\rangle$ as particles. The energy difference $\Delta = E_{|+\rangle} - E_{|-\rangle}$ between $|+\rangle$ and $|-\rangle$ is controlled by the fields. (c) Single-particle band structure along the depicted path through the Brillouin zone for the experimental parameters that are given in the text. h is Planck's constant. The lowest band has the single-particle Chern number $C = 1$. (d) Average particle density n of the many-body ground state as a function of the chemical potential μ. The density shows a plateau at 1/4-filling, indicating an incompressible phase. The density has been calculated by Johannes Mögerle.

The density-density interactions can be written as

$$H_{\text{int}} = \frac{1}{2} \sum_{\substack{i \neq j \\ \alpha,\beta \in \{0,a,b\}}} U_{ij}^{\alpha\beta} \, n_i^\alpha n_j^\beta \, , \tag{7.2}$$

with $n_i^a = a_i^\dagger a_i$, $n_i^b = b_i^\dagger b_i$, and $n_i^0 = 1 - n_i^a - n_i^b$. $U_{ij}^{\alpha\beta}$ is the strength of the density-density interaction between sites i and j. While in principle, additional two-body terms are possible, these terms are two orders of magnitude smaller than the relevant energy scales, at least for the experimental parameters that

we will propose in the following. Thus, the full microscopic Hamiltonian reads

$$H = H_0 + H_{\text{int}} \tag{7.3}$$

in good approximation.

For the realization of a fractional Chern insulator, we find a suitable set of realistic experimental parameters, see Appendix C.1. We propose to use the principal quantum number $n = 60$, the lattice spacing $l = 12$ μm, the electric field $E_z = 0.725$ V/cm, and the magnetic field $B_z = -8$ G. For these parameters, we apply the software `pairinteraction` [1] to calculate the Stark and Zeeman shifted Rydberg states. Within the basis of these states, we calculate the hopping amplitudes and interactions perturbatively [276]. We take into account that the Rydberg states got slightly admixed by the applied electromagnetic fields. For the chosen experimental parameters, the energy difference is $\Delta/h = 18.52$ MHz with Planck's constant h and the nearest-neighbor hoppings are $t^a/h = 1.26$ MHz, $t^b/h = 0.49$ MHz, and $\omega/h = 2.38$ MHz. For large distances, the hopping amplitudes decrease as $1/|\mathbf{r}_{ij}|^3$ in good approximation. The precise values are given in Appendix C.2. There, the values of the density-density interactions are also stated. In general, $|U_{ij}^{\alpha\beta}| \leq 0.3$ MHz and we checked that the results do not change qualitatively if we switch off the density-density interactions. However, to be as close as possible to a potential experiment, we keep the terms for our calculations. Throughout the chapter, we take into account hoppings and interactions up to next-next-nearest neighbor because longer ranging processes will cause issues due to self-interaction in some systems with periodic boundary conditions that we will study later on.

For now, let us focus on the single-particle band structure. Due to the two-site unit cell and the two possible internal states of a particle, it has four bands. The external magnetic field breaks the time-reversal symmetry, enabling topologically non-trivial bands. Indeed, the lowest band has a non-zero single particle Chern number [324] $C = 1$, see Fig. 7.1(c). The fluctuations of the Berry curvature over the Brillouin zone [325] that are quantified by their root-mean-square value $\sigma_B = 0.4$ are small. It has been found that similar honeycomb systems can feature rather flat bands [94]. This is also the case for the experimental parameters proposed by us, the lowest band has a flatness ratio $f = 2.7$. In combination with the strong on-site interaction due to the hard-core constraint, these properties of the single-particle band structure makes our system a promising candidate for the realization of a fractional Chern insulator in the many-body regime.

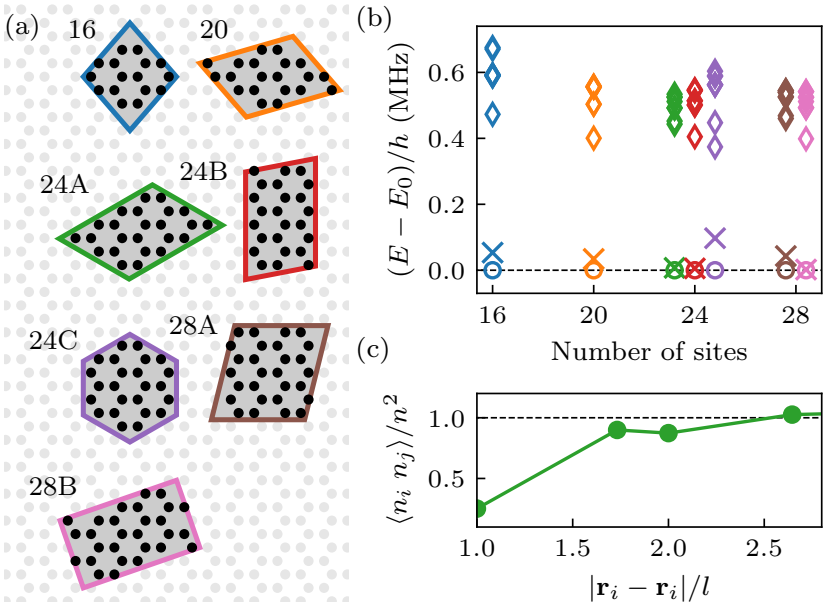

Fig. 7.2: **Ground state on a torus.** (a) For 1/4-filling, the 10 lowest eigenstates are calculated via exact diagonalization for different clusters of the honeycomb lattice with periodic boundary conditions. (b) For all clusters, the ground state is nearly two-fold degenerate and separated from the first excited state by a gap $\Delta E/h \gtrsim 0.2$ MHz. E_0 is the respective energy of the lowest eigenstate. (c) For the ground state, density-density correlations show no order as the function $\langle n_i n_j \rangle / n^2$ is short-ranged, with density operator $n_i = n_i^a + n_i^b$ and average density n. The function is depicted exemplarily for the clusters *24A* that we also consider for the remaining subplots.

Calculations by Johannes Mögerle within infinite-DMRG indicate an incompressible phase at 1/4-filling, see Fig. 7.1(d). Note that the 1/4-filling of the system corresponds to 1/2-filling of the lowest band of the single-particle band structure. This result is compatible with the presence of topological order at 1/4-filling.

7.3 Topological Order

In the following, we study the many-body ground state at 1/4-filling within exact diagonalization and demonstrate that it indeed shows the characteristics of a bosonic fractional Chern insulator.

For this analysis, we consider various clusters [326] of the honeycomb lattice with periodic boundary conditions, see Fig. 7.2(a). The chosen clusters are dif-

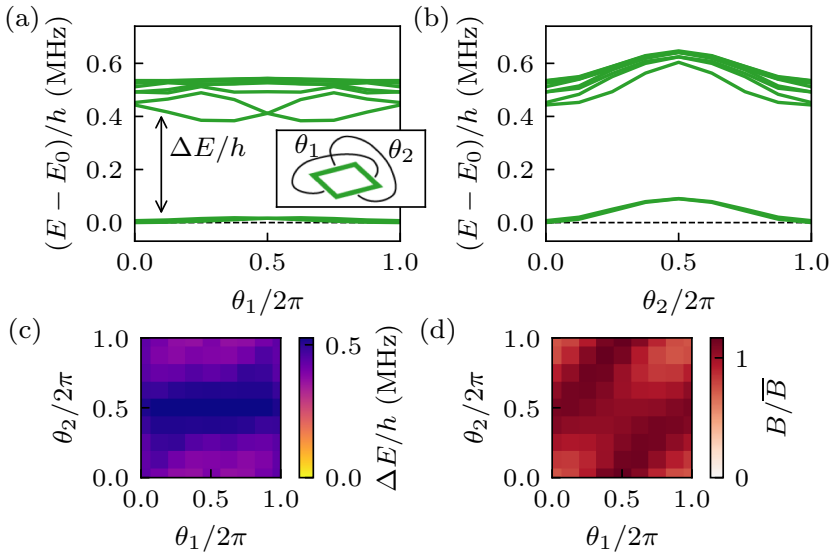

Fig. 7.3: **Twisted boundary conditions.** (a-b) We apply twisted boundary conditions with twist angles θ_1 and θ_2 as illustrated in the inset. We plot the lowest eigenenergies as a function of one twist angle while keeping the other zero. The ground state remains nearly degenerate. (c) The gap to the first excited state stays wide open, independently on the twist angles. (d) The normalized Berry curvature $B/\overline{B}$ of the nearly degenerate ground state is mostly homogeneous as a function of the twist angles. Here, $\overline{B}$ is the average of the Berry curvature B over all angles. The many-body Chern number is $C = 1$.

ferent tessellations of the honeycomb lattice. The periodic boundary conditions make the clusters having the topology of a torus. This statement includes the cluster *24C*, i.e., a regular hexagon with periodic boundary conditions, because it has the geometry of a fattened Möbius band which is homeomorphic to a torus. The clusters consist of 16 to 28 sites.

Thus, for our model, where the particle have two internal states, the resulting many-body bases comprise up to $\sim$ 150 million states at 1/4-filling. Using exact diagonalization, we calculate the 10 lowest eigenstates and find that the ground state of our system fulfills three characteristic features of a bosonic fractional Chern insulator:

First, the ground state is nearly two-fold degenerate [152] and separated from the first excited state by a gap $\Delta E/h \gtrsim 0.2$ MHz for all the studied clusters, see Fig. 7.2(b). These properties are robust by applying twisted boundary conditions on the torus with twist angels θ_1 and θ_2, see Fig. 7.3(a-c). In addition, the ground state degeneracy is lifted for a setup with open boundary

conditions.

Second, all local correlation functions within the ground state decay exponentially in the bulk. As an example, the short ranged behavior of the density-density correlation is shown in Fig. 7.2(c). Therefore, we find absence of any spontaneous symmetry breaking.

Third, we determine the many-body Chern number for the nearly degenerate two-fold ground state manifold. The approach is based on applying twisted boundary conditions and determining the corresponding Berry curvature [327]. The Berry curvature is mostly homogeneous, see Fig. 7.3(d), and we find the many-body Chern number $C = 1$.

These three observations are a clear indication of a ground state exhibiting topological order with long-range entanglement. Furthermore, all these observations are compatible with a 1/2-Laughlin-like state [162], which is the simplest topological phase for bosons in a half-filled topological band and has been predicted in closely related systems [318]. This interpretation is supported by the calculation of the topological entanglement entropy of $\gamma = (0.45 \pm 0.1) \ln 2$ that has been performed by Johannes Mögerle for our upcoming publication, which is currently in preparation.

7.4 Experimental Detection

Our upcoming publication will also demonstrate how a Rydberg quantum simulator could prepare the ground state of the system adiabatically, which has been analyzed by Nastasia Makki. In the following, we study how a quantum simulator could find evidence for the presence of topological order within the prepared ground state.

While quantities like ground state degeneracy, many-body Chern number, and entanglement entropy can be calculated numerically, they are hardly accessible in real world experiments. However, recently, an experimentally feasible scheme for the detection of fractionally charged excitations has been proposed [322]. We adapt the proposal to our Rydberg setup. For fractional Chern insulators, one expects the accumulation of fractionally charged excitations near engineered local defects. The charge, i.e., the particle number, is easy to access experimentally. It is expected to be 1/2 in our case of the 1/2-Laughlin-like ground state.

To engineer a local defect, we propose to locally apply a light shift to the $|-\rangle$ state. The light shift gives rise to a local chemical potential μ.

We simulate this scheme using the full microscopic Hamiltonian (7.3). While

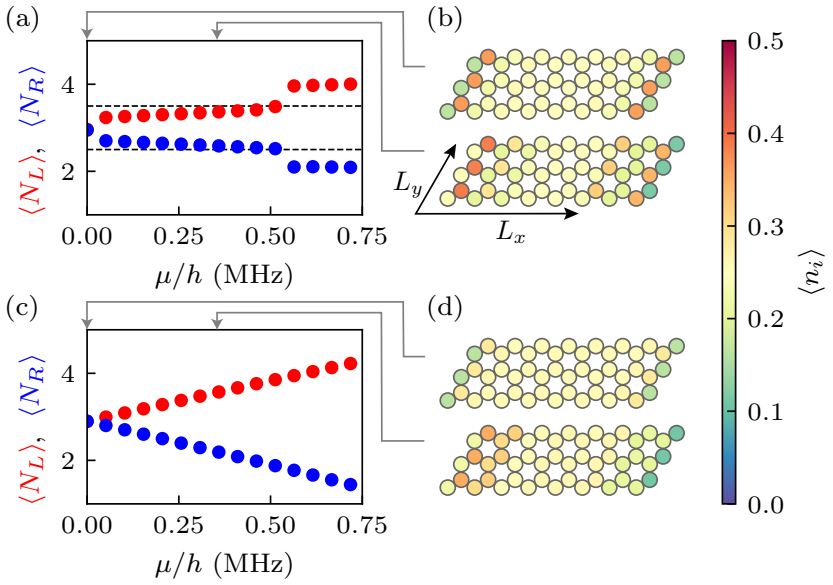

Fig. 7.4: **Detection of fractional charges.** We consider a cylinder with $L_x = 8$ and $L_y = 3$ that is finite along x. We apply a chemical potential $\mu \geq 0$ to the 12 leftmost sites $\mathbb{S}_L$ and the opposite potential to the 12 rightmost sites $\mathbb{S}_R$. Using DMRG with bond dimension $\chi = 200$, we calculate the number of particles on the left $\langle N_L\rangle$ and on the right $\langle N_R\rangle$ as a function of μ with $N_{L,R} = \sum_{i\in\mathbb{S}_{L,R}} n_i$. (a) The number of particles $\langle N_{L,R}\rangle$ jumps in steps of $1/2$, indicated by the dashed lines. (b) The particle density $\langle n_i\rangle$ increases on the leftmost sites and drops on the rightmost ones if μ is increased. (c) For comparison, we study our system in the topologically trivial sector, where the number of particles $\langle N_{L,R}\rangle$ changes continuously. The system was brought into the trivial sector by increasing Δ/h by 50 MHz so that the $|+\rangle$ state can be neglected. (d) Corresponding changes in the particle density $\langle n_i\rangle$.

in an experiment, one might realize a system with open boundary conditions and several hundreds of atoms [24, 25], we consider a finite cylinder of 48 sites to keep the system accessible within DMRG. The periodic boundary condition along the y direction helps us to mitigate finite-size effects, see Fig. 7.4(b,d) where we show an unrolled version of the cylinder. We apply a chemical potential $\mu \geq 0$ to the 12 leftmost sites and the opposite potential to the 12 rightmost sites.

We calculate the ground state at 1/4-filling as a function of μ, using the DMRG implementation of the open-source software `TeNPy` [328]. As a result, we observe that the particle number summed over the leftmost sites jumps up by 1/2 (quasiparticle), the particle number on the rightmost sites jumps

down by the same fraction (quasihole), see Fig. 7.4(a). The creation of the quasiparticle and quasihole happens already for small values of μ because the spectrum is gapless at the edge of the cylinder, except for a finite-size gap. The change of the particle number is a bit smaller than 1/2 because of the finite correlation length of the created excitations.

For comparison, we study our system in the topologically trivial sector. To get into the trivial sector, we increase Δ/h by 50 MHz so that the $|+\rangle$ state can be neglected, and we obtain in reasonable approximation a trivial two-band model. Such a huge increase in Δ can be experimentally realized, for example, by inverting the direction of the magnetic field B_z. In the trivial sector, the number of particles changes continuously.

7.5 Conclusion and Outlook

In this chapter, we presented a blueprint for the realization of a bosonic fractional Chern insulator with Rydberg atoms. The suggested setup relies on Rydberg atoms arranged in a honeycomb lattice and subject to dipolar exchange interaction, giving rise to hard-core bosons hopping in an effective magnetic field. We performed numerical studies, providing three characteristic signatures for the existence of a Laughlin-like state in our realistic microscopic model at 1/4-filling: (i) robust nearly two-fold ground state degeneracy on a torus, (ii) exponential decay of local correlations in the bulk, (iii) many-body Chern number of one.

Moreover, we adapted a recently developed technique for the experimental detection of fractional charges [322] to our setup. Our numerical simulations provide evidence that this technique can be applied for detecting fractional charges in the proposed experiment.

Our detailed proposal paves the way for the quantum simulation of fractional Chern insulators. Because of the microscopic control of the particles within a quantum simulator, this can help to deepen our understanding of topological states of matter.

8

Deterministic Fast Scrambling

In contrast to the previous chapters, this chapter covers a side project that is not linked to quantum simulations of topological phases. Instead, we focus on our proposal for the implementation of a deterministic fast scrambler [8], illustrating the variety of models that can be implemented using Rydberg interactions. Fast scramblers are quantum systems that produce many-body entanglement on a timescale that grows logarithmically with the system size N. In our proposal, we investigate a deterministic, fast scrambling quantum circuit. We show that a fast scrambler can be realized with an array of neutral atoms, using $\mathcal{O}(\log N)$ shuffling and parallel gate operations, where controlled-Z gates are performed using Rydberg interactions. Our protocol can be harnessed to produce highly entangled states on noisy hardware, where a fast generation of entanglement is crucial to limit decoherence.

Most of the work published in the proposal has been conducted by Tomohiro Hashizume, Gregory Bentsen, and Andrew Daley, except for the analyzation of the information scrambling in a realistic setup, which has been performed within this thesis. Here, we focus on this aspect of the proposal, taking into account effects of decoherence. To present a coherent story, we will also provide a general overview of the proposal. The presented plot of the setup has been created by Gregory Bentsen. For more details on the proposal, see the reference [8] and the PhD thesis by Tomohiro Hashizume [329].

8.1 Introduction

Quantum information scrambling refers to a process that delocalizes quantum information by the dynamics of a many-body system and encodes it into a many-body entangled state [330–333], thereby effectively hiding the information from local observers. Thus, this process is a practical tool in the context of

quantum error correction and quantum communication. In particular, strongly scrambling quantum circuits are known to be excellent encoders that optimally protect quantum information against the effects of single-qubit erasure and other forms of local decoherence [334–338].

Quantum information scrambling cannot occur instantaneously: the fast scrambling conjecture states that scrambling can develop on timescales *no shorter than* $t_* \propto \log N$, which scale logarithmically with the system size N. Systems that saturate this conjectured bound on the scrambling time t_* are known as fast scramblers [331]. Fast scrambling dynamics can rapidly generate Page-scrambled states, pure quantum states of a many-body system whose reduced density matrix ρ_A is maximally mixed for almost all subsystems A of size $|A| < N/2$ [330–332]. Prototypical models for fast scrambling [332, 339–343], inspired by the study of quantum information in black holes [330, 331, 334], often feature randomness and long-range couplings as key ingredients, although some recent deterministic models have been proposed with sparse or all-to-all coupling graphs with varying weights [344–346].

We propose a protocol for achieving fast scrambling in near-term experiments with one-dimensional arrays of optically trapped neutral atoms [24, 25, 36, 61, 187, 347–353]. Within these experiments, long-lived atomic ground states can be applied as qubit states. Our protocol for achieving fast scrambling makes use of three experimental tools: (i) global single-qubit rotations, (ii) parallel application of nearest-neighbor controlled-Z gates that are implemented by temporarily exciting the atoms to a Rydberg state and harnessing the strong Rydberg interaction, (iii) shuffling of the atoms via movable optical tweezers. The latter is applied for implementing highly non-local, sparsely coupled quantum circuits that allow for fast scrambling quantum channels [331–333]. Because we realize a *fast* scrambler, only $\mathcal{O}(\log N)$ applications of parallel controlled-Z gates are required. The small number of required parallel controlled-Z gates (interaction layers) is a significant advantage because it minimizes the decoherence that mainly arises from the laser excitation to the finite-lived Rydberg states [126–128, 170, 351, 354].

We analyze iterated circuits built with these tools. The simplest versions of our circuits generate effective controlled-Z interactions on the hypercube coupling graph [355, 356], efficiently producing Page-scrambled states from *some* initially separable state using only $m = \lceil \log_2 N \rceil$ interaction layers [8]. Using $2m$ interaction layers, we can construct deterministic circuits that strongly scramble quantum information *regardless of* the input state. In this thesis, we focus on the latter and evaluate the performance of such a circuit in the presence of decoherence that is expected in real implementations.

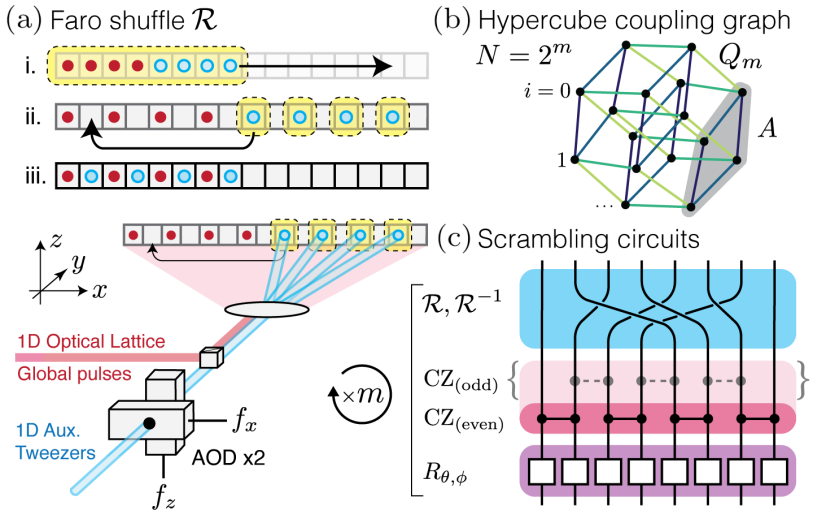

Fig. 8.1: **Fast scrambling via quasi-one-dimensional shuffling.** (a) Neutral atoms (red dots, blue circles) trapped in a static, one-dimensional optical lattice (gray boxes) can be rapidly rearranged via a two-step shuffling operation $\mathcal{R}$ (i-iii) facilitated by an auxiliary one-dimensional tweezer array (bottom left). Iterated shuffling and nearest-neighbor Rydberg interactions yield effective interactions on highly non-local coupling graphs such as the m-regular hypercube graph Q_m (b). More generally, circuits (c) composed of shuffles (blue), nearest-neighbor controlled-Z operations (red), and global rotations (purple) can be harnessed to generate Page-scrambled quantum states in m iterations or strongly scrambling quantum channels in $2m$ iterations.

8.2 Setup

The basis for our protocol is the possibility to realize a family of sparse non-local coupling graphs via a quasi-one-dimensional shuffling procedure, see Fig. 8.1(a), on atoms in optical lattices facilitated by an auxiliary programmable one-dimensional tweezer array. Straightforward stretching and interleaving tweezer operations [44, 46, 47, 357] can be used to rapidly shuffle the atomic positions, see Fig. 8.1(a)(i-iii). For $N = 8$ these motions execute the permutation

$$\mathcal{R} = \begin{pmatrix} 0 & 1 & 2 & 3 & 4 & 5 & 6 & 7 \\ 0 & 4 & 1 & 5 & 2 & 6 & 3 & 7 \end{pmatrix} \tag{8.1}$$

with atoms labeled by $i = 0, 1, \ldots, N-1$. More generally, for system sizes $N = 2^m$ with m an integer, a "perfect" shuffle or "Faro shuffle" operation [358,

359] executes the non-local mapping

$$i' = \mathcal{R}(i = b_m \dots b_2 b_1) = b_1 b_m \dots b_2, \tag{8.2}$$

which cyclically permutes the bit order of the atomic index $i = b_m \dots b_2 b_1$ written in binary such that the least significant bit b_1 of i becomes the most significant bit of $\mathcal{R}(i)$.

Repeated shuffling operations $\mathcal{R}$ dramatically rearrange the atomic positions. As a result, the propagation of quantum information is no longer constrained by the underlying one-dimensional geometry of the fixed optical lattice. By including global Hadamard H and phase P gates, one can implement the strongly scrambling circuit

$$\mathcal{E}_\mathrm{s} = [\mathcal{R}^{-1}\mathrm{CZ}_{(\mathrm{odd})}HP]^m[\mathcal{R}^{-1}\mathrm{CZ}_{(\mathrm{even})}HP]^m\ , \tag{8.3}$$

having only $2m$ interaction layers $\mathrm{CZ}_{(\mathrm{even})}, \mathrm{CZ}_{(\mathrm{odd})}$. Here, $\mathcal{R}^{-1}$ is the inverse of the shuffling operation $\mathcal{R}$. The circuit is visualized in Fig. 8.1(c).

Tomohiro Hashizume and Gregory Bentsen have performed numerical studies of Clifford circuits [360, 361], providing extensive evidence that the circuit $\mathcal{E}_\mathrm{s}$ indeed yields widespread many-body entanglement in the unitary case. For details, see our joint publication [8].

8.3 Possible Experimental Realization

In the following, we discuss a possible experimental realization of $\mathcal{E}_\mathrm{s}$ and how such a realization can be simulated numerically, taking into account effects of decoherence through noise and finite lifetimes that inevitably degrades the performance of a scrambling circuit.

Let us start by discussing possible experimental realizations of the different constituents of the scrambling circuit $\mathcal{E}_\mathrm{s}$:

- The shuffling operations $\mathcal{R}$ and $\mathcal{R}^{-1}$ can be built on established tweezer-assisted techniques for defect removal in atom arrays [44, 46, 47] and can be implemented rapidly using a pair of acousto-optic deflectors (AOD) in crossed configuration and driven by independent RF signals f_x, f_z, see Fig. 8.1(a).

- The Hadamard H and phase P gates can be implemented as single-qubit rotations, for example, via RF pulses or Raman transitions – assuming

that long-lived ground states of neutral atoms are used as qubit states $|0\rangle$ and $|1\rangle$ [43, 128, 362].

- The interaction layers $\mathrm{CZ}_{(\mathrm{even})}$ and $\mathrm{CZ}_{(\mathrm{odd})}$ comprise parallel applications of controlled-Z gates between neighboring atoms as shown in Fig. 8.1(c). The controlled-Z gates can be realized by exciting the qubit state $|1\rangle$ to a Rydberg state and making use of the strong van der Waals interactions between Rydberg atoms [126, 127, 135, 170, 351, 354, 363, 364]. For realizing the controlled-Z gates in parallel, one can use the scheme described in [127]: The state $|1\rangle$ is excited globally to the Rydberg state $|r\rangle$ by a π pulse, using a laser whose Rabi frequency is much larger than the van der Waals interaction $V_{\mathrm{vdW}}(r) \sim 1/r^6$ between adjacent atoms separated by the interatomic distance $r = r_{nn}$, so that all the population in $|1\rangle$ is transferred to $|r\rangle$. After waiting for the time $\pi/V_{\mathrm{vdW}}(r_{nn})$, the state $|rr\rangle$ of two adjacent atoms has picked up the phase π, and we bring back the population to $|1\rangle$ by another global π pulse. We separate neighboring atoms by $2r_{nn}$ if we do not like to perform a controlled-Z gate between them. As a result of this, the picked-up phase gets strongly suppressed by the rapid decay of the van der Waals interaction.

These proposed implementations of the gates have the advantage that they only require global pulses, removing the experimental hurdle of single-site addressability and making the experiment faster to perform.

For realistic numerical simulations of the proposed experimental realization, we consider cross-talk between atoms separated by the distance r, resulting from the $1/r^6$ decay of the van der Waals interaction. Note that this crosstalk results in non-Clifford gates so that we cannot apply the Gottesman–Knill theorem [360] and are thus limited to simulations with a small number of qubits. The experimentally unavoidable decoherence is considered by an effective model, where we apply the depolarizing quantum error channel

$$D(\rho) = (1-p)\rho + p\frac{I}{2} \tag{8.4}$$

to all qubits after each of the $2m$ interaction layers of the circuits. Here, p can be understood as the rate of single-qubit errors. The error channel is treated with a quantum trajectory approach where we randomly sample over 6×10^4 realizations of the total circuit and average over the measurements.

8.4 Information Scrambling in the Presence of Decoherence

Now that we know how to simulate a possible experimental realization of $\mathcal{E}_\mathrm{s}$ realistically, we characterize its scrambling properties.

For performing the characterization, we use the *Hayden-Preskill thought experiment* as a tool [334, 335, 337, 338] as shown on the left side of Fig. 8.2(a). This thought experiment is based around the observation that scrambling channels can be seen as encoding circuits that optimally protect quantum information against local errors. For the experiment, we consider a local observer Alice who wishes to use the scrambling circuit $\mathcal{E}_\mathrm{s}$ for encoding some quantum information that will, later on, be received by another observer Bob. To do so, Alice first creates Einstein-Podolsky-Rosen (EPR) pairs between her qubits A and the same number of input qubits of the circuit $\mathcal{E}_\mathrm{s}$ (i.e., qubits on which the circuit acts). By doing so, she maximally entangles her qubits with the qubits of the circuit. Bob, for his part, creates EPR pairs between his qubits B and the remaining input qubits of the circuit. Then, to actually send quantum information (i.e., a quantum state), Alice can project her maximally entangled qubits onto the desired state. After the operation of the circuit, Bob can recover Alice quantum information with high fidelity by collecting only a small subset R of output qubits and neglecting the rest $\overline{R}$ – he only needs $|R| = |A| + \mathcal{O}(1)$ output qubits. In the case of a unitary scrambling circuit, this is tantamount to the statement that the bipartite mutual information $I_2(A : RB)$ between Alice's qubits A and the qubits $B \cup R$ accessed by Bob is maximal. As shown, for example, in the supplementary material to our publication [329], this is equivalent to vanishing mutual information $I_2(A : \overline{R})$ between A and $\overline{R}$, i.e., the output qubits $\overline{R}$ *alone* do reveal nothing about Alice's information.

This high fidelity teleportation of Alice's quantum information to Bob occurs if and only if the circuit is strongly scrambling [334, 337] and therefore presents a sharp criterion for diagnosing the presence of scrambling dynamics in our circuit $\mathcal{E}_\mathrm{s}$.

However, while the Hayden-Preskill thought experiment tells under which conditions Bob can in principle recover the quantum state that Alice has sent, it does not tell how to do so in practice. To distinguish between scrambling and decoherence, we attempt to recover Alice's information using a *probabilistic decoding circuit* as shown on the right side of Fig. 8.2(a), following the scheme of Yoshida *et al.* [335, 337, 338]. This decoder consists of a complex-conjugated copy of the scrambling circuit and the ability to measure EPR pairs, thus being

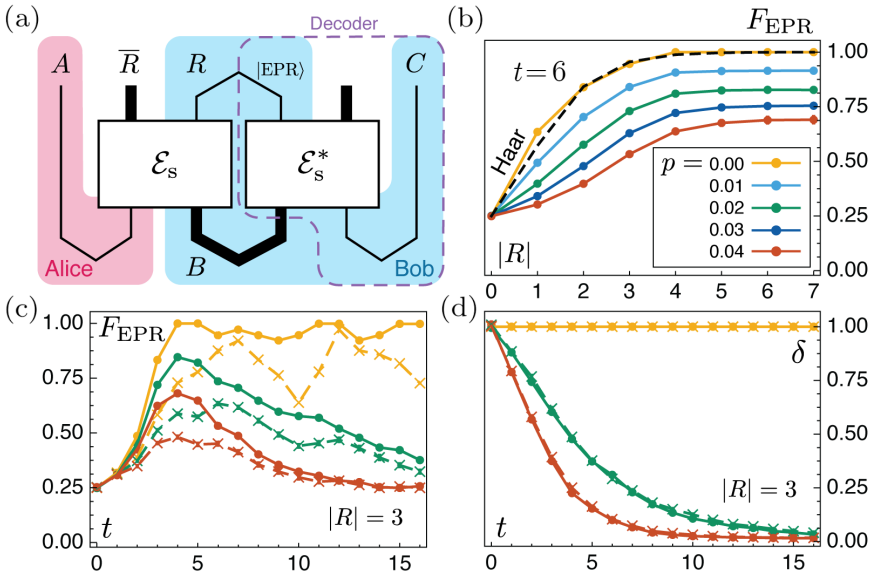

Fig. 8.2: **Information scrambling in the presence of decoherence.** (a) Scrambling in the circuit $\mathcal{E}_s$ is diagnosed by the fidelity F_{EPR} of teleporting quantum information from Alice's qubit A to Bob's qubit C, using the setup of the Hayden-Preskill thought experiment (shown on the left) together with a probabilistic decoding circuit (shown on the right, inside the dotted purple line). (b) For $N = 8$ at fixed number of interaction layers $t = 6$ (here, the number of interaction layers is a measure of time), the fidelity grows with the number of qubits $|R|$ used in the decoder, indicating successful teleportation of Alice's information with fidelity $> 50\%$ even in the presence of single-qubit errors at rates $p = 0.00, 0.01, \ldots, 0.04$ per 2-qubit gate (light to dark). For $p = 0$, the fidelity is nearly identical to that of a Haar-random circuit (dotted black). (c) The fidelity (dots, solid lines) grows with t and substantially outperforms nearest-neighbor circuits of the same circuit depth (crosses, dotted lines) in the presence of decoherence. (d) The decoherence metric δ falls as a function of t in both the scrambling circuit and nearest-neighbor circuit, providing a measure of the decoherence acting on the systems as well as a check of our numerical methods. Each data point is averaged over 6×10^4 quantum trajectories, with error bars smaller than the markers. The lines are guides to the eye.

experimentally feasible. In fact, decoding protocols of this type have been realized in pioneering experiments with trapped ions [365]. Assuming that Alice has one qubit A, the decoder circuit $\mathcal{E}_s^*$ acts on the qubits owned by Bob B and one additional qubit that is maximally entangled with a further qubit given to Bob C.

The qubits' evolution under the scrambling and decoder circuits is calculated

using the state vector simulator of the open-source framework `Qiskit` [366], taking into account single-qubit errors at rate p. After the calculation, we sample over all subsystems of size $|R|$, and evaluate the projector on the corresponding $|R|$ EPR pairs. The projection succeeds with the probability P_{EPR}. In case of success, we evaluate the projector on the EPR pair between qubit A and C. Such an EPR pair, which is measured with probability F_{EPR}, is a resource for teleporting quantum information of Alice to Bob.

In the unitary case $p = 0$, the circuit $\mathcal{E}_{\mathrm{s}}^{*}$ decodes Alice's quantum information with a fidelity $F_{\mathrm{EPR}} = 2^{I_2(A:RB)-2|A|}$, conditioned on successful detection of $|R|$ EPR pairs by Bob with probability $P_{\mathrm{EPR}} = 2^{-I_2(A:RB)}$, see Fig. 8.2(b). Note that the stated formulas for the probabilities hold for $p = 0$ only, where the scrambling circuit $\mathcal{E}_{\mathrm{s}}$ shows behavior similar to a prototypical scrambler consisting of Haar-random unitaries. Bob's ability to recover Alice's information is degraded by decoherence $p > 0$, where the product $\delta \equiv P_{\mathrm{EPR}} F_{\mathrm{EPR}} 2^{2|A|} \leq 1$ gives a natural metric for the strength of decoherence [337, 338].

We compare the scrambling circuit to an analogous circuit without shuffling and thus with controlled-Z gates between nearest neighbors only. Notably, the nearest-neighbor circuit requires a longer time to accomplish scrambling, measured in the number of interaction layers. While the decoherence metric δ behaves the same for the nearest-neighbor circuit and the scrambling circuit $\mathcal{E}_{\mathrm{s}}$, see Fig. 8.2(d), for $p > 0$, the reachable teleportation fidelity F_{EPR} is significantly smaller for the slow scrambling nearest-neighbor circuit, see Fig. 8.2(c). This demonstrates that fast scrambling is crucial in non-error-corrected systems, precisely because fewer gates provide fewer opportunities for decoherence. Our scrambling circuit $\mathcal{E}_{\mathrm{s}}$ is optimal in this regard as it generates strong scrambling using the minimal number of interaction layers $2m \sim \mathcal{O}(\log N)$ allowed by the fast scrambling conjecture [331, 332, 342].

8.5 Conclusion and Outlook

We have analyzed how deterministic, highly non-local iterated circuits can generate fast scrambling dynamics in the presence of decoherence. Our protocol is amenable to direct experimental realization using shuffle operations on neutral atom qubits. This technique allows for rapid long-range spreading of entanglement, while minimizing errors from excitation of atoms to Rydberg states, and uses only shuffling operations, global single-qubit rotations, and parallel nearest-neighbor interactions. Building fast scrambling circuits in the laboratory opens connections to a wide range of ongoing areas, including

fundamental limits on the spreading of quantum information [331, 332, 342, 367], experimental studies of toy models of black holes [344, 368–371], efficient encoders for quantum error-correcting codes [334], and highly entangled resources for quantum computation [372, 373]. We note that the proposed scrambling circuit might also be constructed by other means, for example, via direct wiring of hypercubic coupling graphs in superconducting qubit systems.

Moreover, our protocol for fast scrambling could be immediately combined with another recent Rydberg proposal [371] that discusses nearest-neighbor models with scrambling times $t_* \propto N$.

Ausführliche Zusammenfassung in deutscher Sprache

Quantenmechanische Vielteilchensysteme mit klassischen Computern zu simulieren ist eine große Herausforderung [9, 10]. Dies sieht man bereits daran, dass die Anzahl der zur Beschreibung eines wechselwirkenden Vielteilchensystems benötigten Koeffizienten exponentiell mit der Anzahl der Teilchen wächst. Diese Skalierung führt dazu, dass exponentiell viel Speicher und Rechenzeit benötigt werden. So würde zum Beispiel das Speichern aller Koeffizienten eines quantenmechanischen Zustandes von 50 Spin-1/2-Teilchen bereits mehrere Petabyte erfordern. Approximative numerische Methoden können manche Systeme beschreiben, indem sie die Zustände komprimiert abspeichern, zum Beispiel als Tensornetzwerke [11]. Es wird jedoch angenommen, dass sich hochverschränkte quantenmechanische Systeme von klassischen Systemen nicht mehr effizient simulieren lassen [12]. Außerdem ist es zum Teil schwer, den Gültigkeitsbereich approximativer Methoden abzuschätzen. Richard Feynman schlug 1981 als Lösung vor, quantenmechanische – nicht klassische – Simulatoren zum Simulieren von Quantensystemen zu verwenden [9]. Das Herzstück eines Quantensimulators ist ein gut zu kontrollierendes quantenmechanisches System, das in einem wohldefinierten Quantenzustand initialisiert werden kann, der sich unter einem spezifizierbaren Hamiltonian in der Zeit entwickelt [13–15]. Eine Übersicht über mögliche Anwendungen von Quantensimulatoren geben wir in Abschnitt 2.1. Zusammenfassend lässt sich sagen, dass die Erforschung von Grundzuständen und der Zeitentwicklung von wechselwirkenden Vielteilchensystemen die Hauptanwendungen sind. Zusätzlich wird untersucht, ob sich Quantensimulatoren auch zum Lösen harter klassischer Optimierungsprobleme einsetzen lassen [16, 17]. Des Weiteren können sie zum Benchmarken approximativer numerischer Methoden für Quantensysteme [18] und zukünftiger Quantencomputer verwendet werden.

Man unterscheidet zwischen *digitalen* Quantensimulatoren, die Gatteroperationen zur Simulation eines Systems verwenden, und *analogen* Quantensimulatoren, die Hamiltonians direkt implementieren, sowie hybriden Ansätzen. Diese Doktorarbeit beschäftigt sich mit analogen Quantensimulationen (mit

Ausnahme von Kapitel 8). Ein analoger Quantensimulator hat den Vorteil, dass er in der Regel robuster gegenüber Störungen ist als ein digitaler Simulator, solange dieser noch über keine Fehlerkorrektur verfügt. Es wird angenommen, dass bei einer analogen Simulation einer Phase eines in der Natur vorkommenden quantenmechanischen Systems eine Störung unerheblich ist, die auf einen kleinen Bruchteil der Gitterplätze wirkt. Denn solche Störungen kommen auch in vielen natürlichen Materialien vor [10]. Außerdem vermeiden analoge Simulationen den zusätzlichen Ressourcenbedarf des digitalen Ansatzes. Für letzteren muss die Trotter-Zerlegung verwendet werden, um den Zeitentwicklungsoperator als Gattersequenz anzunähern [14]. Um eine hohe Genauigkeit erreichen zu können, ist eine hohe Anzahl an Gatteroperationen notwendig. Dies ist mit der heutigen NISQ-Hardware[23] jedoch nur schwer umzusetzen [19]. In der Zukunft kann sich das jedoch ändern, wenn leistungsfähige und fehlerkorrigierte digitale Hardware verfügbar ist. Solange die Fehlerkorrektur noch nicht realisiert ist, werden analoge Quantensimulatoren jedoch zum Lösen einiger Probleme besser geeignet sein als ihre digitalen Gegenstücke. Hierdurch sind analoge Quantensimulatoren auch vielversprechende Kandidaten für einen praktischen Quantenvorteil, obwohl Quantenüberlegenheit mit gatterbasierten Quantencomputern demonstriert wurde [20]. Einige aktuelle Quantensimulationen dringen bereits in Bereiche vor, in denen exakte numerische Rechnungen aufgrund der großen Anzahl an Teilchen nicht mehr möglich sind. Es werden Probleme gelöst, die nur noch mit fortschrittlichen, approximativen Methoden von klassischen Computer angegangen werden können [21–28]. Um die Resultate der zitierten analogen Quantensimulationen zu reproduzieren, wurden Tensornetzwerkmethoden oder Quanten-Monte-Carlo-Methoden benötigt. Eine aktuelle Herausforderung ist es, Quantensimulatoren so zu verbessern, dass sie hochverschränkte Systeme mit einer solchen Genauigkeit simulieren können, dass approximative numerische Methoden keine Chance mehr haben.

Diese Herausforderung wird dadurch erschwert, dass analoge Quantensimulatoren nicht beliebige Systeme simulieren können. Stattdessen hängt die Klasse der implementierbaren Hamiltonians von den Details der experimentellen Plattform ab, die dem analogen Quantensimulator zugrunde liegt. Es gibt jedoch bereits viele spannende Modelle, die sich implementieren lassen, wie zum Beispiel Hubbard-Modelle, Modelle ähnlich zum Ising-Modell oder andere Spinmodelle [14, 15]. Außerdem sind analoge Quantensimulatoren gut geeignet, um universelle Eigenschaften zu studieren, die robust gegenüber Störtermen

[23] NISQ-Hardware steht für "noisy intermediate-scale quantum" Hardware [19], also für Quantenhardware mit geringer Rauschresistenz und zu wenig Qubits für Fehlerkorrektur.

sind [19]. In diesem Fall kann es in Ordnung sein, einen Hamiltonian durch das Hinzufügen von Termen an eine spezifische Plattform anzupassen und diesen dann zu implementieren. Außerdem zeigt aktuelle Forschung, dass die Klasse der simulierbaren Hamiltonians durch die Verwendung eines variationellen Simulationsansatzes erweitert werden kann. Hierbei wird ein analoger Quantensimulator zur Präparation eines variationellen Testzustandes eingesetzt [29].

Damit eine Plattform für Quantensimulationen geeignet ist, muss diese ein quantenmechanisches System mit vielen Freiheitsgraden beinhalten, das in einem wohldefinierten Zustand initialisiert werden kann. Zusätzlich müssen Messungen an dem System durchführbar sein und es muss perspektivisch möglich sein, Hamiltonians zu implementieren, die nicht klassisch behandelbar sind [10]. Letzteres impliziert, dass die Wechselwirkung im Vergleich zur Dekohärenz schnell sein muss [30]. Wie im Review [15] gezeigt wurde, erfüllen unterschiedliche Plattformen diese Kriterien, wobei jede Plattform ihre eigenen Vor- und Nachteile hat. Bevor es im nächsten Abschnitt um die Rydberg-Plattform geht, wird im Folgenden ein kurzer Überblick über alternative Plattformen gegeben. Prominente Beispiele sind supraleitende Schaltungen [31, 32], lineare Ionenfallen [33, 34] und neutrale Atome in optischen Gittern [35–37]. Supraleitende Schaltungen und Ionenfallen bieten ein gut zu kontrollierendes Quantensystem und werden für digitale und analoge Quantensimulationen eingesetzt, die analogen Simulationen hauptsächlich für die Simulation von Spin-Hamiltonians. Zum jetzigen Zeitpunkt werden jedoch nur unter hundert Spins unterstützt. Die Skalierung dieser Plattformen hin zu mehr Spins ist eine zentrale Herausforderung. Systeme zu vergrößern, die auf Ionenfallen basieren, erfordert experimentell anspruchsvolle Techniken wie zum Beispiel das Verschieben von Ionen [38, 39]. Im Gegensatz hierzu, können neutrale Atome in optischen Gittern bereits jetzt tausende Teilchen simulieren, allerdings mit deutlich schlechterer Kontrolle über die Teilchen als bei supraleitenden Schaltungen oder Ionenfallen. Mit neutralen Atomen in optischen Gittern wurde 2002 eine der ersten analogen Quantensimulationen realisiert [40]. Diese Plattform unterstützt die native Simulation von Fermionen oder Bosonen durch Verwendung von fermionischen oder bosonischen Atomen. Die Plattform wird typischerweise für die Simulation von Hubbard-Modellen eingesetzt und ist durch die vergleichsweise geringe Anzahl an implementierbaren Gittergeometrien und Hamiltonians limitiert. Eine aktuelle Herausforderung ist es, die Atome in den optischen Gittern zu kühlen. Diese Herausforderung wird zum Beispiel mittels Umverteilung der Entropie in die Randbereiche des Gitters angegangen [37].

In dieser Doktorarbeit geht es um die Rydberg-Plattform [41]. Im Rahmen der

Arbeit verstehen wir unter dieser Plattform einen analogen Quantensimulator mit neutralen Atomen, die in Arrays aus optischen Pinzetten gefangen sind und in den Ryberg-Zustand angeregt werden, um Wechselwirkung zu realisieren. Dieser Ansatz ist vergleichsweise neu, aber liefert bereits gute Ergebnisse [42, 43].

Die optischen Pinzetten können in beliebigen ein-, zwei- und dreidimensionalen Arrays angeordnet werden [44–47] und werden zufällig mit Atomen aus einem lasergekühltem atomaren Gas geladen; lichtinduzierte Kollisionen stellen sicher, dass jede optische Pinzette mit genau einem Atom besetzt oder leer ist. Seit 2016 können die zufällig geladenen optischen Pinzetten zu neuen Arrays mit nahezu vollständiger Besetzung angeordnet werden [44–46]. Dieses Protokoll ermöglicht bereits jetzt, beliebige Geometrien mit mehr als zweihundert Atomen zu realisieren [24, 25].

Indem man die neutralen Atome in den Rydberg-Zustand anregt, lassen sich Wechselwirkungen zwischen den Atomen realisieren. Ein Rydberg-Zustand ist ein Zustand, bei dem das äußerste Elektron in eine hohe Hauptquantenzahl n angeregt ist [48–50]. Hierdurch ist das Elektron schwächer an den Kern gebunden und die Wechselwirkung verstärkt. Die Van-der-Waals-Wechselwirkung [51–54] wächst mit n^{11} an und die dipolare Austauschwechselwirkung [55] skaliert mit n^4. Typisch sind Wechselwirkungsstärken $V/h \gtrsim 1$ MHz für $n = 60$ und einem interatomaren Abstand von 10 μm, wobei h die Planck-Konstante ist [42, 56]. Die radiative Lebenszeit skaliert mit n^3 und erreicht 100 μs bei Raumtemperatur für die in dieser Doktorarbeit betrachteten Rydbergzustände[24]. Somit ist die Wechselwirkung deutlich stärker als die Zerfallsrate und wir können kohärente quantenmechanische Systeme simulieren. In den meisten derzeitigen Experimenten ist die Laufzeit allerdings nicht durch die Lebenszeit beschränkt, sondern durch die Bewegung der Rydberg-Atome. Dies liegt daran, dass die meisten der verwendeten optischen Pinzetten nur Grundzustandsatome fangen können. Um dieses Problem zu lösen, werden zum Beispiel sogenannte magische Fallen entwickelt[25] [59].

Mit der Rydberg-Plattform können sehr unterschiedliche Spin-Hamiltonians realisiert werden. Die grundsätzliche Idee ist, elektronische Zustände des Atoms

[24] Für zirkulare Rydberg-Zustände, also Rydberg-Zustände mit maximaler Drehimpulsquantenzahl und magnetischen Quantenzahl, sind sogar Lebenszeit im Bereich von Sekunden möglich. Diese Zustände sind jedoch schwerer zu präparieren [57, 58].

[25] Die magischen Fallen verwenden feinabgestimmte ("magische") Bedingungen, die es erlauben, sowohl Grundzustandsatome als auch Rydberg-Zutände zu fangen. Solche Bedingungen existieren zum Beispiel für Erdalkalimetalle durch die Polarisierbarkeit durch das zweite Valenzelektron [59].

auf Spinzustände abzubilden. Um diese Abbildung akkurat durchführen und die Wechselwirkung zwischen Atomen kontrollieren zu können, können externe elektrische und magnetische Felder, lichtinduzierte Verschiebungen der Energieniveaus und Techniken zur Beimischung von Zuständen verwendet werden. Zusammen mit der Möglichkeit, beliebige Arrays zu realisieren, erlauben diese Werkzeuge die Implementierung einer Vielzahl unterschiedlicher Hamiltonians auf kontrollierbare Art und Weise. So wurden zum Beispiel verschiedene Ising-artige Modelle [23–25, 60–62] und XY-Hamiltonians [4, 63] simuliert. Künstliche Magnetfelder lassen sich ebenfalls realisieren [6, 64]. Ein detaillierter Überblick über realisierbare Modelle und technische Hintergrundinformationen werden in Abschnitt 2.2 gegeben. Wie diese Beispiele illustrieren, bietet die Rydberg-Plattform eine ansprechende Mischung aus Vielseitigkeit, guter Kontrollierbarkeit und Größe der implementierbaren Systeme.

Diese Doktorarbeit liefert theoretische Grundlagen für die experimentelle Realisierung von Quantensimulationen mit Rydberg-Atomen. Zunächst beschäftigen wir uns mit der genauen Berechnung der Wechselwirkung zwischen Rydberg-Atomen und ihrer Abhängigkeit von experimentellen Parametern. Danach verwenden wir diese Erkenntnisse, um zu zeigen, wie mit Rydberg-Quantensimulationen verschiedene Spinmodelle studiert werden können. Nachstehend wird eine Übersicht über die in der Doktorarbeit erzielten Ergebnisse gegeben.

Berechnung von Rydberg-Wechselwirkungspotentialen: Wie bereits zuvor diskutiert, lässt sich die starke Wechselwirkung zwischen Rydberg-Atomen für Quantensimulationen von unterschiedlichen Spinmodellen einsetzen. Die Rydberg-Wechselwirkung wird auch im Bereich der Quanteninformatik zur Realisierung von Zwei- und Multi-Qubit-Gattern verwendet. Ein genaues Verständnis der Wechselwirkungspotentiale ist essentiell, um für diese Anwendungen geeignete experimentelle Parameter finden zu können. Außerdem hilft es, Experimente zu verstehen, welche die Rydberg-Wechselwirkung sehr präzise oder auf kurzen Entfernungen untersuchen. In all diesen Fällen reichen perturbative Methoden zur Berechnung der Wechselwirkungspotentiale nicht aus. Daher gibt Kapitel 3 eine Einführung in die nicht perturbative Berechnung, basierend auf unserem Tutorial zu diesem Thema [1]. Wir besprechen, wie sich der Wechselwirkungshamiltonian aus der elektrostatischen Multipolentwicklung herleiten lässt, Matrixelemente numerisch berechnet und beliebige externe elektromagnetische Felder berücksichtigt werden können. Wir diskutieren Symmetrien und Auswahlregeln, die es erlauben, Rechnungen schneller durchzuführen. All die besprochenen Feature sind in unserer Open-Source-Software `pairinteraction`

implementiert[26], siehe `https://pairinteraction.github.io`.

Akkurates Abbilden von elektronischen Zuständen auf Spinzustände: In Kapitel 4 wird die `pairinteraction` Software verwendet, um experimentelle Parameter zu finden, die es ermöglichen, elektronische Zustände eines Rydberg-Atoms auf Spinzustände abzubilden. Wir betrachten Arrays aus Atomen, deren Grundzustand mit Lasern an den $nD_{3/2}$-Rydberg-Zustand gekoppelt wird. Um diese Atome akkurat auf Spin-1/2-Teilchen abbilden zu können, ist es wichtig, dass die Wechselwirkung zweier Rydberg-Atome mit einer einzigen Paarpotentialkurve beschrieben werden kann und hierdurch die Anregung ungewollter Rydberg-Zustände vermieden wird. Wir finden heraus, dass diese Näherung sensitiv bezüglich elektrischer Felder ist. Diese können dazu führen, dass an weitere Paarpotentialkurven gekoppelt wird. Dies hat auch zur Folge, dass die Rydberg-Blockade auf kurzen Entfernungen zusammenbricht. Unsere Erkenntnisse erweitern bereits existierende Studien zum Zusammenbruch der Rydberg-Blockade [52, 53, 241, 243, 283, 284]. Wir fanden numerisch einen optimalen Parametersatz, für den dieses Problem nicht auftritt. Experimentelle Ergebnisse aus der Gruppe von Antoine Browaeys bestätigen, dass unser Parametersatz tatsächlich eine akkurate Abbildung auf Spin-1/2-Teilchen ermöglicht [2] – sowohl kleinere Systeme aus zwei Atomen als auch anisotrope Ising-Magnete aus 7×7 Atomen zeigen experimentell die Dynamik, die wir aus numerischen Simulationen von Spin-1/2-Teilchen erwarten. Experimentelle Details finden sich in der Doktorarbeit von Sylvain de Léséleuc [3]. Zusammen mit Kapitel 3 bildet diese Forschung eine Grundlage für verschiedene Quantensimulationen von Spinmodellen, die wir nachfolgend beschreiben.

Realisierung einer durch Symmetrie geschützten topologischen Phase: Die Realisierung von topologischen Phasen ist ein geeignetes Ziel für analoge Quantensimulatoren, da topologische Phasen nicht zu einem spezifischen Hamiltonian gehören, sondern zu einer Äquivalenzklasse von Hamiltonians, wie es für Quantenphasen allgemein der Fall ist. Daher ist es nicht notwendig, einen bestimmten Hamiltonian zu implementieren, sondern wir können den Hamiltonian aus der Klasse auswählen, der auf unserer Hardware am einfachsten zu implementieren ist. Außerdem ist das Ziel lohnenswert, da es zuvor noch nicht gelungen war, mit einem künstlichen System einen topologisch nicht trivialen Vielteilchengrundzustand zu realisieren. Bis dahin sind in künstlichen

[26] Die `ARC` Bibliothek von N. Šibalić *et al.* ist eine weitere Open-Source-Software um Eigenschaften von Rydberg-Systemen zu berechnen [56]. Diese Bibliothek enthält mehr Funktionalität zur Berechnung von Eigenschaften einzelner Rydberg-Atome, kann jedoch keine Wechselwirkungspotentiale in Gegenwart von beliebigen elektrischen und magnetischen Feldern bestimmen.

Systemen topologische Eigenschaften studiert worden, die mit Einteilchenphysik zu erklären sind [65–80]. In Kapitel 5 diskutieren wir die Quantensimulation einer durch Symmetrie geschützten topologischen Phase aus wechselwirkenden Bosonen in einem eindimensionalen Gitter, basierend auf einem gemeinsamen Projekt mit der Experimentalgruppe von Antoine Browaeys [4]. Das Experiment benutzt Atome, die in einem Array aus optischen Pinzetten gefangen und in Rydberg-Zustände angeregt sind. Mit den Rydberg-Zuständen simuliert das Experiment sogenannte Hard-Core-Bosonen mit einem effektiven Hüpfen aufgrund der dipolaren Austauschwechselwirkung. Wir zeigen, dass der adiabatisch präparierte Grundzustand vier charakteristischen Eigenschaften einer durch Symmetrie geschützten topologischen Phase aufweist: (i) eine robuste Grundzustandsentartung, die auf geschützte Randzustände zurückgeführt werden kann, (ii) eine Energielücke zu angeregten Zuständen im Inneren, (iii) ein nicht verschwindender String-Ordnungs-Parameter, (iv) Robustheit dieser Eigenschaften bezüglich Störterme, welche die schützende Symmetrie respektieren. Die experimentellen Ergebnisse sind in sehr guter Übereinstimmung mit unseren theoretischen Untersuchungen. Für eine detailierte Beschreibung des Experiments verweisen wir auf die Doktorarbeit von Sylvain de Léséleuc [3], für die Klassifizierung der topologischen Phase auf die Doktorarbeit von Nicolai Lang [5]. Inzwischen werden Rydberg-Atome für weitere Studien von topologischen Systemen verwendet. So wurden vor Kurzem topologische Spinflüssigkeiten mit Rydberg-Atomen untersucht [23, 81].

Untersuchung von komplexen Hüpfamplituden von Rydberg-Anregungen: In Kapitel 6 analysieren wir komplexe Hüpfamplituden von Rydberg-Anregungen in einem Minimalsystem mit drei Gitterplätzen. Dieses System wurde von der Gruppe von Antoine Browaeys realisiert [6]. Die nicht trivialen komplexen Hüpfamplituden entstehen aus der Kombination von intrinsischer Spin-Orbit-Kopplung der dipolaren Austauschwechselwirkung und gebrochener Zeitumkehrsymmetrie. Im Experiment wird die Zeitumkehrsymmetrie durch ein externes Magnetfeld gebrochen. Experimentell zeigt sich das Vorhandensein der komplexen Hüpfamplituden in der charakteristischen chiralen Bewegung einer Anregung. Die chirale Bewegung lässt sich am besten im perturbativen Regime verstehen, in welchem die Spin-Orbit-Kopplung zu einer Peierls-Phase führt, die ein effektives Magnetfeld beschreibt. Der Wert der Peierls-Phase der Hüpfamplituden zwischen zwei Gitterplätzen hängt von der Geometrie und dem Vorhandensein einer weiteren Anregung auf dem verbleibenden Gitterplatz ab. Wir vergleichen unsere theoretische Beschreibung des Setups mit experimentellen Ergebnissen und erhalten eine hervorragende Übereinstimmung. Das Experiment ist im Detail in der Doktorarbeit von Vincent Lienhard bespro-

chen [7].

Proposal für die Realisierung eines fraktionalen Chern-Isolators: Eine aktuelle Herausforderung ist es, fraktionale Chern-Isolatoren in künstlichen Systemen zu realisieren, die mikroskopische Kontrolle über Teilchen bieten und hierdurch ermöglichen, ein besseres Verständnis dieser topologischen Zustände zu bekommen. In Kapitel 7 präsentierten wir ein Proposal, wie ein fraktionaler Chern-Isolator mit Rydberg-Atomen realisiert werden kann. Die vorgeschlagene Realisierung basiert auf einem Zusammenspiel der nicht trivialen Topologie der Bandstruktur und der Wechselwirkung zwischen Teilchen. Die nicht triviale Topologie resultiert aus einem effektiven Magnetfeld, das wie im vorherigen Kapitel beschrieben realisiert werden kann. Die Wechselwirkung zwischen den Teilchen kommt dadurch zustande, dass sich an einem Gitterplatz nur eine einzige Rydberg-Anregung befinden kann. Die Rydberg-Atome ordnen wir in einem Honigwabengitter an und verwenden homogene externe eletrische und magnetische Felder zur Feinabstimmung des Hamiltonians. Für realistische experimentelle Parameter finden wir einen Bereich, in dem unsere Simulationen zeigen, dass der Grundzustand des Systems charakteristische Eigenschaften eines fraktionalen Chern-Isolators aufweist: (i) robuste zweifache Quasientartung des Grundzustandes auf einem Torus, (ii) exponentiell abfallende Korrelationen, (iii) Charakterisierung des quasientarteten Grundzustandes durch eine Vielteilchen-Chern-Zahl von Eins. Unser Proposal beinhaltet auch einen Vorschlag zur experimentellen Detektion des fraktionalen Charakters von Anregungen im System.

Realisierung eines deterministischen, schnellen Scramblers mit Rydberg-Atomen: In Kapitel 8 stellen wir ein Nebenprojekt vor, an dem wir in Kooperation mit der Gruppe von Andrew Daley und mit Gregory Bentsen mitwirkten [8]. Dieses Nebenprojekt illustriert, dass sich neben topologischen System auch vollkommen andere Systeme mit Rydberg-Wechselwirkung realisieren lassen: Wir machen einen Vorschlag, wie ein deterministischer, schneller Scrambler implementiert werden kann. Schnelle Scrambler sind Quantensysteme, die eine Vielteilchen-Verschränkung auf einer Zeitskala aufbauen, die logarithmisch mit der Systemgröße N wächst. Wir zeigen, dass sich ein schneller Scrambler mit einem eindimensionalen Array neutraler Atome unter Verwendung von $\mathcal{O}(\log N)$ Verschiebeoperationen und parallelen Gatteroperationen realisieren lässt. Die hierbei verwendeten CZ-Gatter basieren auf der Rydberg-Wechselwirkung. In dieser Doktorarbeit analysieren wir das Scrambling von Information in einem realistischen Setup, bei dem wir Dekoheränz berücksichtigten. Für andere Aspekte des Systems verweisen wir auf unser Paper [8] und die Doktorarbeit von Tomohiro Hashizume [329]. Unser Protokoll kann zur Erzeugung hoch-

verschränkter Zustände auf Systemen mit geringer Rauschresistenz verwendet werden, bei denen eine schnelle Erzeugung von Verschränkung wichtig ist, um Dekoheränz zu beschränken.

A

Supplementary Material to Rydberg Interaction Potentials

Here, we briefly review the required steps to assemble the Hamiltonian (3.1) for the interaction potential calculation presented in Chapter 3. As discussed in Section 3.2.1, this requires the Rydberg level energies (3.3), and the matrix elements of the single-atom electric multipole operators (3.8). Exact calculations of both the energy spectrum and electron wave functions are possible only for the hydrogen atom. We consider Rydberg atoms with a single electron in a highly excited state (principal quantum number $n \gg 1$), which behave very similar to hydrogen, since the Rydberg electron is effectively bound to a core with charge number $Z - (Z - 1) = 1$, consisting of the actual nucleus (with charge Z) and $Z - 1$ inner electrons screening the core charge. This results in expressions for the Rydberg level series which are only slightly modified from the well-known hydrogen result and there exist relatively simple approaches for calculating single-electron wave functions that capture the physics of Rydberg atoms very well.

A.1 Energy Levels

We consider Rydberg states including spin-orbit coupling, because the fine-structure of Rydberg states with low angular momentum l is well resolved in current experiments on interacting Rydberg atoms. The Rydberg levels are specified by the quantum numbers of the single Rydberg electron, namely n (principal quantum number), l (orbital angular momentum), $j = l \pm 1/2$ (total angular momentum), and m_j (magnetic quantum number). We neglect the hyperfine splitting caused by the coupling of the electron angular momentum j to the nuclear spin I. Although experiments are now resolving hyperfine

Series	Li	Na	K	Rb	Cs
$S_{1/2}$	[375] (1986)	[376] (1992)	[377] (1981)	[378] (2011)	[379] (2016)
$P_{1/2}$	[375] (1986)	[380] (1995)	[381] (1983)	[257] (2003)	[379] (2016)
$P_{3/2}$	[375] (1986)	[380] (1995)	[381] (1983)	[257] (2003)	[379] (2016)
$D_{3/2}$	[382] (1958)	[380] (1995)	[377] (1981)	[378] (2011)	[383] (1982)
$D_{5/2}$	[382] (1958)	[380] (1995)	[377] (1981)	[378] (2011)	[379] (2016)
$F_{5/2,7/2}$	[382] (1958)	[384] (1997)	[385] (1956)	[386] (2006)	[387] (1987)
$G_{7/2,9/2}$	-	[384] (1997)	-	[388] (2006)	[387] (1987)
$H_{9/2,11/2}$	-	[384] (1997)	-	-	-

Singlet Series	Sr
$^1S_0$	[389] (1982)
$^1P_1$	[390] (1978)
$^1D_2$	[389] (1982)
$^1F_3$	[390] (1978)

Triplet Series	Sr
$^3S_1$	[391] (1982)
$^3P_0$	[392] (1979)
$^3P_1$	[392] (1979)
$^3P_2$	[392] (1979)
$^3D_1$	[391] (1982)
$^3D_2$	[391] (1982)
$^3D_3$	[391] (1982)
$^3F_2$	[390] (1978)
$^3F_3$	[390] (1978)
$^3F_4$	[390] (1978)

Table A.1: References (with year) used for quantum defects in this thesis and in our `pairinteraction` software. For divalent atoms, we must distinguish between the singlet and triplet series.

levels of low-l Rydberg states up to very high principal quantum numbers $n \approx 90$ [256] and the hyperfine structure of Rydberg states can be a matter of importance in some quantum information experiments [374], the typical splitting $\Delta_{\text{hfs}} < 11\,\text{MHz}$ for $n \geq 40$ [257, 258] makes the hyperfine level structure (so far) irrelevant for interactions between Rydberg atoms.

The energy of Rydberg levels can be concisely written in analogy to the Rydberg expression for hydrogen as

$$E_{nlj} = -\frac{hcR^*}{n^{*2}}, \tag{A.1}$$

Here, n^* is an effective, non-integer principal quantum number, which contains

the species-dependent deviation from hydrogen, while

$$R^* = \frac{1}{1 + m_e/M_{\text{atom}}} R_\infty \tag{A.2}$$

is the modified Rydberg constant taking into account the species dependent mass M_{atom} of the atomic core. The effective quantum number is parameterized by introducing the quantum defects as $n^* = n - \delta_{nlj}$. The quantum defects in turn are written as a series expansion of the form

$$\delta_{nlj} = \delta_0 + \frac{\delta_2}{(n-\delta_0)^2} + \frac{\delta_4}{(n-\delta_0)^4} + \frac{\delta_6}{(n-\delta_0)^6} + \cdots \,. \tag{A.3}$$

The coefficients in this polynomial expression are obtained from fits to experimentally measured transition energies for specific species. The fine-structure splitting is usually included in the quantum defects, which results in them depending on the quantum number j. The quantum defects decrease rapidly with increasing orbital angular momentum l, since for high-l states the influence of the non-hydrogenic core on the single Rydberg electron orbit becomes less relevant. Thus, quantum defects have been experimentally determined for Rydberg states with low orbital angular momentum l, with the most precise data being available for the alkali atoms. Table A.1 lists the references for the coefficients of the quantum defects for the alkali atoms used for the calculations in this thesis and of quantum defects for strontium. These quantum defects are also implemented by default in our `pairinteraction` software, but can be replaced or extended by new values. The accuracy of the quantum defects used to compute the potential energies of Rydberg states is a key element to the precise determination of Rydberg interaction potentials. Note that the closed-form expression A.3 is motivated by, but differs from the analytic result obtained in quantum-defect-theory [261, 393] by the fact that δ_0 appears in the higher-order terms instead of δ_{nlj}. This truncation "spoils the theoretical significance" of the quantum defects [272], but is of course necessary when fitting experimental data and provides a simple and elegant expression for the energy of Rydberg levels.

Since Rydberg levels become more hydrogen-like with increasing l, we can use the analytic expression for hydrogen fine-structure energies for levels without an experimentally determined quantum defect. In addition, we include a correction

term proportional to the core dipole polarizability α_d of the considered species:

$$E_{nlj} = -\frac{hcR^*}{n^2}\left(1+\frac{\alpha^2}{n(j+1/2)}+\frac{\alpha^2}{n^2}\right) - \frac{e^2}{(4\pi\varepsilon_0)^2 a_0^4}\frac{3\alpha_d}{4n^3 l^5}. \tag{A.4}$$

The derivation of this formula and a detailed discussion of the core polarizability can be found in [48].

A.2 Electronic Wave Functions

Reducing the Rydberg atom to a single electron orbiting an extended core consisting of the atomic nucleus and the inner electrons, enables us to calculate effective single-electron Rydberg wave functions. Most importantly, the more complex structure of the effective core does not lift the spherical symmetry of the problem, thus the usual separation of variables for the Rydberg electron wave function into radial and angular part holds. The angular part is solved analytically and, when fine-structure is included, given by the spin spherical harmonics

$$Y_{j\pm\frac{1}{2},\frac{1}{2},j,m_j} = \frac{1}{\sqrt{2\left(j\pm\frac{1}{2}\right)+1}} \times \begin{pmatrix} \mp\sqrt{j\pm\frac{1}{2}\mp m_j+\frac{1}{2}}\,Y_{j\pm\frac{1}{2},m_j-\frac{1}{2}} \\ \sqrt{j\pm\frac{1}{2}\pm m_j+\frac{1}{2}}\,Y_{j\pm\frac{1}{2},m_j+\frac{1}{2}} \end{pmatrix}. \tag{A.5}$$

Based on this expression, the angular part of the electric multipole moments can be calculated. This is discussed in detail in Appendix A.4. Non-relativistic quantum defect theory provides analytical solutions for the radial part, known as *Coulomb functions* [261, 394]. The basic idea is to consider large distances r from the nucleus, where the screening of the inner electrons results in an effective core charge $Z = 1$. There, the radial Schrödinger equation reduces to the well-known hydrogen case, except that the energy eigenvalues of the bound states are fixed via the experimentally determined quantum defects. As a consequence, the resulting solutions depend on the (non-integer) effective

principal quantum number n^*:

$$\Psi_{n^*l}^{\mathrm{rad}}(r) = \left(\frac{1}{a_0}\right)^{3/2} \frac{1}{\sqrt{(n^*)^2\Gamma(n^*+l+1)\Gamma(n^*-l)}} \times W_{n^*,l+1/2}\left(\frac{2r}{n^*a_0}\right). \tag{A.6}$$

Here, $\Gamma(z)$ is the Gamma function, and $W_{k,m}(z)$ is the Whittaker function. The Coulomb functions are obtained by solving the hydrogen Coulomb radial equation where the energies corresponding to non-integer principal quantum numbers have already been inserted. These are approximate wave functions with the correct behavior for large r and the right binding energy. For the calculation of transition matrix elements between Rydberg states, these are the important criteria. A relativistic generalization of the quantum-defect theory exists [395], but for the high-n Rydberg states of interest here, the modification of the radial wave function due to the fine-structure correction turns out to be negligible.

An alternative approach to obtaining single-electron wave functions is numerically solving the radial Schrödinger equation including a species-dependent *model potential* [396]. Compared to Coulomb functions this approach enables calculation of wave functions in the inner region if the model potentials are correctly determined. Typically, the model potential for alkali atoms contains three contributions:

$$V_{\mathrm{mod}}(r) = V_{\mathrm{C}}(r) + V_{\mathrm{P}}(r) + V_{\mathrm{s.o.}}(r). \tag{A.7}$$

Here, $V_{\mathrm{C}}(r)$ is a modified Coulomb potential describing the distance dependent screening of the core charge by the inner electrons, $V_{\mathrm{P}}(r)$ describes the core polarization due to the Rydberg electron, and $V_{\mathrm{s.o.}}(r)$ is the spin-orbit coupling. The different terms are chosen such that the eigenvalues from the numerical solution of the radial Schrödinger equation reproduce the experimentally measured Rydberg energies. If in turn the energies are fixed, the radial Schrödinger equation reduces to a one-dimensional differential equation, and the electron wave functions can be obtained simply by numerical integration (usually from outside to inside). This approach, as well as the analytic Coulomb functions, are implemented in our `pairinteraction` software. In particular, for the alkali atoms we use expressions for $V_{\mathrm{C}}(r)$ and $V_{\mathrm{P}}(r)$ introduced by Marinescu *et al.* [397], which yield very good agreement with experimentally observed Rydberg level energies [398]. In the model potential by Marinescu *et al.*, the Coulomb

interaction with the smeared out charge distribution of the inner shells is written as:

$$V_{\mathrm{C}}(r) = -\frac{e^2}{4\pi\varepsilon_0}\frac{1+(Z-1)\mathrm{e}^{-\alpha_1 r} - r(\alpha_3+\alpha_4 r)\mathrm{e}^{-\alpha_2 r}}{r}, \tag{A.8}$$

with coefficients $\alpha_{1,2,3,4}$ depending on the atomic species and the orbital angular momentum l [397]. For the core polarization, only the leading dipole term is considered, which results in:

$$V_{\mathrm{P}}(r) = -\frac{e^2}{(4\pi\varepsilon_0)^2}\frac{\alpha_d}{2r^4}\left[1-\mathrm{e}^{-(r/r_c)^6}\right]. \tag{A.9}$$

Here, α_d is again the core dipole polarizability and r_c is the effective core size, obtained by comparing the numerical solutions with the experimentally observed energy levels. In addition to these two terms, we add an effective expression for the spin-orbit interaction [399]

$$V_{\mathrm{s.o.}}(r > r_c) = \frac{1}{2}\left(\frac{e^2}{4\pi\varepsilon_0}\right)\left(\frac{g_s}{2m_e^2c^2}\right)\frac{\boldsymbol{l}\cdot\boldsymbol{s}}{r^3}. \tag{A.10}$$

This expression is only valid for large r and for smaller distances from the core the full expression derived from the Dirac equation has to be taken into account [396].

The spin-orbit interaction $V_{\mathrm{s.o.}}$ depends on the radial coordinate r, thus the numerical radial wave function depends on the total angular momentum j. In practice, one usually does not solve the radial Schrödinger equation as eigenvalue problem, but instead inserts the level energies determined from experimental quantum defects (A.4). Here, care must be taken when combining model potentials (e.g. from [397]) with independently measured quantum defects, since the inserted energies most likely are not eigenenergies of the model potential. Improvements to the model potentials including the fine structure term have recently been discussed by Sanayei *et al.* [400].

A.3 Radial Matrix Elements

Calculating the radial parts of the electric multipole matrix elements appearing in the interaction Hamiltonian (3.7) amounts to solving integrals of the form

$$\langle nlj|\hat{p}_\kappa^{\mathrm{rad}}|n'l'j'\rangle = e\int \Psi_{nlj}^{\mathrm{rad}}(r)\Psi_{n'l'j'}^{\mathrm{rad}}(r)r^{2+\kappa}\,dr, \tag{A.11}$$

where $\Psi^{\mathrm{rad}}_{nlj}(r)$ are the radial wave functions discussed in Appendix A.2, obtained either numerically or in the form of Coulomb functions (A.6), and κ is the order of the multipole operator from (3.8) in Section 3.2.1. Note, that the radial wave functions obtained by either approach are real, so that the complex conjugation in the matrix element can be omitted. The matrix elements can be straightforwardly calculated by numerical integration [394, 401]. To optimize the numerics it is useful to rescale the radial coordinate and the wave functions according to

$$x = \sqrt{r}\ , \quad X^{\mathrm{rad}}_{nlj}(x) = x^{3/2}\Psi^{\mathrm{rad}}_{nlj}(r). \tag{A.12}$$

This scaling keeps the number of grid points between nodes of the wave function constant [402]. As an alternative to numerical integration, various analytical expressions for electric dipole matrix elements exist [402–404].

It is important to note that the rather simple methods of calculating single-electron wave functions only yield accurate results for $n > 30$. Significantly more advanced methods for calculating energy levels and matrix elements than what we present here have been developed for low-n states, see e.g. [405, 406].

A.4 Angular Matrix Elements

In addition to the radial part discussed in Appendix A.3, we also need the angular part of the electric multipole matrix elements. In this appendix, we review the general formalism for calculating matrix elements of spherical tensor operators, which can be applied to determine the angular parts appearing when the multipole operators are expressed in the spherical basis. A more comprehensive discussion of this topic can be found for example in [407]. The formalism relies on the Wigner-Eckart theorem [269], which states that matrix elements of spherical tensor operators $\hat{T}_{\kappa q}$ can be expressed as products of a Wigner 3-j symbol (alternatively a Clebsch-Gordan coefficient) and a reduced matrix element, which is independent of the angular momentum orientation. As we perform calculations in the fine-structure basis, we show the Wigner-Eckart theorem for the total angular momentum $j = l + s$. It reads

$$\begin{aligned}\langle lsjm_j|\hat{T}_{\kappa q}|l's'j'm'_j\rangle &= (-1)^{j-m_j}(lsj||\hat{T}_{\kappa 0}||l's'j') \\ &\times \begin{pmatrix} j & \kappa & j' \\ -m_j & q & m'_j \end{pmatrix}\ ,\end{aligned} \tag{A.13}$$

where $(lsj||\hat{T}_{\kappa 0}||l's'j')$ is the reduced matrix element for the total angular momentum. In case of the Wigner-Eckart theorem for the orbital angular momentum l or spin s, the reduced matrix element $(l||\hat{T}_{\kappa 0}||l')$ or $(s||\hat{T}_{\kappa 0}||s')$ would occur instead.

If $\hat{T}_{\kappa q}$ commutes with the spin s, we can relate the different reduced matrix elements via the equation

$$\begin{aligned}(lsj||\hat{T}_{\kappa 0}||l'sj') &= (-1)^{l+s+j'+\kappa}(l||\hat{T}_{\kappa 0}||l') \\ &\times\sqrt{(2j+1)(2j'+1)}\begin{Bmatrix} l & j & s \\ j' & l' & \kappa \end{Bmatrix}, \end{aligned} \tag{A.14}$$

where the last term is the Wigner 6-j symbol. If $\hat{T}_{\kappa q}$ commutes with the orbital angular momentum l, we have the relation

$$\begin{aligned}(lsj||\hat{T}_{\kappa 0}||ls'j') &= (-1)^{l+s'+j+\kappa}(s||\hat{T}_{\kappa 0}||s') \\ &\times\sqrt{(2j+1)(2j'+1)}\begin{Bmatrix} s & j & l \\ j' & s' & \kappa \end{Bmatrix}. \end{aligned} \tag{A.15}$$

These equations facilitate the calculation of arbitrary matrix elements, provided that we know the value of the reduced matrix element $(l||\hat{T}_{\kappa 0}||l')$ or $(s||\hat{T}_{\kappa 0}||s')$, respectively. If the considered spherical tensor operator is a spherical harmonic $Y_{\kappa q}(\hat{\vartheta},\hat{\varphi})$, it commutes with the spin and the value of the relevant reduced matrix element is

$$(l||\hat{Y}_{\kappa 0}||l') = (-1)^l\sqrt{\frac{(2l+1)(2\kappa+1)(2l'+1)}{4\pi}}\begin{pmatrix} l & \kappa & l' \\ 0 & 0 & 0 \end{pmatrix}. \tag{A.16}$$

Given that spherical harmonics are proportional to the angular part of the multipole operator $\hat{p}^{\text{ang}}_{\kappa q} = \sqrt{\frac{4\pi}{2\kappa+1}}Y_{\kappa q}(\hat{\vartheta},\hat{\varphi})$, we can evaluate multipole matrix elements as well. In order to calculate matrix elements of the momentum operators $\hat{J}_{1q} \in \{\hat{l}_{1q},\hat{s}_{1q}\}$, we need the reduced matrix element

$$(J||\hat{J}_{10}||J') = \hbar\sqrt{J(J+1)(2J+1)}\;\delta_{JJ'}\,. \tag{A.17}$$

B

Supplementary Material to Symmetry-Protected Topological Phase of Interacting Bosons

We present an additional comparison between experimental data and numerical simulations, completing the study shown in Fig. 5.7 of the main text, where we break the chiral symmetry by engineering a perturbation introducing a coupling J'' between the rightmost site and its second neighbor. Following a microwave sweep ending at a given detuning Δ_{f}, our experimental collaborators perform a spectroscopy of the many-body state corresponding to this final detuning. The energy difference $|\Delta E|$ is extracted by fitting with Gaussian functions the measured occupancies of the left and right edge sites.

Fig. B.1(a) shows $|\Delta E|$ as a function of Δ_{f} for two experimental datasets. The blue dashed line (single-particle spectroscopy) and the point at $\Delta_{\mathrm{f}}/(2\pi) = -1$ MHz corresponds to the two measurements presented in Fig. 5.7 of the main text. The red points correspond to a second dataset for which Δ_{f} is varied. For Δ_{f} largely negative (positive), an empty (filled) chain is prepared and the spectroscopy experiment probes the single-particle eigenmodes, whose degeneracy is broken by the J'' perturbation. In turn, for Δ_{f} in the half-filled region, the energy difference is much smaller as the ground state degeneracy is protected by the unbroken symmetry $\mathcal{S}_B$. For intermediate values of Δ_{f} (gray regions), the many-body state is gapless, which precludes an adiabatic preparation, and we observe a smooth transition between the two regions (empty/full or half-filled chains).

The larger energy difference observed in the red dataset is most likely caused by an electric field gradient creating an energy difference of $\sim 30 - 40$ kHz between the leftmost and righmost site due to the Stark effect. This gradient was

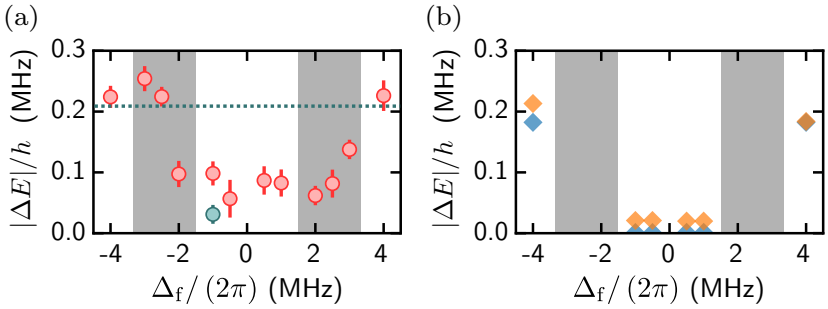

Fig. B.1: Energy difference ΔE between the left and right edge states extracted from a spectroscopy experiment performed after a microwave sweep ending at a detuning Δ_f. (a) Experimental values for two datasets. Blue: data presented in the main text, the dashed line corresponding to the single-particle spectroscopy performed on an empty chain. Red: additional data where Δ_f is varied. (b) Numerical simulations including (yellow) or excluding (blue) van der Waals terms.

carefully compensated by our collaborators for the other dataset (blue point). However, even in this case, there is a slight energy offset $|\Delta E|/h = 0.03(2)$ MHz. We explain it by a different van der Waals interaction of the leftmost and rightmost Rydberg atoms with their neighbors when displacing the rightmost site to engineer the J'' term, breaking the protecting symmetry. Including van der Waals terms in the simulation, we indeed obtain an energy difference of about ~ 0.02 MHz as shown in Fig. B.1(b).

C

Supplementary Material to Fractional Chern Insulator

C.1 Details on the Experimental Realization

In this section, we explain how the parameters of the Hamiltonian (7.3) depend on the experimental parameters and motivate the chosen parameter set.

Let us start by explaining how we obtained the parameters of the Hamiltonian from the experimental parameters. We first calculated the effect of the electric and magnetic fields on the Rydberg states, using the `pairinteraction` software [1]. For this calculation, we took into account Rydberg states that are at most 80 GHz away in energy from the states of the V-structure and have principal quantum numbers $57 \leq n \leq 63$ and azimuthal quantum numbers $l \leq 4$. Then, within the basis of the Stark and Zeeman shifted states, we calculated the interactions between the states of the V-structure using perturbation theory [276], taking into account that the Rydberg states were slightly admixed by the applied electromagnetic fields. For the perturbative calculations, we restricted ourselves to pair states that differ at most by 2 GHz from the pair states that can be constructed from the V-structure.

We performed our calculations for the principal quantum number $n = 60$ as the corresponding Rydberg states have already been studied experimentally in the past. For our choice of the lattice spacing, $l = 12$ μm, we took care that it is large enough to ensure that interactions can be described perturbatively. At the same time, it is small enough to allow for dipolar exchange interactions (order of a MHz) being much faster than the Rydberg decay (the natural lifetime is on the order of 100 μs). The magnetic field $B_z = -8$ G was applied to break the Zeeman degeneracy. For the realization of our V-level structure, it had been crucial that the sign of the field is negative so that we could compensate

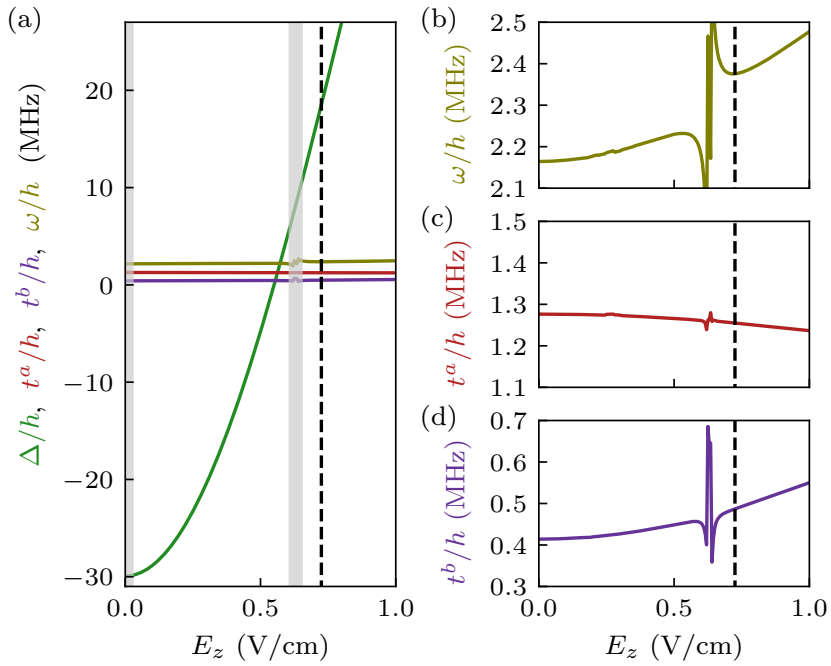

Fig. C.1: **Dependence of parameters of the Hamiltonian on the electric field.** (a) The energy difference Δ depends strongly on the electric field E_z through the Stark effect. In comparison, the nearest-neighbor hopping amplitudes barley change with E_z. The dashed lines indicate the value of $E_z = 0.725$ V/cm that was used throughout the Chapter 7. Note that for some other values, other Rydberg pair states get resonant and are admixed to the states of the V-structure (gray regions indicate an admixture $> 5\%$). There, our perturbative calculation of the hopping amplitudes break down. (b-d) Close-up views of the electric field dependence of the nearest-neighbor hopping amplitudes.

for the huge resulting energy splitting between $|+\rangle$ and $|-\rangle$ by applying an electric field of about $E_z = 0.7$ V/cm. We can use E_z to fine-tune Δ without affecting the other parameters much, see Fig. C.1.

For finding the optimal value for the electric field E_z, we first calculate the flatness ratio f and Berry curvature fluctuations σ_B as a function of E_z, see Fig. C.2(a-b). A large f and a small σ_B are beneficial for realizing a fractional Chern insulator in the many-body regime. However, these two quantities reach their respective optimal values for different E_z — we have to make some compromise. We calculate the three lowest eigenenergies on a torus at 1/4-filling for the clusters *20* and *24A* to determine the optimal value of E_z, see Fig. C.2(c). The ground state is nearly two-fold degenerate in a small region

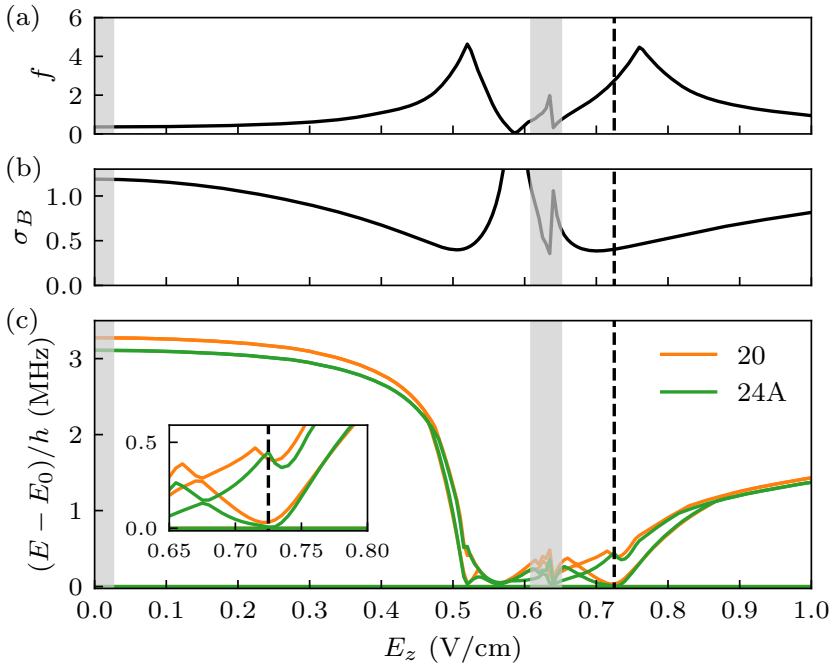

Fig. C.2: **Optimization of the electric field.** (a) Flatness ratio f of the lowest band of the single particle band structure as a function of the electric field E_z (gray regions indicate regimes where our perturbative calculation of hopping amplitudes failed). A large flatness ratio is beneficial for realizing a fractional Chern insulator in the many-body regime. (b) Berry curvature fluctuations σ_B. Typically, a small value is desirable. Note that f and σ_B reach their respective optimal values for different E_z. Thus, we have to make some compromise. (c) To figure out the optimal value of E_z, we calculate the three lowest eigenenergies on a torus at 1/4-filling for the clusters *20* and *24A*. The ground state is nearly two-fold degenerate in a small region around the optimal value $E_z = 0.725$ V/cm (dashed lines). For a zoom into this region, see inset.

around $E_z = 0.725$ V/cm. Remarkably, this is not the case for the region around $E_z = 0.52$ V/cm, despite promising values of f and σ_B. We attribute the lack of a two-fold degenerate ground state for this value of the electric field to the fact that there, the two lowest bands are not energetically separated from the other bands. The determinant condition, which holds for two band models, might potentially be violated [325]. Thus, $E_z = 0.725$ V/cm is the optimal value for the electric field.

Note that the proposed parameter set is not unique. We can, for example, use a different principal quantum number if we scale the other experimental parameters accordingly.

C.2 Parameters of the Hamiltonian

This section contains the values of the parameters of the Hamiltonian (7.3) that we used throughout the Chapter 7. Table C.1 shows the values of the hopping amplitudes (7.1). Table C.2 depicts the values of the considered interactions (7.2). All other two-body terms, for example, $b_i^\dagger b_j^\dagger a_i a_j$, are on the order of 0.01 MHz or less and hence neglected.

	$r_{ij}/l = 1$	$r_{ij}/l = \sqrt{3}$	$r_{ij}/l = 2$
t_{ij}^a/h	1.26	0.24	0.16
t_{ij}^b/h	0.49	0.09	0.06
ω_{ij}/h	2.38	0.45	0.29

Table C.1: Hopping amplitudes up to next-next-nearest-neighbor hopping in MHz. To avoid self-interaction in systems with periodic boundary conditions, we neglect longer ranging processes.

	$r_{ij}/l = 1$	$r_{ij}/l = \sqrt{3}$	$r_{ij}/l = 2$
$U_{ij}^{0,0}/h$	0.03	0.00	0.00
$U_{ij}^{0,a}/h$	0.07	0.01	0.01
$U_{ij}^{0,b}/h$	-0.20	0.00	0.00
$U_{ij}^{a,a}/h$	0.19	0.04	0.03
$U_{ij}^{a,b}/h$	0.25	0.05	0.03
$U_{ij}^{b,b}/h$	0.28	0.05	0.04

Table C.2: Interactions in MHz. Note that $U_{ij}^{\alpha,\beta} = U_{ij}^{\beta,\alpha}$.

Bibliography

[1] S. Weber, C. Tresp, H. Menke, A. Urvoy, O. Firstenberg, H. P. Büchler, and S. Hofferberth, "Calculation of Rydberg interaction potentials", Journal of Physics B: Atomic, Molecular and Optical Physics **50**, 133001 (2017) (cited on pages 4, 8, 20, 27, 28, 32, 41, 66, 81, 99, 102, 115, 135, 151).

[2] S. de Léséleuc, S. Weber, V. Lienhard, D. Barredo, H. P. Büchler, T. Lahaye, and A. Browaeys, "Accurate Mapping of Multilevel Rydberg Atoms on Interacting Spin-1/2 Particles for the Quantum Simulation of Ising Models", Physical Review Letters **120**, 113602 (2018) (cited on pages 4, 8, 65, 136).

[3] S. de Léséleuc, *Quantum simulation of spin models with assembled arrays of Rydberg atoms* (PhD Thesis. Université Paris Saclay, 2018) (cited on pages 4, 8, 9, 29, 30, 31, 65, 75, 136, 137).

[4] S. de Léséleuc, V. Lienhard, P. Scholl, D. Barredo, S. Weber, N. Lang, H. P. Büchler, T. Lahaye, and A. Browaeys, "Observation of a symmetry-protected topological phase of interacting bosons with Rydberg atoms", Science **365**, 775 (2019) (cited on pages 4, 9, 20, 21, 35, 40, 42, 75, 79, 89, 94, 100, 103, 112, 135, 137).

[5] N. Lang, *One-dimensional topological states of synthetic quantum matter* (PhD Thesis. Universität Stuttgart, Verlag Dr. Hut, 2019) (cited on pages 4, 9, 37, 75, 79, 137).

[6] V. Lienhard*, P. Scholl*, S. Weber, D. Barredo, S. de Léséleuc, R. Bai, N. Lang, M. Fleischhauer, H. P. Büchler, T. Lahaye, and A. Browaeys, "Realization of a Density-Dependent Peierls Phase in a Synthetic, Spin-Orbit Coupled Rydberg System", Physical Review X **10**, 021031 (2020) (cited on pages 5, 9, 20, 21, 39, 93, 100, 112, 113, 135, 137).

[7] V. Lienhard, *Experimental quantum many-body physics with arrays of Rydberg atoms* (PhD Thesis. Université Paris Saclay, 2019) (cited on pages 5, 9, 93, 100, 138).

[8] T. Hashizume, G. S. Bentsen, S. Weber, and A. J. Daley, "Deterministic Fast Scrambling with Neutral Atom Arrays", Physical Review Letters **126**, 200603 (2021) (cited on pages 5, 10, 121, 122, 124, 138).

[9] R. P. Feynman, "Simulating physics with computers", International Journal of Theoretical Physics **21**, 467 (1982) (cited on pages 17, 24, 131).

[10] J. I. Cirac and P. Zoller, "Goals and opportunities in quantum simulation", Nature Physics **8**, 264 (2012) (cited on pages 17, 18, 19, 26, 131, 132, 133).

[11] R. Orús, "A practical introduction to tensor networks: Matrix product states and projected entangled pair states", Annals of Physics **349**, 117 (2014) (cited on pages 17, 131).

[12] J. Preskill, "Quantum computing and the entanglement frontier", arXiv:1203.5813 (2012) (cited on pages 17, 24, 131).

[13] S. Lloyd, "Universal Quantum Simulators", Science **273**, 1073 (1996) (cited on pages 17, 26, 131).

[14] I. M. Georgescu, S. Ashhab, and F. Nori, "Quantum simulation", Reviews of Modern Physics **86**, 153 (2014) (cited on pages 17, 18, 23, 94, 131, 132).

[15] E. Altman et al., "Quantum Simulators: Architectures and Opportunities", PRX Quantum **2**, 017003 (2021) (cited on pages 17, 18, 19, 23, 131, 132, 133).

[16] H. Pichler, S.-T. Wang, L. Zhou, S. Choi, and M. D. Lukin, "Quantum optimization for maximum independent set using Rydberg atom arrays", arXiv:1808.10816 (2018) (cited on pages 17, 24, 25, 131).

[17] G. Pagano, A. Bapat, P. Becker, K. S. Collins, A. De, P. W. Hess, H. B. Kaplan, A. Kyprianidis, W. L. Tan, C. Baldwin, L. T. Brady, A. Deshpande, F. Liu, S. Jordan, A. V. Gorshkov, and C. Monroe, "Quantum approximate optimization of the long-range Ising model with a trapped-ion quantum simulator", Proceedings of the National Academy of Sciences of the United States of America **117**, 25396 (2020) (cited on pages 17, 24, 131).

[18] S. Scherg, T. Kohlert, I. Bloch, M. Aidelsburger, et al., "Benchmarking a novel efficient numerical method for localized 1D Fermi-Hubbard systems on a quantum simulator", arXiv:2105.06372 (2021) (cited on pages 17, 24, 131).

[19] J. Preskill, "Quantum Computing in the NISQ era and beyond", Quantum **2**, 79 (2018) (cited on pages 18, 26, 132, 133).

[20] F. Arute et al., "Quantum supremacy using a programmable superconducting processor", Nature **574**, 505 (2019) (cited on pages 18, 132).

[21] J.-y. Choi, S. Hild, J. Zeiher, P. Schauß, A. Rubio-Abadal, T. Yefsah, V. Khemani, D. A. Huse, I. Bloch, and C. Gross, "Exploring the many-body localization transition in two dimensions", Science **352**, 1547 (2016) (cited on pages 18, 132).

[22] T. B. Wahl, A. Pal, and S. H. Simon, "Signatures of the many-body localized regime in two dimensions", Nature Physics **15**, 164 (2018) (cited on pages 18, 132).

[23] G. Semeghini, H. Levine, A. Keesling, S. Ebadi, T. T. Wang, D. Bluvstein, R. Verresen, H. Pichler, M. Kalinowski, R. Samajdar, et al., "Probing Topological Spin Liquids on a Programmable Quantum Simulator", arXiv:2104.04119 (2021) (cited on pages 18, 20, 21, 39, 112, 132, 135, 137).

[24] P. Scholl, M. Schuler, H. J. Williams, A. A. Eberharter, D. Barredo, K.-N. Schymik, V. Lienhard, L.-P. Henry, T. C. Lang, T. Lahaye, A. M. Läuchli, and A. Browaeys, "Quantum simulation of 2D antiferromagnets with hundreds of Rydberg atoms", Nature **595**, 233 (2021) (cited on pages 18, 19, 20, 31, 34, 94, 112, 119, 122, 132, 134, 135).

[25] S. Ebadi, T. T. Wang, H. Levine, A. Keesling, G. Semeghini, A. Omran, D. Bluvstein, R. Samajdar, H. Pichler, W. W. Ho, S. Choi, S. Sachdev, M. Greiner, V. Vuletić, and M. D. Lukin, "Quantum phases of matter on a 256-atom programmable quantum simulator", Nature **595**, 227 (2021) (cited on pages 18, 19, 20, 31, 34, 94, 112, 119, 122, 132, 134, 135).

[26] J. Koepsell, D. Bourgund, P. Sompet, S. Hirthe, A. Bohrdt, Y. Wang, F. Grusdt, E. Demler, G. Salomon, C. Gross, and I. Bloch, "Microscopic evolution of doped Mott insulators from polaronic metal to Fermi liquid", Science **374**, 82 (2021) (cited on pages 18, 132).

[27] P. T. Brown, D. Mitra, E. Guardado-Sanchez, R. Nourafkan, A. Reymbaut, C.-D. Hébert, S. Bergeron, A.-M. S. Tremblay, J. Kokalj, D. A. Huse, P. Schauß, and W. S. Bakr, "Bad metallic transport in a cold atom Fermi-Hubbard system", Science **363**, 379 (2019) (cited on pages 18, 132).

[28] M. A. Nichols, L. W. Cheuk, M. Okan, T. R. Hartke, E. Mendez, T. Senthil, E. Khatami, H. Zhang, and M. W. Zwierlein, "Spin transport in a Mott insulator of ultracold fermions", Science **363**, 383 (2019) (cited on pages 18, 132).

[29] C. Kokail, C. Maier, R. van Bijnen, T. Brydges, M. K. Joshi, P. Jurcevic, C. A. Muschik, P. Silvi, R. Blatt, C. F. Roos, and P. Zoller, "Self-verifying variational quantum simulation of lattice models", Nature **569**, 355 (2019) (cited on pages 18, 133).

[30] W. H. Zurek, "Decoherence, einselection, and the quantum origins of the classical", Reviews of Modern Physics **75**, 715 (2003) (cited on pages 19, 133).

[31] P. Krantz, M. Kjaergaard, F. Yan, T. P. Orlando, S. Gustavsson, and W. D. Oliver, "A quantum engineer's guide to superconducting qubits", Applied Physics Reviews **6**, 021318 (2019) (cited on pages 19, 133).

[32] M. Kjaergaard, M. E. Schwartz, J. Braumüller, P. Krantz, J. I.-J. Wang, S. Gustavsson, and W. D. Oliver, "Superconducting Qubits: Current State of Play", Annual Review of Condensed Matter Physics **11**, 369 (2020) (cited on pages 19, 133).

[33] R. Blatt and C. F. Roos, "Quantum simulations with trapped ions", Nature Physics **8**, 277 (2012) (cited on pages 19, 133).

[34] C. Monroe, W. C. Campbell, L.-M. Duan, Z.-X. Gong, A. V. Gorshkov, P. W. Hess, R. Islam, K. Kim, N. M. Linke, G. Pagano, P. Richerme, C. Senko, and N. Y. Yao, "Programmable quantum simulations of spin systems with trapped ions", Reviews of Modern Physics **93**, 025001 (2021) (cited on pages 19, 133).

[35] M. Lewenstein, A. Sanpera, V. Ahufinger, B. Damski, A. Sen(De), and U. Sen, "Ultracold atomic gases in optical lattices: mimicking condensed matter physics and beyond", Advances in Physics **56**, 243 (2007) (cited on pages 19, 133).

[36] C. Gross and I. Bloch, "Quantum simulations with ultracold atoms in optical lattices", Science **357**, 995 (2017) (cited on pages 19, 122, 133).

[37] F. Schäfer, T. Fukuhara, S. Sugawa, Y. Takasu, and Y. Takahashi, "Tools for quantum simulation with ultracold atoms in optical lattices", Nature Reviews Physics **2**, 411 (2020) (cited on pages 19, 133).

[38] D. Kielpinski, C. Monroe, and D. J. Wineland, "Architecture for a large-scale ion-trap quantum computer", Nature **417**, 709 (2002) (cited on pages 19, 133).

[39] V. Kaushal, B. Lekitsch, A. Stahl, J. Hilder, D. Pijn, C. Schmiegelow, A. Bermudez, M. Müller, F. Schmidt-Kaler, and U. Poschinger, "Shuttling-based trapped-ion quantum information processing", AVS Quantum Science **2**, 014101 (2020) (cited on pages 19, 133).

[40] M. Greiner, O. Mandel, T. Esslinger, T. W. Hänsch, and I. Bloch, "Quantum phase transition from a superfluid to a Mott insulator in a gas of ultracold atoms", Nature **415**, 39 (2002) (cited on pages 19, 133).

[41] H. Weimer, M. Müller, I. Lesanovsky, P. Zoller, and H. P. Büchler, "A Rydberg quantum simulator", Nature Physics **6**, 382 (2010) (cited on pages 19, 42, 94, 133).

[42] A. Browaeys and T. Lahaye, "Many-body physics with individually controlled Rydberg atoms", Nature Physics **16**, 132 (2020) (cited on pages 19, 20, 27, 30, 31, 112, 134).

[43] M. Morgado and S. Whitlock, "Quantum simulation and computing with Rydberg-interacting qubits", AVS Quantum Science **3**, 023501 (2021) (cited on pages 19, 26, 27, 32, 112, 125, 134).

[44] D. Barredo, S. de Léséleuc, V. Lienhard, T. Lahaye, and A. Browaeys, "An atom-by-atom assembler of defect-free arbitrary two-dimensional atomic arrays", Science **354**, 1021 (2016) (cited on pages 19, 30, 42, 80, 94, 99, 123, 124, 134).

[45] W. Lee, H. Kim, and J. Ahn, "Three-dimensional rearrangement of single atoms using actively controlled optical microtraps", Optics Express **24**, 9816 (2016) (cited on pages 19, 30, 134).

[46] M. Endres, H. Bernien, A. Keesling, H. Levine, E. R. Anschuetz, A. Krajenbrink, C. Senko, V. Vuletic, M. Greiner, and M. D. Lukin, "Atom-by-atom assembly of defect-free one-dimensional cold atom arrays", Science **354**, 1024 (2016) (cited on pages 19, 30, 42, 80, 94, 123, 124, 134).

[47] D. Barredo, V. Lienhard, S. de Léséleuc, T. Lahaye, and A. Browaeys, "Synthetic three-dimensional atomic structures assembled atom by atom", Nature **561**, 79 (2018) (cited on pages 19, 30, 94, 123, 124, 134).

[48] T. F. Gallagher, *Rydberg Atoms* (Cambridge University Press, 1994) (cited on pages 19, 27, 28, 29, 42, 112, 134, 144).

[49] R. Löw, H. Weimer, J. Nipper, J. B. Balewski, B. Butscher, H. P. Büchler, and T. Pfau, "An experimental and theoretical guide to strongly interacting Rydberg gases", Journal of Physics B: Atomic, Molecular and Optical Physics **45**, 113001 (2012) (cited on pages 19, 27, 134).

[50] N. Šibalić and C. S. Adams, *Rydberg Physics* (IOP Publishing, 2018) (cited on pages 19, 27, 30, 31, 112, 134).

[51] K. Singer, J. Stanojevic, M. Weidemüller, and R. Côté, "Long-range interactions between alkali Rydberg atom pairs correlated to the $ns-ns$, $np-np$ and $nd-nd$ asymptotes", Journal of Physics B: Atomic, Molecular and Optical Physics **38**, S295 (2005) (cited on pages 20, 43, 45, 134).

[52] A. Reinhard, T. C. Liebisch, B. Knuffman, and G. Raithel, "Level shifts of rubidium Rydberg states due to binary interactions", Physical Review A **75**, 032712 (2007) (cited on pages 20, 43, 66, 74, 134, 136).

[53] T. G. Walker and M. Saffman, "Consequences of Zeeman degeneracy for the van der Waals blockade between Rydberg atoms", Physical Review A **77**, 032723 (2008) (cited on pages 20, 43, 66, 68, 74, 134, 136).

[54] D. Comparat and P. Pillet, "Dipole blockade in a cold Rydberg atomic sample", Journal of the Optical Society of America B **27**, A208 (2010) (cited on pages 20, 43, 134).

[55] M. R. Flannery, D. Vrinceanu, and V. N. Ostrovsky, "Long-range interaction between polar Rydberg atoms", Journal of Physics B: Atomic, Molecular and Optical Physics **38**, S279 (2005) (cited on pages 20, 43, 45, 134).

[56] N. Šibalić, J. D. Pritchard, C. S. Adams, and K. J. Weatherill, "ARC: An open-source library for calculating properties of alkali Rydberg atoms", Computer Physics Communications **220**, 319 (2017) (cited on pages 20, 28, 32, 41, 68, 134, 136).

[57] T. L. Nguyen, J. M. Raimond, C. Sayrin, R. Cortiñas, T. Cantat-Moltrecht, F. Assemat, I. Dotsenko, S. Gleyzes, S. Haroche, G. Roux, T. Jolicoeur, and M. Brune, "Towards Quantum Simulation with Circular Rydberg Atoms", Physical Review X **8**, 011032 (2018) (cited on pages 20, 29, 35, 134).

[58] S. R. Cohen and J. D. Thompson, "Quantum Computing with Circular Rydberg Atoms", PRX Quantum **2**, 030322 (2021) (cited on pages 20, 134).

[59] R. Mukherjee, J. Millen, R. Nath, M. P. A. Jones, and T. Pohl, "Many-body physics with alkaline-earth Rydberg lattices", Journal of Physics B: Atomic, Molecular and Optical Physics **44**, 184010 (2011) (cited on pages 20, 31, 134).

[60] H. Labuhn, D. Barredo, S. Ravets, S. de Léséleuc, T. Macrì, T. Lahaye, and A. Browaeys, "Tunable two-dimensional arrays of single Rydberg atoms for realizing quantum Ising models", Nature **534**, 667 (2016) (cited on pages 20, 34, 36, 42, 65, 66, 67, 68, 70, 72, 94, 112, 135).

[61] H. Bernien, S. Schwartz, A. Keesling, H. Levine, A. Omran, H. Pichler, S. Choi, A. S. Zibrov, M. Endres, M. Greiner, V. Vuletić, and M. D. Lukin, "Probing many-body dynamics on a 51-atom quantum simulator", Nature **551**, 579 (2017) (cited on pages 20, 34, 65, 66, 67, 94, 112, 122, 135).

[62] H. Kim, Y. Park, K. Kim, H.-S. Sim, and J. Ahn, "Detailed Balance of Thermalization Dynamics in Rydberg-Atom Quantum Simulators", Physical Review Letters **120**, 180502 (2018) (cited on pages 20, 94, 112, 135).

[63] D. Barredo, H. Labuhn, S. Ravets, T. Lahaye, A. Browaeys, and C. S. Adams, "Coherent Excitation Transfer in a Spin Chain of Three Rydberg Atoms", Physical Review Letters **114**, 113002 (2015) (cited on pages 20, 35, 42, 94, 99, 112, 135).

[64] S. Weber, S. d. Léséleuc, V. Lienhard, D. Barredo, T. Lahaye, A. Browaeys, and H. P. Büchler, "Topologically protected edge states in small Rydberg systems", Quantum Science and Technology **3**, 044001 (2018) (cited on pages 20, 21, 39, 94, 108, 111, 112, 113, 135).

[65] G. Jotzu, M. Messer, R. Desbuquois, M. Lebrat, T. Uehlinger, D. Greif, and T. Esslinger, "Experimental realization of the topological Haldane model with ultracold fermions", Nature **515**, 237 (2014) (cited on pages 21, 39, 76, 94, 112, 137).

[66] N. Flaschner, B. S. Rem, M. Tarnowski, D. Vogel, D.-S. Luhmann, K. Sengstock, and C. Weitenberg, "Experimental reconstruction of the Berry curvature in a Floquet Bloch band", Science **352**, 1091 (2016) (cited on pages 21, 76, 137).

[67] M. Aidelsburger, M. Lohse, C. Schweizer, M. Atala, J. T. Barreiro, S. Nascimbène, N. R. Cooper, I. Bloch, and N. Goldman, "Measuring the Chern number of Hofstadter bands with ultracold bosonic atoms", Nature Physics **11**, 162 (2014) (cited on pages 21, 76, 137).

[68] B. K. Stuhl, H.-I. Lu, L. M. Aycock, D. Genkina, and I. B. Spielman, "Visualizing edge states with an atomic Bose gas in the quantum Hall regime", Science **349**, 1514 (2015) (cited on pages 21, 39, 76, 94, 112, 137).

[69] M. Mancini, G. Pagano, G. Cappellini, L. Livi, M. Rider, J. Catani, C. Sias, P. Zoller, M. Inguscio, M. Dalmonte, and L. Fallani, "Observation of chiral edge states with neutral fermions in synthetic Hall ribbons", Science **349**, 1510 (2015) (cited on pages 21, 39, 76, 94, 112, 137).

[70] M. Lohse, C. Schweizer, O. Zilberberg, M. Aidelsburger, and I. Bloch, "A Thouless quantum pump with ultracold bosonic atoms in an optical superlattice", Nature Physics **12**, 350 (2015) (cited on pages 21, 76, 137).

[71] M. E. Tai, A. Lukin, M. Rispoli, R. Schittko, T. Menke, D. Borgnia, P. M. Preiss, F. Grusdt, A. M. Kaufman, and M. Greiner, "Microscopy of the interacting Harper–Hofstadter model in the two-body limit", Nature **546**, 519 (2017) (cited on pages 21, 76, 77, 137).

[72] R. Süsstrunk and S. D. Huber, "Observation of phononic helical edge states in a mechanical topological insulator", Science **349**, 47 (2015) (cited on pages 21, 76, 137).

[73] L. M. Nash, D. Kleckner, A. Read, V. Vitelli, A. M. Turner, and W. T. M. Irvine, "Topological mechanics of gyroscopic metamaterials", Proceedings of the National Academy of Sciences of the United States of America **112**, 14495 (2015) (cited on pages 21, 76, 137).

[74] M. Hafezi, S. Mittal, J. Fan, A. Migdall, and J. M. Taylor, "Imaging topological edge states in silicon photonics", Nature Photonics **7**, 1001 (2013) (cited on pages 21, 76, 137).

[75] M. C. Rechtsman, J. M. Zeuner, Y. Plotnik, Y. Lumer, D. Podolsky, F. Dreisow, S. Nolte, M. Segev, and A. Szameit, "Photonic Floquet topological insulators", Nature **496**, 196 (2013) (cited on pages 21, 76, 137).

[76] C. W. Ling, M. Xiao, C. T. Chan, S. F. Yu, and K. H. Fung, "Topological edge plasmon modes between diatomic chains of plasmonic nanoparticles", Optics Express **23**, 2021 (2015) (cited on pages 21, 76, 137).

[77] L. Lu, J. D. Joannopoulos, and M. Soljačić, "Topological states in photonic systems", Nature Physics **12**, 626 (2016) (cited on pages 21, 76, 137).

[78] J. Ningyuan, C. Owens, A. Sommer, D. Schuster, and J. Simon, "Time- and Site-Resolved Dynamics in a Topological Circuit", Physical Review X **5**, 021031 (2015) (cited on pages 21, 76, 137).

[79] P. St-Jean, V. Goblot, E. Galopin, A. Lemaître, T. Ozawa, L. Le Gratiet, I. Sagnes, J. Bloch, and A. Amo, "Lasing in topological edge states of a one-dimensional lattice", Nature Photonics **11**, 651 (2017) (cited on pages 21, 76, 79, 137).

[80] M. A. Bandres, S. Wittek, G. Harari, M. Parto, J. Ren, M. Segev, D. N. Christodoulides, and M. Khajavikhan, "Topological insulator laser: Experiments", Science **359**, eaar4005 (2018) (cited on pages 21, 76, 137).

[81] H. Kong, J. Taylor, Y. Dong, and K. Choi, "Melting a Rydberg ice to a topological spin liquid with cavity vacuum fluctuation", arXiv:2109.03741 (2021) (cited on pages 21, 39, 112, 137).

[82] J. Dalibard, F. Gerbier, G. Juzeliūnas, and P. Öhberg, "Colloquium: Artificial gauge potentials for neutral atoms", Reviews of Modern Physics **83**, 1523 (2011) (cited on pages 21, 39, 94, 112).

[83] V. Galitski and I. B. Spielman, "Spin–orbit coupling in quantum gases", Nature **494**, 49 (2013) (cited on pages 21, 39, 94, 112).

[84] H. Zhai, "Degenerate quantum gases with spin–orbit coupling: a review", Reports on Progress in Physics **78**, 026001 (2015) (cited on pages 21, 39, 94, 112).

[85] M. Aidelsburger, S. Nascimbene, and N. Goldman, "Artificial gauge fields in materials and engineered systems", Comptes Rendus Physique **19**, 394 (2018) (cited on pages 21, 39, 94, 112).

[86] N. R. Cooper, J. Dalibard, and I. B. Spielman, "Topological bands for ultracold atoms", Reviews of Modern Physics **91**, 015005 (2019) (cited on pages 21, 39, 94, 112).

[87] M. Aidelsburger, M. Atala, S. Nascimbène, S. Trotzky, Y.-A. Chen, and I. Bloch, "Experimental Realization of Strong Effective Magnetic Fields in an Optical Lattice", Physical Review Letters **107**, 255301 (2011) (cited on pages 21, 39, 94, 112).

[88] A. R. Kolovsky, "Creating artificial magnetic fields for cold atoms by photon-assisted tunneling", EPL **93**, 20003 (2011) (cited on pages 21, 39, 94, 112).

[89] J. Struck, C. Ölschläger, M. Weinberg, P. Hauke, J. Simonet, A. Eckardt, M. Lewenstein, K. Sengstock, and P. Windpassinger, "Tunable Gauge Potential for Neutral and Spinless Particles in Driven Optical Lattices", Physical Review Letters **108**, 225304 (2012) (cited on pages 21, 39, 94, 112).

[90] T. Chalopin, T. Satoor, A. Evrard, V. Makhalov, J. Dalibard, R. Lopes, and S. Nascimbene, "Probing chiral edge dynamics and bulk topology of a synthetic Hall system", Nature Physics **16**, 1017 (2020) (cited on pages 21, 39, 94, 112).

[91] P. Roushan, C. Neill, A. Megrant, Y. Chen, R. Babbush, R. Barends, B. Campbell, Z. Chen, B. Chiaro, A. Dunsworth, A. Fowler, E. Jeffrey, J. Kelly, E. Lucero, J. Mutus, P. J. J. O'Malley, M. Neeley, C. Quintana, D. Sank, A. Vainsencher, J. Wenner, T. White, E. Kapit, H. Neven, and J. Martinis, "Chiral ground-state currents of interacting photons in a synthetic magnetic field", Nature Physics **13**, 146 (2016) (cited on pages 21, 94, 98, 105).

[92] T. Ozawa, H. M. Price, A. Amo, N. Goldman, M. Hafezi, L. Lu, M. C. Rechtsman, D. Schuster, J. Simon, O. Zilberberg, and I. Carusotto, "Topological photonics", Reviews of Modern Physics **91**, 015006 (2019) (cited on pages 21, 94).

[93] Y. Liu, X. Chen, and Y. Xu, "Topological Phononics: From Fundamental Models to Real Materials", Advanced Functional Materials **30**, 1904784 (2019) (cited on pages 21, 94).

[94] D. Peter, N. Y. Yao, N. Lang, S. D. Huber, M. D. Lukin, and H. P. Büchler, "Topological bands with a Chern number $C = 2$ by dipolar exchange interactions", Physical Review A **91**, 053617 (2015) (cited on pages 21, 94, 108, 113, 115).

[95] J. A. Sokolowski and C. M. Banks, *Principles of Modeling and Simulation* (John Wiley & Sons, Inc., 2009) (cited on page 24).

[96] T. Felser, S. Notarnicola, and S. Montangero, "Efficient Tensor Network Ansatz for High-Dimensional Quantum Many-Body Problems", Physical Review Letters **126**, 170603 (2021) (cited on page 24).

[97] Y. Zhou, E. M. Stoudenmire, and X. Waintal, "What Limits the Simulation of Quantum Computers?", Physical Review X **10**, 041038 (2020) (cited on page 24).

[98] A. Das and B. K. Chakrabarti, "Colloquium: Quantum annealing and analog quantum computation", Reviews of Modern Physics **80**, 1061 (2008) (cited on page 24).

[99] M. R. Garey and D. S. Johnson, *Computers and Intractability: A Guide to the Theory of NP-Completeness* (W.H. Freeman & Co, 1979) (cited on page 25).

[100] C. R. Laumann, R. Moessner, A. Scardicchio, and S. L. Sondhi, "Quantum annealing: The fastest route to quantum computation?", European Physical Journal Special Topics **224**, 75 (2015) (cited on page 25).

[101] E. Farhi, J. Goldstone, and S. Gutmann, "A quantum approximate optimization algorithm", arXiv:1411.4028 (2014) (cited on page 25).

[102] V. Giovannetti, S. Lloyd, and L. Maccone, "Advances in quantum metrology", Nature Photonics **5**, 222 (2011) (cited on page 25).

[103] P. Hauke, F. M. Cucchietti, L. Tagliacozzo, I. Deutsch, and M. Lewenstein, "Can one trust quantum simulators?", Reports on Progress in Physics **75**, 082401 (2012) (cited on page 25).

[104] E. Derbyshire, J. Y. Malo, A. J. Daley, E. Kashefi, and P. Wallden, "Randomized benchmarking in the analogue setting", Quantum Science and Technology **5**, 034001 (2020) (cited on page 26).

[105] D. Aharonov, W. van Dam, J. Kempe, Z. Landau, S. Lloyd, and O. Regev, "Adiabatic Quantum Computation Is Equivalent to Standard Quantum Computation", SIAM Review **50**, 755 (2008) (cited on page 26).

[106] D. P. DiVincenzo, "The Physical Implementation of Quantum Computation", Fortschritte der Physik **48**, 771 (2000) (cited on page 26).

[107] E. Crane, A. Schuckert, N. H. Le, and A. J. Fisher, "Rydberg entangling gates in silicon", Physical Review Research **3**, 033086 (2021) (cited on page 27).

[108] C. Zhang, F. Pokorny, W. Li, G. Higgins, A. Pöschl, I. Lesanovsky, and M. Hennrich, "Submicrosecond entangling gate between trapped ions via Rydberg interaction", Nature **580**, 345 (2020) (cited on page 27).

[109] C. L. Vaillant, M. P. A. Jones, and R. M. Potvliege, "Long-range Rydberg–Rydberg interactions in calcium, strontium and ytterbium", Journal of Physics B: Atomic, Molecular and Optical Physics **45**, 135004 (2012) (cited on pages 28, 54).

[110] C. L. Vaillant, M. P. A. Jones, and R. M. Potvliege, "Multichannel quantum defect theory of strontium bound Rydberg states", Journal of Physics B: Atomic, Molecular and Optical Physics **47**, 155001 (2014) (cited on pages 28, 54).

[111] A. Osterwalder and F. Merkt, "Using High Rydberg States as Electric Field Sensors", Physical Review Letters **82**, 1831 (1999) (cited on page 29).

[112] R. P. Abel, C. Carr, U. Krohn, and C. S. Adams, "Electrometry near a dielectric surface using Rydberg electromagnetically induced transparency", Physical Review A **84**, 023408 (2011) (cited on page 29).

[113] W. D. Phillips, "Nobel Lecture: Laser cooling and trapping of neutral atoms", Reviews of Modern Physics **70**, 721 (1998) (cited on page 30).

[114] N. Schlosser, G. Reymond, I. Protsenko, and P. Grangier, "Sub-poissonian loading of single atoms in a microscopic dipole trap", Nature **411**, 1024 (2001) (cited on page 30).

[115] F. Nogrette, H. Labuhn, S. Ravets, D. Barredo, L. Béguin, A. Vernier, T. Lahaye, and A. Browaeys, "Single-Atom Trapping in Holographic 2D Arrays of Microtraps with Arbitrary Geometries", Physical Review X **4**, 021034 (2014) (cited on page 30).

[116] S. Bergamini, B. Darquié, M. Jones, L. Jacubowiez, A. Browaeys, and P. Grangier, "Holographic generation of microtrap arrays for single atoms by use of a programmable phase modulator", Journal of the Optical Society of America B **21**, 1889 (2004) (cited on page 30).

[117] Y. Yu, N. R. Hutzler, J. T. Zhang, L. R. Liu, J. D. Hood, T. Rosenband, and K.-K. Ni, "Motional-ground-state cooling outside the Lamb-Dicke regime", Physical Review A **97**, 063423 (2018) (cited on page 31).

[118] T. A. Johnson, E. Urban, T. Henage, L. Isenhower, D. D. Yavuz, T. G. Walker, and M. Saffman, "Rabi Oscillations between Ground and Rydberg States with Dipole-Dipole Atomic Interactions", Physical Review Letters **100**, 113003 (2008) (cited on page 31).

[119] Y. Miroshnychenko, A. Gaëtan, C. Evellin, P. Grangier, D. Comparat, P. Pillet, T. Wilk, and A. Browaeys, "Coherent excitation of a single atom to a Rydberg state", Physical Review A **82**, 013405 (2010) (cited on page 31).

[120] D. Barredo, V. Lienhard, P. Scholl, S. de Léséleuc, T. Boulier, A. Browaeys, and T. Lahaye, "Three-Dimensional Trapping of Individual Rydberg Atoms in Ponderomotive Bottle Beam Traps", Physical Review Letters **124**, 023201 (2020) (cited on page 31).

[121] S. Zhang, F. Robicheaux, and M. Saffman, "Magic-wavelength optical traps for Rydberg atoms", Physical Review A **84**, 043408 (2011) (cited on page 31).

[122] R. J. Le Roy, "Long-Range Potential Coefficients From RKR Turning Points: C_6 and C_8 for $B(3\Pi^+_{Ou})$-State Cl_2, Br_2, and I_2", Canadian Journal of Physics **52**, 246 (1974) (cited on pages 32, 46).

[123] H. B. G. Casimir and D. Polder, "The Influence of Retardation on the London-van der Waals Forces", Physical Review **73**, 360 (1948) (cited on pages 32, 46).

[124] A. Browaeys, D. Barredo, and T. Lahaye, "Experimental investigations of dipole–dipole interactions between a few Rydberg atoms", Journal of Physics B: Atomic, Molecular and Optical Physics **49**, 152001 (2016) (cited on pages 32, 77, 80, 94).

[125] D. Peter, *Quantum states with topological properties via dipolar interactions* (PhD Thesis. Universität Stuttgart, Verlag Dr. Hut, 2015) (cited on page 32).

[126] M. D. Lukin, M. Fleischhauer, R. Cote, L. M. Duan, D. Jaksch, J. I. Cirac, and P. Zoller, "Dipole Blockade and Quantum Information Processing in Mesoscopic Atomic Ensembles", Physical Review Letters **87**, 037901 (2001) (cited on pages 32, 42, 122, 125).

[127] D. Jaksch, J. I. Cirac, P. Zoller, S. L. Rolston, R. Côté, and M. D. Lukin, "Fast Quantum Gates for Neutral Atoms", Physical Review Letters **85**, 2208 (2000) (cited on pages 32, 42, 122, 125).

[128] M. Saffman, T. G. Walker, and K. Mølmer, "Quantum information with Rydberg atoms", Reviews of Modern Physics **82**, 2313 (2010) (cited on pages 32, 42, 80, 94, 122, 125).

[129] T. Keating, K. Goyal, Y.-Y. Jau, G. W. Biedermann, A. J. Landahl, and I. H. Deutsch, "Adiabatic quantum computation with Rydberg-dressed atoms", Physical Review A **87**, 052314 (2013) (cited on page 32).

[130] Y. O. Dudin and A. Kuzmich, "Strongly Interacting Rydberg Excitations of a Cold Atomic Gas", Science **336**, 887 (2012) (cited on pages 32, 42).

[131] N. Stiesdal, H. Busche, K. Kleinbeck, J. Kumlin, M. G. Hansen, H. P. Büchler, and S. Hofferberth, "Controlled multi-photon subtraction with cascaded Rydberg superatoms as single-photon absorbers", Nature Communications **12**, 4328 (2021) (cited on page 32).

[132] A. Gaëtan, Y. Miroshnychenko, T. Wilk, A. Chotia, M. Viteau, D. Comparat, P. Pillet, A. Browaeys, and P. Grangier, "Observation of collective excitation of two individual atoms in the Rydberg blockade regime", Nature Physics **5**, 115 (2009) (cited on pages 33, 42, 66, 70).

[133] E. Urban, T. A. Johnson, T. Henage, L. Isenhower, D. D. Yavuz, T. G. Walker, and M. Saffman, "Observation of Rydberg blockade between two atoms", Nature Physics **5**, 110 (2009) (cited on pages 33, 42, 66, 70).

[134] T. Wilk, A. Gaëtan, C. Evellin, J. Wolters, Y. Miroshnychenko, P. Grangier, and A. Browaeys, "Entanglement of Two Individual Neutral Atoms Using Rydberg Blockade", Physical Review Letters **104**, 010502 (2010) (cited on pages 33, 42).

[135] L. Isenhower, E. Urban, X. Zhang, A. Gill, T. Henage, T. A. Johnson, T. Walker, and M. Saffman, "Demonstration of a neutral atom controlled-NOT quantum gate", Physical Review Letters **104**, 010503 (2010) (cited on pages 33, 125).

[136] A. Keesling, A. Omran, H. Levine, H. Bernien, H. Pichler, S. Choi, R. Samajdar, S. Schwartz, P. Silvi, S. Sachdev, P. Zoller, M. Endres, M. Greiner, V. Vuletić, and M. D. Lukin, "Quantum Kibble–Zurek mechanism and critical dynamics on a programmable Rydberg simulator", Nature **568**, 207 (2019) (cited on page 34).

[137] P. Schauß, J. Zeiher, T. Fukuhara, S. Hild, M. Cheneau, T. Macrì, T. Pohl, I. Bloch, and C. Gross, "Crystallization in Ising quantum magnets", Science **347**, 1455 (2015) (cited on pages 34, 42, 65, 67).

[138] V. Lienhard, S. de Léséleuc, D. Barredo, T. Lahaye, A. Browaeys, M. Schuler, L.-P. Henry, and A. M. Läuchli, "Observing the Space- and Time-Dependent Growth of Correlations in Dynamically Tuned Synthetic Ising Models with Antiferromagnetic Interactions", Physical Review X **8**, 021070 (2018) (cited on page 34).

[139] E. Guardado-Sanchez, P. T. Brown, D. Mitra, T. Devakul, D. A. Huse, P. Schauß, and W. S. Bakr, "Probing the Quench Dynamics of Antiferromagnetic Correlations in a 2D Quantum Ising Spin System", Physical Review X **8**, 021069 (2018) (cited on page 34).

[140] C. Gaul, B. J. DeSalvo, J. A. Aman, F. B. Dunning, T. C. Killian, and T. Pohl, "Resonant Rydberg Dressing of Alkaline-Earth Atoms via Electromagnetically Induced Transparency", Physical Review Letters **116**, 243001 (2016) (cited on pages 34, 43).

[141] J. Zeiher, R. van Bijnen, P. Schauß, S. Hild, J.-y. Choi, T. Pohl, I. Bloch, and C. Gross, "Many-body interferometry of a Rydberg-dressed spin lattice", Nature Physics **12**, 1095 (2016) (cited on pages 34, 43, 66).

[142] Y.-Y. Jau, A. M. Hankin, T. Keating, I. H. Deutsch, and G. W. Biedermann, "Entangling atomic spins with a Rydberg-dressed spin-flip blockade", Nature Physics **12**, 71 (2015) (cited on pages 34, 43, 66, 74).

[143] P. Scholl, H. Williams, G. Bornet, F. Wallner, D. Barredo, T. Lahaye, A. Browaeys, L. Henriet, A. Signoles, C. Hainaut, et al., "Microwave-engineering of programmable XXZ Hamiltonians in arrays of Rydberg atoms", arXiv:2107.14459 (2021) (cited on page 35).

[144] X.-G. Wen, "Colloquium : Zoo of quantum-topological phases of matter", Reviews of Modern Physics **89**, 041004 (2017) (cited on pages 37, 40).

[145] L. D. Landau, "Zur Theorie der Phasenumwandlungen I", Physikalische Zeitschrift der Sowjetunion **11**, 26 (1937) (cited on page 37).

[146] L. D. Landau, "Zur Theorie der Phasenumwandlungen II", Physikalische Zeitschrift der Sowjetunion **11**, 545 (1937) (cited on page 37).

[147] S. Sachdev, *Quantum Phase Transitions* (Cambridge University Press, 2009) (cited on page 37).

[148] F. D. M. Haldane, "Topological Quantum Matter", International Journal of Modern Physics B **32**, 1830004 (2018) (cited on page 37).

[149] X. Chen, Z.-C. Gu, and X.-G. Wen, "Local unitary transformation, long-range quantum entanglement, wave function renormalization, and topological order", Physical Review B **82**, 155138 (2010) (cited on page 38).

[150] D. C. Tsui, H. L. Stormer, and A. C. Gossard, "Two-Dimensional Magnetotransport in the Extreme Quantum Limit", Physical Review Letters **48**, 1559 (1982) (cited on page 38).

[151] H. L. Stormer, D. C. Tsui, and A. C. Gossard, "The fractional quantum Hall effect", Reviews of Modern Physics **71**, S298 (1999) (cited on page 38).

[152] X. G. Wen and Q. Niu, "Ground-state degeneracy of the fractional quantum Hall states in the presence of a random potential and on high-genus Riemann surfaces", Physical Review B **41**, 9377 (1990) (cited on pages 38, 117).

[153] E. Dennis, A. Kitaev, A. Landahl, and J. Preskill, "Topological quantum memory", Journal of Mathematical Physics **43**, 4452 (2002) (cited on pages 38, 111).

[154] B. J. Brown, D. Loss, J. K. Pachos, C. N. Self, and J. R. Wootton, "Quantum memories at finite temperature", Reviews of Modern Physics **88**, 045005 (2016) (cited on pages 38, 111).

[155] C. Nayak, S. H. Simon, A. Stern, M. Freedman, and S. Das Sarma, "Non-Abelian anyons and topological quantum computation", Reviews of Modern Physics **80**, 1083 (2008) (cited on pages 38, 111).

[156] A. Y. Kitaev, "Fault-tolerant quantum computation by anyons", Annals of Physics **303**, 2 (2003) (cited on pages 38, 111).

[157] H. Simmons, *An Introduction to Category Theory* (Cambridge University Press, 2009) (cited on page 38).

[158] B. Coecke and E. O. Paquette, "Categories for the Practising Physicist", *New Structures for Physics* (Springer Berlin Heidelberg, 2010), pp. 173–286 (cited on pages 38, 111).

[159] R. Willett, J. P. Eisenstein, H. L. Störmer, D. C. Tsui, A. C. Gossard, and J. H. English, "Observation of an even-denominator quantum number in the fractional quantum Hall effect", Physical Review Letters **59**, 1776 (1987) (cited on pages 38, 111).

[160] W. Pan, J.-S. Xia, V. Shvarts, D. E. Adams, H. L. Stormer, D. C. Tsui, L. N. Pfeiffer, K. W. Baldwin, and K. W. West, "Exact Quantization of the Even-Denominator Fractional Quantum Hall State at $\nu = 5/2$ Landau Level Filling Factor", Physical Review Letters **83**, 3530 (1999) (cited on page 38).

[161] K. Pakrouski, M. R. Peterson, T. Jolicoeur, V. W. Scarola, C. Nayak, and M. Troyer, "Phase diagram of the $\nu = 5/2$ fractional quantum Hall effect: effects of Landau-level mixing and nonzero width", Physical Review X **5**, 021004 (2015) (cited on pages 38, 111).

[162] M. Gerster, M. Rizzi, P. Silvi, M. Dalmonte, and S. Montangero, "Fractional quantum Hall effect in the interacting Hofstadter model via tensor networks", Physical Review B **96**, 195123 (2017) (cited on pages 39, 111, 118).

[163] J. Block and S. Scheel, "van der Waals interaction potential between Rydberg atoms near surfaces", Physical Review A **96**, 062509 (2017) (cited on page 42).

[164] W. R. Anderson, J. R. Veale, and T. F. Gallagher, "Resonant Dipole-Dipole Energy Transfer in a Nearly Frozen Rydberg Gas", Physical Review Letters **80**, 249 (1998) (cited on page 42).

[165] I. Mourachko, D. Comparat, F. de Tomasi, A. Fioretti, P. Nosbaum, V. M. Akulin, and P. Pillet, "Many-Body Effects in a Frozen Rydberg Gas", Physical Review Letters **80**, 253 (1998) (cited on page 42).

[166] K. Singer, M. Reetz-Lamour, T. Amthor, L. G. Marcassa, and M. Weidemüller, "Suppression of Excitation and Spectral Broadening Induced by Interactions in a Cold Gas of Rydberg Atoms", Physical Review Letters **93**, 163001 (2004) (cited on page 42).

[167] D. Tong, S. M. Farooqi, J. Stanojevic, S. Krishnan, Y. P. Zhang, R. Côté, E. E. Eyler, and P. L. Gould, "Local Blockade of Rydberg Excitation in an Ultracold Gas", Physical Review Letters **93**, 063001 (2004) (cited on pages 42, 66).

[168] T. C. Liebisch, A. Reinhard, P. R. Berman, and G. Raithel, "Atom Counting Statistics in Ensembles of Interacting Rydberg Atoms", Physical Review Letters **95**, 253002 (2005) (cited on page 42).

[169] T. Vogt, M. Viteau, J. Zhao, A. Chotia, D. Comparat, and P. Pillet, "Dipole Blockade at Förster Resonances in High Resolution Laser Excitation of Rydberg States of Cesium Atoms", Physical Review Letters **97**, 083003 (2006) (cited on pages 42, 44).

[170] R. Heidemann, U. Raitzsch, V. Bendkowsky, B. Butscher, R. Löw, L. Santos, and T. Pfau, "Evidence for Coherent Collective Rydberg Excitation in the Strong Blockade Regime", Physical Review Letters **99**, 163601 (2007) (cited on pages 42, 122, 125).

[171] C. S. E. van Ditzhuijzen, A. F. Koenderink, J. V. Hernández, F. Robicheaux, L. D. Noordam, and H. B. van Linden van den Heuvell, "Spatially Resolved Observation of Dipole-Dipole Interaction between Rydberg Atoms", Physical Review Letters **100**, 243201 (2008) (cited on page 42).

[172] A. Reinhard, K. C. Younge, T. C. Liebisch, B. Knuffman, P. R. Berman, and G. Raithel, "Double-Resonance Spectroscopy of Interacting Rydberg-Atom Systems", Physical Review Letters **100**, 233201 (2008) (cited on pages 42, 44).

[173] R. Heidemann, U. Raitzsch, V. Bendkowsky, B. Butscher, R. Löw, and T. Pfau, "Rydberg Excitation of Bose-Einstein Condensates", Physical Review Letters **100**, 033601 (2008) (cited on page 42).

[174] U. Raitzsch, V. Bendkowsky, R. Heidemann, B. Butscher, R. Löw, and T. Pfau, "Echo Experiments in a Strongly Interacting Rydberg Gas", Physical Review Letters **100**, 013002 (2008) (cited on page 42).

[175] M. Reetz-Lamour, T. Amthor, J. Deiglmayr, and M. Weidemüller, "Rabi Oscillations and Excitation Trapping in the Coherent Excitation of a Mesoscopic Frozen Rydberg Gas", Physical Review Letters **100**, 253001 (2008) (cited on page 42).

[176] I. I. Ryabtsev, D. B. Tretyakov, I. I. Beterov, and V. M. Entin, "Observation of the Stark-Tuned Förster Resonance between Two Rydberg Atoms", Physical Review Letters **104**, 073003 (2010) (cited on pages 42, 44).

[177] A. Schwarzkopf, R. E. Sapiro, and G. Raithel, "Imaging Spatial Correlations of Rydberg Excitations in Cold Atom Clouds", Physical Review Letters **107**, 103001 (2011) (cited on page 42).

[178] Y. O. Dudin, L. Li, F. Bariani, and A. Kuzmich, "Observation of coherent many-body Rabi oscillations", Nature Physics **8**, 790 (2012) (cited on page 42).

[179] M. Ebert, A. Gill, M. Gibbons, X. Zhang, M. Saffman, and T. G. Walker, "Atomic Fock State Preparation Using Rydberg Blockade", Physical Review Letters **112**, 043602 (2014) (cited on page 42).

[180] T. M. Weber, M. Höning, T. Niederprüm, T. Manthey, O. Thomas, V. Guarrera, M. Fleischhauer, G. Barontini, and H. Ott, "Mesoscopic Rydberg-blockaded ensembles in the superatom regime and beyond", Nature Physics **11**, 157 (2015) (cited on page 42).

[181] J. Zeiher, P. Schauß, S. Hild, T. Macrì, I. Bloch, and C. Gross, "Microscopic Characterization of Scalable Coherent Rydberg Superatoms", Physical Review X **5**, 031015 (2015) (cited on page 42).

[182] T. Baluktsian, B. Huber, R. Löw, and T. Pfau, "Evidence for Strong van der Waals Type Rydberg-Rydberg Interaction in a Thermal Vapor", Physical Review Letters **110**, 123001 (2013) (cited on page 42).

[183] C. Carr, R. Ritter, C. G. Wade, C. S. Adams, and K. J. Weatherill, "Nonequilibrium Phase Transition in a Dilute Rydberg Ensemble", Physical Review Letters **111**, 113901 (2013) (cited on page 42).

[184] A. Urvoy, F. Ripka, I. Lesanovsky, D. Booth, J. P. Shaffer, T. Pfau, and R. Löw, "Strongly Correlated Growth of Rydberg Aggregates in a Vapor Cell", Physical Review Letters **114**, 203002 (2015) (cited on pages 42, 43, 57, 58, 59).

[185] T. Xia, M. Lichtman, K. Maller, A. W. Carr, M. J. Piotrowicz, L. Isenhower, and M. Saffman, "Randomized Benchmarking of Single-Qubit Gates in a 2D Array of Neutral-Atom Qubits", Physical Review Letters **114**, 100503 (2015) (cited on page 42).

[186] B. J. Lester, N. Luick, A. M. Kaufman, C. M. Reynolds, and C. A. Regal, "Rapid Production of Uniformly Filled Arrays of Neutral Atoms", Physical Review Letters **115**, 073003 (2015) (cited on page 42).

[187] H. Kim, W. Lee, H.-g. Lee, H. Jo, Y. Song, and J. Ahn, "In situ single-atom array synthesis using dynamic holographic optical tweezers", Nature Communications **7**, 13317 (2016) (cited on pages 42, 80, 94, 122).

[188] D. Møller, L. B. Madsen, and K. Mølmer, "Quantum Gates and Multiparticle Entanglement by Rydberg Excitation Blockade and Adiabatic Passage", Physical Review Letters **100**, 170504 (2008) (cited on page 42).

[189] M. Müller, I. Lesanovsky, H. Weimer, H. P. Büchler, and P. Zoller, "Mesoscopic Rydberg Gate Based on Electromagnetically Induced Transparency", Physical Review Letters **102**, 170502 (2009) (cited on page 42).

[190] G. Gunter, H. Schempp, M. Robert-de-Saint-Vincent, V. Gavryusev, S. Helmrich, C. S. Hofmann, S. Whitlock, and M. Weidemuller, "Observing the Dynamics of Dipole-Mediated Energy Transport by Interaction-Enhanced Imaging", Science **342**, 954 (2013) (cited on pages 42, 43, 44).

[191] D. Barredo, S. Ravets, H. Labuhn, L. Béguin, A. Vernier, F. Nogrette, T. Lahaye, and A. Browaeys, "Demonstration of a Strong Rydberg Blockade in Three-Atom Systems with Anisotropic Interactions", Physical Review Letters **112**, 183002 (2014) (cited on pages 42, 69).

[192] W. Maineult, B. Pelle, R. Faoro, E. Arimondo, P. Pillet, and P. Cheinet, "Dipole–quadrupole Förster resonance in cesium Rydberg gas", Journal of Physics B: Atomic, Molecular and Optical Physics **49**, 214001 (2016) (cited on page 42).

[193] O. Firstenberg, C. S. Adams, and S. Hofferberth, "Nonlinear quantum optics mediated by Rydberg interactions", Journal of Physics B: Atomic, Molecular and Optical Physics **49**, 152003 (2016) (cited on page 42).

[194] I. Friedler, D. Petrosyan, M. Fleischhauer, and G. Kurizki, "Long-range interactions and entanglement of slow single-photon pulses", Physical Review A **72**, 043803 (2005) (cited on page 42).

[195] J. D. Pritchard, D. Maxwell, A. Gauguet, K. J. Weatherill, M. P. A. Jones, and C. S. Adams, "Cooperative Atom-Light Interaction in a Blockaded Rydberg Ensemble", Physical Review Letters **105**, 193603 (2010) (cited on page 42).

[196] A. V. Gorshkov, J. Otterbach, M. Fleischhauer, T. Pohl, and M. D. Lukin, "Photon-Photon Interactions via Rydberg Blockade", Physical Review Letters **107**, 133602 (2011) (cited on page 42).

[197] E. Shahmoon, G. Kurizki, M. Fleischhauer, and D. Petrosyan, "Strongly interacting photons in hollow-core waveguides", Physical Review A **83**, 033806 (2011) (cited on page 42).

[198] S. Sevinçli, N. Henkel, C. Ates, and T. Pohl, "Nonlocal Nonlinear Optics in Cold Rydberg Gases", Physical Review Letters **107**, 153001 (2011) (cited on page 42).

[199] T. Peyronel, O. Firstenberg, Q.-Y. Liang, S. Hofferberth, A. V. Gorshkov, T. Pohl, M. D. Lukin, and V. Vuletić, "Quantum nonlinear optics with single photons enabled by strongly interacting atoms", Nature **488**, 57 (2012) (cited on page 42).

[200] C. S. Hofmann, G. Günter, H. Schempp, M. Robert-de-Saint-Vincent, M. Gärttner, J. Evers, S. Whitlock, and M. Weidemüller, "Sub-Poissonian Statistics of Rydberg-Interacting Dark-State Polaritons", Physical Review Letters **110**, 203601 (2013) (cited on page 42).

[201] L. Li, Y. O. Dudin, and A. Kuzmich, "Entanglement between light and an optical atomic excitation", Nature **498**, 466 (2013) (cited on page 42).

[202] S. Baur, D. Tiarks, G. Rempe, and S. Dürr, "Single-Photon Switch Based on Rydberg Blockade", Physical Review Letters **112**, 073901 (2014) (cited on page 42).

[203] H. Gorniaczyk, C. Tresp, J. Schmidt, H. Fedder, and S. Hofferberth, "Single-Photon Transistor Mediated by Interstate Rydberg Interactions", Physical Review Letters **113**, 053601 (2014) (cited on pages 42, 43).

[204] D. Tiarks, S. Baur, K. Schneider, S. Dürr, and G. Rempe, "Single-Photon Transistor Using a Förster Resonance", Physical Review Letters **113**, 053602 (2014) (cited on pages 42, 43).

[205] H. Gorniaczyk, C. Tresp, P. Bienias, A. Paris-Mandoki, W. Li, I. Mirgorodskiy, H. P. Büchler, I. Lesanovsky, and S. Hofferberth, "Enhancement of Rydberg-mediated single-photon nonlinearities by electrically tuned Förster resonances", Nature Communications **7**, 12480 (2016) (cited on pages 42, 44).

[206] C. Tresp, C. Zimmer, I. Mirgorodskiy, H. Gorniaczyk, A. Paris-Mandoki, and S. Hofferberth, "Single-Photon Absorber Based on Strongly Interacting Rydberg Atoms", Physical Review Letters **117**, 223001 (2016) (cited on page 42).

[207] D. Tiarks, S. Schmidt, G. Rempe, and S. Dürr, "Optical π phase shift created with a single-photon pulse", Science Advances **2**, e1600036 (2016) (cited on page 42).

[208] O. Firstenberg, T. Peyronel, Q.-Y. Liang, A. V. Gorshkov, M. D. Lukin, and V. Vuletić, "Attractive photons in a quantum nonlinear medium", Nature **502**, 71 (2013) (cited on page 42).

[209] J. Otterbach, M. Moos, D. Muth, and M. Fleischhauer, "Wigner Crystallization of Single Photons in Cold Rydberg Ensembles", Physical Review Letters **111**, 113001 (2013) (cited on page 43).

[210] P. Bienias, S. Choi, O. Firstenberg, M. F. Maghrebi, M. Gullans, M. D. Lukin, A. V. Gorshkov, and H. P. Büchler, "Scattering resonances and bound states for strongly interacting Rydberg polaritons", Physical Review A **90**, 053804 (2014) (cited on page 43).

[211] B. Olmos, W. Li, S. Hofferberth, and I. Lesanovsky, "Amplifying single impurities immersed in a gas of ultracold atoms", Physical Review A **84**, 041607 (2011) (cited on page 43).

[212] G. Günter, M. Robert-de-Saint-Vincent, H. Schempp, C. S. Hofmann, S. Whitlock, and M. Weidemüller, "Interaction Enhanced Imaging of Individual Rydberg Atoms in Dense Gases", Physical Review Letters **108**, 013002 (2012) (cited on page 43).

[213] D. Maxwell, D. J. Szwer, D. Paredes-Barato, H. Busche, J. D. Pritchard, A. Gauguet, K. J. Weatherill, M. P. A. Jones, and C. S. Adams, "Storage and Control of Optical Photons Using Rydberg Polaritons", Physical Review Letters **110**, 103001 (2013) (cited on page 43).

[214] W. Li, D. Viscor, S. Hofferberth, and I. Lesanovsky, "Electromagnetically Induced Transparency in an Entangled Medium", Physical Review Letters **112**, 243601 (2014) (cited on page 43).

[215] Y.-M. Liu, X.-D. Tian, D. Yan, Y. Zhang, C.-L. Cui, and J.-H. Wu, "Nonlinear modifications of photon correlations via controlled single and double Rydberg blockade", Physical Review A **91**, 043802 (2015) (cited on page 43).

[216] G. Pupillo, A. Micheli, M. Boninsegni, I. Lesanovsky, and P. Zoller, "Strongly Correlated Gases of Rydberg-Dressed Atoms: Quantum and Classical Dynamics", Physical Review Letters **104**, 223002 (2010) (cited on page 43).

[217] N. Henkel, R. Nath, and T. Pohl, "Three-Dimensional Roton Excitations and Supersolid Formation in Rydberg-Excited Bose-Einstein Condensates", Physical Review Letters **104**, 195302 (2010) (cited on page 43).

[218] J. Honer, H. Weimer, T. Pfau, and H. P. Büchler, "Collective Many-Body Interaction in Rydberg Dressed Atoms", Physical Review Letters **105**, 160404 (2010) (cited on page 43).

[219] M. Mattioli, M. Dalmonte, W. Lechner, and G. Pupillo, "Cluster Luttinger Liquids of Rydberg-Dressed Atoms in Optical Lattices", Physical Review Letters **111**, 165302 (2013) (cited on page 43).

[220] J. B. Balewski, A. T. Krupp, A. Gaj, S. Hofferberth, R. Löw, and T. Pfau, "Rydberg dressing: understanding of collective many-body effects and implications for experiments", New Journal of Physics **16**, 063012 (2014) (cited on page 43).

[221] S. Weber*, P. Bienias*, and H. P. Büchler, "Topological bands in the continuum using Rydberg states", arXiv:2101.08363 (2021) (cited on page 43).

[222] A. W. Glaetzle, M. Dalmonte, R. Nath, I. Rousochatzakis, R. Moessner, and P. Zoller, "Quantum Spin-Ice and Dimer Models with Rydberg Atoms", Physical Review X **4**, 041037 (2014) (cited on pages 43, 66).

[223] A. W. Glaetzle, M. Dalmonte, R. Nath, C. Gross, I. Bloch, and P. Zoller, "Designing Frustrated Quantum Magnets with Laser-Dressed Rydberg Atoms", Physical Review Letters **114**, 173002 (2015) (cited on pages 43, 66).

[224] R. M. W. van Bijnen and T. Pohl, "Quantum Magnetism and Topological Ordering via Rydberg Dressing near Förster Resonances", Physical Review Letters **114**, 243002 (2015) (cited on page 43).

[225] C. Boisseau, I. Simbotin, and R. Côté, "Macrodimers: Ultralong Range Rydberg Molecules", Physical Review Letters **88**, 133004 (2002) (cited on page 43).

[226] S. M. Farooqi, D. Tong, S. Krishnan, J. Stanojevic, Y. P. Zhang, J. R. Ensher, A. S. Estrin, C. Boisseau, R. Côté, E. E. Eyler, and P. L. Gould, "Long-Range Molecular Resonances in a Cold Rydberg Gas", Physical Review Letters **91**, 183002 (2003) (cited on pages 43, 59).

[227] K. R. Overstreet, A. Schwettmann, J. Tallant, D. Booth, and J. P. Shaffer, "Observation of electric-field-induced Cs Rydberg atom macrodimers", Nature Physics **5**, 581 (2009) (cited on pages 43, 45, 59).

[228] H. Saßmannshausen and J. Deiglmayr, "Observation of Rydberg-Atom Macrodimers: Micrometer-Sized Diatomic Molecules", Physical Review Letters **117**, 083401 (2016) (cited on pages 43, 44, 59).

[229] A. Schwettmann, J. Crawford, K. R. Overstreet, and J. P. Shaffer, "Cold Cs Rydberg-gas interactions", Physical Review A **74**, 020701 (2006) (cited on pages 43, 44, 57, 59).

[230] J. Stanojevic, R. Côté, D. Tong, E. E. Eyler, and P. L. Gould, "Long-range potentials and $(n-1)d+ns$ molecular resonances in an ultracold Rydberg gas", Physical Review A **78**, 052709 (2008) (cited on pages 43, 59).

[231] J. Deiglmayr, "Long-range interactions between Rydberg atoms", Physica Scripta **91**, 104007 (2016) (cited on pages 43, 45, 51, 56, 57, 59).

[232] S. Hollerith, J. Zeiher, J. Rui, A. Rubio-Abadal, V. Walther, T. Pohl, D. M. Stamper-Kurn, I. Bloch, and C. Gross, "Quantum gas microscopy of Rydberg macrodimers", Science **364**, 664 (2019) (cited on page 43).

[233] H. Margenau, "Van der waals forces", Reviews of Modern Physics **11**, 1 (1939) (cited on page 43).

[234] M. E. Rose, "The Electrostatic Interaction of Two Arbitrary Charge Distributions", Journal of Mathematics and Physics **37**, 215 (1958) (cited on pages 43, 47).

[235] P. R. Fontana, "Theory of Long-Range Interatomic Forces. I. Dispersion Energies between Unexcited Atoms", Physical Review **123**, 1865 (1961) (cited on pages 43, 47).

[236] A. Dalgarno and W. D. Davidson, "The Calculation of Van Der Waals Interactions", Advances in Atomic and Molecular Physics **2**, 1 (1966) (cited on pages 43, 47).

[237] J. Deiglmayr, H. Saßmannshausen, P. Pillet, and F. Merkt, "Observation of Dipole-Quadrupole Interaction in an Ultracold Gas of Rydberg Atoms", Physical Review Letters **113**, 193001 (2014) (cited on pages 43, 44, 57).

[238] J. B. Balewski, A. T. Krupp, A. Gaj, D. Peter, H. P. Büchler, R. Löw, S. Hofferberth, and T. Pfau, "Coupling a single electron to a Bose–Einstein condensate", Nature **502**, 664 (2013) (cited on page 43).

[239] X. Zhang, F. B. Dunning, S. Yoshida, and J. Burgdörfer, "Rydberg blockade effects at $n \sim 300$ in strontium", Physical Review A **92**, 051402 (2015) (cited on page 43).

[240] C. Tresp, P. Bienias, S. Weber, H. Gorniaczyk, I. Mirgorodskiy, H. P. Büchler, and S. Hofferberth, "Dipolar Dephasing of Rydberg D-State Polaritons", Physical Review Letters **115**, 083602 (2015) (cited on pages 43, 44, 74).

[241] A. Derevianko, P. Kómár, T. Topcu, R. M. Kroeze, and M. D. Lukin, "Effects of molecular resonances on Rydberg blockade", Physical Review A **92**, 063419 (2015) (cited on pages 44, 66, 74, 136).

[242] A. Fioretti, D. Comparat, C. Drag, T. F. Gallagher, and P. Pillet, "Long-Range Forces between Cold Atoms", Physical Review Letters **82**, 1839 (1999) (cited on page 44).

[243] T. G. Walker and M. Saffman, "Zeros of Rydberg–Rydberg Föster interactions", Journal of Physics B: Atomic, Molecular and Optical Physics **38**, S309 (2005) (cited on pages 44, 66, 68, 74, 136).

[244] K. A. Safinya, J. F. Delpech, F. Gounand, W. Sandner, and T. F. Gallagher, "Resonant Rydberg-Atom-Rydberg-Atom Collisions", Physical Review Letters **47**, 405 (1981) (cited on page 44).

[245] A. Reinhard, K. C. Younge, and G. Raithel, "Effect of Förster resonances on the excitation statistics of many-body Rydberg systems", Physical Review A **78**, 060702 (2008) (cited on page 44).

[246] J. Nipper, J. B. Balewski, A. T. Krupp, S. Hofferberth, R. Löw, and T. Pfau, "Atomic Pair-State Interferometer: Controlling and Measuring an Interaction-Induced Phase Shift in Rydberg-Atom Pairs", Physical Review X **2**, 031011 (2012) (cited on page 44).

[247] J. Nipper, J. B. Balewski, A. T. Krupp, B. Butscher, R. Löw, and T. Pfau, "Highly Resolved Measurements of Stark-Tuned Förster Resonances between Rydberg Atoms", Physical Review Letters **108**, 113001 (2012) (cited on page 44).

[248] J. M. Kondo, D. Booth, L. F. Gonçalves, J. P. Shaffer, and L. G. Marcassa, "Role of multilevel Rydberg interactions in electric-field-tuned Förster resonances", Physical Review A **93**, 012703 (2016) (cited on page 44).

[249] K. Afrousheh, P. Bohlouli-Zanjani, D. Vagale, A. Mugford, M. Fedorov, and J. D. D. Martin, "Spectroscopic Observation of Resonant Electric Dipole-Dipole Interactions between Cold Rydberg Atoms", Physical Review Letters **93**, 233001 (2004) (cited on page 44).

[250] P. Bohlouli-Zanjani, J. A. Petrus, and J. D. D. Martin, "Enhancement of Rydberg Atom Interactions Using ac Stark Shifts", Physical Review Letters **98**, 203005 (2007) (cited on page 44).

[251] D. B. Tretyakov, V. M. Entin, E. A. Yakshina, I. I. Beterov, C. Andreeva, and I. I. Ryabtsev, "Controlling the interactions of a few cold Rb Rydberg atoms by radio-frequency-assisted Förster resonances", Physical Review A **90**, 041403 (2014) (cited on page 44).

[252] S. Ravets, H. Labuhn, D. Barredo, T. Lahaye, and A. Browaeys, "Measurement of the angular dependence of the dipole-dipole interaction between two individual Rydberg atoms at a Förster resonance", Physical Review A **92**, 020701 (2015) (cited on pages 44, 60, 61, 62).

[253] A. Paris-Mandoki, H. Gorniaczyk, C. Tresp, I. Mirgorodskiy, and S. Hofferberth, "Tailoring Rydberg interactions via Förster resonances: state combinations, hopping and angular dependence", Journal of Physics B: Atomic, Molecular and Optical Physics **49**, 164001 (2016) (cited on page 44).

[254] M. Born and R. Oppenheimer, "Zur Quantentheorie der Molekeln", Annalen der Physik **389**, 457 (1927) (cited on page 45).

[255] H. A. Bethe and E. E. Salpeter, *Quantum Mechanics of One- and Two-Electron Atoms* (Springer, 1977) (cited on page 46).

[256] H. Saßmannshausen, F. Merkt, and J. Deiglmayr, "High-resolution spectroscopy of Rydberg states in an ultracold cesium gas", Physical Review A **87**, 032519 (2013) (cited on pages 45, 142).

[257] W. Li, I. Mourachko, M. W. Noel, and T. F. Gallagher, "Millimeter-wave spectroscopy of cold Rb Rydberg atoms in a magneto-optical trap: Quantum defects of the *ns*, *np*, and *nd* series", Physical Review A **67**, 052502 (2003) (cited on pages 45, 142).

[258] A. Tauschinsky, R. Newell, H. B. van Linden van den Heuvell, and R. J. C. Spreeuw, "Measurement of ^{87}Rb Rydberg-state hyperfine splitting in a room-temperature vapor cell", Physical Review A **87**, 042522 (2013) (cited on pages 45, 142).

[259] I. I. Beterov and M. Saffman, "Rydberg blockade, Förster resonances, and quantum state measurements with different atomic species", Physical Review A **92**, 042710 (2015) (cited on page 45).

[260] Y. Zeng, P. Xu, X. He, Y. Liu, M. Liu, J. Wang, D. J. Papoular, G. V. Shlyapnikov, and M. Zhan, "Entangling Two Individual Atoms of Different Isotopes via Rydberg Blockade", Physical Review Letters **119**, 160502 (2017) (cited on page 45).

[261] M. J. Seaton, "Quantum defect theory", Reports on Progress in Physics **46**, 167 (1983) (cited on pages 46, 143, 144).

[262] J. D. Jackson, *Classical Electrodynamics*, 3rd ed. (Wiley, 1998) (cited on page 47).

[263] L. C. Biedenharn, J. D. Louck, and P. A. Carruthers, *Angular Momentum in Quantum Physics: Theory and Application*, Encyclopedia of Mathematics and its Applications (Cambridge University Press, 1984) (cited on page 48).

[264] D. A. Steck, *Quantum and Atom Optics*, available online at `http://steck.us/teaching` (revision 0.10.6, 25 May 2016) (cited on page 48).

[265] P. W. Milonni, *The Quantum Vacuum: An Introduction to Quantum Electrodynamics* (Elsevier Science, 2013) (cited on page 48).

[266] G. Herzberg, *Spectra of diatomic molecules*, Molecular spectra and molecular structure (Van Nostrand, 1950) (cited on page 50).

[267] J. M. Brown and A. Carrington, *Rotational Spectroscopy of Diatomic Molecules* (Cambridge University Press, 2003) (cited on page 51).

[268] J. Stanojevic, R. Côté, D. Tong, S. M. Farooqi, E. E. Eyler, and P. L. Gould, "Long-range Rydberg-Rydberg interactions and molecular resonances", The European Physical Journal D: Atomic, Molecular, Optical and Plasma Physics **40**, 3 (2006) (cited on page 51).

[269] E. P. Wigner, *Group Theory and its Application to the Quantum Mechanics of Atomic Spectra* (Academic Press, 1959) (cited on pages 54, 147).

[270] D. A. Varshalovich, A. N. Moskalev, and V. K. Khersonskii, *Quantum Theory of Angular Momentum* (World Scientific, 1988) (cited on page 54).

[271] E. J. Robertson, N. Šibalić, R. M. Potvliege, and M. P. A. Jones, "ARC 3.0: An expanded Python toolbox for atomic physics calculations", Computer Physics Communications **261**, 107814 (2021) (cited on page 55).

[272] G. W. F. Drake and R. A. Swainson, "Quantum defects and the $1/n$ dependence of Rydberg energies: Second-order polarization effects", Physical Review A **44**, 5448 (1991) (cited on pages 55, 143).

[273] J. Hostetter, J. D. Pritchard, J. E. Lawler, and M. Saffman, "Measurement of holmium Rydberg series through magneto-optical trap depletion spectroscopy", Physical Review A **91**, 012507 (2015) (cited on page 55).

[274] P. Bientinesi, F. D. Igual, D. Kressner, and E. S. Quintana-Ortí, "Reduction to condensed forms for symmetric eigenvalue problems on multi-core architectures", International Conference on Parallel Processing and Applied Mathematics (Springer, 2009), pp. 387–395 (cited on page 55).

[275] J. W. Demmel, O. A. Marques, B. N. Parlett, and C. Vömel, "Performance and Accuracy of LAPACK's Symmetric Tridiagonal Eigensolvers", SIAM Journal on Scientific Computing **30**, 1508 (2008) (cited on page 55).

[276] C. Cohen and J. D. Tannoudji, *Roc and G. Grynberg: Atom–Photon Interactions; Basic Processes and Applications* (Wiley, New York, 1998) (cited on pages 63, 115, 151).

[277] J. R. Schrieffer and P. A. Wolff, "Relation between the Anderson and Kondo Hamiltonians", Physical Review **149**, 491 (1966) (cited on page 63).

[278] S. Bravyi, D. P. DiVincenzo, and D. Loss, "Schrieffer–Wolff transformation for quantum many-body systems", Annals of Physics **326**, 2793 (2011) (cited on page 63).

[279] P. Schauß, M. Cheneau, M. Endres, T. Fukuhara, S. Hild, A. Omran, T. Pohl, C. Gross, S. Kuhr, and I. Bloch, "Observation of spatially ordered structures in a two-dimensional Rydberg gas", Nature **491**, 87 (2012) (cited on pages 65, 67).

[280] A. M. Hankin, Y.-Y. Jau, L. P. Parazzoli, C. W. Chou, D. J. Armstrong, A. J. Landahl, and G. W. Biedermann, "Two-atom Rydberg blockade using direct $6S$ to nP excitation", Physical Review A **89**, 033416 (2014) (cited on page 66).

[281] J. Lee, M. J. Martin, Y.-Y. Jau, T. Keating, I. H. Deutsch, and G. W. Biedermann, "Demonstration of the Jaynes-Cummings ladder with Rydberg-dressed atoms", Physical Review A **95**, 041801 (2017) (cited on page 66).

[282] J. Zeiher, J.-y. Choi, A. Rubio-Abadal, T. Pohl, R. van Bijnen, I. Bloch, and C. Gross, "Coherent Many-Body Spin Dynamics in a Long-Range Interacting Ising Chain", Physical Review X **7**, 041063 (2017) (cited on page 66).

[283] T. Pohl and P. R. Berman, "Breaking the Dipole Blockade: Nearly Resonant Dipole Interactions in Few-Atom Systems", Physical Review Letters **102**, 013004 (2009) (cited on pages 66, 74, 136).

[284] B. Vermersch, A. W. Glaetzle, and P. Zoller, "Magic distances in the blockade mechanism of Rydbergpanddstates", Physical Review A **91**, 023411 (2015) (cited on pages 66, 68, 69, 72, 74, 136).

[285] S. Ravets, H. Labuhn, D. Barredo, L. Béguin, T. Lahaye, and A. Browaeys, "Coherent dipole–dipole coupling between two single Rydberg atoms at an electrically-tuned Förster resonance", Nature Physics **10**, 914 (2014) (cited on page 72).

[286] K. v. Klitzing, G. Dorda, and M. Pepper, "New Method for High-Accuracy Determination of the Fine-Structure Constant Based on Quantized Hall Resistance", Physical Review Letters **45**, 494 (1980) (cited on page 76).

[287] C. L. Kane and E. J. Mele, "Quantum Spin Hall Effect in Graphene", Physical Review Letters **95**, 226801 (2005) (cited on page 76).

[288] M. Z. Hasan and C. L. Kane, "Colloquium: Topological insulators", Reviews of Modern Physics **82**, 3045 (2010) (cited on page 76).

[289] X.-L. Qi and S.-C. Zhang, "Topological insulators and superconductors", Reviews of Modern Physics **83**, 1057 (2011) (cited on page 76).

[290] C.-K. Chiu, J. C. Y. Teo, A. P. Schnyder, and S. Ryu, "Classification of topological quantum matter with symmetries", Reviews of Modern Physics **88**, 035005 (2016) (cited on pages 76, 79).

[291] A. W. W. Ludwig, "Topological phases: classification of topological insulators and superconductors of non-interacting fermions, and beyond", Physica Scripta **2016**, 014001 (2015) (cited on pages 76, 79).

[292] X. Chen, Z.-C. Gu, Z.-X. Liu, and X.-G. Wen, "Symmetry-Protected Topological Orders in Interacting Bosonic Systems", Science **338**, 1604 (2012) (cited on pages 76, 79).

[293] F. D. M. Haldane, "Nonlinear Field Theory of Large-Spin Heisenberg Antiferromagnets: Semiclassically Quantized Solitons of the One-Dimensional Easy-Axis Néel State", Physical Review Letters **50**, 1153 (1983) (cited on page 76).

[294] M. Hagiwara, K. Katsumata, I. Affleck, B. I. Halperin, and J. P. Renard, "Observation of $S = 1/2$ degrees of freedom in an $S = 1$ linear-chain Heisenberg antiferromagnet", Physical Review Letters **65**, 3181 (1990) (cited on page 76).

[295] S. H. Glarum, S. Geschwind, K. M. Lee, M. L. Kaplan, and J. Michel, "Observation of fractional spin $S = 1/2$ on open ends of $S = 1$ linear antiferromagnetic chains: Nonmagnetic doping", Physical Review Letters **67**, 1614 (1991) (cited on page 76).

[296] M. Di Liberto, A. Recati, I. Carusotto, and C. Menotti, "Two-body physics in the Su-Schrieffer-Heeger model", Physical Review A **94**, 062704 (2016) (cited on page 77).

[297] W. P. Su, J. R. Schrieffer, and A. J. Heeger, "Solitons in Polyacetylene", Physical Review Letters **42**, 1698 (1979) (cited on page 77).

[298] M. Atala, M. Aidelsburger, J. T. Barreiro, D. Abanin, T. Kitagawa, E. Demler, and I. Bloch, "Direct measurement of the Zak phase in topological Bloch bands", Nature Physics **9**, 795 (2013) (cited on page 79).

[299] E. J. Meier, F. A. An, and B. Gadway, "Observation of the topological soliton state in the Su–Schrieffer–Heeger model", Nature Communications **7**, 13986 (2016) (cited on page 79).

[300] R. Chaunsali, E. Kim, A. Thakkar, P. G. Kevrekidis, and J. Yang, "Demonstrating an In Situ Topological Band Transition in Cylindrical Granular Chains", Physical Review Letters **119**, 024301 (2017) (cited on page 79).

[301] S. R. Manmana, "Time evolution of one-dimensional Quantum Many Body Systems", AIP Conference Proceedings, Vol. 789, 1 (American Institute of Physics, 2005), pp. 269–278 (cited on page 81).

[302] S. de Léséleuc, D. Barredo, V. Lienhard, A. Browaeys, and T. Lahaye, "Optical Control of the Resonant Dipole-Dipole Interaction between Rydberg Atoms", Physical Review Letters **119**, 053202 (2017) (cited on page 84).

[303] T. Kennedy and H. Tasaki, "Hidden $Z_2 \times Z_2$ symmetry breaking in Haldane-gap antiferromagnets", Physical Review B **45**, 304 (1992) (cited on page 89).

[304] K. Hida, "Ground-state phase diagram of the spin-1/2 ferromagnetic-antiferromagnetic alternating Heisenberg chain with anisotropy", Physical Review B **46**, 8268 (1992) (cited on page 89).

[305] E. J. Bergholtz and Z. Liu, "Topological Flat Band Models and Fractional Chern Insulators", International Journal of Modern Physics B **27**, 1330017 (2013) (cited on page 94).

[306] D. R. Hofstadter, "Energy levels and wave functions of Bloch electrons in rational and irrational magnetic fields", Physical Review B **14**, 2239 (1976) (cited on page 94).

[307] D. Jaksch and P. Zoller, "Creation of effective magnetic fields in optical lattices: the Hofstadter butterfly for cold neutral atoms", New Journal of Physics **5**, 56 (2003) (cited on page 94).

[308] N. Goldman, G. Juzeliūnas, P. Öhberg, and I. B. Spielman, "Light-induced gauge fields for ultracold atoms", Reports on Progress in Physics **77**, 126401 (2014) (cited on page 94).

[309] Y. Miroshnychenko, W. Alt, I. Dotsenko, L. Förster, M. Khudaverdyan, A. Rauschenbeutel, and D. Meschede, "Precision preparation of strings of trapped neutral atoms", New Journal of Physics **8**, 191 (2006) (cited on page 94).

[310] D. Ohl de Mello, D. Schäffner, J. Werkmann, T. Preuschoff, L. Kohfahl, M. Schlosser, and G. Birkl, "Defect-Free Assembly of 2D Clusters of More Than 100 Single-Atom Quantum Systems", Physical Review Letters **122**, 203601 (2019) (cited on page 94).

[311] S. V. Syzranov, M. L. Wall, V. Gurarie, and A. M. Rey, "Spin–orbital dynamics in a system of polar molecules", Nature Communications **5**, 5391 (2014) (cited on page 94).

[312] M. Kiffner, E. O'Brien, and D. Jaksch, "Topological spin models in Rydberg lattices", Applied Physics B **123**, 46 (2017) (cited on pages 94, 112).

[313] U.-J. Wiese, "Ultracold quantum gases and lattice systems: quantum simulation of lattice gauge theories", Annalen der Physik **525**, 777 (2013) (cited on page 95).

[314] F. Görg, K. Sandholzer, J. Minguzzi, R. Desbuquois, M. Messer, and T. Esslinger, "Realization of density-dependent Peierls phases to engineer quantized gauge fields coupled to ultracold matter", Nature Physics **15**, 1161 (2019) (cited on page 95).

[315] L. W. Clark, B. M. Anderson, L. Feng, A. Gaj, K. Levin, and C. Chin, "Observation of Density-Dependent Gauge Fields in a Bose-Einstein Condensate Based on Micromotion Control in a Shaken Two-Dimensional Lattice", Physical Review Letters **121**, 030402 (2018) (cited on page 95).

[316] S. de Léséleuc, D. Barredo, V. Lienhard, A. Browaeys, and T. Lahaye, "Analysis of imperfections in the coherent optical excitation of single atoms to Rydberg states", Physical Review A **97**, 053803 (2018) (cited on page 103).

[317] F. D. M. Haldane, "Model for a Quantum Hall Effect without Landau Levels: Condensed-Matter Realization of the "Parity Anomaly"", Physical Review Letters **61**, 2015 (1988) (cited on page 108).

[318] Y.-F. Wang, Z.-C. Gu, C.-D. Gong, and D. N. Sheng, "Fractional Quantum Hall Effect of Hard-Core Bosons in Topological Flat Bands", Physical Review Letters **107**, 146803 (2011) (cited on pages 109, 118).

[319] Y.-F. Wang, H. Yao, C.-D. Gong, and D. N. Sheng, "Fractional quantum Hall effect in topological flat bands with Chern number two", Physical Review B **86**, 201101 (2012) (cited on page 109).

[320] V. Kalmeyer and R. B. Laughlin, "Equivalence of the resonating-valence-bond and fractional quantum Hall states", Physical Review Letters **59**, 2095 (1987) (cited on page 112).

[321] N. Regnault and B. A. Bernevig, "Fractional Chern Insulator", Physical Review X **1**, 021014 (2011) (cited on page 112).

[322] M. Račiūnas, F. N. Ünal, E. Anisimovas, and A. Eckardt, "Creating, probing, and manipulating fractionally charged excitations of fractional Chern insulators in optical lattices", Physical Review A **98**, 063621 (2018) (cited on pages 112, 118, 120).

[323] U. Schollwöck, "The density-matrix renormalization group", Reviews of Modern Physics **77**, 259 (2005) (cited on page 113).

[324] T. Fukui, Y. Hatsugai, and H. Suzuki, "Chern Numbers in Discretized Brillouin Zone: Efficient Method of Computing (Spin) Hall Conductances", Journal of the Physical Society of Japan **74**, 1674 (2005) (cited on page 115).

[325] T. S. Jackson, G. Möller, and R. Roy, "Geometric stability of topological lattice phases", Nature Communications **6**, 1 (2015) (cited on pages 115, 153).

[326] C. N. Varney, K. Sun, V. Galitski, and M. Rigol, "Quantum phases of hard-core bosons in a frustrated honeycomb lattice", New Journal of Physics **14**, 115028 (2012) (cited on page 116).

[327] Y. Hatsugai, "Characterization of Topological Insulators: Chern Numbers for Ground State Multiplet", Journal of the Physical Society of Japan **74**, 1374 (2005) (cited on page 118).

[328] J. Hauschild and F. Pollmann, "Efficient numerical simulations with Tensor Networks: Tensor Network Python (TeNPy)", SciPost Physics Lecture Notes, 5 (2018), Code available from `https://github.com/tenpy/tenpy` (cited on page 119).

[329] T. Hashizume, *in preparation* (PhD Thesis. University of Strathclyde, 2021) (cited on pages 121, 126, 138).

[330] D. N. Page, "Average entropy of a subsystem", Physical Review Letters **71**, 1291 (1993) (cited on pages 121, 122).

[331] Y. Sekino and L. Susskind, "Fast scramblers", Journal of High Energy Physics **2008**, 065 (2008) (cited on pages 121, 122, 128, 129).

[332] N. Lashkari, D. Stanford, M. Hastings, T. Osborne, and P. Hayden, "Towards the fast scrambling conjecture", Journal of High Energy Physics **2013**, 22 (2013) (cited on pages 121, 122, 128, 129).

[333] P. Hosur, X.-L. Qi, D. A. Roberts, and B. Yoshida, "Chaos in quantum channels", Journal of High Energy Physics **2016**, 4 (2016) (cited on pages 121, 122).

[334] P. Hayden and J. Preskill, "Black holes as mirrors: quantum information in random subsystems", Journal of High Energy Physics **2007**, 120 (2007) (cited on pages 122, 126, 129).

[335] B. Yoshida and A. Kitaev, "Efficient decoding for the Hayden-Preskill protocol", arXiv:1710.03363 (2017) (cited on pages 122, 126).

[336] M. J. Gullans and D. A. Huse, "Dynamical Purification Phase Transition Induced by Quantum Measurements", Physical Review X **10**, 041020 (2020) (cited on page 122).

[337] B. Yoshida and N. Y. Yao, "Disentangling Scrambling and Decoherence via Quantum Teleportation", Physical Review X **9**, 011006 (2019) (cited on pages 122, 126, 128).

[338] N. Bao and Y. Kikuchi, "Hayden-Preskill decoding from noisy Hawking radiation", Journal of High Energy Physics **2021**, 1 (2021) (cited on pages 122, 126, 128).

[339] J. Ye, S. Sachdev, and N. Read, "Solvable spin glass of quantum rotors", Physical Review Letters **70**, 4011 (1993) (cited on page 122).

[340] A. Kitaev, *A simple model of quantum holography*, 2015, Part 1 and Part 2 (cited on page 122).

[341] J. Maldacena and D. Stanford, "Remarks on the Sachdev-Ye-Kitaev model", Physical Review D **94**, 106002 (2016) (cited on page 122).

[342] G. Bentsen, Y. Gu, and A. Lucas, "Fast scrambling on sparse graphs", Proceedings of the National Academy of Sciences of the United States of America **116**, 6689 (2019) (cited on pages 122, 128, 129).

[343] L. Piroli, C. Sünderhauf, and X.-L. Qi, "A random unitary circuit model for black hole evaporation", Journal of High Energy Physics **2020**, 1 (2020) (cited on page 122).

[344] G. Bentsen, T. Hashizume, A. S. Buyskikh, E. J. Davis, A. J. Daley, S. S. Gubser, and M. Schleier-Smith, "Treelike Interactions and Fast Scrambling with Cold Atoms", Physical Review Letters **123**, 130601 (2019) (cited on pages 122, 129).

[345] R. Belyansky, P. Bienias, Y. A. Kharkov, A. V. Gorshkov, and B. Swingle, "Minimal Model for Fast Scrambling", Physical Review Letters **125**, 130601 (2020) (cited on page 122).

[346] Z. Li, S. Choudhury, and W. V. Liu, "Fast scrambling without appealing to holographic duality", Physical Review Research **2**, 043399 (2020) (cited on page 122).

[347] D. S. Weiss, J. Vala, A. V. Thapliyal, S. Myrgren, U. Vazirani, and K. B. Whaley, "Another way to approach zero entropy for a finite system of atoms", Physical Review A **70**, 040302 (2004) (cited on page 122).

[348] J. Yang, X. He, R. Guo, P. Xu, K. Wang, C. Sheng, M. Liu, J. Wang, A. Derevianko, and M. Zhan, "Coherence preservation of a single neutral atom qubit transferred between magic-intensity optical traps", Physical Review Letters **117**, 123201 (2016) (cited on page 122).

[349] J. Zhang, G. Pagano, P. W. Hess, A. Kyprianidis, P. Becker, H. Kaplan, A. V. Gorshkov, Z.-X. Gong, and C. Monroe, "Observation of a many-body dynamical phase transition with a 53-qubit quantum simulator", Nature **551**, 601 (2017) (cited on page 122).

[350] H. Levine, A. Keesling, A. Omran, H. Bernien, S. Schwartz, A. S. Zibrov, M. Endres, M. Greiner, V. Vuletić, and M. D. Lukin, "High-Fidelity Control and Entanglement of Rydberg-Atom Qubits", Physical Review Letters **121**, 123603 (2018) (cited on page 122).

[351] H. Levine, A. Keesling, G. Semeghini, A. Omran, T. T. Wang, S. Ebadi, H. Bernien, M. Greiner, V. Vuletić, H. Pichler, and M. D. Lukin, "Parallel Implementation of High-Fidelity Multiqubit Gates with Neutral Atoms", Physical Review Letters **123**, 170503 (2019) (cited on pages 122, 125).

[352] M. Kim, Y. Song, J. Kim, and J. Ahn, "Quantum Ising Hamiltonian Programming in Trio, Quartet, and Sextet Qubit Systems", PRX Quantum **1**, 020323 (2020) (cited on page 122).

[353] A. W. Young, W. J. Eckner, W. R. Milner, D. Kedar, M. A. Norcia, E. Oelker, N. Schine, J. Ye, and A. M. Kaufman, "Half-minute-scale atomic coherence and high relative stability in a tweezer clock", Nature **588**, 408 (2020) (cited on page 122).

[354] M. M. Müller, M. Murphy, S. Montangero, T. Calarco, P. Grangier, and A. Browaeys, "Implementation of an experimentally feasible controlled-phase gate on two blockaded Rydberg atoms", Physical Review A **89**, 032334 (2014) (cited on pages 122, 125).

[355] D. B. West, *Introduction to graph theory*, Vol. 2 (Prentice Hall Upper Saddle River, 2001) (cited on page 122).

[356] B. Bollobás, *Modern graph theory*, Vol. 184 (Springer Science and Business Media, 2013) (cited on page 122).

[357] J. Beugnon, C. Tuchendler, H. Marion, A. Gaëtan, Y. Miroshnychenko, Y. R. P. Sortais, A. M. Lance, M. P. A. Jones, G. Messin, A. Browaeys, and P. Grangier, "Two-dimensional transport and transfer of a single atomic qubit in optical tweezers", Nature Physics **3**, 696 (2007) (cited on page 123).

[358] P. Diaconis, R. L. Graham, and W. M. Kantor, "The mathematics of perfect shuffles", Advances in Applied Mathematics **4**, 175 (1983) (cited on page 123).

[359] D. Aldous and P. Diaconis, "Shuffling Cards and Stopping Times", The American Mathematical Monthly **93**, 333 (1986) (cited on page 123).

[360] D. Gottesman, "The Heisenberg representation of quantum computers", arXiv:quant-ph/9807006 (1998) (cited on pages 124, 125).

[361] S. Aaronson and D. Gottesman, "Improved simulation of stabilizer circuits", Physical Review A **70**, 052328 (2004) (cited on page 124).

[362] L. Henriet, L. Beguin, A. Signoles, T. Lahaye, A. Browaeys, G.-O. Reymond, and C. Jurczak, "Quantum computing with neutral atoms", Quantum **4**, 327 (2020) (cited on page 125).

[363] L. S. Theis, F. Motzoi, F. K. Wilhelm, and M. Saffman, "High-fidelity Rydberg-blockade entangling gate using shaped, analytic pulses", Physical Review A **94**, 032306 (2016) (cited on page 125).

[364] I. S. Madjarov, J. P. Covey, A. L. Shaw, J. Choi, A. Kale, A. Cooper, H. Pichler, V. Schkolnik, J. R. Williams, and M. Endres, "High-fidelity entanglement and detection of alkaline-earth Rydberg atoms", Nature Physics **16**, 857 (2020) (cited on page 125).

[365] K. A. Landsman, C. Figgatt, T. Schuster, N. M. Linke, B. Yoshida, N. Y. Yao, and C. Monroe, "Verified quantum information scrambling", Nature **567**, 61 (2019) (cited on page 127).

[366] H. Abraham et al., *Qiskit: An Open-source Framework for Quantum Computing*, 2019 (cited on page 128).

[367] M. B. Hastings and T. Koma, "Spectral Gap and Exponential Decay of Correlations", Communications in Mathematical Physics **265**, 781 (2006) (cited on page 129).

[368] D. I. Pikulin and M. Franz, "Black Hole on a Chip: Proposal for a Physical Realization of the Sachdev-Ye-Kitaev model in a Solid-State System", Physical Review X **7**, 031006 (2017) (cited on page 129).

[369] A. Chew, A. Essin, and J. Alicea, "Approximating the Sachdev-Ye-Kitaev model with Majorana wires", Physical Review B **96**, 121119 (2017) (cited on page 129).

[370] I. Danshita, M. Hanada, and M. Tezuka, "Creating and probing the Sachdev–Ye–Kitaev model with ultracold gases: Towards experimental studies of quantum gravity", Progress of Theoretical and Experimental Physics **2017**, 083I01 (2017) (cited on page 129).

[371] T. Schuster, B. Kobrin, P. Gao, I. Cong, E. T. Khabiboulline, N. M. Linke, M. D. Lukin, C. Monroe, B. Yoshida, and N. Y. Yao, "Many-body quantum teleportation via operator spreading in the traversable wormhole protocol", arXiv:2102.00010 (2021) (cited on page 129).

[372] R. Raussendorf and H. J. Briegel, "A One-Way Quantum Computer", Physical Review Letters **86**, 5188 (2001) (cited on page 129).

[373] R. Raussendorf, D. E. Browne, and H. J. Briegel, "Measurement-based quantum computation on cluster states", Physical Review A **68**, 022312 (2003) (cited on page 129).

[374] K. M. Maller, M. T. Lichtman, T. Xia, Y. Sun, M. J. Piotrowicz, A. W. Carr, L. Isenhower, and M. Saffman, "Rydberg-blockade controlled-not gate and entanglement in a two-dimensional array of neutral-atom qubits", Physical Review A **92**, 022336 (2015) (cited on page 142).

[375] P. Goy, J. Liang, M. Gross, and S. Haroche, "Quantum defects and specific-isotopic-shift measurements innsandnphighly excited states of lithium: Exchange effects between Rydberg and core electrons", Physical Review A **34**, 2889 (1986) (cited on page 142).

[376] M. Ciocca, C. E. Burkhardt, J. J. Leventhal, and T. Bergeman, "Precision Stark spectroscopy of sodium: Improved values for the ionization limit and bound states", Physical Review A **45**, 4720 (1992) (cited on page 142).

[377] C.-J. Lorenzen, K. Niemax, and L. R. Pendrill, "Precise measurements of ^{39}K nS and nD energy levels with an evaluated wavemeter", Optics Communications **39**, 370 (1981) (cited on page 142).

[378] M. Mack, F. Karlewski, H. Hattermann, S. Höckh, F. Jessen, D. Cano, and J. Fortágh, "Measurement of absolute transition frequencies of ^{87}Rb to nS and nD Rydberg states by means of electromagnetically induced transparency", Physical Review A **83**, 052515 (2011) (cited on page 142).

[379] J. Deiglmayr, H. Herburger, H. Saßmannshausen, P. Jansen, H. Schmutz, and F. Merkt, "Precision measurement of the ionization energy of Cs i", Physical Review A **93**, 013424 (2016) (cited on page 142).

[380] S. F. Dyubko, M. N. Efimenko, V. A. Efremov, and S. V. Podnos, "Quantum defect and fine structure of terms of Rydberg Na I atoms in S, P, and D states", Quantum Electronics **25**, 914 (1995) (cited on page 142).

[381] C.-J. Lorenzen and K. Niemax, "Quantum Defects of the $n^2P_{1/2,3/2}$ Levels in ^{39}K I and ^{85}Rb I", Physica Scripta **27**, 300 (1983) (cited on pages 142, 187).

[382] I. Johansson, Arkiv för Fysik **15**, 169 (1958), as cited in [381] (cited on page 142).

[383] P. Goy, J. M. Raimond, G. Vitrant, and S. Haroche, "Millimeter-wave spectroscopy in cesium Rydberg states. Quantum defects, fine- and hyperfine-structure measurements", Physical Review A **26**, 2733 (1982) (cited on page 142).

[384] S. Dyubko, V. Efremov, S. Podnos, X. Sun, and K. B. MacAdam, "Quantum defects of the sodium atom in f, g and h states", Journal of Physics B: Atomic, Molecular and Optical Physics **30**, 2345 (1997) (cited on page 142).

[385] P. Risberg, "A revision of the term systems for Na I and K I based on hollow-cathode observations", Arkiv för Fysik **10**, 583 (1956), as cited in [381] (cited on page 142).

[386] J. Han, Y. Jamil, D. V. L. Norum, P. J. Tanner, and T. F. Gallagher, "Rb nf quantum defects from millimeter-wave spectroscopy of cold ^{85}Rb Rydberg atoms", Physical Review A **74**, 054502 (2006) (cited on page 142).

[387] K.-H. Weber and C. J. Sansonetti, "Accurate energies of nS, nP, nD, nF, and nG levels of neutral cesium", Physical Review A **35**, 4650 (1987) (cited on page 142).

[388] K. Afrousheh, P. Bohlouli-Zanjani, J. A. Petrus, and J. D. D. Martin, "Determination of the ^{85}Rb ng-series quantum defect by electric-field-induced resonant energy transfer between cold Rydberg atoms", Physical Review A **74**, 062712 (2006) (cited on page 142).

[389] R. Beigang, K. Lücke, A. Timmermann, P. J. West, and D. Frölich, "Determination of absolute level energies of 5sns^{1}S$_0$ and 5snd^{1}D$_2$ Rydberg series of Sr", Optics Communications **42**, 19 (1982) (cited on page 142).

[390] J. R. Rubbmark and S. A. Borgström, "Rydberg Series in Strontium Found in Absorption by Selectively Laser-Excited Atoms", Physica Scripta **18**, 196 (1978) (cited on page 142).

[391] R. Beigang, K. Lücke, D. Schmidt, A. Timmermann, and P. J. West, "One-Photon Laser Spectroscopy of Rydberg Series from Metastable Levels in Calcium and Strontium", Physica Scripta **26**, 183 (1982) (cited on page 142).

[392] J. A. Armstrong, J. J. Wynne, and P. Esherick, "Bound, odd-parity $J = 1$ spectra of the alkaline earths: Ca, Sr, and Ba", Journal of the Optical Society of America **69**, 211 (1979) (cited on page 142).

[393] M. J. Seaton, "The Quantum Defect Method", Monthly Notices of the Royal Astronomical Society **118**, 504 (1958) (cited on page 143).

[394] D. R. Bates and A. Damgaard, "The calculation of the absolute strengths of spectral lines", Philosophical Transactions of the Royal Society A **242**, 101 (1949) (cited on pages 144, 147).

[395] W. R. Johnson and K. T. Cheng, "Quantum defects for highly stripped ions", Journal of Physics B: Atomic, Molecular and Optical Physics **12**, 863 (1979) (cited on page 145).

[396] C. E. Theodosiou, "Lifetimes of alkali-metal—atom Rydberg states", Physical Review A **30**, 2881 (1984) (cited on pages 145, 146).

[397] M. Marinescu, H. R. Sadeghpour, and A. Dalgarno, "Dispersion coefficients for alkali-metal dimers", Physical Review A **49**, 982 (1994) (cited on pages 145, 146).

[398] M. Pawlak, N. Moiseyev, and H. R. Sadeghpour, "Highly excited Rydberg states of a rubidium atom: Theory versus experiments", Physical Review A **89**, 042506 (2014) (cited on page 145).

[399] C. H. Greene and M. Aymar, "Spin-orbit effects in the heavy alkaline-earth atoms", Physical Review A **44**, 1773 (1991) (cited on page 146).

[400] A. Sanayei, N. Schopohl, J. Grimmel, M. Mack, F. Karlewski, and J. Fortágh, "Quasiclassical quantum defect theory and the spectrum of highly excited rubidium atoms", Physical Review A **91**, 032509 (2015) (cited on page 146).

[401] M. L. Zimmerman, M. G. Littman, M. M. Kash, and D. Kleppner, "Stark structure of the Rydberg states of alkali-metal atoms", Physical Review A **20**, 2251 (1979) (cited on page 147).

[402] S. A. Bhatti, C. L. Cromer, and W. E. Cooke, "Analysis of the Rydberg character of the $5d7d\,^1D_2$ state of barium", Physical Review A **24**, 161 (1981) (cited on page 147).

[403] B. Kaulakys, "Consistent analytical approach for the quasi-classical radial dipole matrix elements", Journal of Physics B: Atomic, Molecular and Optical Physics **28**, 4963 (1995) (cited on page 147).

[404] G. L. Kamta, S. G. N. Engo, M. G. K. Njock, and B. Oumarou, "Consistent description of Klein-Gordon dipole matrix elements", Journal of Physics B: Atomic, Molecular and Optical Physics **31**, 963 (1998) (cited on page 147).

[405] M. S. Safronova and U. I. Safronova, "Critically evaluated theoretical energies, lifetimes, hyperfine constants, and multipole polarizabilities in ^{87}Rb", Physical Review A **83**, 052508 (2011) (cited on page 147).

[406] M. S. Safronova, U. I. Safronova, and C. W. Clark, "Magic wavelengths, matrix elements, polarizabilities, and lifetimes of Cs", Physical Review A **94**, 012505 (2016) (cited on page 147).

[407] I. I. Sobelman, *Atomic Spectra and Radiative Transitions* (Springer, 1992) (cited on page 147).

Acknowledgements

This thesis would not have been possible without the great people with which I was privileged to work together and from whom I learned a lot.

First of all, I would like to thank Hans Peter Büchler for a wonderful time. Thank you for many insightful discussions about various topics and for leaving me a lot of freedom to follow my own ideas as well. I am grateful for your thoughtful advice, your physical intuition, and providing me an inspiring research environment.

I enjoyed my time as a PhD student very much, also because of the excellent atmosphere at the institute. Lengthy lunch break discussions about politics and about physics problems balanced each other in a nearly perfect way. Many thanks go to Jan Kumlin for stimulating conversations since the beginning of our physics studies and Nicolai Lang who provided a lot of advice and assistance in particular but not limited to questions about topology and our computing cluster. Rukmani Bai, Nastasia Makki, and Johannes Mögerle, I enjoyed working with you on the fractional Chern insulator project a lot. Further thanks go to David Peter, Przemyslaw Bienias, Krzysztof Jachymski, Christoph Tresp, Tobias Ilg, Kevin Kleinbeck, Luka Jibuti, Disha Gupta, Katharina Brechtelsbauer, Chris Bühler, and Felix Roser. The last years would not have been as joyful without you. Also, many thanks to Oliver Nagel. Thank you for your extraordinary administrative support that keeps the institute running.

Furthermore, I thank Antoine Browaeys and Thierry Lahaye. Thank you for giving me the possibility to work together on various exciting projects and providing me the opportunity for several visits. It was always very interesting for me to learn details of your experiments so that I could include them in my simulations and think about how one can make use of them for new proposals. Many thanks go to Sylvain de Léséleuc, Vincent Lienhard, Pascal Scholl, and Daniel Barredo for patiently explaining me all the experimental particularities.

Huge thanks also go to Tomohiro Hashizume, Gregory Bentsen, and Andrew Daley. I greatly appreciate your hospitality, the joint projects, and the informative discussions – both in real life and, due to the coronavirus, virtually. Andrew Daley, thank you for letting me visit your research group.

I would also like to thank Maria Daghofer who immediately agreed to review

my thesis and Tilman Pfau who promptly accepted to preside the examination. Moreover, many thanks go to Henri Menke; it is awesome to have such a skilled co-developer for the `pairinteraction` software. I learned a lot from you about continuous integration and unit testing. Also, many thanks to Sebastian Hofferberth who helped us understanding the physics that underlies the software. In addition, I would like to thank the members of the QRydDemo project for many inspiring discussions, in particular Alice Pagano, Philipp Ilzhöfer, and Florian Meinert. Huge thanks also go to my friends for some (physics) discussions but also countless hiking adventures, board games nights, and much more.

Finally, I would like to thank my parents and my brother. Thank you for all your support along my way, without which I would not be where I am today. Nina, thank you for always supporting me!